CWP-236
December 1996

Seismic Processing in Transversely Isotropic Media

Tariq Alkhalifah

— Doctoral Thesis —
Geophysics

Center for Wave Phenomena
Colorado School of Mines
Golden, Colorado 80401
303/273-3557

ABSTRACT

The main difficulty in extending seismic processing to anisotropic media is the recovery of anisotropic velocity fields from surface reflection data. Here, I suggest carrying out velocity analysis for transversely isotropic (TI) media by inverting the dependence of P-wave moveout velocities on the ray parameter. The inversion technique is based on the exact analytic equation for the normal-moveout (NMO) velocity for dipping reflectors in anisotropic media, derived by Tsvankin (1995).

I show that P-wave NMO velocity in homogeneous TI media with a vertical symmetry axis (VTI media) depends just on the zero-dip value $V_{\rm nmo}(0)$ and a new effective parameter η that reduces to the difference between Thomsen parameters ϵ and δ in the limit of weak anisotropy. The inversion procedure makes it possible to obtain η and reconstruct the NMO velocity as a function of ray parameter using moveout velocities for two different dips. Moreover, $V_{\rm nmo}(0)$ and η determine not only the NMO velocity, but also long-spread (nonhyperbolic) P-wave moveout for horizontal reflectors and time-migration impulse response. This means that inversion of dip-moveout information allows one to perform all time-processing steps in TI media [NMO, dip-moveout correction (DMO), and time migration] using only surface P-wave data. Isotropic time-processing methods remain entirely valid for elliptical anisotropy ($\epsilon = \delta$).

Accurate time-to-depth conversion, however, requires that the vertical velocity V_{P0} be resolved independently. In some cases V_{P0} is known (e.g., from check shots or well logs); then the anisotropies ϵ and δ can be found by inverting two P-wave NMO velocities corresponding to a horizontal and a dipping reflector. If no well information is available, all three parameters (V_{P0}, ϵ, and δ) can be obtained by combining the dip inversion results with shear-wave information, such as the P-SV or SV-SV wave NMO velocities for a horizontal reflector.

Generalization of the single-layer NMO equation for layered anisotropic media with a dipping reflector provides a basis for extending anisotropic velocity analysis to vertically inhomogeneous media. This NMO equation is based on a root-mean-square (rms) average of interval NMO velocities that correspond to a single ray parameter, that of the dipping event. Therefore, interval NMO velocities [including the normal-moveout velocity for horizontal events, $V_{\rm nmo}(0)$] can be extracted from the stacking velocities using a Dix-type differentiation procedure.

DMO impulse responses in typical transversely isotropic (TI) models (such as those associated with shales) deviate substantially from the familiar elliptical shape associated with responses in homogeneous isotropic media (to the extent that triplications arise even where the medium is homogeneous). Such deviations can exceed those caused by vertical inhomogeneity, thus emphasizing the importance of taking anisotropy into account in DMO processing.

Time migration, like dip moveout, depends on the same two parameters in vertically inhomogeneous media, namely $V_{\text{nmo}}(0)$ and η, both of which can vary with depth. Therefore, $V_{\text{nmo}}(0)$ and η estimated using the dip dependency of P-wave moveout velocity can be used for TI time migration.

Application of anisotropic processing to P-wave data from offshore Africa and offshore Trinidad demonstrates the importance of considering anisotropy, especially as it pertains to focussing and imaging of dipping events.

TABLE OF CONTENTS

ACKNOWLEDGMENTS

First and foremost, thanks to my advisor through my master and Phd studies, Professor Ken Larner, who was instrumental in my scientific development to this point. His guidance helped me at key moments and his review of the Thesis made it the way it is now.

Thanks to my co-advisor Dr. Ilya Tsvankin for the many suggestions and discussions. Thanks to Professors Tom Boyd, John Scales, Norm Bleistien and Tim Brown for serving on my committee.

A special mention to my dear Professor Jack Cohen, who passed away just prior to the completion of my thesis. He served in my committee, was always extremely helpful. He is one of the nicest persons I ever met, and I will miss him.

Thanks to John Toldi of Chevron Overseas Petroleum, Inc., for many helpful suggestions and for providing the Angola field data. Thanks to Dave Rampton of Amoco for providing the Trinidad field data.

Everybody at the Center for Wave Phenomena (CWP) has been very kind and helpful. My study at Colorado School of Mines was financially supported by KACST, Saudi Arabia, and technically supported by CWP; I am grateful to them.

I am in debt to my parents; my father Ali Alkhalifah, and my mother Monira for their endless support.

Finally, I am definitely in debt to my wife Athra; her sacrifice, love, and support through the years made this possible.

Chapter 1

INTRODUCTION

Progress in accounting for anisotropy in seismic processing has been slow, mostly as a result of the difficulty in obtaining anisotropic velocity fields from surface seismic data. For instance, there exist a number of migration algorithms for transversely isotropic media (VerWest, 1989; Sena and Toksoz, 1993; Alkhalifah, 1995b), but their application requires knowledge of the anisotropic velocity model. Clearly, the recovery of several independent elastic coefficients needed to reconstruct the anisotropic velocity function is much more complicated than is conventional velocity analysis for isotropic media, especially due to the limited angle coverage of reflection surveys.

Despite the growing recognition in the geophysical community of the presence of anisotropy, skepticism still exists regarding its importance. It is tempting to suggest that anisotropy does not exist for surface seismic P-wave data or that it is weak enough to ignore. The isotropic assumption seems to have worked well through the years; this is understandable since if one does not look for the existence of anisotropy in P-wave data, it can often go unnoticed. In addition, the laws that govern the physics of wave propagation in anisotropic media result in equations of wave propagation that are much more complicated than those associated with isotropic media, requiring, among other things, multi-parameter representation and extraction. Since simple isotropic processing seems to work in practice, what then is the issue with ignoring the presence of anisotropy? Simply, where the subsurface is anisotropic, and evidence increasingly suggests that anisotropy is rather pervasive, processing that makes the erroneous assumption of isotropy yields errors in seismic images and, thus, interpretations. One of the anisotropy-related phenomena that was recognized more than a decade ago is that of mis-ties in time-to-depth conversion caused by the difference between the stacking and vertical velocity in anisotropic media (Banik, 1984). Also recently attracting the attention of the exploration community are the difficulties experienced by conventional processing methods (i.e., those based on the assumption of isotropy) in imaging of dipping reflectors, such as fault planes, below transversely isotropic formations (Larner and Cohen, 1993; Alkhalifah and Larner, 1994). Therefore, the first question that comes to mind pertains to the existence and importance of considering anisotropy in seismic processing.

1.1 Does anisotropy exist on the surface seismic exploration scale, and is it important?

The presence of anisotropy has been, through the years, well documented in laboratory studies of cores using high-frequency ($>$ 100 kHz; i.e., short wavelength)

seismic waves (e.g., Thomsen, 1986). Researchers have noticed velocity variations of more than 30% between vertical and horizontal directions of wave propagation in such cores. However, the behavior of low-frequency ($\approx$ 30 Hz; i.e., long wavelength) seismic waves (associated typically with surface exploration) penetrating the subsurface differs from that of the high-frequency ones; the high-frequency portion of the seismic wavefield reacts to subsurface features of various size differently than do low-frequency portions. Such behavior is referred to as dispersion.

Most of the emphasis during the past decade has been focused on the influence of anisotropy on the behavior of shear waves (e.g., Crampin, 1985). Splitting of the shear waves into two components (a fast shear wave and a slow one) has been routinely observed both in vertical seismic profiles (VSP) and in surface seismic exploration data. Such splitting cannot be explained within the confines of the isotropic theory; anisotropy must be present to cause splitting of the components. Thus, if long-wavelength shear waves are influenced by anisotropy due to fractures, then theory tells us that P-waves would also be influenced by the same anisotropy that caused the shear-wave splitting. The influence for P-waves is manifested in the change of its velocity with direction.

Some of the anisotropy on the surface-seismic exploration scale, unlike that on laboratory-size samples, which may be attributed primarily to intrinsic anisotropy (anisotropy inherent in the crystal structure of the rock), is caused by layering of thickness that is smaller than the typical seismic wavelength. Rarely do we look at outcrops without noticing their fine layering. These outcrops are usually of a size of a single typical surface seismic wavelength ($\approx$ 100 m). Therefore, seismic P-waves traveling parallel to the thin layering is expected to encounter greater stiffness, and thus travel faster than those traveling perpendicular to the layering, where the sediments, due to the layering, are looser. Although the fine layering is usually considered as 1-D heterogeneity, its influence on long-period seismic waves is well approximated (especially kinematically) by a transversely isotropic medium with a symmetry axis perpendicular to layering (Postma, 1955; Krey and Helbig, 1956; Berryman, 1979; Hudson, 1981). Such heterogeneous media are thus considered to be equivalently anisotropic.

What better way to prove the existence of P-wave anisotropy and its importance than to observe its influence on actual field data? Figure 1.1 shows constant-velocity stacks extracted from data from offshore Africa (more details on these data are given later) after applying normal moveout correction, with each of several constant stacking velocities, followed by isotropic homogeneous dip-moveout (DMO) correction (such DMO is independent of velocity). A goal of DMO processing is to focus both horizontal and dipping events on the same velocity panel. Here, however, while reflectors with relatively small dip ($\approx$6 degrees) in Figure 1.1 are imaged best with a stacking velocity of 2200 m/s, the steep reflector (fault) comes into focus at a much higher velocity (2400-2450 m/s). Thus, the conventional DMO processing has failed to remove the dip-dependence of stacking velocity. As a result, stacking will produce a weak, poorly-focussed image of the dipping fault plane.

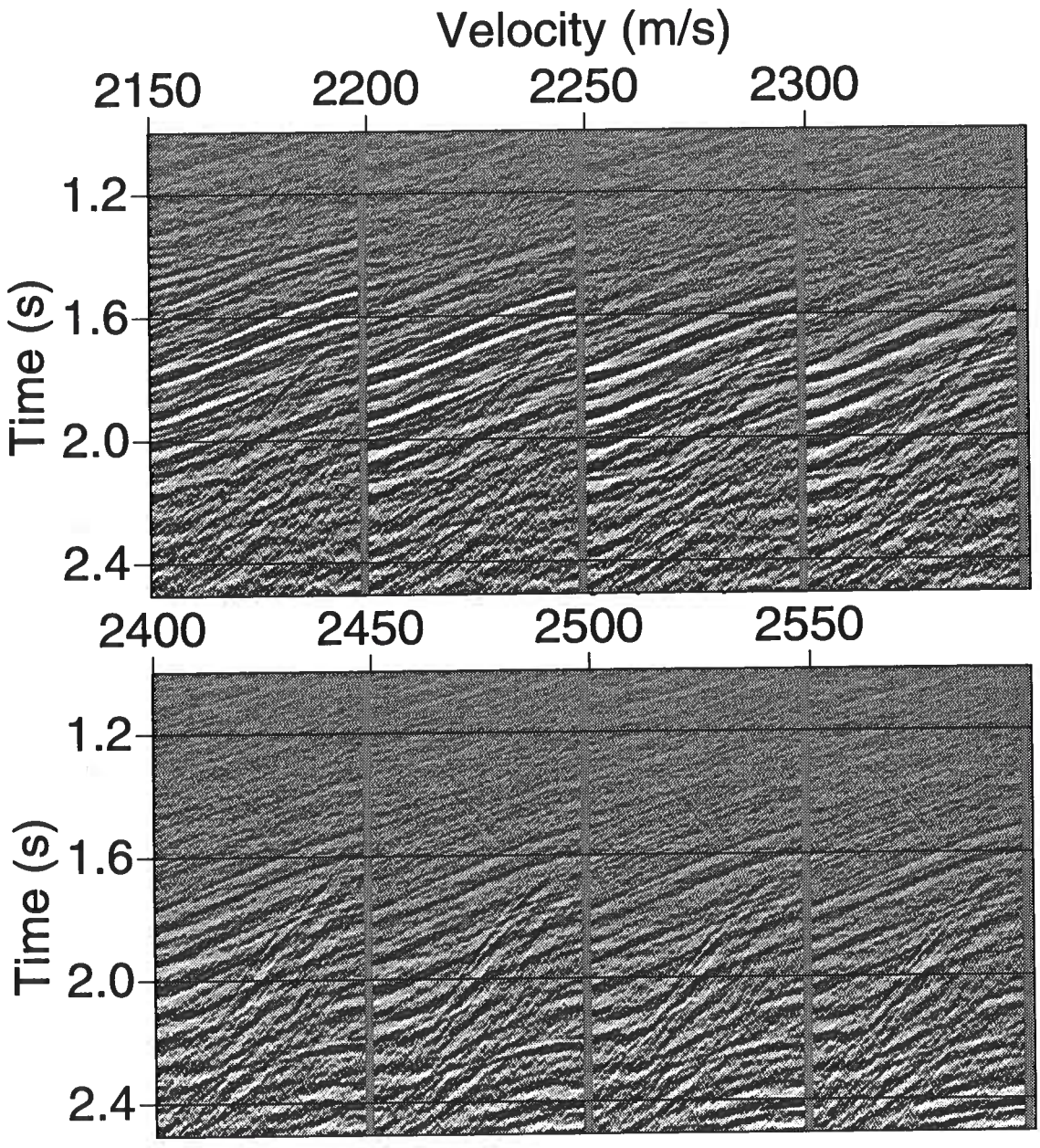

FIG. 1.1. Constant-velocity stacks for the offshore Africa area (below the gray bar in Figure 1.4) after the conventional sequence of NMO and constant-velocity, isotropic DMO. The velocity values at the top correspond to stacking velocities for horizontal reflectors.

Conventional DMO fails here because the stacking (moveout) velocity increases with dip much faster than in the isotropic media assumed in the DMO algorithm. If the shortcoming of the DMO processing had been caused by a vertical velocity gradient, then the steep event in Figure 1.1 would have been imaged at a *lower* stacking velocity than that of the events with small dips (Hale and Artley, 1993). Given that velocity increases overall with depth, the implication is that, here, anisotropy introduces an error in conventional (isotropic, homogeneous) DMO that is contrary to and stronger than that due to vertical velocity variation.

Anisotropy also often manifests itself through mis-ties in time-to-depth conversion. Probably, there is no clearer or more telling evidence to the presence of anisotropy than the constant and consistent over-estimation of reflector depths using seismic (imaging) velocities when shales are present (Banik, 1984). Such over-estimation is unexplainable under the isotropic medium assumption. Although the imaging issues (i.e., DMO and time migration) are the primary subject of this thesis, a brief look at errors in time-to-depth conversion shows evidence of large anisotropy and provides some insight into the geologic formations responsible for the anisotropic phenomena. Figure 1.2 presents such evidence in the form of a comparison between average velocities derived from check shots and those derived from reflection moveout in the surface-seismic data from offshore Africa. Note that the separation of the two curves continues to increase down to about 2 s two-way time, then remains constant for the remainder of the measurements. The maximum separation amounts to a 12% mis-tie in the average velocity; similar sizable mis-ties have been observed by Ball (1995) in an adjacent area and attributed to the influence of anisotropy. Such mis-ties are not exclusive to the Western African region; mis-ties have been observed in the Gulf of Mexico (Meadows and Abriel, 1994), the North Sea (Banik, 1984; Whitmore et al., 1995), Southeast Asia (Desegaulx et al., 1994), and South America (Uzcategui and Mujica, 1995), as well as many other places. All these authors attribute the mis-ties to anisotropy most often in shale formations.

Shales, no doubt, are anisotropic and represent the main source of anisotropy sedimentary basins (Banik, 1984). Specifically, shales which overlay over 70 percent of hydrocarbon exploration targets, are known to be transversely isotropic due to microstructure associated with the layering of fine clay platelets (Sayers, 1994). In most cases, the extent of the presence of shales determines the level of the anisotropy influence on seismic processing.

1.2 What's next?

Once the importance of anisotropy is accepted, two further impediments to taking its presence into account must be overcome: (1) processing algorithms that include anisotropy are more complex than those that ignore it, and (2) even with such processing capability at hand, heretofore it has been difficult to estimate the anisotropy parameters required by these algorithms. The second problem has seemed to be especially intimidating. Estimation of the four or more parameters that fully characterize

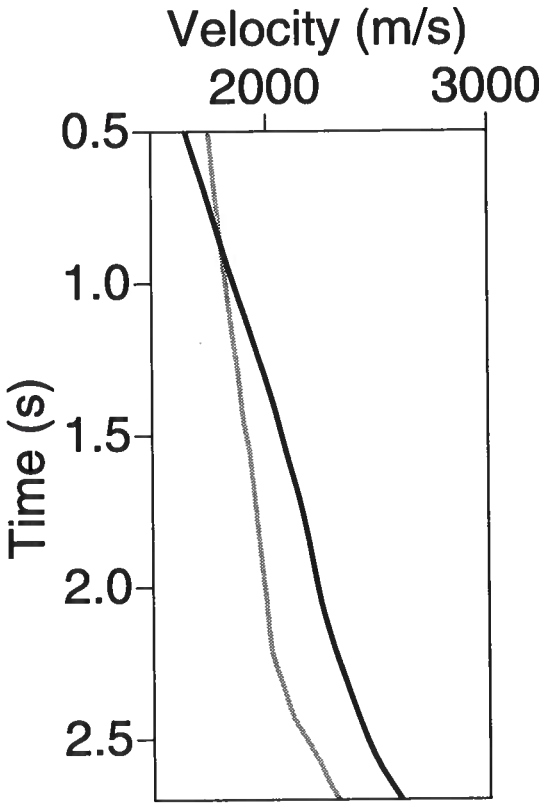

FIG. 1.2. Average P-wave vertical velocity from check-shot data (gray curve) and stacking velocity from surface seismic data converted into the average velocity (black curve), both as functions of vertical time. The data are taken from same area as in Figure 1.4.

P-wave propagation in typical anisotropic media has seemed not only difficult (estimating the one critical parameter for isotropic media — velocity — is difficult enough), the task also seemed to require additional measurements beyond those obtained in conventional seismic surveys [e.g., cross-well, vertical seismic profile (VSP), or auxiliary S-wave data]. For instance, conventional velocity analysis based on short-spread moveout (stacking) velocities does not provide enough information to determine the true vertical velocity in transversely isotropic media with a vertical symmetry axis (VTI media). (Velocity in VTI media varies with direction of propagation away from the vertical, but not with azimuth.) In this thesis, I address these two impediments; the rest of this introduction is basically an outline of the succeeding chapters.

The focus of this work is on P-wave (or quasi-P-wave) anisotropy. This is partly because most seismic reflection surveys currently available are tuned to recording P-waves and partly because of the high quality of P-wave data compared to S-wave data. Throughout the thesis I also consider the most common anisotropic model – VTI media – but I *do not* assume that anisotropy is weak or elliptical. Both assumptions are inappropriate for shales, which represent, as mentioned earlier, the most common source of transverse isotropy in sedimentary basins.

1.2.1 Anisotropic inversion

Existing work on anisotropic traveltime inversion of reflection data has focussed on horizontally layered subsurface models (Byun and Corrigan, 1990; Sena, 1991; Tsvankin and Thomsen, 1995). As shown by Tsvankin and Thomsen (1995), P-wave moveout from horizontal reflectors is insufficient to recover the parameters of transversely isotropic media with a vertical symmetry axis (VTI), even if long spreads (twice the reflector depth) are used. The reason for this ambiguity is the trade-off between the vertical velocity and anisotropic coefficients, which cannot be overcome even by using the nonhyperbolic portion of the moveout curve. Tsvankin and Thomsen (1995) conclude that the only way to carry out stable inversion of surface reflection data is to combine long-spread P and SV moveouts; however, this method encounters many practical difficulties. Therefore, to make the anisotropic inversion feasible, P-wave reflection moveout in laterally homogeneous media should be supplemented by additional information (e.g., the vertical velocity from check shots or well logs).

The presence of dipping reflectors provides us with the opportunity of extending the angle coverage of the input data beyond that available from data where the subsurface is horizontal. Here, I develop an inversion technique for transversely isotropic media based on the analytic equation for normal moveout (NMO) velocity for dipping reflectors derived by Tsvankin (1995). I recast this equation as a function of ray parameter and use it in inverting dip-dependent P-wave NMO velocities for the anisotropic coefficients. Analysis of the stability of the inverse problem by means of the Jacobian matrix is followed by the actual numerical inversion procedure via the Newton-Raphson method. I show that this approach makes it possible to obtain a family of anisotropy solutions that all have the same NMO velocity for all possible

dips, as well as the same nonhyperbolic moveout for horizontal reflectors, and the same time-migration impulse response. This family of solutions is fully described by just two, rather than four, anisotropy parameters: the NMO velocity for a horizontal reflector and a new anisotropic coefficient that I denote as η. Then, the results are extended to vertically inhomogeneous anisotropic media by developing a Dix-type procedure (Dix, 1955) intended to give estimates of the NMO velocity in any individual layer from surface reflection data.

1.2.2 Anisotropic DMO

After we estimate the parameters, the next step is to apply processing that takes anisotropy into consideration and makes use of the estimations. Conventional processing flow includes NMO and DMO followed by poststack migration. The process of transforming prestack data to zero offset (TZO) accomplishes moveout correction for reflections from horizontal and dipping reflectors. Specifically, in an isotropic, homogeneous medium, TZO includes kinematically both normal moveout correction (NMO) and dip moveout correction (DMO). I use the term TZO to describe the one-step ray-tracing process used here to map nonzero-offset traveltimes directly to zero-offset times. Therefore, DMO correction corresponds to TZO without the moveout correction for horizontal reflectors.

To properly correct for horizontal events prior to stacking the data, a nonhyperbolic moveout correction instead of conventional hyperbolic NMO is needed. Such modification will require adjustment in the DMO step to include the nonhyperbolic correction. Simply stated, NMO plus DMO should result in a perfect kinematic correction from nonzero-offset to zero-offset. It is preferable, however, to apply NMO even in anisotropic media and leave the nonhyperbolic correction to the DMO step.

Extensions of DMO algorithms to anisotropic media have been discussed in several papers. Uren et al. (1990) showed that the DMO method of Forel-Gardner (1988) can be modified to handle, in a straightforward way, elliptically anisotropic models. Elliptical anisotropy, however, is a special case of transverse isotropy that is not typical of the subsurface (Thomsen, 1986). Anderson and Tsvankin (1995) extended the dip-moveout method developed by Hale (1984) to treat TI media using the analytic formulation for NMO velocity as a function of reflector dip given by Tsvankin (1995). Nevertheless, Hale's original DMO and its anisotropic counterpart are relatively slow; moreover, the process is based on the hyperbolic moveout approximation, which, as we shall see, is invalid for typical TI media. Although Anderson and Tsvankin (1995) show that nonhyperbolic moveout is small for dipping reflectors, it is significant for horizontal and mildly dipping reflectors.

The combination of anisotropic ray tracing (Červený, 1972) and dip-decomposition (Jakubowicz, 1990) in transforming prestack data to zero-offset (or in applying DMO) is particularly well suited to handling the nonhyperbolic moveout in homogeneous or inhomogeneous TI media. For such media, with accurate traveltime computations such as by ray tracing, data can be transformed to zero-offset, thus lessening the severity

of muting conventionally done on the far offsets. Artley and Hale (1994) have shown that such a DMO method, although slower than log-stretch Fourier methods (Notfors and Godfrey, 1987), is efficient and more accurate. Here, I find that the ray-tracing approach is as efficient for anisotropic media as for isotropic media.

1.2.3 Anisotropic migration

Although modern migration algorithms now can treat 3-D data from areas of relatively complex structure and can accommodate turning waves associated with dip beyond 90 degrees, only recently has anisotropy been taken into account. Anisotropy may cause considerable departure of traveltime curves from those expected in comparable isotropic media. Such departures will influence the accuracy of both migration and velocity analysis. For some transversely isotropic (TI) media, for example, large position errors could arise for steep reflectors when anisotropy is ignored in poststack migration (Larner and Cohen, 1993; Alkhalifah and Larner, 1994).

Migration algorithms for special cases of anisotropy have been developed in the past few years. VerWest (1989) developed a seismic migration algorithm for elliptically anisotropic media; however, as mentioned above, this type of anisotropy is usually a poor approximation for subsurface formations. Uren, Gardner and McDonald (1990) found a migrator equation for anisotropic homogeneous media that works in the frequency-wavenumber (f-k) domain. Kitchenside (1991) describes a phase-shift-based approach to poststack migration for transversely isotropic media with vertical and mild lateral heterogeneity. Gonzalez, et al. (1991) made an adjustment to prestack migration approach of Stolt (1978) that takes transverse isotropy into account, and Uzcategui (1995) uses stable explicit operators for poststack depth migration for TI media.

Because the main assumption in the new parameterization is that the data remain in the time rather than depth domain, the poststack migration considered here is primarily a time one. (Implications where depth migration is a necessity will be discussed later.) Two popular algorithms fit the time-domain criterion; Stolt's (1978) Fourier domain zero-offset migration and Gazdag's (1978) phase-shift migration. The latter kinematically handles vertical inhomogeneity, whereas the Stolt method does not. Both algorithms can be modified to handle anisotropy (Kitchenside, 1991; Gonzalez, et al., 1991). By using stretch techniques (chosen empirically), Stolt migration can be modified to handle factorized TI media (i.e., the TI model in which all ratios among the elastic coefficients for TI media are independent of position). The modification to both algorithms includes using a dispersion relation suited for TI media.

Depth migration is also useful when information regarding the vertical velocity is available, using, for example, well-log data. Gaussian beam migration (GBM) has emerged in the past few years as a desirable method for subsurface depth imaging (Hale and Witte, 1992). Among its features are acceptable computational efficiency, robustness with respect to ray caustics and shadows, the ability to image reflector dips greater than 90 degrees with turning waves, and straightforward extensions for

migration of nonzero-offset sections and 3-D data (Hill, 1990; Hale, 1992).

For a couple of reasons, Gaussian beam migration is particularly suited for anisotropic media. Primarily, the relatively small amount of ray tracing needed to perform Gaussian beam migration minimizes the incremental cost in modifying the algorithm for anisotropic media. Second, the method can readily handle caustics including those associated specifically with anisotropic media, such as, for example, SV-wave caustics that arise even in homogeneous media. Also, the Gaussian beam method can readily treat data from general inhomogeneous and anisotropic media with any reflector orientation.

1.3 Field data application

Probably, the greatest testament to the importance of considering anisotropy in processing is improvements achieved on real data when anisotropy is taken into consideration over that obtained using isotropic methods.

In addition to many other places in the world, the western Africa region is known to have massive shale formations. These shales have considerable anisotropy that can be well approximated using a VTI model. The sedimentary sequences of West Africa are economically important because the basinal lake shales include exceptional source rocks for petroleum. Most of the oil reserves of Gabon, Congo, Zaire and Angola are sourced from this lacustrine section. In addition, the same lacustrine section on the South American side of the continental rift between Africa and South America has been proven to contain source rocks for nearly all of Brazil's petroleum reserves (Brice et al., 1983).

Cabinda is a small, detached enclave of Angola (Figure 1.3) that contains most of that country's oil reserves. To date, approximately 25 percent of the oil in Cabinda has been found within presalt reservoirs of marginal lacustrine carbonate and sandstone. As in other areas of the Lower Congo basin, basinal lacustrine shale is the source rock for this oil. Figure 1.4 is a seismic section from that region that I will study in this thesis.

The sedimentary sequence up to 2 s in Figure 1.4 corresponds to a regional subsidence period (Brice et al., 1983). The structural style of the regional subsidence sequence is typical of a rapidly deposited regressive sequence. It is marked by high-pressure shale movement and related growth faulting. Sedimentation during the regional subsidence period resulted in a shaley, clastic sequence. This unit is dominated by prograding wedges (Figure 1.5) with a sigmodial shape, implying that these prograding wedges are dominated by shales rather than sands. A tectonic rift has induced regional subsidence that resulted in numerous faults within the Tertiary shale deposits. Some of these faults serve as important seals for some post-salt reservoirs. Therefore, to get a better idea of the reservoir location and geometry, we must properly focus and image these faults. Because of the presence of shales this task requires use of an anisotropic processing sequence.

To counter any perception that anisotropy is present only in the West African

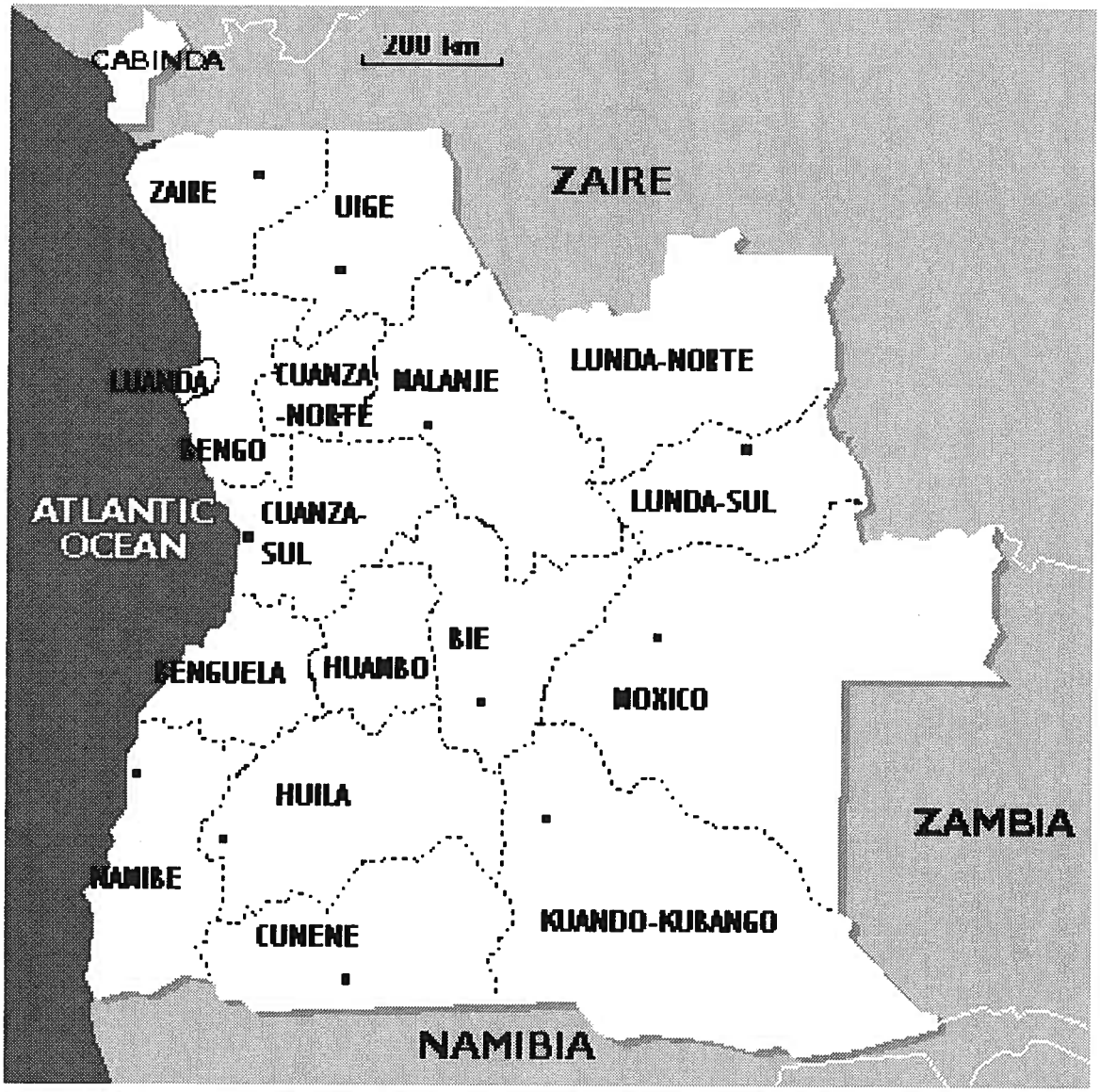

FIG. 1.3. Location map, Cabinda, R. P. Angola (Brice et al., 1983).

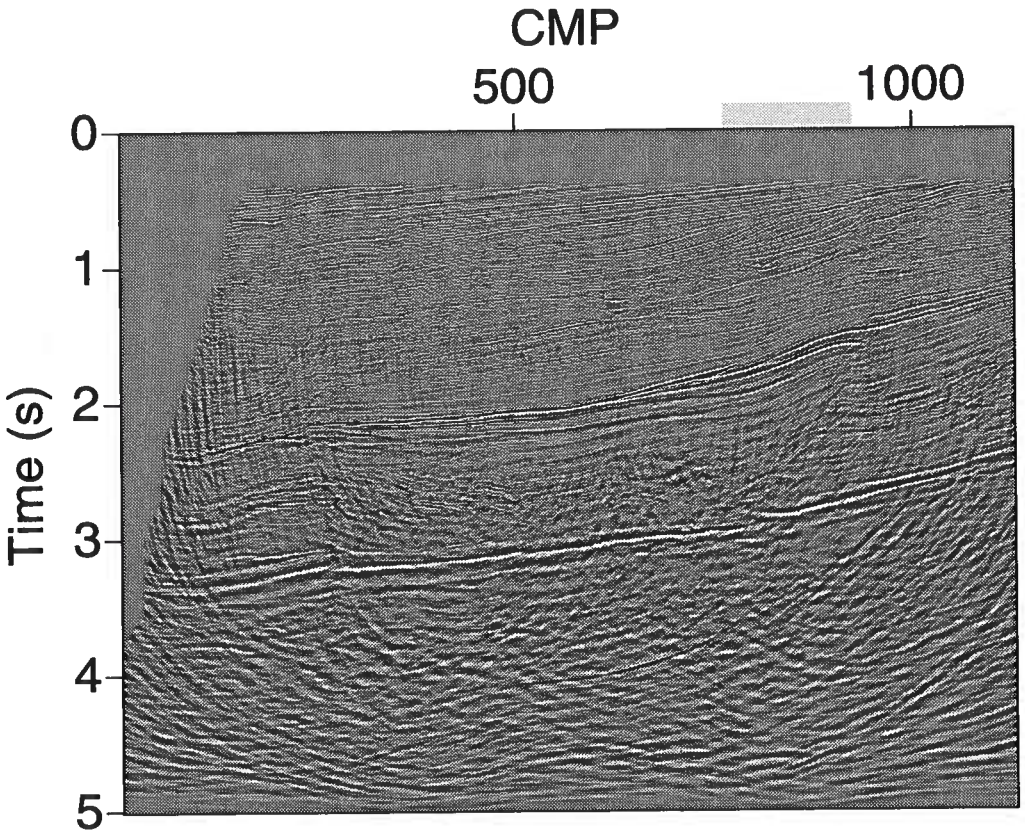

FIG. 1.4. Time-migrated seismic line (offshore Africa). The gray bar to the left of CMP 1000 shows the CMP gathers that are examined in Figures 1.1.

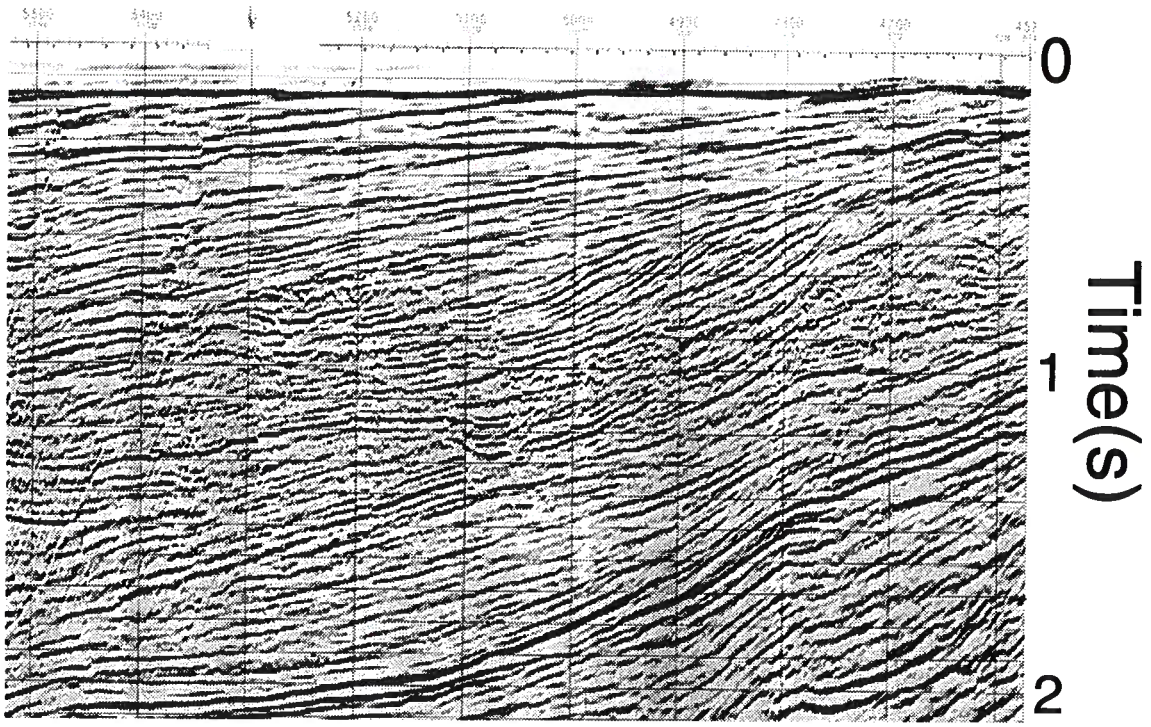

FIG. 1.5. Seismic section from the Cabinda region depicting the presence of prograding wedges.

region, I also include examples from Trinidad, South America. This recently oil-enriched region is dominated by clastic deposits that contain a mixture of shales and sands. Because of the presence of sands, the influence of anisotropy in the region is less evident than in the western African example. Nevertheless, taking anisotropy into account yields better images, as well as better understanding of the subsurface structure.

Chapter 2

A NEW PARAMETERIZATION FOR TIME-RELATED PROCESSING IN TI MEDIA

As mentioned earlier, the presence of dipping reflectors provides us with the opportunity of extending the angle coverage of the input data without using long CMP spreads. Here, I develop an inversion technique for transversely isotropic media based on the analytic equation for NMO velocity for dipping reflectors derived by Tsvankin (1995). I recast this equation as a function of ray parameter and use it in inverting dip-dependent P-wave NMO velocities for the anisotropic coefficients. Analysis of the stability of the inverse problem by means of the Jacobian matrix is followed by the actual numerical inversion procedure via the Newton-Raphson method. I show that the inversion of NMO velocity makes it possible to obtain a family of solutions that all have the same NMO velocity for all possible dips, as well as the same nonhyperbolic moveout for horizontal reflectors, and the same time-migration impulse response. This family of solutions is fully described just by two parameters: the NMO velocity for a horizontal reflector and a new anisotropic coefficient that I denote as η.

2.1 NMO velocity for dipping reflectors in TI media

The analysis here is based on the equation for the normal-moveout (short-spread) velocity for dipping reflectors in a homogeneous anisotropic medium derived by Tsvankin (1995):

$$V_{\rm nmo}(\phi) = \frac{V(\phi)}{\cos\phi}\,\frac{\sqrt{1+\frac{1}{V(\phi)}\frac{d^2V}{d\theta^2}}}{1-\frac{\tan\phi}{V(\phi)}\frac{dV}{d\theta}}\,, \tag{2.1}$$

where V is the phase velocity as a function of the phase angle θ (θ is measured from vertical) and ϕ is the dip of the reflector; the derivatives are evaluated at the dip ϕ.

Formula (2.1) is valid in symmetry planes of any anisotropic medium and is not restricted to any particular wave type; it assumes, however, that the incidence (sagittal) plane is the dip plane of the reflector. Although equation (2.1) is applicable to any single-mode propagation (P-wave or S-wave), here I will use it only for P-waves in VTI media.

The NMO velocity [equation (2.1)] is a function of phase velocity $V(\theta)$ and its first two derivatives taken at the dip ϕ. Unfortunately, reflection data do not carry any explicit information about the dip; rather, we can count on recovering the ray parameter $p(\phi)$ corresponding to the zero-offset reflection.

$$p(\phi) = \frac{1}{2}\frac{dt_0}{dx_0} = \frac{\sin\phi}{V(\phi)}, \tag{2.2}$$

where $t_0(x_0)$ is the two-way traveltime on the zero-offset (or stacked) section, and x_0 is the midpoint position.

In the numerical analysis of the NMO velocity, the replacement of the angle ϕ by the ray parameter p (horizontal slowness) does not pose any serious problem. Phase velocity and phase angle can be found from the Christoffel equations in a straightforward fashion if horizontal slowness is known, as shown in Appendix A. At the same time, the substitution of p may change the influence of the elastic coefficients on the NMO velocity since the form of the equation will change.

In conventional notation, P-wave propagation in transversely isotropic models is described by four stiffness coefficients: c_{11}, c_{33}, c_{13}, and c_{44}. The number of independent parameters, however, can be reduced by using the notation suggested by Thomsen (1986). Formally, P-wave phase and group velocity depend on four Thomsen parameters: P- and S-wave vertical velocities, V_{P0} and V_{S0}, and the dimensionless anisotropy parameters ϵ and δ defined as

$$\epsilon \equiv \frac{c_{11} - c_{33}}{2c_{33}} \tag{2.3}$$

and

$$\delta \equiv \frac{(c_{13} + c_{44})^2 - (c_{33} - c_{44})^2}{2c_{33}(c_{33} - c_{44})}. \tag{2.4}$$

However, the influence of the shear-wave vertical velocity on P-wave velocities and traveltimes is practically negligible, even for strong anisotropy (Tsvankin and Thomsen, 1994; Alkhalifah and Larner, 1994). Therefore, in my inversion procedure I will attempt to recover only the parameters V_{P0}, ϵ, and δ.

For a horizontal reflector, equation (2.1) reduces to the well-known formula for NMO velocity (Thomsen, 1986):

$$V_{\rm nmo}(0) = V_{P0}\sqrt{1 + 2\delta}. \tag{2.5}$$

The trade-off between the vertical velocity V_{P0} and parameter δ cannot be resolved even if the NMO velocities for all three (P, SV, and SH) waves from a horizontal reflector are known (Tsvankin and Thomsen, 1995). On the other hand, if V_{P0} is known (e.g., from check shots or well logs), the zero-dip moveout velocity [equation (2.5)] can be used to obtain δ.

Analytic and numerical analysis performed by Tsvankin (1995) shows that the dip-dependence of P-wave NMO velocities is controlled mostly by the difference between ϵ and δ. Therefore, if δ has been determined from $V_{\rm nmo}(0)$, we should be able to find ϵ from a single NMO velocity for a dipping reflector. It is also interesting to examine the possibility of recovering all three parameters (V_{P0}, ϵ and δ) from NMO velocities at three (or more) distinct dips. This analysis is performed in the next sections.

2.2 NMO velocity for elliptical and weak anisotropy

Before proceeding with the numerical inversion procedure, I will elucidate the peculiarities of equation (2.1) by considering the special cases of elliptical and weak anisotropy. Unfortunately, NMO equation (2.1) is too complex to allow for analytic insight into the contributions of the anisotropic coefficients for general transverse isotropy.

For elliptical anisotropy ($\epsilon = \delta$), the NMO velocity as a function of ray parameter is given by (Appendix A)

$$V_{\text{nmo}}(p) = \frac{V_{\text{nmo}}(0)}{\sqrt{1 - p^2 V_{\text{nmo}}^2(0)}}. \tag{2.6}$$

Equation (2.6) is a good illustration of the difference between the NMO equations expressed through the dip angle and ray parameter. Tsvankin (1995) shows that if the dip ϕ is used as the argument, the distortion in the NMO velocity due to elliptical anisotropy is proportional to the ratio of the phase velocities $V(\phi)/V(0) = \sqrt{1 + 2\delta \sin^2 \phi}$. Therefore, $V_{\text{nmo}}(\phi)$ contains a separate contribution of the parameter δ. However, V_{nmo} expressed through ray parameter [equation (2.6)] is a function just of the zero-dip NMO velocity with no separate dependence on the vertical velocity or on δ. In fact, equation (2.6) coincides with the NMO formula for isotropic media; the influence of the anisotropy in formula (2.6) is absorbed by the value of $V_{\text{nmo}}(0)$, given by equation (2.5).

In terms of the inversion procedure, this result means that for elliptical models, the trade-off between V_{P0} and δ in equation (2.5) cannot be resolved from the dip-dependence of P-wave NMO velocity [equation (2.6)]. Moreover, the reflection moveout for elliptical anisotropy is purely hyperbolic and does not provide any information other than the zero-dip NMO (short-spread) velocity [equation (2.5)], which is identical (for a vertical symmetry axis) to the horizontal velocity of the medium. On the other hand, the NMO velocity as a function of p can be easily reconstructed from the NMO velocity for a horizontal reflector using the conventional isotropic algorithms; this conclusion has important implications in dip-moveout processing. We should remember, however, that elliptical anisotropy is just a convenient mathematical model that does not seem to be typical for subsurface formations (Thomsen, 1986).

To understand the behavior of $V_{\text{nmo}}(p)$ for non-elliptical models, I use the weak-anisotropy approximation ($\epsilon \ll 1$, $\delta \ll 1$). Equation (2.1) as a function of ray parameter for weak transverse isotropy is derived in Appendix A:

$$V_{\text{nmo}}(p) = \frac{V_{\text{nmo}}(0)}{\sqrt{1 - y}} \left[1 + (\epsilon - \delta) f(y)\right], \tag{2.7}$$

where

$$f(y) \equiv \frac{y\,(4y^2 - 9y + 6)}{1 - y}, \quad y \equiv p^2 V_{\text{nmo}}^2(0)\,.$$

Note that for elliptical anisotropy the weak-anisotropy approximation [equation (2.7)] reduces to the exact NMO equation (2.6).

Again, it is interesting to compare equation (2.7) with the corresponding weak-anisotropy NMO equation as a function of the dip, given by Tsvankin (1995). Although Tsvankin emphasized the difference $\epsilon - \delta$ as the most influential parameter in his NMO equation, $V_{\rm nmo}(\phi)$ does contain a separate contribution of δ. However, when the dip is replaced by the ray parameter, the NMO velocity explicitly contains the anisotropy parameters only in the form of the combination $\epsilon - \delta$. Of course, δ is also hidden in the value of $V_{\rm nmo}(0)$.

This result has important implications in the inversion procedure. Instead of the three original unknown parameters (V_{P0}, ϵ and δ), in the limit of weak anisotropy the NMO velocity contains just two combinations of them — $V_{\rm nmo}(0)$ and $\epsilon - \delta$. Therefore, moveout (stacking) velocities from just two distinct dips should provide enough information to recover the two effective parameters and reconstruct the NMO velocity as a function of ray parameter. In the most common case, when the zero-dip NMO velocity has been found by conventional NMO analysis, a single additional dipping reflector makes it possible to recover the difference $\epsilon - \delta$. The trade-off between V_{P0}, ϵ and δ, however, cannot be resolved from P-wave NMO velocities for weak transverse isotropy, no matter how many reflectors (dips) are used. Normal moveout velocities from more than two dipping reflectors just provide redundancy in the estimation of $V_{\rm nmo}(0)$ and $\epsilon - \delta$.

Although these conclusions have been drawn for weak transverse isotropy, the numerical analysis in the following sections leads to similar results for VTI media with arbitrary strength of the anisotropy.

2.3 Conditioning of the problem

To estimate the sensitivity of NMO velocity to the anisotropic parameters, I evaluate the Jacobian of equation (2.1) expressed as a function of ray parameter. The Jacobian is obtained by calculating the derivatives of the NMO velocity equation with respect to the model parameters V_{P0}, ϵ and δ. First, I consider the case of inverting for two parameters (namely, ϵ and δ, with a known V_{P0}) using two different dips; next, I examine the inversion for all three parameters.

Although the NMO velocity equation is nonlinear, its dependence on the anisotropy parameters is smooth enough to use the Jacobian approximation. Figure 2.1 is a 3-D plot of the values of $V_{\rm nmo}$ as a function of ϵ and δ for a reflector dip of nearly 40 degrees (for a given p, the dip changes somewhat with ϵ and δ) and a vertical velocity V_{P0} of 3.0 km/s. The smoothness of equation (2.1) over a practical range of ϵ and δ is evident.

The derivatives used to form the Jacobian are as follows:

$$d_1(p) = \frac{V_{P0}}{V_{\rm nmo}(p)} \frac{\partial V_{\rm nmo}(p)}{\partial V_{P0}},$$

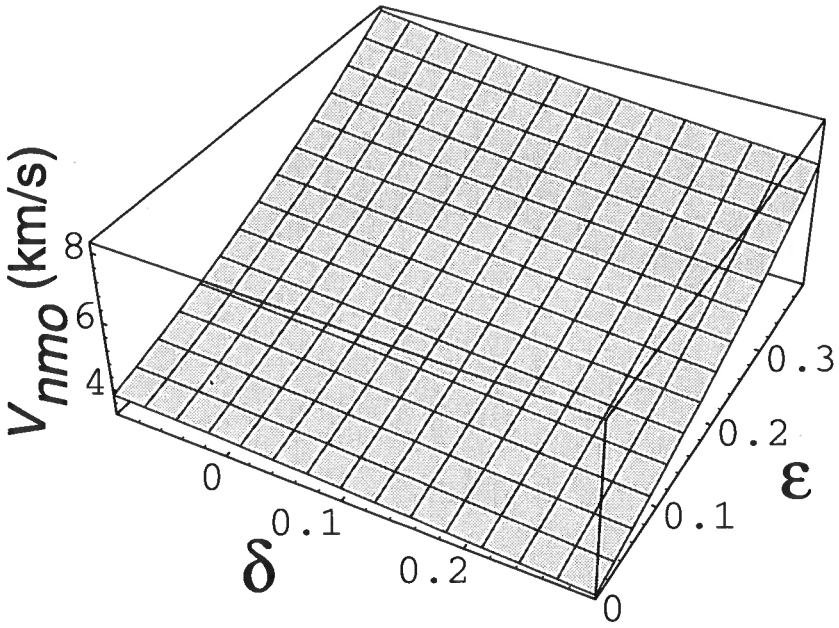

FIG. 2.1. 3-D plot of the NMO velocity as a function of ϵ and δ for the reflector dip corresponding to $p = 0.2$ s/km; $V_{P0} = 3.0$ km/s.

$$d_2(p) = \frac{1}{V_{\rm nmo}(p)} \frac{\partial V_{\rm nmo}(p)}{\partial \delta},$$
$$d_3(p) = \frac{1}{V_{\rm nmo}(p)} \frac{\partial V_{\rm nmo}(p)}{\partial \epsilon}.$$

I calculate d_1, d_2, and d_3 numerically using equation (2.1). The above normalization of the derivatives makes them easier to use. For example, $d_3 = 1$ implies that, when solving only for ϵ, a 5 percent error in the measured NMO velocity would cause an error of 0.05 in the calculated value of ϵ.

If two distinct reflector dips are available, it may be possible to solve for two of the three parameters provided the remaining parameter is known. The sensitivity of this inversion to errors in the input data (NMO velocities) can be measured from the Jacobian matrix,

$$J = \begin{pmatrix} d_2(p_1) & d_3(p_1) \\ d_2(p_2) & d_3(p_2) \end{pmatrix}.$$

This Jacobian corresponds to the inversion for ϵ and δ when V_{P0} is known.

The condition number κ for Jacobian matrix J can be computed as follows:

$$\kappa = \sqrt{\frac{\mid \lambda_{max} \mid}{\mid \lambda_{min} \mid}},$$

where λ_{max} and λ_{min} are the maximum and minimum eigenvalues, respectively, of the matrix

$$A = JJ^T.$$

J^T is the transpose of the matrix J. A large condition number implies an ill-conditioned (i.e., nearly singular) problem, while a low condition number (for example, smaller than 10) usually implies a well-conditioned problem. The absolute errors in the computed anisotropy parameters and the relative error in the computed V_{P0} are close to κ times the relative error in the measured NMO velocity. In most cases, this estimate provides the maximum possible error.

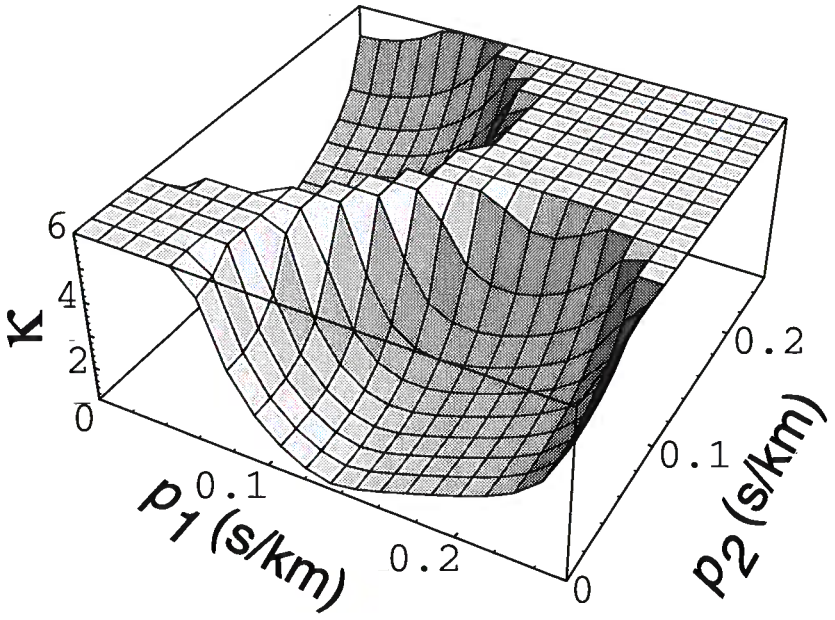

FIG. 2.2. 3-D plot of the condition number as a function of p_1 and p_2 (ray parameters of the two reflectors). The model parameters are $V_{P0} = 3.0$ km/s, $\epsilon = 0.2$, and $\delta = 0.1$.

Figure 2.2 shows the condition number as a function of ray parameter for the inversion of the NMO velocities measured at two dips, corresponding to p_1 and p_2. The dips range from 0 to 60 degrees. The flat (clipped) parts of the 3-D plot correspond to high condition numbers (≥ 6.0). When the dips are close to each other, the problem becomes highly ill-conditioned (i.e., the diagonal line where $p_1 = p_2$). If the

difference between the dips is 10-15 degrees or more, the problem becomes reasonably conditioned, unless both dip angles are large (> 25 degrees). The latter case, however, is hardly typical. In a typical case of horizontal and dipping reflectors, an acceptable resolution in resolving ϵ and δ is achieved (for the model from Figure 2.2) for a wide range of ray parameters that excludes only those corresponding to mild dips.

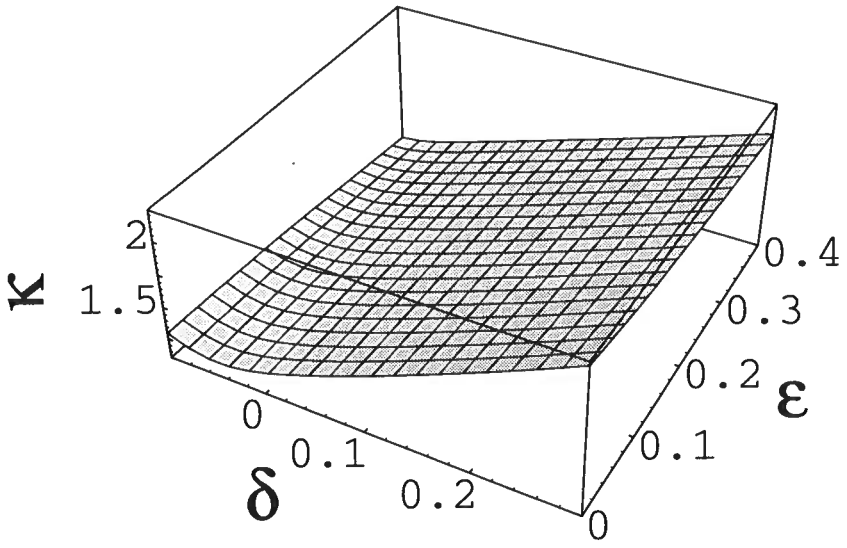

FIG. 2.3. 3-D plot of the condition number as a function of ϵ and δ. Two reflector dips used in the inversion correspond to ray parameters of $p_1 = 0.0$ s/km (horizontal reflector) and $p_2 = 0.16$ s/km. The vertical velocity V_{P0} is 3.0 km/s.

The inversion for the important case of a horizontal and a dipping reflector needs to be considered in more detail. Figure 2.3 shows the condition number for the inversion for ϵ and δ (V_{P0} is considered to be known), with reflector dips given by $p_1 = 0.0$ (horizontal reflector) and $p_2 = 0.16$ (near 30-degree dip). The low values of the condition number mean that overall we obtain a reasonably good resolution over a wide range of values of ϵ and δ.

Next, I examine the feasibility of inverting for all three parameters (V_{P0}, ϵ and δ) using NMO velocities for three different dips. The Jacobian matrix for this problem is

$$J = \begin{pmatrix} d_1(p_1) & d_2(p_1) & d_3(p_1) \\ d_1(p_2) & d_2(p_2) & d_3(p_2) \\ d_1(p_3) & d_2(p_3) & d_3(p_3) \end{pmatrix} . \tag{2.8}$$

Figure 2.4 shows the condition number for the Jacobian (2.8) calculated for re-

flector dips $p_1 = 0.0$ (horizontal reflector), $p_2 = 0.16$ s/km (near 30-degree dip), and $p_3 = 0.23$ s/km (near 50-degree dip). The huge values of the condition number over the entire range of ϵ indicate that the problem is thoroughly ill-posed. In other words, we could find models with a wide range of V_{P0}, ϵ, and δ that have almost the same NMO velocities for the dips considered here. This ill-conditioned nature of the inverse problem holds for all choices of ray parameters, V_{P0}, ϵ, and δ that I have studied.

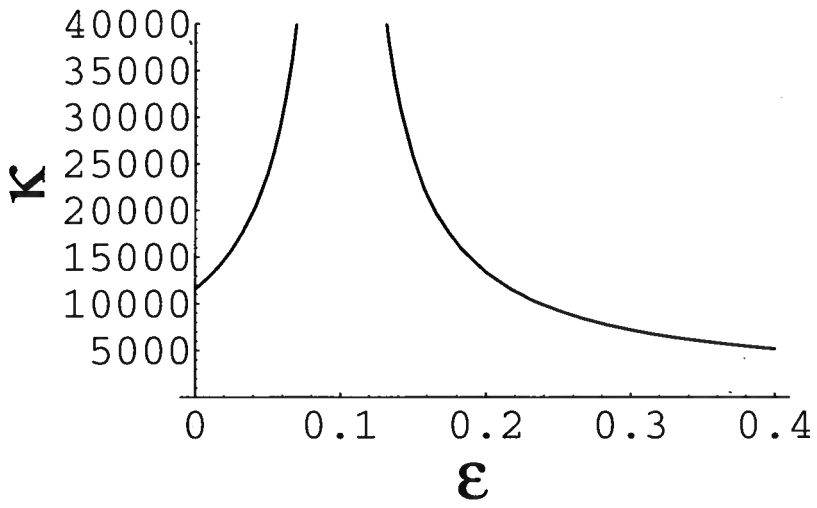

FIG. 2.4. Condition number as a function of ϵ for the inversion using three reflector dips corresponding to $p_1 = 0.0$ s/km, $p_2 = 0.16$ s/km, and $p_3 = 0.23$ s/km. The vertical velocity is $V_{P0} = 3.0$ km/s; δ=0.1.

Note that for models close to elliptical ($\epsilon = \delta$), the condition number goes to infinity, and the inversion cannot be carried out at all. Above, I obtained this result analytically by showing that the NMO equation for elliptical anisotropy (2.6) depends only on the ray parameter and the zero-dip NMO velocity.

I conclude that, given the uncertainties usually associated with seismic data, we cannot count on resolving all three parameters using this method, even if we had more than three different reflector dips. The ambiguity of the inversion procedure is caused by the trade-off between the anisotropy parameters ϵ and δ in the NMO equation. In the limit of weak anisotropy, this trade-off is demonstrated by the NMO formula (2.7), which contains only the *difference* $\epsilon - \delta$ and the zero-dip NMO velocity rather than either of the coefficients individually. However, as we have seen, if one of the parameters (V_{P0}, ϵ, δ) is known, the other two can be reliably recovered from NMO velocities for two different dips.

2.4 Numerical inversion

The above analysis based on the Jacobian matrix is still approximate since the NMO velocity equation is nonlinear. In this section, I perform the actual nonlinear inversion by means of the Newton-Raphson method and study the range of solutions as well as the sensitivity of the results to errors in the input information. I will concentrate on models with $\epsilon - \delta \geq 0$, which are believed to be most typical for subsurface formations (Thomsen, 1986; Tsvankin and Thomsen, 1994).

2.4.1 Inversion using two reflector dips

The input data for the inversion procedure are the P-wave NMO velocities and ray parameters for two different reflector dips; one of the reflectors can be (but is not necessarily) horizontal. For conventional spreadlengths, usually limited to the distance between the CMP and the reflector, NMO velocity is well-approximated by the finite-spread stacking velocity routinely used in seismic processing (Tsvankin and Thomsen, 1994; Tsvankin, 1995). The analysis in the previous section indicates that the inversion for all three parameters using three reflector dips is unstable; besides, for this method to be practical we can seldom count on having reliable NMO velocities from more than two distinctly different dips.

The convergence of the inversion procedure is related to the value of the condition number examined in the previous section. As illustrated by Figure 2.2, the condition number is low for a wide range of dips, except for those close to each other. This implies good convergence properties of the inversion procedure provided that we pick a plausible initial model. In my implementation, I used the isotropic model ($\delta = \epsilon = 0$) as the initial guess and achieved a fast enough convergence in the numerical examples described below.

In the first example (Figure 2.5), I consider a horizontal reflector and a reflector dipping at 50 degrees ($p = 0.23$ s/km) for the same model as in Figure 2.2 ($V_{P0} = 3.0$ km/s, $\epsilon = 0.2$, and $\delta = 0.1$).

If we know the vertical velocity V_{P0}, the inversion of two NMO velocities should make it possible to recover ϵ and δ. Indeed, as shown in Figure 2.5, if the actual velocity $V_{P0} = 3.0$ km/s is used in the Newton-Raphson inversion algorithm, I obtain the correct values for both anisotropic parameters.

If only surface data are available, however, the exact vertical velocity may not be known. Therefore, it is interesting to examine the family of solutions corresponding to a range of vertical velocities around the actual value (from 2.6 km/s to 3.5 km/s in Figure 2.5). For all these solutions, the difference between ϵ and δ is close to the exact value ($\epsilon - \delta = 0.1$). Therefore, in close agreement with the weak-anisotropy approximation [equation (2.7)], the inversion of the P-wave NMO velocities provides us with a good estimate of the difference $\epsilon - \delta$. The only way to resolve the coefficients individually is to obtain the vertical velocity V_{P0} using some other source of information (e.g., check shots or well logs).

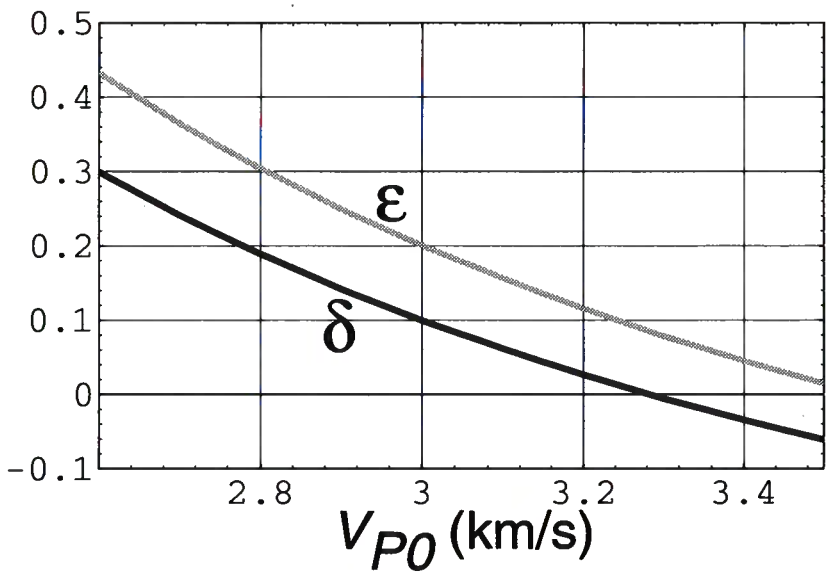

FIG. 2.5. Parameters ϵ and δ obtained from NMO velocities corresponding to a horizontal reflector and $p = 0.23$ s/km (50 degrees dip). The values of V_{P0} used in the inversion are shown on the horizontal axis. The model parameters are $V_{P0} = 3.0$ km/s, $\epsilon = 0.2$, and $\delta = 0.1$.

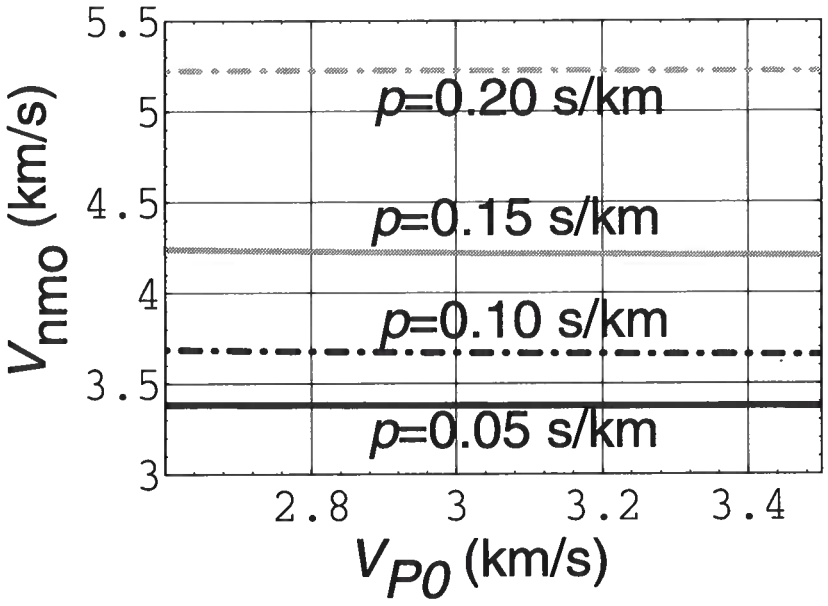

FIG. 2.6. NMO velocity for a family of solutions in Figure 2.5 and four different values of the ray parameter.

The most important property of the family of solutions shown in Figure 2.5 is that all of them have practically the same NMO velocity as a function of ray parameter for all possible dipping reflectors, not just for the two dips used in the inversion scheme. This is illustrated by Figure 2.6, which shows that the NMO velocity for any given reflector dip (i.e., any fixed value of p) is practically the same within the range of solutions in Figure 2.5, independent of the guess for V_{P0}. Therefore, if we perform the inversion procedure using the NMO velocities for any two dipping reflectors (of course, the dips should not be close to each other), we end up with the same family of equivalent models as in Figure 2.5. In the following, I refer to models obtained by the inversion of P-wave NMO velocity as the "equivalent solutions," or ES.

Thus, the normal moveout velocities measured at two different dips are sufficient to obtain the NMO velocity for any ray-parameter value. This means that the dip-dependent P-wave NMO velocity is controlled by just two combinations of the parameters V_{P0}, ϵ, and δ, rather than by the three parameters individually.

Another example, for a medium with stronger anisotropy, is shown in Figure 2.7. Here, I have considered a typical case of horizontal and dipping reflectors (the dip is 40 degrees); it should be emphasized that any pair of dips sufficiently different from each other yields the same family of ES. Thus, as for the previous model, all ES have the same NMO velocity for the full range of dips. However, in contrast with the previous example, the velocity anisotropy is too pronounced for the weak-anisotropy equation (2.7) to hold, and the inversion does not provide an accurate value of $\epsilon - \delta$,

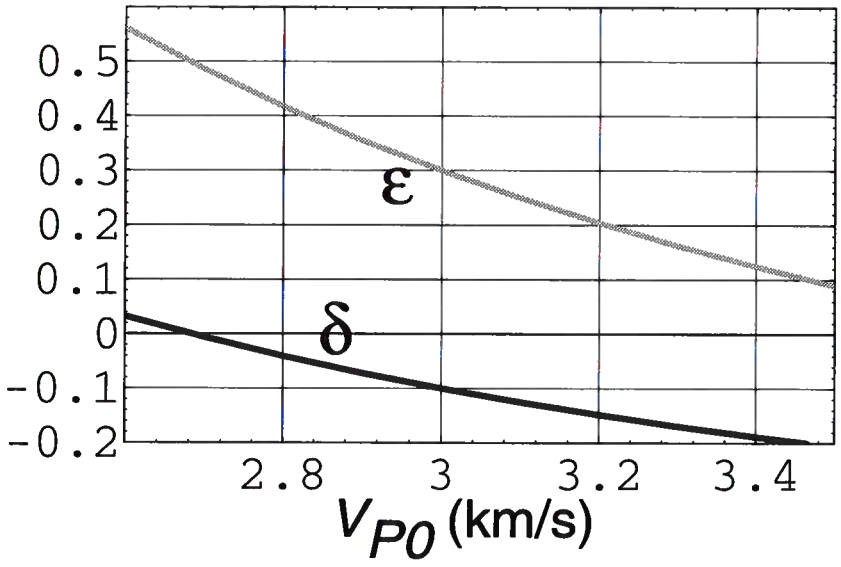

FIG. 2.7. Inverted values of ϵ and δ as functions of V_{P0} for the model with $V_{P0} = 3.0$ km/s, $\epsilon = 0.3$, and $\delta = -0.1$.

unless we have a good estimate of the vertical velocity.

The accuracy of the estimation of $\epsilon - \delta$ is further illustrated by Figure 2.8, which shows the inversion results for the models with $\epsilon - \delta = 0.1, 0.2$, and 0.3. While the recovery of $\epsilon - \delta$ is unique for elliptical anisotropy ($\epsilon = \delta$, not shown on the plot), it becomes less accurate with increasing $\epsilon - \delta$.

In essence, I have shown that the exact NMO velocity expressed through ray parameter depends just on the zero-dip NMO velocity and some combination of the anisotropy parameters close to the difference $\epsilon - \delta$. This conclusion is in agreement not only with the weak-anisotropy equation (2.7), but also with the analysis of the Jacobian matrix in the previous section (it explains the ambiguity in the inversion for all three parameters – V_{P0}, ϵ, and δ).

2.4.2 Description of the equivalent solutions

Clearly, the combination of ϵ and δ that describes the family of ES deviates from the difference $\epsilon - \delta$ with increasing anisotropy. An analytic description of this combination for arbitrary strength of the anisotropy is given below.

I have shown that all ES obtained by my inversion technique have the same dip-dependent NMO velocity, including that for a horizontal reflector. Therefore,

$$V_{\rm nmo}(0) = V_{P0}\sqrt{1+2\delta} = const \tag{2.9}$$

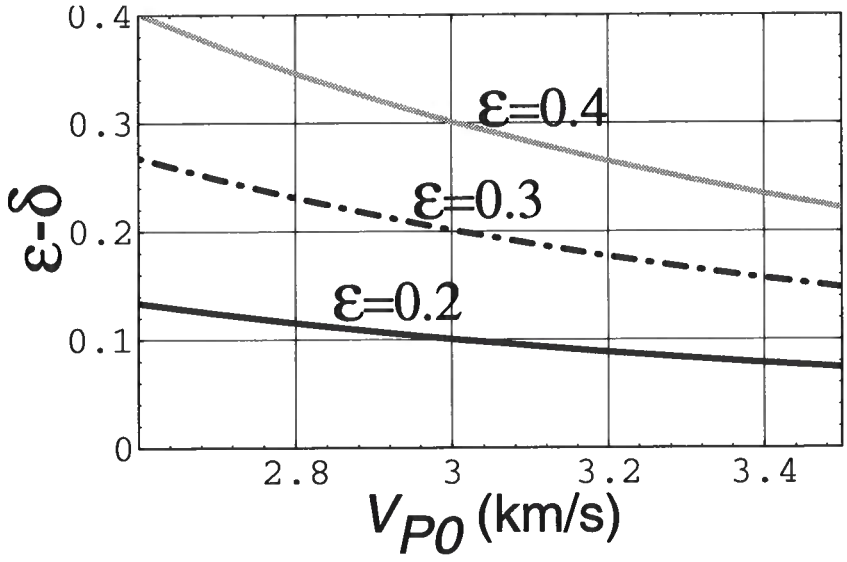

FIG. 2.8. Inverted value of $\epsilon - \delta$ as a function of V_{P0} for three models with different ϵ; V_{P0}=3.0 km/s, δ=0.1.

within the family of ES. This equation provides a relation between V_{P0} and δ that accurately describes the curves $\delta(V_{P0})$ in Figures 2.5 and 2.7.

However, a single equation is not sufficient to characterize the ES analytically. To obtain another relation between the parameters that would involve ϵ, I examine the behavior of group-velocity curves for the family of ES. Figure 2.9 shows the group velocity as a function of the group angle for three solutions corresponding to V_{P0}=2.8, 3.0 and 3.2 km/s. The computations were performed for the two models shown in Figures 2.5 and 2.7. For both media, all three ES yield practically the same velocity at an angle of 90 degrees, which coincides with the actual horizontal velocity. I have obtained the same result for all other VTI models I have studied.

This implies that for all ES

$$V_h = V_{P0}\sqrt{1+2\epsilon} = const\,. \tag{2.10}$$

However, it is more convenient to replace the horizontal velocity by a dimensionless parameter, common for all ES, that goes to zero for isotropic media. Combining equations (2.9) and (2.10), I choose to define a new anisotropic parameter (denoted by η) as follows:

$$\eta \equiv 0.5\left(\frac{V_h^2}{V_{\rm nmo}^2} - 1\right) = \frac{\epsilon - \delta}{1+2\delta}\,. \tag{2.11}$$

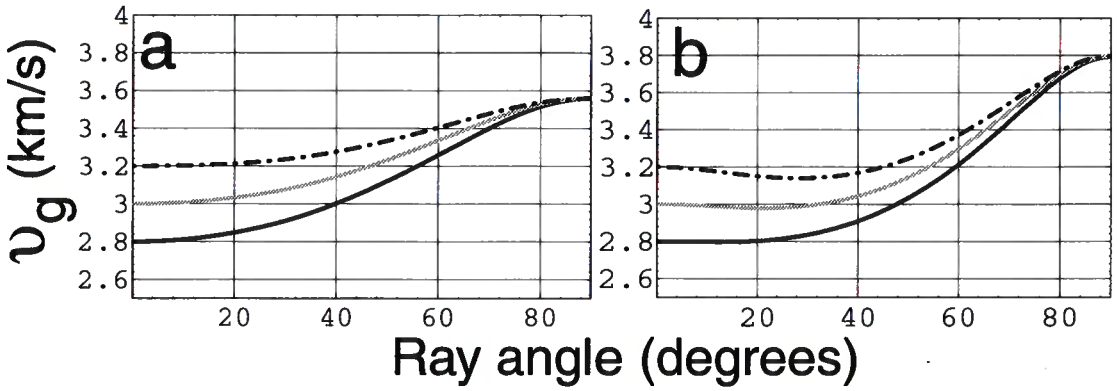

FIG. 2.9. Group velocity v_g as a function of the group (ray) angle for solutions from (a) Figure 2.5 (V_{P0}=3.0 km/s, $\epsilon = 0.2$, $\delta = 0.1$), and (b) Figure 2.7 (V_{P0}=3.0 km/s, $\epsilon = 0.3$, $\delta = -0.1$). The curves correspond to solutions with V_{P0}=2.8 km/s and the corresponding values of δ and ϵ (black); V_{P0}=3.0 km/s (actual values, gray); and V_{P0}=3.2 km/s (dashed).

Then

$$V_h = V_{\rm nmo}(0)\sqrt{1+2\eta} \tag{2.12}$$

[compare the form with equations (2.9) and (2.10)]. Therefore, the family of ES can be described by two effective parameters: $V_{\rm nmo}(0)$ (or V_h) and η. Only these parameters can be resolved by inverting dip-dependent P-wave NMO velocity. In principle, two distinct dips are sufficient to recover the values of $V_{\rm nmo}(0)$ and η; additional dipping reflectors just provide redundancy in the inversion procedure, so that, for example, a least-square approach can be used to solve the overdetermined problem.

Although this result for strong anisotropy has been obtained numerically, it is in good agreement with the analytic weak-anisotropy approximation (2.7). Essentially, by performing numerical inversion I have generalized the weak-anisotropy equation (2.7) to transversely isotropic media with arbitrary strength of anisotropy. While the weak-anisotropy P-wave NMO equation (expressed through ray parameter) is a function of $V_{\rm nmo}(0)$ and $\epsilon-\delta$, the P-wave NMO velocity for general transverse isotropy is fully characterized by $V_{\rm nmo}(0)$ and η. Clearly, in the limit of weak anisotropy η reduces to the difference $\epsilon-\delta$. The family of ES from the first example in Figure 2.5 can be represented by $V_{\rm nmo} = 3.29$ km/s and $\eta = 0.0833$. The example from Figure 2.7 is characterized by $V_{\rm nmo} = 2.68$ km/s and a much larger $\eta = 0.5$.

Also, note that η is zero not only for isotropy, but also for elliptical anisotropy. In this sense, it is similar to the parameter $\sigma = V_{P0}^2/V_{S0}^2\,(\epsilon-\delta)$ introduced by Tsvankin and Thomsen (1994) to describe SV-wave moveout. Its magnitude is a measure of the departure of a medium from being elliptically anisotropic.

The dominant role of the parameter η is illustrated by Figure 2.10a, which shows

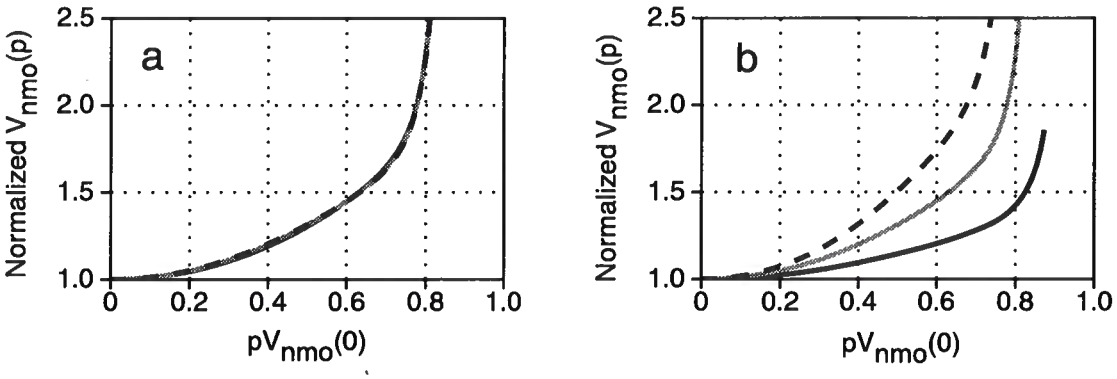

FIG. 2.10. *P*-wave moveout velocity calculated from formula (2.1) and normalized by the expression for isotropic media (2.6). The dip angles range between 0 and 70 degrees. (a) Different models with the same $\eta = 0.2$: $\epsilon = 0.1$, $\delta = -0.071$ (solid); $\epsilon = 0.2$, $\delta = 0$. (gray); $\epsilon = 0.3$, $\delta = 0.071$ (dashed) — the curves practically coincide with each other. (b) Models with different η: $\eta = 0.1$ (solid); $\eta = 0.2$ (gray); $\eta = 0.3$ (dashed).

that the *P*-wave dip-moveout signature does not depend on the individual values of the anisotropy parameters ϵ and δ, if η is fixed. Figure 2.10b, on the other hand, shows large sensitivity of V_{nmo} to variations in η.

While η is determined by the values of the zero-dip moveout velocity and the horizontal velocity, the choice of form for η is not unique. I could have combined $V_{\text{nmo}}(0)$ and V_h in a different fashion to obtain, for instance, $1 + 2\epsilon$ instead of $1 + 2\delta$ in the denominator of η. In whatever form, however, any such anisotropic parameter describing the dip-dependence of NMO velocity would represent a measure of "nonellipticity," i.e., deviation from the elliptically anisotropic model.

Equation (2.11) leads us to another observation. If it is possible to obtain an accurate value for the horizontal velocity V_h (e.g., from head waves traveling along a horizontal reflector or from cross-hole tomography), then the zero-dip velocity $V_{\text{nmo}}(0)$ is sufficient to find η and to build the *P*-wave NMO velocity as a function of ray parameter. Dipping reflectors in this case are not needed at all.

As demonstrated in later sections, the importance of the family of ES goes well beyond the dip-dependence of *P*-wave NMO velocities.

2.4.3 Accuracy of the inversion

Next, I study the sensitivity of the inversion procedure to errors in the measured moveout velocities. In the typical case of a horizontal and a dipping reflector, we measure two velocities: $V_{\text{nmo}}(p)$ and $V_{\text{nmo}}(0)$. Since $V_{\text{nmo}}(0)$ is obtained directly, η remains the only unknown to be solved for. As illustrated in Figure 2.10b, the NMO-velocity corresponding to different η values are well resolved within a wide range of

dips; this indicates that the inversion procedure should be reasonably stable.

To quantify errors in η, let us use the following sensitivity equation:

$$\Delta V_{\rm nmo}(p) = \frac{\partial V_{\rm nmo}(p)}{\partial V_{\rm nmo}(0)} \Delta V_{\rm nmo}(0) + \frac{\partial V_{\rm nmo}(p)}{\partial \eta} \Delta \eta \,. \tag{2.13}$$

Normalizing the velocities, we can represent equation (2.13) as

$$\frac{\Delta V_{\rm nmo}(p)}{V_{\rm nmo}(p)} = \frac{V_{\rm nmo}(0)}{V_{\rm nmo}(p)} \frac{\partial V_{\rm nmo}(p)}{\partial V_{\rm nmo}(0)} \frac{\Delta V_{\rm nmo}(0)}{V_{\rm nmo}(0)} + \frac{1}{V_{\rm nmo}(p)} \frac{\partial V_{\rm nmo}(p)}{\partial \eta} \Delta \eta \,. \tag{2.14}$$

Using equation (2.14), the error in η can be expressed through the errors in the NMO velocities.

$$\Delta \eta = \left[\frac{V_{\rm nmo}(p)}{f_2} \right] \frac{\Delta V_{\rm nmo}(p)}{V_{\rm nmo}(p)} - \left[f_1 \frac{V_{\rm nmo}(0)}{f_2} \right] \frac{\Delta V_{\rm nmo}(0)}{V_{\rm nmo}(0)} \,, \tag{2.15}$$

where

$$f_1 = \frac{\partial V_{\rm nmo}(p)}{\partial V_{\rm nmo}(0)} \,,$$

and

$$f_2 = \frac{\partial V_{\rm nmo}(p)}{\partial \eta} \,.$$

If the NMO velocity for a horizontal reflector is measured exactly or contains only a small error, the error in η would be controlled just by the first term in formula (2.15). However, assuming that the errors in $V_{\rm nmo}(p)$ and $V_{\rm nmo}(0)$ have comparable magnitude, I can characterize the sensitivity of η by the quantity E defined as

$$E = \frac{\sqrt{V_{\rm nmo}^2(p) + [f_1 V_{\rm nmo}(0)]^2}}{f_2} \,. \tag{2.16}$$

Figure 2.11 shows E as a function of the ray parameter for the models from Figures 2.5 and 2.7. In both examples, as expected, errors decrease with dip, and are large when the dipping reflector has a dip close to zero, but reach a minimum at some dip [about 46 degrees (a), and 51 degrees (b)]. The minimum in E is caused by relatively higher sensitivity to errors in $V_{\rm nmo}(0)$ at steep dips; if the error in $V_{\rm nmo}(0)$ is negligibly small, the minimum does not exist, and the inversion for η is most stable at dips up to 90 degrees.

However, in the discussion above I have not considered two factors that make steep reflectors (beyond 50-60 degrees) less desirable for the inversion algorithm. First, at large dip the inversion for η becomes more sensitive to errors in the ray parameter. Second, the recovery of the NMO velocity itself from reflection moveouts becomes less stable because the magnitude of the quadratic moveout term (and of moveout as a whole) decreases with dip (due to higher NMO velocity).

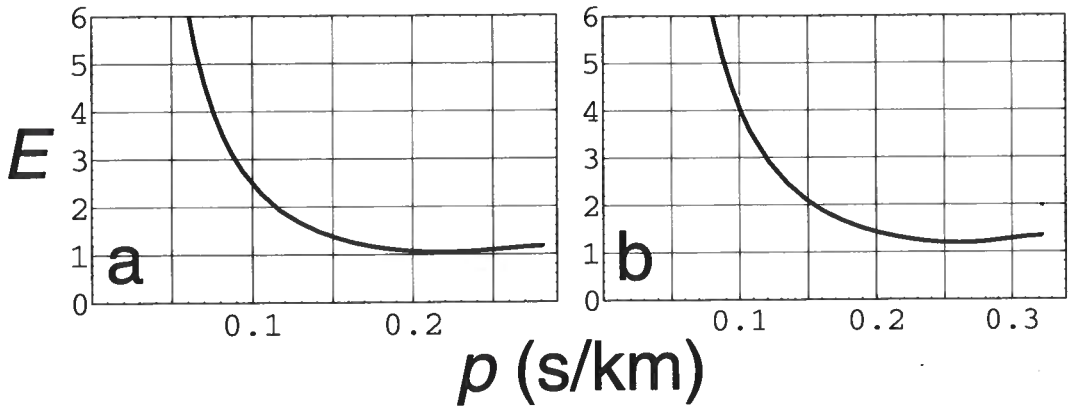

FIG. 2.11. E as a function of the ray parameter corresponding to the dipping reflector for (a) the model used to generate Figure 2.5 (V_{P0}=3.0 km/s, $\epsilon = 0.2$, $\delta = 0.1$), and (b) the model used to generate Figure 2.7 (V_{P0}=3.0 km/s, $\epsilon = 0.3$, $\delta = -0.1$).

It may also be instructive to examine numerically the sensitivity of the effective parameter η and the horizontal velocity V_h (2.12) to errors in the measured values of $V_{\rm nmo}(p)$. In Figure 2.12, I have introduced errors into the input values of NMO velocities for reflector dips of 0 and 40 degrees. The percentage error in V_h and the absolute error in η are quite small, which indicates that this inversion is reasonably stable. In fact, a 5-percent error in $V_{\rm nmo}(p)$ causes less than a 2.5-percent error in V_h. The percentage error in η is larger, but this can be expected in the inversion for so small an anisotropic coefficient.

2.5 Properties of the family of solutions

2.5.1 Nonhyperbolic reflection moveout

The inversion of the dip-dependence of P-wave normal moveout velocities enables one to obtain a family of equivalent solutions (ES) described by the zero-dip NMO velocity $V_{\rm nmo}(0)$ and the effective anisotropic parameter η. In this section, I show a remarkable property of ES: any model with the same $V_{\rm nmo}(0)$ and η yields the same long-spread (nonhyperbolic) P-wave moveout from a horizontal reflector.

P-wave long-spread moveout in horizontally-layered transversely isotropic media can be well-approximated by the equation (Tsvankin and Thomsen, 1994)

$$t^2(X) = t_{P0}^2 + A_2 X^2 + \frac{A_4 X^4}{1 + AX^2}, \tag{2.17}$$

where t_{P0} is the two-way, zero-offset time.

For a single layer, the coefficients in formula (2.17) are

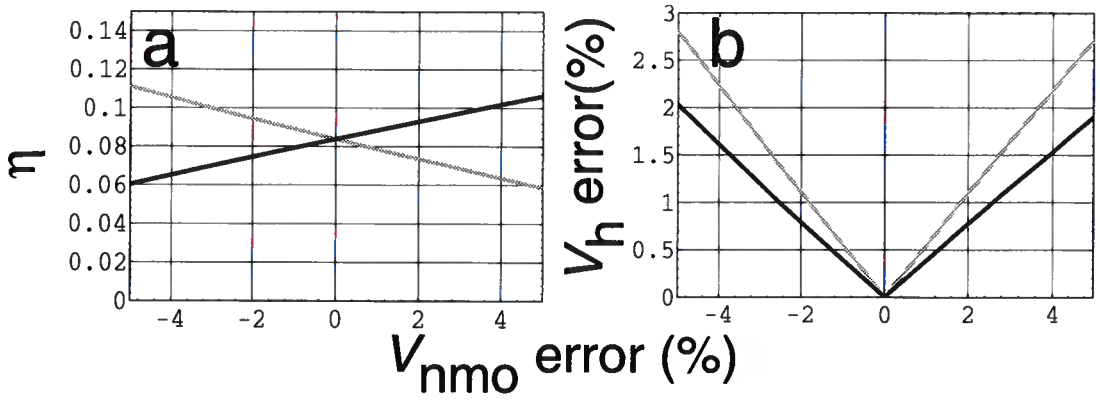

FIG. 2.12. Dependence of the inverted values of η (a) and V_h (b) on the error in the measured NMO velocities. The model parameters are $V_{P0} = 3.0$ km/s, $\epsilon = 0.2$, and $\delta = 0.1$; reflector dips of 0 and 40 degrees were used. Black lines correspond to errors in the NMO velocity for only the dipping reflector. Gray lines correspond to identical errors in both $V_{\rm nmo}$ values.

$$A_2 = \frac{1}{V_{P0}^2(1+2\delta)} = \frac{1}{V_{\rm nmo}^2(0)},$$

$$A_4 = -\frac{2(\epsilon-\delta)}{t_{P0}^2 V_{P0}^4}\frac{1+\frac{2\delta}{1-V_{S0}^2/V_{P0}^2}}{(1+2\delta)^4},$$

$$A = \frac{A_4}{\frac{1}{V_h^2} - A_2},$$

where V_h is the horizontal velocity.

Equation (2.17) remains numerically accurate for long spreads (2 to 3 times, and more, the reflector depth) and pronounced anisotropy. The hyperbolic moveout term, which makes the main contribution to short-spread moveout, depends on just the NMO velocity $V_{\rm nmo}(0)$. The last term in equation (2.17) describes nonhyperbolic moveout on long spreads.

Substituting the parameters $V_{\rm nmo}(0)$ and η into formula (2.17) and ignoring the contribution of V_{S0} to the quartic term A_4 (V_{S0} has a negligible influence on P-wave moveout in TI media), I obtain

$$t^2(X) = t_{P0}^2 + \frac{X^2}{V_{\rm nmo}^2(0)} - \frac{2\eta X^4}{V_{\rm nmo}^2(0)\left[t_{P0}^2 V_{\rm nmo}^2(0) + (1+2\eta)X^2\right]}. \qquad (2.18)$$

Thus, P-wave long-spread moveout can be adequately described by the vertical traveltime and just the two effective parameters – $V_{\text{nmo}}(0)$ and η, with no separate dependence on V_{P0}, ϵ, or δ. For given $V_{\text{nmo}}(0)$ and t_{P0}, η describes the amount of deviation from hyperbolic moveout; if $\eta = 0$, the medium is elliptical and the moveout is purely hyperbolic.

Although equation (2.17) is approximate, and I have made one more small approximation by assuming that $V_{S0} = 0$, the results in the next section show that P-wave long-spread moveout is indeed controlled by $V_{\text{nmo}}(0)$ and η. Since the inversion algorithm makes it possible to recover $V_{\text{nmo}}(0)$ and η, it provides enough information to build P-wave long-spread moveout curves. Stated differently, although the inversion is unable to resolve V_{P0}, ϵ, and δ, the two parameters it does give are sufficient to describe P-wave long-spread moveout.

2.5.2 Migration impulse response

Although equation (2.18) describes moveout for a horizontal reflector, it also can be regarded as the diffraction curve, accurate to a certain dip, on the zero-offset section (poststack domain). Since time migration is based on collapsing such diffraction curves to their apexes, the values of $V_{\text{nmo}}(0)$ and η should be sufficient to generate a time-migration impulse response that is accurate up to that certain dip. With accurate values of $V_{\text{nmo}}(0)$ and η, all lateral position errors that arise in migration for homogeneous models when anisotropy is ignored (Larner and Cohen, 1993; Alkhalifah and Larner, 1994), will be eliminated. Poststack depth migration, however, may produce depth errors if the value V_{P0} is inaccurate, but this is a different issue.

Figure 2.13 shows the exact zero-offset time-migration impulse responses (right half only) for different ES from (a) Figure 2.5 and (b) Figure 2.7. The curves for all three ES practically coincide with each other, implying that there is no difference between the impulse responses of the three input models. This confirms that $V_{\text{nmo}}(0)$ and η are sufficient to generate an accurate time-migration impulse response for all dips and, therefore, P-wave long-spread moveout is indeed controlled by $V_{\text{nmo}}(0)$ and η.

This point is illustrated further by Figure 2.15, which shows anisotropic poststack time migrations (Gazdag's phase-shift migration modified for anisotropic media; discussed later) of the synthetic data generated for the model in Figure 2.14. The reflectors are embedded in a homogeneous transversely isotropic medium with V_{P0}=3.0 km/s, ϵ=0.2, and δ=0.1 (the same model as in Figure 2.5). The migrations were performed (a) using the actual model parameters, and (b) using an equivalent solution from Figure 2.5 with V_{P0}=2.5 km/s, ϵ=0.43, and δ=0.3. Although model (b) is substantially different from the actual one, it has the correct values of $V_{\text{nmo}}(0)$ and η and, consequently, produces an accurate image.

As opposed to this situation for time migration, however, depth migration will produce depth errors if the wrong value of V_{P0} were used. Such depth errors ΔD can be described by

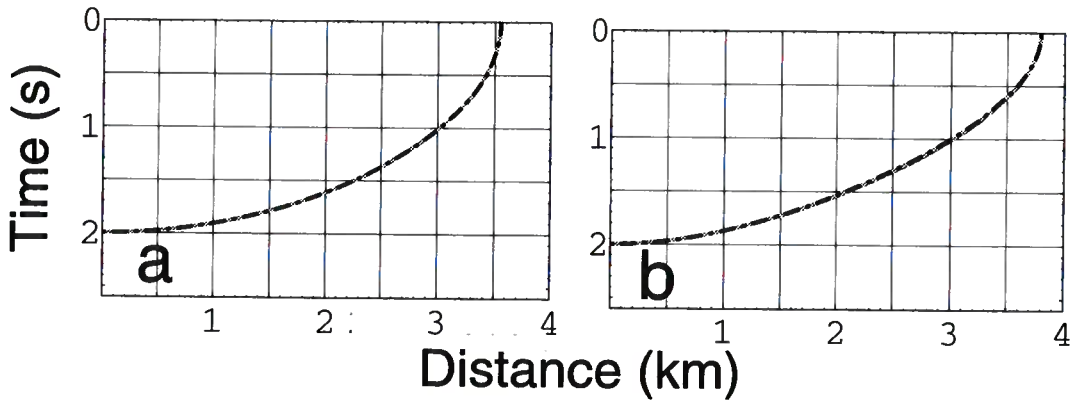

FIG. 2.13. Anisotropic time-migration impulse response for solutions from (a) Figure 2.5, and (b) Figure 2.7. The three curves on each plot correspond to the solutions with $V_{P0} = 2.8$ km/s (solid black line), 3 km/s (solid gray line), and 3.2 km/s (dashed black line).

$$\Delta D = (\frac{V_{P0}}{V_{\text{actual}}} - 1)D\,,$$

where V_{actual} is the true vertical velocity, and D is the true depth.

Therefore, all ES have the same poststack depth migration impulse response with a simple depth scaling depending on the value of the vertical velocity.

Since all ES, characterized by $V_{\text{nmo}}(0)$ and η, have the same NMO velocity $V_{\text{nmo}}(p)$ in the prestack domain and the same time-migration impulse response in the poststack domain, they should also have the same time-migration impulse in the *prestack* domain. Thus, media with the same $V_{\text{nmo}}(0)$ and η yield the same prestack and poststack diffraction curves for surface seismic data.

I conclude that the inversion of P-wave NMO velocities provides enough information to perform all major time-processing steps including dip moveout (DMO), and prestack and poststack time migration. However, time-to-depth conversion requires an accurate value of the vertical velocity, which cannot be obtained from NMO velocities alone.

2.6 Refining inversion results using poststack migration

In many cases one can assess the accuracy of the migration algorithm or of the velocity field used in the migration by observing the quality of the migrated image. For example, upward parabolic shapes, resulting from diffracting edges, imply overmigration, whereas downward hyperbolic shapes indicate undermigration.

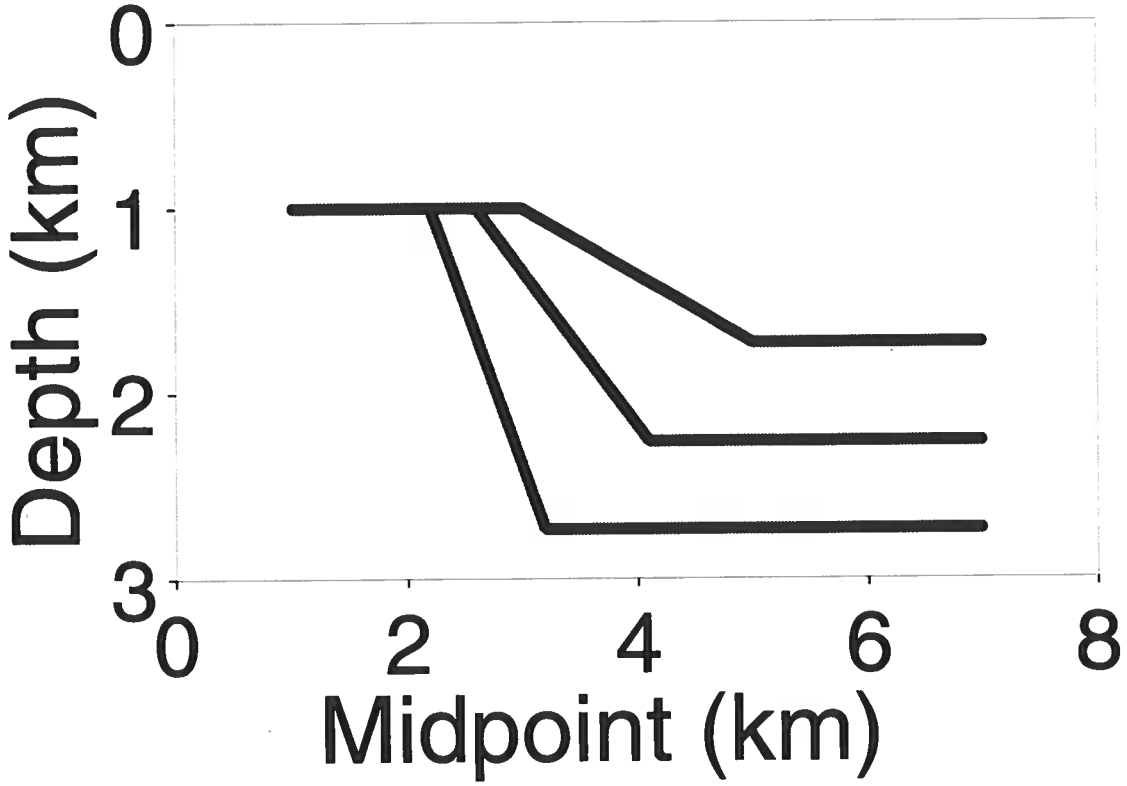

FIG. 2.14. Model with reflectors dipping at 0,20,40, and 60 degrees.

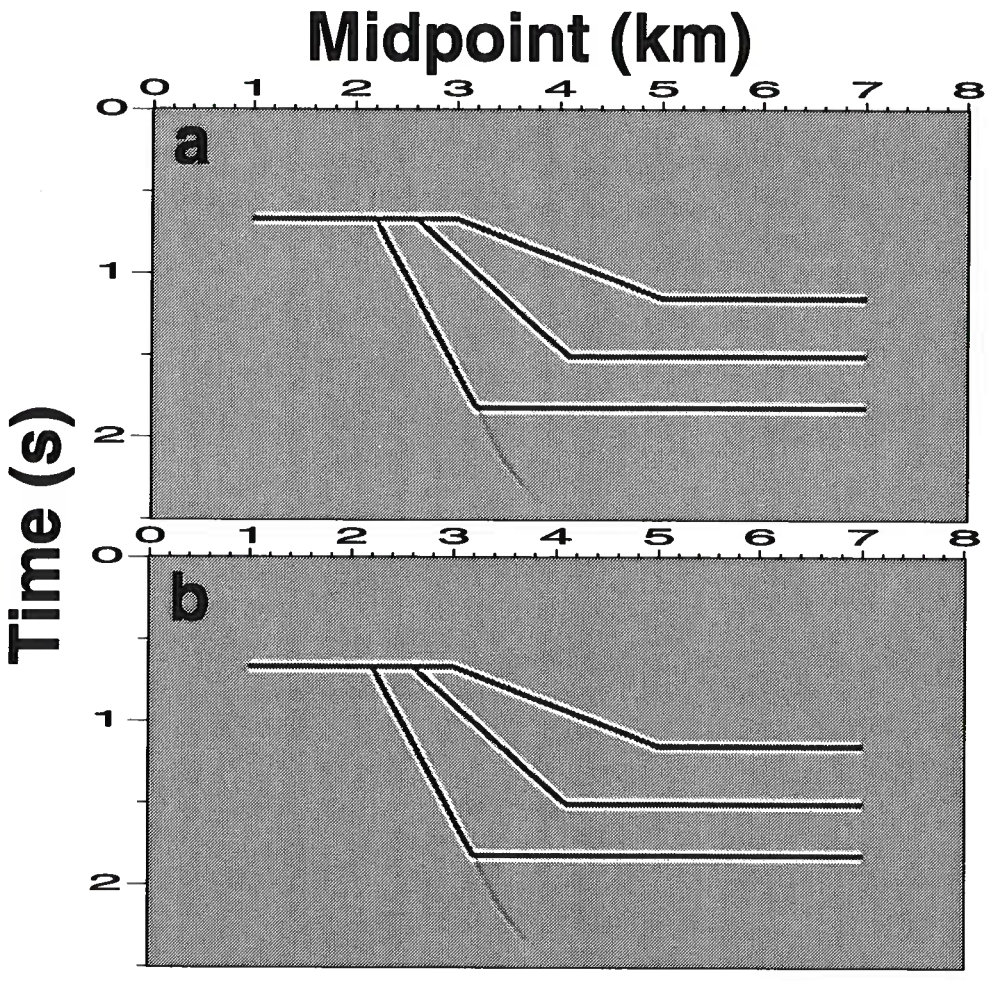

FIG. 2.15. Anisotropic time migrations of synthetic data generated for the model in Figure 2.14 using (a) the actual model values of $V_{P0} = 3.0$ km/s, $\epsilon = 0.2$, and $\delta = 0.1$; and (b) an equivalent solution $V_{P0} = 2.6$ km/s, $\epsilon = 0.43$, and $\delta = 0.3$.

This approach can be used to refine the results of our inversion procedure. Errors in the measured NMO velocity may lead to an inaccurate value of η, which, in turn, may distort the migrated image. Figure 2.16 shows anisotropic poststack time migration of a synthetic data set generated for the model in Figure 2.14 using inaccurate values of η (the correct value, V_{nmo}=3.29 km/s, is used in both cases). The errors, apparent in both cases, show the sensitivity of the migration results to the value of η. Predictably, the distortions are more pronounced for the model with a larger error in η: not only do the reflectors cross, but also the reflector edges are not imaged well.

Usually we can expect to obtain the zero-dip NMO velocity with a higher accuracy than that for the parameter η. The inverted value of η, however, can be refined by inspecting migrated images. In isotropic media, undermigration is usually corrected by increasing the migration velocity. According to equation (2.12), an increase in η leads to a higher horizontal velocity. Therefore, a corresponding correction in transversely isotropic media can be achieved by increasing η (the case in Figure 2.16). If, however, we have more confidence in the measured value of the NMO velocity for the dipping reflector than that for the horizontal one, a proper choice would be to change both $V_{\text{nmo}}(0)$ and η. In fact, then, given that error likely exists in both, the data processor now has two parameters that can be adjusted to improve the quality of the image.

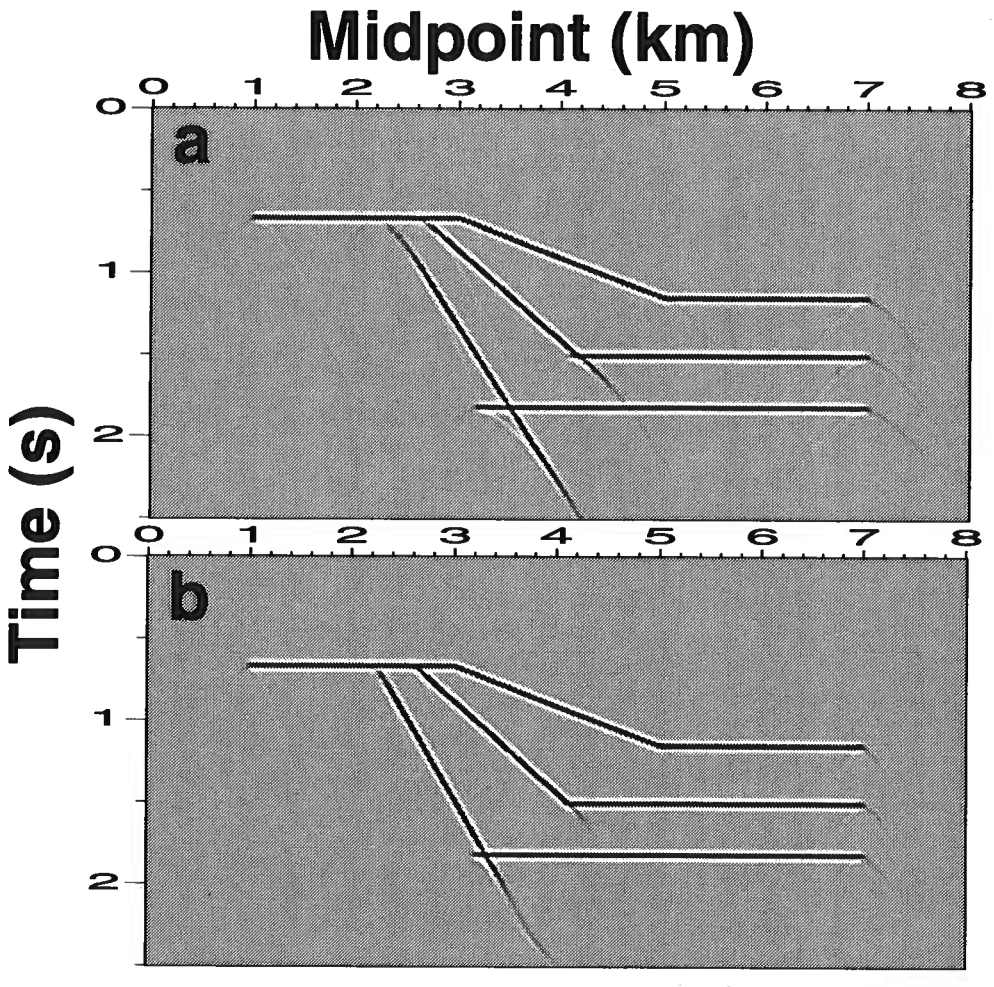

FIG. 2.16. Anisotropic poststack time migrations of a synthetic data set generated for the model in Figure 2.14 using distorted values of η: (a) η=0.01, (b) η=0.06; the actual value $\eta = 0.0833$. In both cases $V_{\text{nmo}}(0)$=3.29 km/s, the correct value.

Chapter 3

VELOCITY ANALYSIS IN $V(Z)$ MEDIA

While it is convenient to consider the earth's subsurface to be homogeneous, it is at a minimum vertically inhomogeneous. Through the combined action of gravity and sedimentation, velocity variation with depth represents the most important first-order inhomogeneity in the earth. This is one reason why time migration (based on lateral homogeneity) works well in so many places. Dip moveout (DMO) and migration algorithms that can handle isotropic $v(z)$ media are well established, and velocity estimation in such media is even considered trivial. Nevertheless, problems remain in focussing images, estimating depths, and preserving dipping events in $v(z)$ media. It may be that the problem at this point is the restrictive assumption that the medium is isotropic. Because basic processes that developed the earth's crust (i.e., sedimentation, stress and gravity) have a preferred direction (vertical in most cases), seismic wave speed can vary with propagation direction in the vertical plane. Otherwise, it is difficult to explain the success of isotropic homogeneous DMO in areas with a clear velocity increase with depth (Gonzalez et al., 1992), knowing that such an increase in velocity would cause the dipping events to stack at a lower velocity than would horizontal ones (Artley and Hale, 1994) where the subsurface is isotropic.

The bulk of this chapter concentrates on the $v(z)$ inversion process for the parameters $V_{\text{nmo}}(0)$ and η. Here, I extend the inversion technique discussed in Chapter 2 to treat layered VTI media based on the fact that NMO velocity for dipping reflectors under laterally homogeneous overburden is a root-mean-square (rms) average of its interval values. Thus, a methodology for inversion is developed to estimate these parameters using this rms relation, which depends only on $V_{\text{nmo}}(0)$ and η. Next, I study the dependence of both DMO and time migration on $V_{\text{nmo}}(0)$ and η in vertically inhomogeneous media.

3.1 Velocity analysis in $v(z)$ media

The inversion technique discussed in Chapter 2 is designed for a homogeneous medium above the reflector. Inversion in layered VTI media can be implemented through a layer-stripping algorithm where the parameters of a certain layer (or interval) are estimated by removing the influence of the overlying layers. The layer-stripping portion of the inversion is similar to what Dix (1955) used to estimate interval velocities from stacking velocities based on a small-offset approximation.

3.1.1 NMO velocity equation for dipping reflectors in $v(z)$ media

For horizontal layers, whether the medium is isotropic or VTI, the NMO velocity at a certain zero-offset time, t_0, (equivalent to the migrated time, for horizontal layers) is given by an rms relation (Hake et al., 1984; Tsvankin and Thomsen, 1994)

$$V^2_{\rm nmo}(t_0) = \frac{1}{t_0}\int_0^{t_0} v^2_{\rm nmo}(\tau)d\tau, \tag{3.1}$$

where $v_{\rm nmo}(\tau)$ are "interval NMO velocities" given by

$$v_{\rm nmo}(\tau) = v(\tau)\sqrt{1+2\delta(\tau)},$$

and $v(\tau)$ is the interval vertical velocity. For isotropic media, $\delta(\tau)=0$, and therefore, $v_{\rm nmo}(\tau) = v(\tau)$. For the sake of simplicity and without loss of generality, I will use the integral operator to represent summation.

For a dipping reflector beneath a horizontally layered medium, when expressed in terms of ray parameter p, NMO velocity is also given by a similar rms relation (as shown in Appendix B for discrete layers).

$$V^2_{\rm nmo}[p,t_0(p)] = \frac{1}{t_0(p)}\int_0^{t_0(p)} v^2_{\rm nmo}[p,t_m(\tau)]d\tau, \tag{3.2}$$

where $v_{\rm nmo}[p,t_m]$ is the interval NMO velocity as a function of vertical time (migrated time) t_m, and $t_0(p)$ is the zero-offset time for the ray parameter p. This ray parameter is the half slope, in a zero-offset section, of the reflection from the dipping reflector at time $t_0(p)$ used to measure $V_{\rm nmo}[p,t_0(p)]$, and $t_0(0)=t_m$ is the two-way traveltime to a horizontal reflector.

The integral in equation (3.2) can be expressed in terms of migrated time, t_m, as follows

$$V^2_{\rm nmo}[p,t_0(p)] = \frac{1}{t_0(p)}\int_0^{t_m} v^2_{\rm nmo}(p,\tau)\frac{dt_0(p)}{d\tau}d\tau. \tag{3.3}$$

This equation reduces to equation (3.1) for horizontal reflectors ($p=0$), where $\frac{dt_0(p)}{d\tau}$=1. Further, $v_{\rm nmo}(p,\tau)$ depends only on the interval values $v_{\rm nmo}(0,\tau)$ and $\eta(\tau)$ in each layer or, equivalently, at each time sample.

To apply equation (3.3), it is also necessary to express the traveltime $t_0(p)$ through the zero-offset time $t_0(0)$ and NMO velocity for a horizontal reflector. In Appendix B, I derive an equation for $t_0(p)$ valid for isotropy or elliptical anisotropy:

$$t_0(p) = t_0(0)\sqrt{1+p^2\,V^2_{\rm nmo}(p)}\,. \tag{3.4}$$

Therefore, if the overburden layers are isotropic or elliptically anisotropic, the two-way traveltime along the ray with any ray-parameter value p can be found from just the vertical traveltime $t_0(0)$ and the NMO velocity $V_{\rm nmo}(p)$ already determined in Appendix A as a function of $V_{\rm nmo}(0)$ and η.

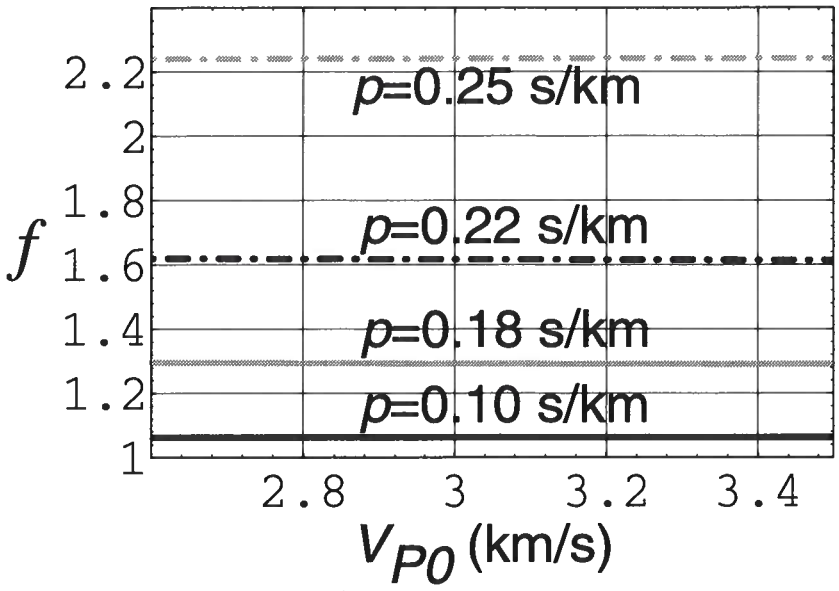

FIG. 3.1. Curves of the value of $f = \frac{t_0(p)}{t_0(0)}$ in equation (3.5), for a range of equivalent solutions and four different values of the ray parameter p. Here, V_{nmo}=3.29 km/s and $\eta = 0.0833$.

If the horizontal layers are vertically transversely isotropic (but not elliptically anisotropic), we have seen that it is necessary to know the value of η in addition to the zero-dip NMO velocity to find $V_{\text{nmo}}(p)$. As illustrated by Figure 3.1, the parameters $V_{\text{nmo}}(0)$ and η are also sufficient to calculate $t_0(p)$ given the zero-dip time $t_0(0)$.

$$t_0(p) = t_0(0)\, f[\eta, V_{\text{nmo}}(0), p]\,, \tag{3.5}$$

where f is independent of the vertical velocity and the individual values of the anisotropies ϵ and δ. Therefore, the NMO velocity, in layered VTI media, is a function of the interval values of V_{nmo} and η only. Recognizing that $t_0(0)$ is the migrated time, we can replace $t_0(0)$ by t_m to get

$$t_0(p) = t_m f[\eta, v_{\text{nmo}}(0), p]. \tag{3.6}$$

Thus,

$$\frac{dt_0(p)}{dt_m} = f[\eta, v_{\text{nmo}}(0), p], \tag{3.7}$$

where f is the operator that relates the vertical time to the zero-offset time, which can be obtained through ray tracing in TI media. As a result, $V_{\text{nmo}}[p, t_0(p)]$ based on equation (3.3) depends on η and $v_{\text{nmo}}(0)$ in each layer. For isotropic media, $\eta = 0$,

and

$$f[v_{\rm nmo}(0),p]=\frac{1}{\sqrt{1-p^2\,v^2_{\rm nmo}(0)}}.$$

Equation (3.2), for a model consisting of homogeneous layers (see Appendix B), is given by

$$[V^{(n)}_{\rm nmo}(p)]^2=\frac{1}{t_0(p)}\sum_{i=1}^{n}\Delta t_0^{(i)}(p)\,[v^{(i)}_{\rm nmo}(p)]^2\,, \tag{3.8}$$

where $\Delta t_0^{(i)}(p)$ is the two-way zero-offset traveltime through layer i for ray parameter p.

To obtain the NMO interval velocity in any layer i (including the one immediately above the reflector), I apply the formula of Dix (1955) to the NMO velocities at the top $[V^{(i-1)}_{\rm nmo}]$ and bottom $[V^{(i)}_{\rm nmo}]$ of the layer:

$$[v^{(i)}_{\rm nmo}(p)]^2=\frac{t_0^{(i)}(p)[V^{(i)}_{\rm nmo}(p)]^2-t_0^{(i-1)}(p)[V^{(i-1)}_{\rm nmo}(p)]^2}{t_0^{(i)}(p)-t_0^{(i-1)}(p)}\,, \tag{3.9}$$

where $t_0^{(i-1)}(p)$ and $t_0^{(i)}(p)$ are the two-way traveltimes to the top and bottom of the layer, respectively, calculated along the ray given by the ray parameter p for normal-incidence reflection from the dipping reflector All NMO velocities here correspond to a single ray-parameter value p. Suppose, we wish to use equation (3.9) to obtain the normal moveout velocity $[v^{(n)}_{\rm nmo}(p)]$ in the medium immediately above the reflector for use as an input value in the inversion algorithm discussed above. Clearly, from equation (3.8), the recovery of $v^{(n)}_{\rm nmo}(p)$ requires obtaining the moveout velocities in the overlying medium for the same value of the ray parameter. We can obtain such velocities only if the parameters η and $v_{\rm nmo}(0)$ are resolved above this layer. As we will see later, such a problem can be simplified by using an interpolation procedure.

However, for the special case of isotropic or elliptically anisotropic horizontal layers, the normal moveout velocity at any ray-parameter value can be obtained from the zero-dip NMO velocity in a straightforward fashion (see Appendix A).

3.1.2 Inversion in $v(z)$ media

When interval NMO velocity values, $v^{(n)}_{\rm nmo}(p)$, are obtained for at least two distinct dips, the problem within each layer (or time sample, if the inversion was based on the integral form) reduces to the inversion for a homogeneous medium, which can be performed in the way described in Chapter 2. Therefore, interval values $v^{(n)}_{\rm nmo}(p)$ for two distinct dips in each layer (or each time sample) are used to estimate $\eta(\tau)$ and $v_{\rm nmo}(0,\tau)$. Since estimating $v^{(n)}_{\rm nmo}(p)$ using equation (3.9) depends on obtaining $v^{(i)}_{\rm nmo}(p)$ for previous layers *at the same ray parameter*, estimation of $\eta(\tau)$ and $v_{\rm nmo}(0,\tau)$ must be done simultaneously with the layer-stripping process for $v^{(i)}_{\rm nmo}(p)$.

First, I use the values $V^{(1)}_{\rm nmo}(p_1)$ and $V^{(1)}_{\rm nmo}(p_2)$, which correspond to the first interval, to estimate $\eta^{(1)}$ and $v^{(1)}_{\rm nmo}(0)$ using the inversion procedure described earlier for

a homogeneous medium. Here p_1 and p_2 are ray parameters of the dipping reflectors in this first interval (one of these reflectors could be horizontal). Each subsequent interval is considered homogeneous. Then, I use the estimated $\eta^{(1)}$ and $v^{(1)}_{\text{nmo}}(0)$ to obtain $V^{(1)}_{\text{nmo}}(p_3)$ and $V^{(1)}_{\text{nmo}}(p_4)$, as well as $\frac{dt_0(p_3)}{dt_0(0)}$ and $\frac{dt_0(p_4)}{dt_0(0)}$, in the first interval, where ray parameters p_3 and p_4 correspond to the dipping reflectors (one of which, again, can be horizontal) in the second interval. Using the Dix-type equation, equation (3.9), from $V^{(2)}_{\text{nmo}}(p_3)$ and $V^{(2)}_{\text{nmo}}(p_4)$ I then obtain the interval values $v^{(2)}_{\text{nmo}}(p_3)$ and $v^{(2)}_{\text{nmo}}(p_4)$, pertinent to the second interval, and in turn use them to obtain $\eta^{(2)}$ and $v^{(2)}_{\text{nmo}}(0)$, and so on.

Although the method requires NMO velocities measured at two different dips in each interval, one can define interval thicknesses that insure the presence of at least two different dips in each interval. Specifically, each interval can be chosen to include two dips and assumed to be homogeneous, no matter how large that interval gets. Here, however, I use a more practical approach based on curve fitting and interpolation. Specifically, for each of the ray parameters of the dipping reflections used to measure the stacking velocities, I fit interval-velocity models, based on piecewise-linear, continuous-interval η values, to equation (3.3). These velocity models satisfy the measured stacking velocities and zero-offset times through equation (3.3); also, the interval η values that are used to compute the interval NMO velocities are taken to be continuous at the times of the measured stacking velocities and linear in between. A detailed description of the inversion procedure is given in Appendix C. This interpolation approach is more practical than the discrete layer approach.

As with isotropic media, intermediate interval values (i.e., values between measured ones) can be estimated using any preferred interpolation technique. The sole requirement is that interval values yield the measured stacking velocities and zero-offset times based on equation (3.3). For example, we could consider the measured values to be constant between its measured times. Here, however, the application is based on a linear interpolation that keeps the inverted interval values continuous. This continuity is important for various ray tracing applications.

3.2 Error Analysis

The primary objective of the anisotropic inversion (layer stripping), described here, is to obtain an improved image of the subsurface over that obtained using isotropic inversion. Therefore, focusing the image is the main goal of this inversion process, with estimation of the parameters a secondary goal. Based on this order of importance, the accuracy of the inverted parameters in terms of their lithological interpretation is of minor importance. What is important is the result of using these parameters in imaging and focussing the section. Therefore, as in practice for isotropic media, error bounds on these interval parameters for the purpose stated above is not necessary.

If, however, the interval parameters are used for lithology discrimination, error bounds on these parameters should be calculated. To do so, we must investigate the

sensitivity of the inverted parameters to the measured ones. This is not trivial in nonlinear problems, where only local analysis can be performed by evaluating derivatives. Nevertheless, if the problem is well behaved and the NMO velocity function is smoothly varying, which is the case here, the linearized analysis is acceptable.

Errors in the inverted interval values of η can arise both from the linear interpolation of η used in the layer-stripping process, and from the inversion in each homogeneous interval used to obtain η. The interpolation errors are similar to those encountered in layer-stripping applications for isotropic media. Errors associated with the homogeneous inversion, described in detail in Chapter 2, depend mainly on the accuracy of the measured quantities, primarily the stacking velocities.

Here, I concentrate on the significance of the layer-stripping errors. The interval NMO velocity in a homogeneous layer can be determined uniquely from the rms NMO velocities above and below that layer; therefore, as we saw earlier,

$$[v^{(i)}_{\rm nmo}(p)]^2 = \frac{t^{(i)}_0(p)[V^{(i)}_{\rm nmo}(p)]^2 - t^{(i-1)}_0(p)[V^{(i-1)}_{\rm nmo}(p)]^2}{t^{(i)}_0(p) - t^{(i-1)}_0(p)}, \tag{3.10}$$

Using the chain rule

$$v^{(i)}_{\rm nmo}(p)\partial v^{(i)}_{\rm nmo}(p) = \frac{t^{(i)}_0(p)}{t^{(i)}_0(p) - t^{(i-1)}_0(p)} V^{(i)}_{\rm nmo}(p)\partial V^{(i)}_{\rm nmo}(p) - \frac{t^{(i-1)}_0(p)}{t^{(i)}_0(p) - t^{(i-1)}_0(p)} V^{(i-1)}_{\rm nmo}(p)\partial V^{(i-1)}_{\rm nmo}(p).$$

Considering the worse-case scenario, where errors due to both measured parameters act in the same direction and therefore add up,

$$\Delta v^{(i)}_{\rm nmo}(p) = \frac{t^{(i)}_0(p)}{t^{(i)}_0(p) - t^{(i-1)}_0(p)} \frac{V^{(i)}_{\rm nmo}(p)}{v^{(i)}_{\rm nmo}(p)} |\Delta V^{(i)}_{\rm nmo}(p)| + \frac{t^{(i-1)}_0(p)}{t^{(i)}_0(p) - t^{(i-1)}_0(p)} \frac{V^{(i-1)}_{\rm nmo}(p)}{v^{(i)}_{\rm nmo}(p)} |\Delta V^{(i-1)}_{\rm nmo}(p)|.$$

Clearly, as in isotropic media, the error in the interval NMO velocity is a function of the ratio of the layer thickness (in time) to the zero-offset traveltime to the bottom of that layer. The errors actually increase linearly with zero-offset time. Simply stated, the velocity in a thin shallow layer is better resolved and less sensitive to errors than that at depth. In addition, because reflection moveout at a fixed offset decreases with depth even if velocity remains the same, the accuracy of measuring the NMO velocity (using for example semblance analysis) also decreases with depth. Therefore, error bars for the inverted parameters will increase with depth.

3.2.1 Stacking-velocity measurements

The stacking velocity for steep reflectors (equal to $\frac{V_{\rm nmo}(0)}{\cos(\phi)}$ in isotropic homogeneous media, where ϕ is the reflector dip) is large; therefore, the moveout is small and insensitive to velocity. Specifically, the curvature of reflection moveout, dt^2/dX^2 $[\propto 1/V^2_{\rm nmo}]$, where X is the source-receiver offset, decreases with increase in velocity. As a result, the resolution of velocity analyses is poor, causing problems in picking

the appropriate stacking velocities corresponding to dipping reflectors.

One way to mitigate this problem is to pick the stacking velocity after applying DMO to the data. At this stage in the process, it is sufficient that the DMO be based on the assumption of a homogeneous isotropic medium. The DMO operation reduces the stacking velocity of dipping reflectors (approximately equivalent to multiplying by $\cos\phi$), therefore increasing the sensitivity of moveout to velocity. As a result, I modify the NMO velocity equation in TI media to account for the DMO operation. This is accomplished by subtracting the traveltime shifts that correspond to the DMO operation ($= -p^2X^2$) in the NMO equation for dipping reflectors.

$$t^2(p,X) = t_0^2(p) + (\frac{1}{V_{\text{nmo}}^2(p)} + p^2)X^2 = t_0^2(p) + \frac{X^2}{V_{\text{stk}}^2(p)},$$

where t is the two-way traveltime as a function of offset, X. Therefore, the NMO velocity for a dipping reflector after isotropic constant-velocity DMO is given by

$$V_{\text{stk}}(p) = \frac{V_{\text{nmo}}(p)}{\sqrt{1 + p^2V_{\text{nmo}}^2(p)}}. \tag{3.11}$$

Equation (3.11) can, therefore, be used to replace the $V_{\text{nmo}}(p)$ function in inverting for η and $V_{\text{nmo}}(0)$. For isotropic homogeneous media,

$$V_{\text{nmo}}(p) = \frac{V_{\text{nmo}}(0)}{\sqrt{1 - V_{\text{nmo}}^2(0)p^2}};$$

therefore, $V_{\text{stk}}(p)$ reduces to $V_{\text{nmo}}(0)$, and the stacking velocity becomes independent of p as a result of applying the isotropic DMO.

There is an additional advantage to applying the DMO operation prior to velocity analysis when inverting for η. Specifically, we can verify the presence of anisotropy by comparing the NMO velocity of the sloping event (after DMO) to that of a horizontal event (or any other distinct lesser slope). If the velocity of the sloping event is higher, then, in most cases, anisotropy is present, and η is positive. If the medium is also vertically inhomogeneous, then the anisotropy must be even more significant then for homogeneous media, because inhomogeneity tends to reduce the influence of anisotropy on the DMO operation (Lynn et. al., 1991; Alkhalifah, 1996a). If the velocity of the sloping event is lower than that of the horizontal event after applying homogeneous isotropic DMO, then there are two possibilities: the first is that the medium is vertically inhomogeneous (Artley and Hale, 1994) and at most only mildly anisotropic, and the second is that the medium is anisotropic with a negative η, which is unlikely (Tsvankin and Thomsen, 1994).

If the NMO velocities of the sloping and horizontal reflections are equal after applying homogeneous isotropic DMO (which is the main goal of applying the DMO) then the medium may be isotropic and homogeneous, in concurrence with the type

of operation used. If, however, velocity analysis of horizontal events implies vertical inhomogeneity (which is typically the case), then anisotropy is present and has the same size (with an opposite sign) influence as does the vertical inhomogeneity on the DMO operation for these two dips (Gonzalez et al., 1992; Alkhalifah, 1996a). Nevertheless, although the homogeneous isotropic DMO focussed these two reflections (the sloping and horizontal) at the same stacking velocity, it still might not focus reflections with other slopes as well because the isotropic $v(z)$ DMO impulse response is not identical to the anisotropic one for all slopes (Alkhalifah, 1996a). Here, I have tried to outline the main possibilities. The presence of strong lateral inhomogeneity would introduce further complications.

3.3 Time-related processing

The main argument used to show the dependence of time-related processing (e.g., DMO and time migration) on only $V_{\text{nmo}}(0)$ and η in homogeneous VTI media is that such time-related processing become independent of the vertical velocity V_{P0} when expressed in terms of $V_{\text{nmo}}(0)$ and η. That is, it does not matter what values of V_{P0}, ϵ, and δ are used; only $V_{\text{nmo}}(0)$ and η need to be specified. To support such an assertion, I next compare changes in impulse responses (e.g., migration impulse responses) for a range of tests in which V_{P0}, ϵ and δ are varied from one test to another while keeping $V_{\text{nmo}}(0)$ and η fixed. In Chapter 2, I used such an argument for homogeneous media. Here I apply it to vertically inhomogeneous media.

Figure 3.2 shows parameter variations as a function of vertical time that I use below to generate impulse responses. The vertical velocity (V_{P0}) given by the solid black curve is the same as the $v_{\text{nmo}}(0)$ curve; therefore, δ for this model equals zero. When combined with $v_{\text{nmo}}(0)$, the other two V_{P0} curves correspond to δ values that do not equal zero [see equation (2.5)]. The dashed curve (vertical velocity is a constant, 1500 m/s), when combined with $v_{\text{nmo}}(0)$, results in δ reaching values as large as the unrealistically high value of 2. Therefore, in terms of Thomsen's parameters, for any of the η curves the difference between the model given by the solid black V_{P0} curve and the model given the dashed curve is large, but the parameters have been chosen such that $v_{\text{nmo}}(0)$ and η are nevertheless the same for all three models with the different V_{P0}.

3.3.1 Dip-moveout correction

As demonstrated in Chapter 2, the NMO velocity for dipping reflectors depends on only two medium parameters in homogeneous VTI media, namely $V_{\text{nmo}}(0)$ and η. It should follow, then, that the DMO operation itself, as well as its impulse response, depends solely on these two parameters.

Figure 3.3 shows four DMO impulse responses generated using the anisotropic DMO algorithm described later. The first of these responses (Figure 3.3a) corresponds to the parameters given by the solid black curves in Figure 3.2 for V_{P0}, $v_{\text{nmo}}(0)$ and

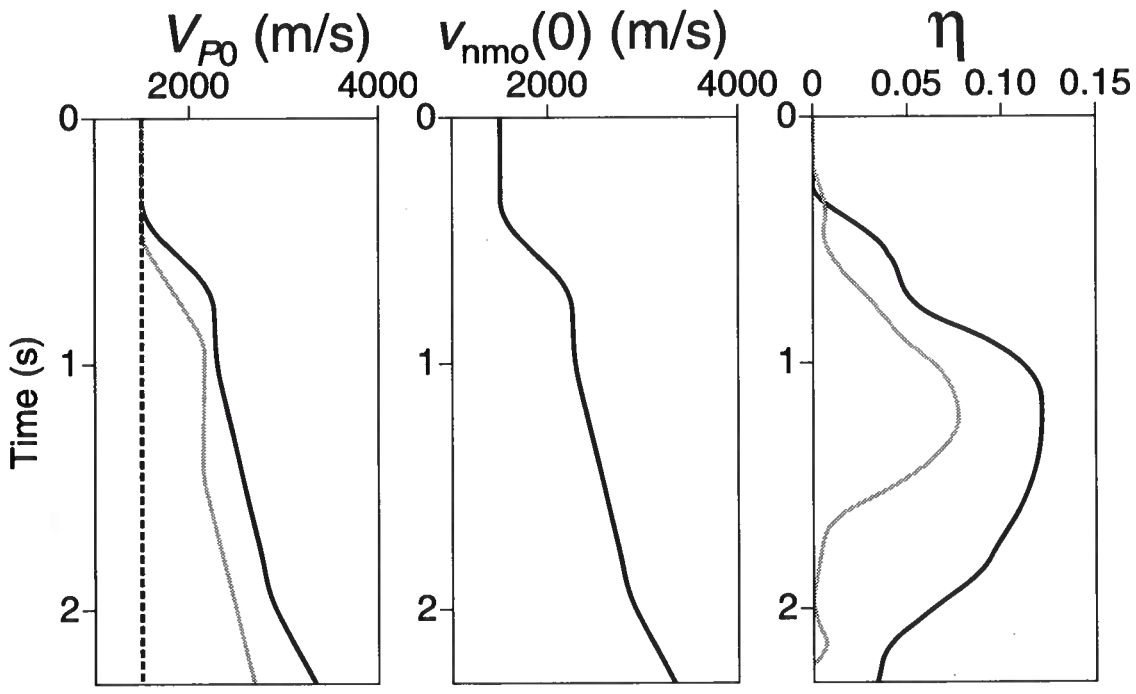

FIG. 3.2. Parameter variation as a function of vertical time. The parameters here correspond to the interval vertical velocity V_{P0}, the interval NMO velocity for horizontal reflectors $v_{\text{nmo}}(0)$, and the anisotropy parameter η. Different combinations of these parameters result in different models.

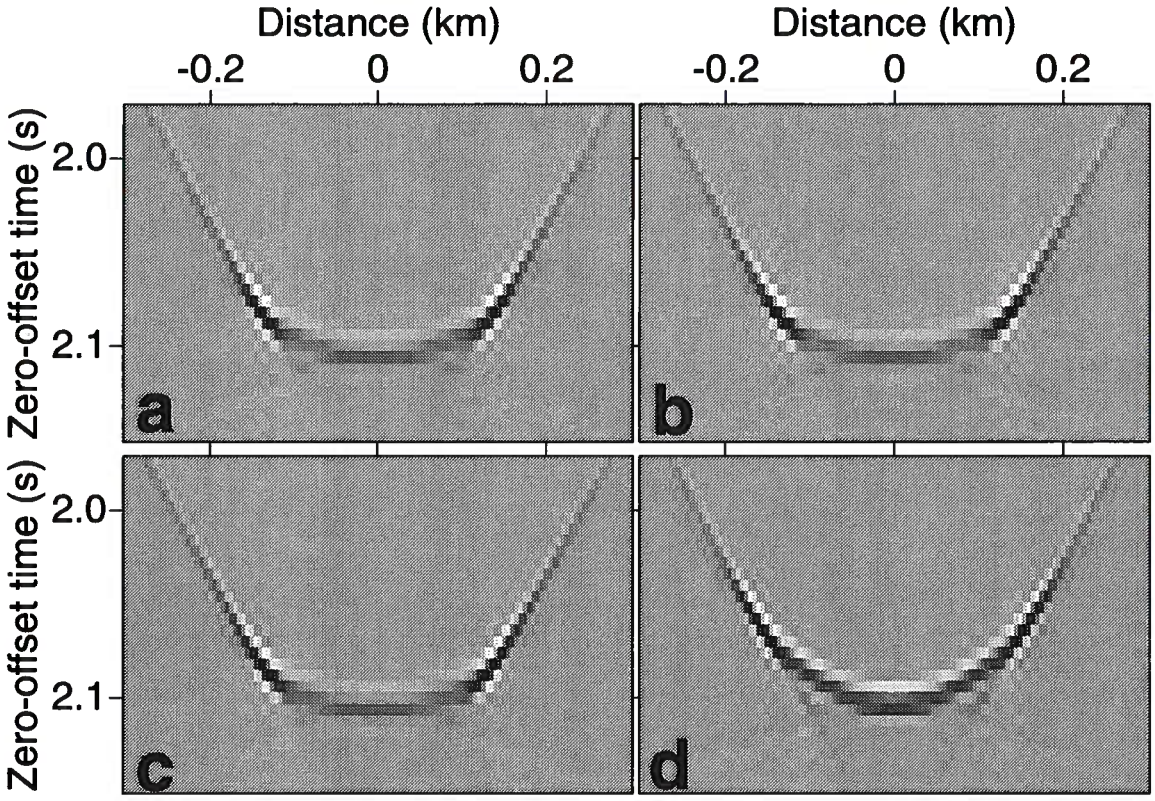

FIG. 3.3. DMO impulse responses for an impulse at time 2.1 s and offset 1.5 km using (a) the parameters represented by solid black curves in Figure 3.2, (b) the vertical velocity given by the gray curve in Figure 3.2 while keeping the other parameters the same as for (a), (c) the vertical velocity given by the dashed curve in Figure 3.2 while keeping the other parameters the same as for (a), and (d) the η values represented by the gray curve in Figure 3.2 while keeping V_{P0} and $v_{\text{nmo}}(0)$ the same as for (a).

η. Note how different this DMO impulse response for a VTI medium is from the elliptical shape we have grown accustomed to for isotropic media. The responses in Figure 3.3b and 3.3c correspond to using the gray and the dashed curves of V_{P0} in Figure 3.2, respectively, while keeping the values of $v_{\text{nmo}}(0)$ and η the same as those used in Figure 3.3a (the solid black curves). The three DMO impulse responses look exactly the same; that is, they are independent of the value of V_{P0}, in support of the result that was partially suggested by equation (3.2), a small-offset approximation of the moveout. (Recall that for the response in Figure 3.3c, δ reaches such uncommenly high values as 2!) On the other hand, if we change η, using the gray curve for η in Figure 3.2 (which is closer to an isotropic model, where η=0) instead of the black one, the response changes dramatically, implying that it is highly dependent on η. In fact, the impulse response for the gray curve, as expected, has a shape that is much closer to the elliptical shape we observe for isotropic media.

3.3.2 Time migration

In Chapter 2, we saw that the nonhyperbolic moveout based on a Taylor's series expansion for vertically inhomogeneous VTI media is likewise dependent on only $v_{\text{nmo}}(0,\tau)$ and $\eta(\tau)$. Since this moveout equation represents a small-dip approximation of a zero-offset diffraction curve, we should expect that time migration also depends on just these two parameters.

Figure 3.4 shows four poststack, time-migration impulse responses generated using an anisotropic phase-shift time migration (Kitchenside, 1991). The first of these responses (Figure 3.4a) corresponds to the parameters given by the solid black curves in Figure 3.2 for V_{P0}, $v_{\text{nmo}}(0)$ and η. In contrast, the responses in Figure 3.4b and 3.4c correspond to using the gray and the dashed curves of vertical velocity (V_{P0}) from Figure 3.2, respectively, while keeping $v_{\text{nmo}}(0)$ and η the same as those used in Figure 3.4a. The three time migration impulse responses look identical. Given the large difference between the Thomsen's parameters used to generate Figure 3.4a from those used to generate Figure 3.4c, the similarity of the responses that are based on the exact traveltime calculation (within the framework of ray theory) is striking. Therefore, time migration in VTI media is also seen to be independent of vertical velocity when expressed in terms of $v_{\text{nmo}}(0)$ and η. However, if the gray η curve in Figure 3.2 is used, differences appear. Specifically, note that, because of the overall lower η, the response in this case (Figure 3.4d) is slightly squeezed (see arrows). For a near-vertical reflector the lateral position difference is about 5 percent. Although the time migration responses appear to have less variation with change in η than do the DMO responses, note that the scales at which the responses in the case of DMO and time migration are plotted differ substantially. The conclusion in any event is that for modest dip, migration will be less sensitive to ignoring anisotropy than is DMO. This is consistent with the results of Alkhalifah and Larner (1994).

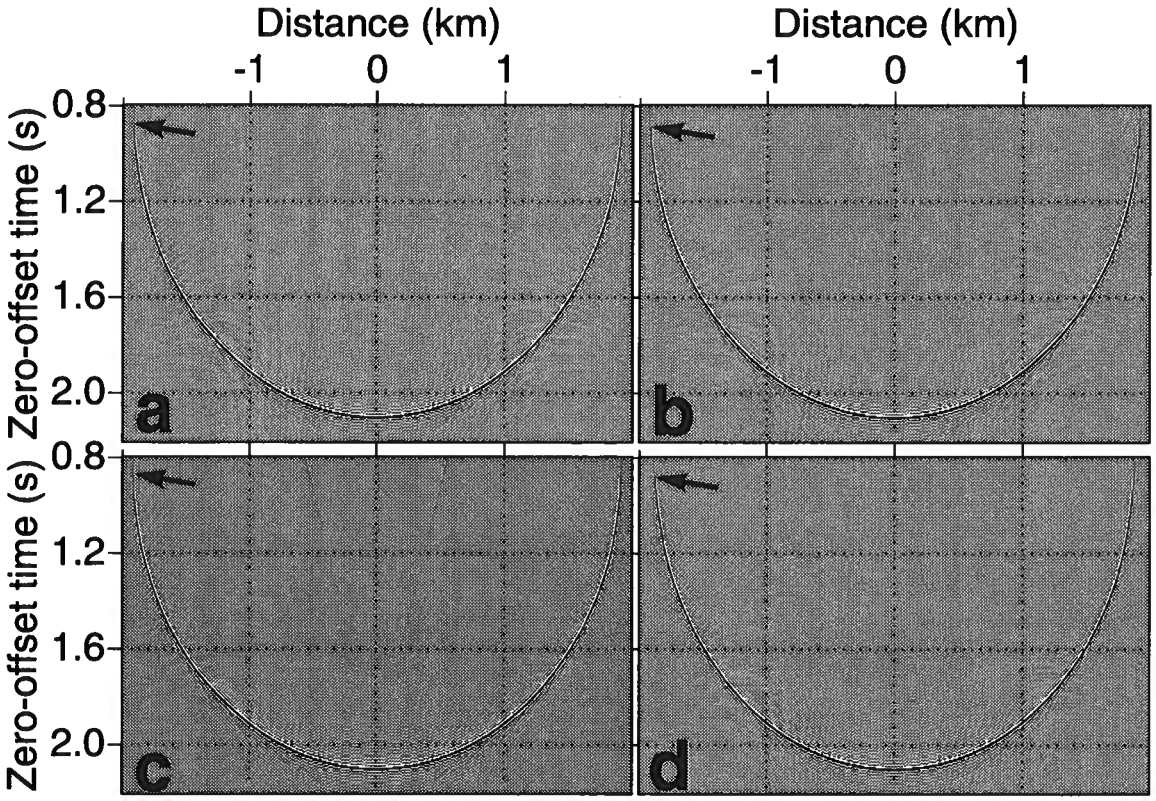

FIG. 3.4. Zero-offset time-migration impulse responses for an impulse at time 2.1 s, using (a) the parameters in Figure 3.2 represented by the solid black curves, (b) the vertical velocity given by the gray curve in Figure 3.2 while keeping the other parameters the same as for (a), (c) the vertical velocity given by the dashed curve in Figure 3.2 while keeping the other parameters the same as for (a), and (d) the η values represented by the gray curve in Figure 3.2 while keeping V_{P0} and $v_{\text{nmo}}(0)$ the same as for (a).

Chapter 4

DIP-MOVEOUT CORRECTION IN VTI MEDIA

The process of transforming prestack data to zero offset (TZO) accomplishes moveout correction for reflections from horizontal and dipping reflectors. Specifically, in an isotropic, homogeneous medium, TZO includes both normal moveout correction (NMO) and dip moveout correction (DMO). I use the term TZO to describe the one-step ray-tracing process used here to map nonzero-offset traveltimes directly to zero-offset times. Therefore, DMO correction corresponds to TZO with the moveout correction for horizontal reflectors applied.

The combination of anisotropic ray tracing (Červený, 1972) and dip-decomposition (Jakubowicz, 1990) in transforming prestack data to zero-offset (or in applying DMO) is particularly well suited to handling the nonhyperbolic moveout in homogeneous or inhomogeneous TI media. For such media, with accurate traveltime computations such as by ray tracing, data can be transformed to zero-offset, thus lessening the severity of muting necessary for the far offsets. After outlining the DMO method, I generate and study DMO impulse responses in VTI media, and compare them with the familiar elliptical DMO response for isotropic, homogeneous media. Finally, I apply this DMO approach to synthetic data, demonstrating the need to take anisotropy into account in order to achieve the goals of DMO.

4.1 Transformation to zero offset

The DMO approach of Artley and Hale (1994), appropriate for isotropic $v(z)$ media, is based on a combination of Jakubowicz's (1990) dip-decomposition method and ray tracing in isotropic $v(z)$ media. Their DMO algorithm results from subtracting an NMO correction after transformation to zero offset. The advantage of using DMO, as opposed to full TZO, is that the separately-applied NMO correction can accommodate smooth lateral velocity variations in the media, while the full TZO treats only $v(z)$ media.

4.1.1 Solving for the zero-offset time and position

The method of Artley and Hale requires solution of a system of nonlinear equations to find a trio of rays needed to calculate the zero-offset time, t_0, and position, x_0 (see Figure 4.1). This ray trio includes the rays from the source, receiver, and zero-offset locations to each (potential) specular reflection point in the subsurface. These rays are characterized by their ray parameter p_s, p_g, and p_0, respectively. Solution of a system of four equations and four unknowns is necessary in order to obtain the ray

trio. In particular, one of these equations is based on Snell's law, which requires that the incident and reflection angles be equal. That is,

$$\theta_0 = \frac{\theta_s + \theta_g}{2}, \tag{4.1}$$

where θ_0 is the angle between the normal to the reflector and the vertical axis (the reflector dip), θ_s is the angle between the incident ray originating from the source and the vertical, and θ_g is the angle between the reflected ray and the vertical. A detailed description of the algorithm is given by Artley and Hale (1994).

Using ray tracing for anisotropic media, as described in Appendix A, and replacing equation (4.1) with

$$\frac{\sin(\theta_s - \theta_0)}{V(\theta_s)} = \frac{\sin(\theta_0 - \theta_g)}{V(\theta_g)},$$

where $V(\theta)$ is the phase velocity, modifies the TZO of Artley and Hale to accommodate $v(z)$ anisotropic media. Here θ corresponds to the phase angle, which generally differs from the ray angle in TI media. Because the components of the ray position (the vertical time τ and surface position x), as a function ray parameter, are applicable to all midpoints for a $v(z)$ medium, they need to be tabulated only once. As a result, the cost of the modification of the ray-tracing algorithm to treat TI media is negligible compared with the overall cost of the DMO, especially for large data volumes.

The system of four nonlinear equations,

$$\begin{aligned} 0 &= x(p_g, 2t_g) - x[p_s, 2(t_{sg} - t_g)] + 2h \\ 0 &= \tau(p_g, 2t_g) - \tau[p_s, 2(t_{sg} - t_g)] \\ 0 &= \tau(p_g, 2t_g) - \tau(p_0, t_0), \\ 0 &= \frac{\sin(\theta_s - \theta_0)}{V(\theta_s)} - \frac{\sin(\theta_0 - \theta_g)}{V(\theta_g)} \end{aligned} \tag{4.2}$$

is used to solve for four unknowns p_s, p_g, t_g, and t_0. The first equation in system (4.2) is the requirement that the lateral distances, x, from each of the source and receiver to the specular reflection point (SRP) add up to equal the source-receiver offset, $2h$, while the second and third equations imply that the vertical times, τ (or depths) from each of the source, receiver, and zero-offset surface positions to SRP are the same. This system is solved for a given half-offset h, total traveltime t_{sg}, and p_0. Once t_0 is obtained, we can calculate x_0 using

$$x_0 = x(p_g, 2t_g) - x(p_0, t_0) + h.$$

A detailed description of these parameters is shown in Figure 4.1, and given in Artley and Hale (1994) and Artley (1992). This system of equations can be solved using, for example, multi-dimensional Newton-Raphson iteration (see, e.g., Press et al., 1986, pp. 269–273).

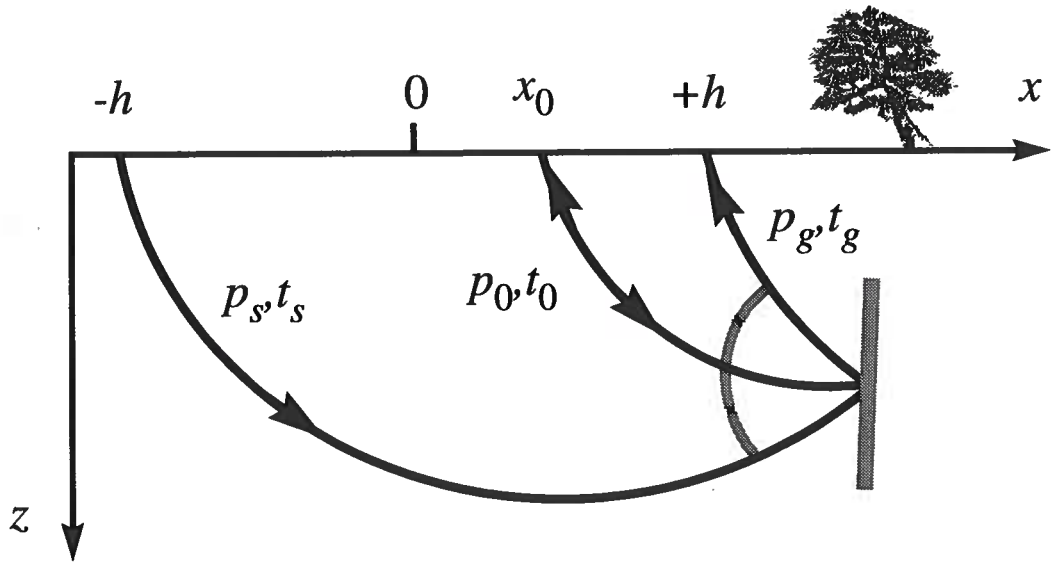

FIG. 4.1. Diagram showing a DMO raypath trio. All three rays must terminate at the reflection point and the zero-offset ray bisects the angle formed by the source ray and the geophone ray. The zero-offset ray is normal to the reflecting surface at the reflection point.

To apply the algorithm as a DMO operation, it is sufficient to subtract from the full TZO traveltime calculations the traveltime portion that corresponds to either NMO correction (Artley and Hale, 1994) or nonhyperbolic moveout correction (Tsvankin and Thomsen, 1994; Alkhalifah, 1996b) for horizontal reflectors. The approach of removing a nonhyperbolic moveout correction is used below to generate DMO impulse responses in VTI media. Ultimately, however, I implement DMO by subtracting from the full TZO traveltime calculations the traveltime portion that corresponds to NMO correction only,

$$t_{sg}^2 = t_n^2 + \frac{4h^2}{V_{\rm rms}^2(t_n)}, \tag{4.3}$$

where $V_{\rm rms}(t)$ denotes the root mean square average of the interval time-dependent NMO velocity function $v_{\rm nmo}(t)$,

$$V_{\rm rms}(t) = \left[\frac{1}{t}\int_0^t ds\, v_{\rm nmo}^2(s)\right]^{1/2}.$$

The resulting recording time is then used as a parameter of the system. Therefore, the input to the DMO is the NMO-corrected section with the time axis given by t_n.

To get the slope-dependent moveout required for DMO by the dip-decomposition approach, the zero-offset time t_0 corresponding to a particular slope p_0 must be projected back to the midpoint along the line tangent to the DMO operator at (x_0, t_0). This is equivalent to applying a τ-p transform to the impulse response. By definition, the slope of this tangent is $\partial t_0/\partial x_0 = p_0$, so the projection is

$$\tilde{t}_0 = t_0 + p_0 x_0.$$

It is actually this $\tilde{t}_0$ that is referred to as simply t_0 in the DMO mapping $t_n(\tilde{t}_0, p_0)$ required for applying DMO by dip-decomposition. At this point, however, t_n is an independent variable and $\tilde{t}_0 = \tilde{t}_0(t_n, p_0)$. Inverse interpolation is used to make $\tilde{t}_0$ the independent variable. For a fixed value of p_0, assume that $\tilde{t}_0(t_n)$ is a monotonically increasing function of t_n. This ensures that no two NMO times t_n correspond to the same zero-offset time t_0, which is a practical assumption for a single ray parameter. Then linear interpolation can be used to find $t_n(\tilde{t}_0)$ for that slope, and $\tilde{t}_n(t_0, p_0)$ in general.

Because this method is based on ray tracing, the traveltime calculations are exact (within the framework of ray theory), and therefore can appropriately map nonhyperbolic moveout. This is an advantage over DMO methods based on hyperbolic moveout equations (i.e., Anderson and Tsvankin, 1995), which often ignore the large nonhyperbolic moveout in VTI media. This advantage will be exemplified in the discussion of the field data example.

4.1.2 DMO by Dip Decomposition

After obtaining the DMO mapping $\tilde{t}_n(t_0, p_0)$, I then use it in the DMO by dip decomposition. For a flat reflector dipping at an angle θ in a medium of constant velocity v, the relationship between zero-offset time t_0 and NMO time t_n at a common midpoint is

$$t_0^2 = t_n^2 + \frac{4h^2 \sin^2 \theta}{v^2}$$

(Hale, 1984). By noting that $p_0 = 2 \sin \theta / v = k/\omega_0$, where $p_0 \equiv \partial t_0 / \partial x$ is the reflection slope measured on a zero-offset section, Jakubowicz (1990) wrote this relationship as

$$t_n^2 = t_0^2 - p_0^2 h^2. \tag{4.4}$$

Note that for a single reflection slope, DMO reduces to a simple slope-dependent moveout operation.

As a result, Hale's original DMO formula (1984) can be written for a single slope $p_0 = k/\omega_0$ as

$$\tilde{Q}_0(\omega_0, k) = \int_0^\infty d\tilde{t}_0 \, e^{i\omega_0 \tilde{t}_0} q_n[t_n(\tilde{t}_0, p_0), k], \tag{4.5}$$

where q_n is the NMO corrected data. By defining

$$\tilde{q}_0(\tilde{t}_0, k) \equiv q_n[t_n(\tilde{t}_0, p_0), k], \tag{4.6}$$

equation (4.5) becomes

$$\tilde{Q}_0(\omega_0, k) = \int_0^\infty d\tilde{t}_0 \, e^{i\omega_0 \tilde{t}_0} \tilde{q}_0(\tilde{t}_0, k), \tag{4.7}$$

which is simply the Fourier transform of the interpolated data $\tilde{q}_0(t_0, k)$.

Jakubowicz's method proceeds by *decomposing* the zero-offset section $Q_0(\omega_0, k)$ into its component slopes, $p_0 = k/\omega_0$. The contribution of each slope component is computed separately via equations (4.6) and (4.7). For this reason, the method is sometimes referred to as *DMO by dip-decomposition* (Hale, 1988), or, perhaps more precisely, reflection *slope*-decomposition.

Jakubowicz (1990) showed that the dip-decomposition technique is equivalent to Hale's (1984) DMO by Fourier transform formulation provided that the sampling of reflection slope is sufficiently fine. Hale (1988) derived a sampling criterion that avoids spatial aliasing of the zero-offset data.

The scheme for computing the $v(z)$ DMO mapping $t_n(t_0, p_0)$ is outlined in the algorithm of Figure 4.2 (Artley, 1992).

4.2 DMO impulse responses in VTI media

Following Artley and Hale (1994), I use ray tracing (but now in VTI media) to generate exact trajectories for DMO impulse responses in VTI $v(z)$ media. Using this

Computation of the DMO mapping:

Compute ray tables $x(p,t)$, $\tau(p,t)$, $\theta(p,t)$ *(now using VTI raytracing)*
For all half-offsets h {
    For all NMO times $t_n = 0, \Delta t_n, 2\Delta t_n, \ldots$ {
        Compute recording time via $t_{sg}^2 = t_n^2 + 4h^2/v_2^2(t_n)$
        Compute trial solution to system for $p_0 = 0$,
            assuming $v = \text{const} = v_2(t_n)$
        For all $p_0^2 = 0, \Delta p_0^2, 2\Delta p_0^2, \ldots$ {
            Refine trial solution to system using
                Newton-Raphson iteration
            Project t_0 *back to the midpoint with*
                $t_0(t_n, p_0) := t_0(t_n, p_0) + p_0 x_0(t_n, p_0)$
            Save the inverse DMO mapping $t_0(t_n, p_0)$
            Use final solution for this p_0 *as*
                trial solution for next p_0
        }
    }
    For all $p_0^2 = 0, \Delta p_0^2, 2\Delta p_0^2, \ldots$ {
        Compute the DMO mapping $t_n(t_0, p_0)$ *from*
            $t_0(t_n, p_0)$ *via inverse interpolation*
    }
    Apply DMO via dip-decomposition to common-
        offset section (as described in the
        section on DMO by Dip Decomposition)
}

FIG. 4.2. Algorithm for computing and applying $v(z)$ DMO correction.

DMO impulse-response generator, I study the dependence of the response shape on the various parameters that control DMO in VTI media. These parameters are: η, $V_{\text{nmo}}(0)$, offset, and NMO-corrected time, t_n. Let us begin by examining the dependence of the DMO impulse response on the anisotropy, specifically on the parameter η in homogeneous VTI media.

4.2.1 Dependence on η

The impulse responses in Figure 4.3 pertain to $V_{\text{nmo}}(0)$=2.0 km/s, offset=1.5 km, and NMO time, t_n =1.5 s. Superimposed on these black curves is the corresponding DMO trajectory for a homogeneous isotropic or elliptically isotropic medium (gray curves), both of which are characterized by $\eta = 0$ and the same $V_{\text{nmo}}(0)$ as that of the VTI model. Typical η values in the subsurface range from -0.1 to 0.3 (Thomsen, 1986; Alkhalifah and Tsvankin, 1995). Departures from the familiar elliptical shape for DMO responses in isotropic media ($\eta = 0$) in this range are evident. It is also interesting to observe the impulse-response behavior for models that are possible, in principle, but not typical. For instance, at $\eta = -0.3$, the DMO impulse response looks somewhat like an inverse DMO operator. At the opposite extreme ($\eta = 0.6$), the impulse response is highly flattened, with sizeable triplications at the sides (note again that all models in Figure 4.3 are homogeneous). However, unlike the triplications encountered in isotropic $v(z)$ media (Artley and Hale, 1994), the triplications here always correspond to reflector dips less than 90 degrees.

The most striking feature of the impulse responses is the triplications that develop as η increases. For positive η (i.e., $\eta = 0.3$), the impulse response in VTI media has three branches. The central one corresponds to the concave-upward region, which includes dips between 0 and 24$\pm$6 degrees [the upper limit of this range depends on η and $V_{\text{nmo}}(0)$]. This branch flattens with increase in η, and can be somewhat approximated by a stretched ellipse. Another branch is seen at the limbs of the previous branch as a concave-downward section of the triplication (this branch reduces to a point for $\eta = 0.1$). This portion corresponds to dips between 24$\pm$6 and 48$\pm$5 degrees; clearly, no flattened ellipse can approximate it. A third branch is represented by a somewhat straight line at the sides of the responses. These line shifts downward with an increase in η, and this region includes dips between 48$\pm$5 and 85 degrees. This line would project to the source and receiver locations at the surface, where the associated dip is 90 degrees.

For $\eta < -0.1$, a different kind of triplication develops. This one is centered on the symmetry axis, which implies that it acts on reflections from reflectors with small dips. Moreover, negative-sign reflector dips now appear to the right of the impulse-response symmetry point, instead of the left, as is the case for isotropic media.

As a consequence of the unusual shapes of the DMO operators in VTI media, the energy distributions along the response differ from those in isotropic media. The nonuniform distribution is necessary to insure that the summation of amplitudes along impulse responses in the DMO process yields proper amplitudes of reflections. Fig-

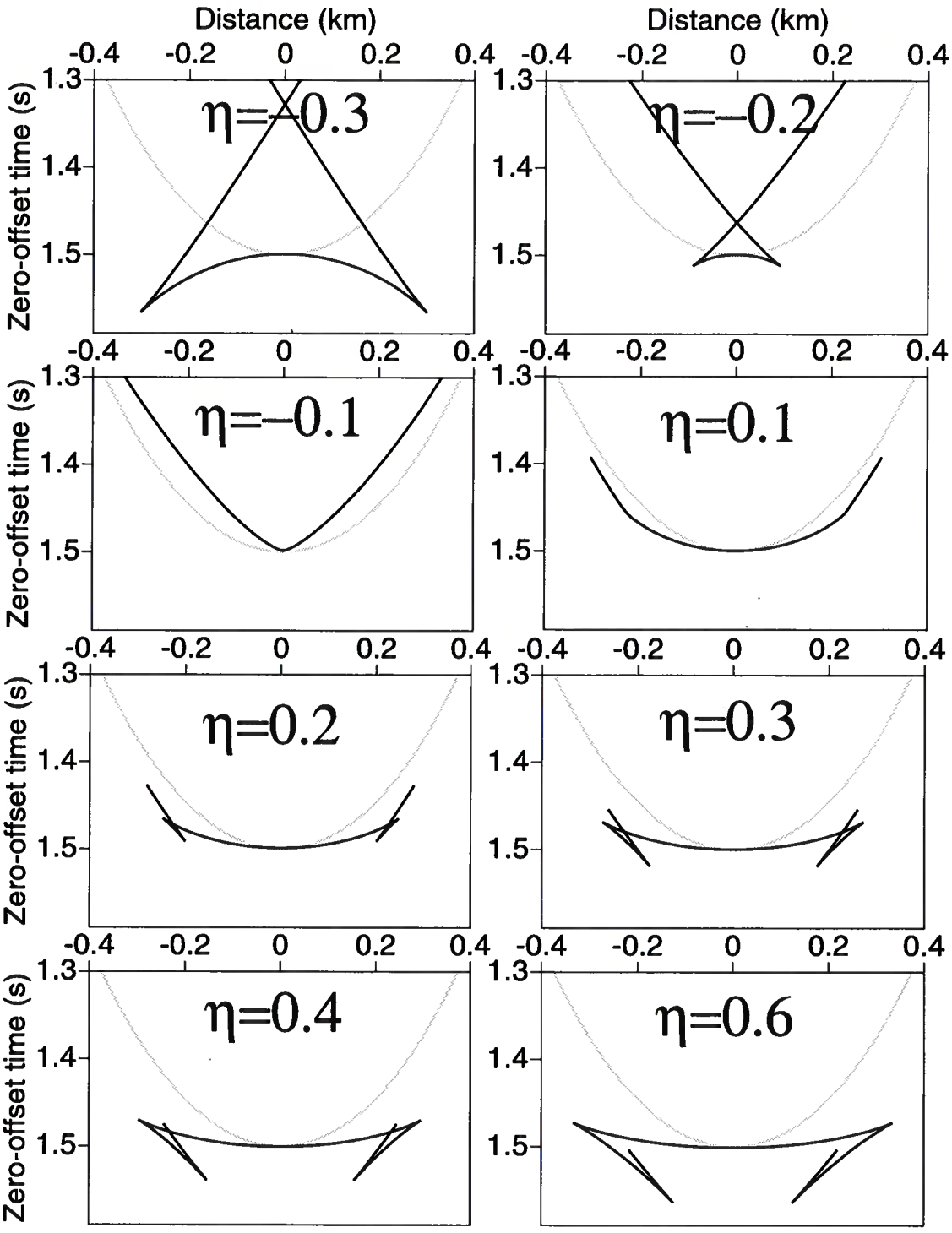

FIG. 4.3. Shapes of DMO impulse responses in homogeneous VTI media for various η values (black curves). Here, offset=1.5 km, t_n=1.5 s, and $V_{\text{nmo}}(0)$=2.0 km/s. These curves are superimposed on the corresponding isotropic ($\eta = 0$) constant-velocity DMO trajectories (gray curves). Lateral distance here, and throughout, is measured from the symmetry point of each response.

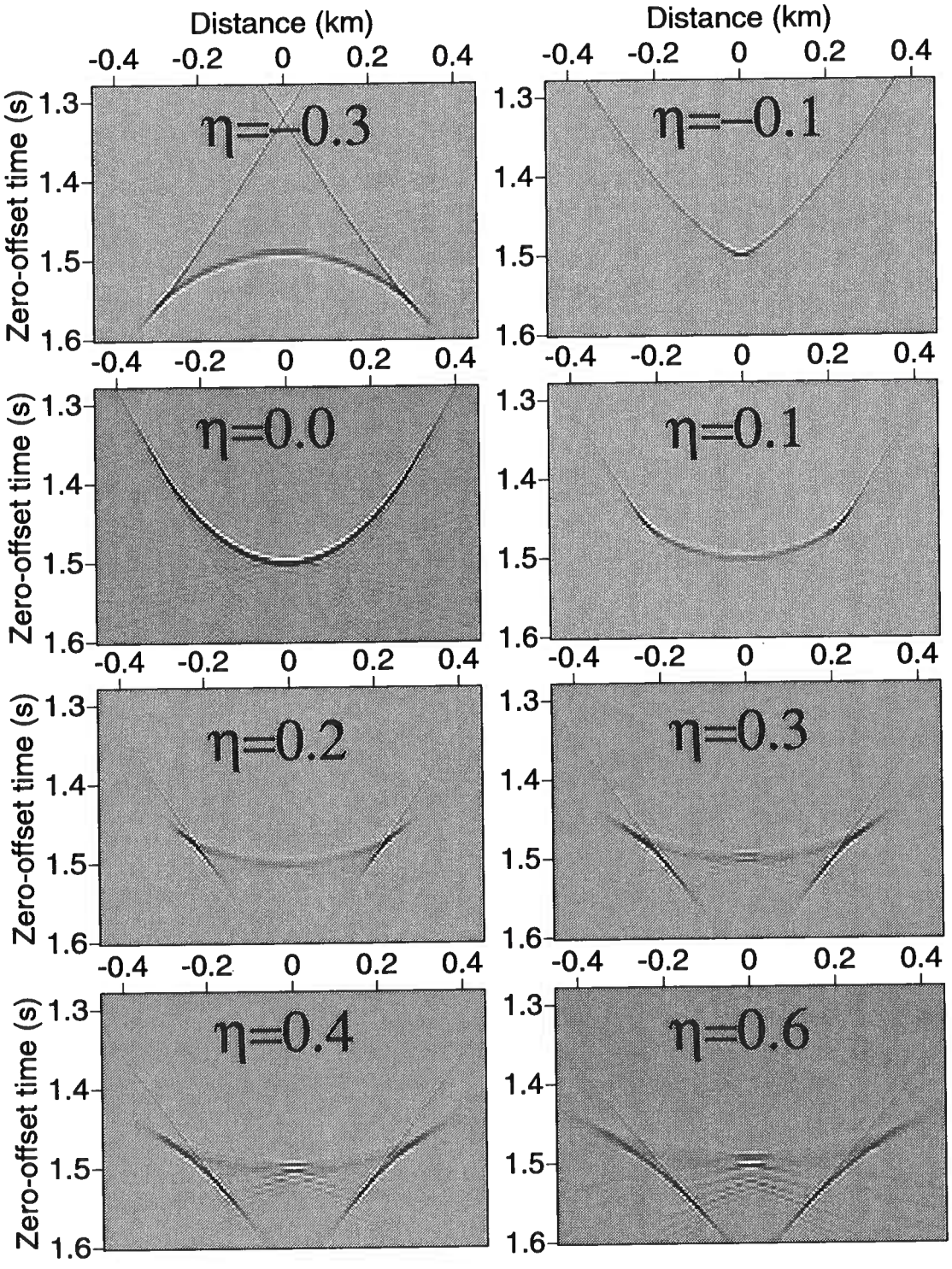

FIG. 4.4. DMO impulse responses in VTI media for various η values. Here offset=1.5 km, t_n=1.5 s, and $V_{\mathrm{nmo}}(0)$=2.0 km/s.

ure 4.4 exemplifies such varying energy distributions and includes a comparison with the isotropic impulse response, given by $\eta = 0$. These impulse responses were generated by applying anisotropic DMO, described above, to an input file that contains a single impulse. Clearly, the parts of the response with less curvature have smaller amplitude than do those with more curvature. For example, when $\eta = 0.1$, for which the response is flattened (see Figure 4.3), the reflection from a horizontal reflector in the common-offset domain receives contributions from many adjacent responses, and the amplitude of each contribution must be small enough to insure that the superposition of the contributions for this dip is the same as for all other dips.

Such large differences between the isotropic, homogeneous response and the responses in VTI media imply that the special effort to take anisotropy into account in DMO will be rewarded where data are from VTI media with $\eta \neq 0$.

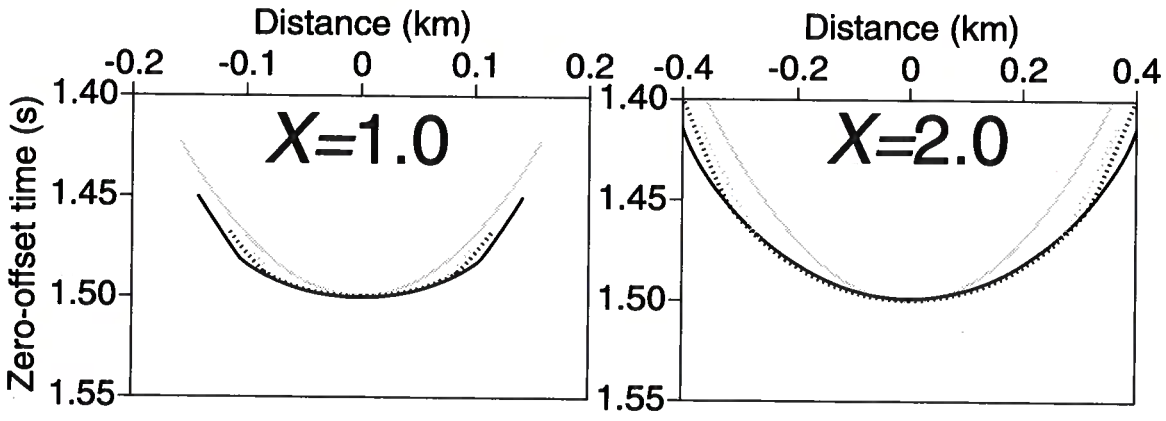

FIG. 4.5. DMO impulse responses in VTI media with $V_{\text{nmo}}(0)$=2.0 km/s (solid black curve), $V_{\text{nmo}}(0)$=2.5 km/s (dashed black curve), and $V_{\text{nmo}}(0)$=3.0 km/s (dashed gray curve). Here, offset=1.5 km, t_n=1.5 s, and $\eta = 0.1$. As before, the impulse responses are superimposed on the corresponding isotropic constant-velocity operators (gray curve).

4.2.2 Dependence on $V_{\text{nmo}}(0)$

It is well known that the DMO operator for isotropic homogeneous media is independent of velocity. This is not true for VTI media with $\eta \neq 0$. However, as seen in Figure 4.5, $V_{\text{nmo}}(0)$ has only small influence on the DMO impulse response, and practically no influence on the region of the impulse response corresponding to moderate and mild dips (dips up to 30 degrees). Specifically, the concave-upward branch does not change with a change in $V_{\text{nmo}}(0)$. It varies in width only; that is, with increase in $V_{\text{nmo}}(0)$, the concave-downward and straight-line branches are shifted

somewhat inward. This shift arises because, for a given reflector dip, slopes on the DMO impulse responses decrease with increase in velocity, and the transition between branches occurs at about the same dip, independent of velocity. In isotropic media, all shifts caused by velocity variation take place along the elliptical operator, and therefore do not alter the shape at all. The range of $V_{\text{nmo}}(0)$ displayed in Figure 4.5 (2.0 to 3.0 km/s) is far greater than the range of errors usually associated with measuring $V_{\text{nmo}}(0)$ (i.e., from velocity analysis). This implies that, especially for dips corresponding to the first branch, the DMO process in VTI media is practically independent of the NMO velocity, thus approximating the velocity-independence for isotropic media. This is consistent with the weak-anisotropy approximation of Anderson and Tsvankin (1995).

Thus, of the two key parameters, $V_{\text{nmo}}(0)$ and η, only η has a strong influence on the shape of the DMO impulse response. Therefore, after applying NMO correction to the data, a process of estimating the η value that best corrects the moveout to zero-offset can be used. For example, a semblance analysis technique can be developed using successive applications of DMO, each based on a different constant value of η.

Although η forms essentially a one-parameter control on the shape of the impulse response in VTI media, clearly the responses in Figure 4.3 are not squeezed or stretched versions of the isotropic ones, as in isotropic $v(z)$ media. They exhibit a much more complicated departure from the typical elliptical shape.

4.2.3 Dependence on offset and NMO time

As is known, the importance of DMO correction increases with offset; i.e., the elliptical impulse responses of the DMO process broaden with increasing offset in homogeneous, isotropic media. Likewise, the impulse responses for VTI media broaden, but, as we have seen, the shapes are not elliptical. The influence of offset on the impulse responses in a homogeneous VTI medium with $\eta = 0.1$ is shown in Figure 4.6. Note that the general shape of the response remains the same with increasing offset; however, the departure of the VTI impulse response (black curve) from the isotropic homogeneous operator (gray curve) increases with increasing offset.

The DMO impulse responses in Figure 4.7, generated for various NMO-corrected times, pertain to an offset of 1.5 km. As with isotropic media, the width of the impulse response decreases with increasing t_n. However, the departure of the shapes of the impulse responses for VTI media (black curves) from the ones corresponding to homogeneous, isotropic media (gray curves) remains practically the same. In contrast, Artley and Hale (1994) showed that the differences between the impulse responses for isotropic homogeneous and $v(z)$ media decrease with increasing time, to a point where the two responses practically coincide. This implies that, for example, if inhomogeneity was large enough to offset the action of anisotropy in the shallow part of a section, the relative importance of inhomogeneity would reduce with depth.

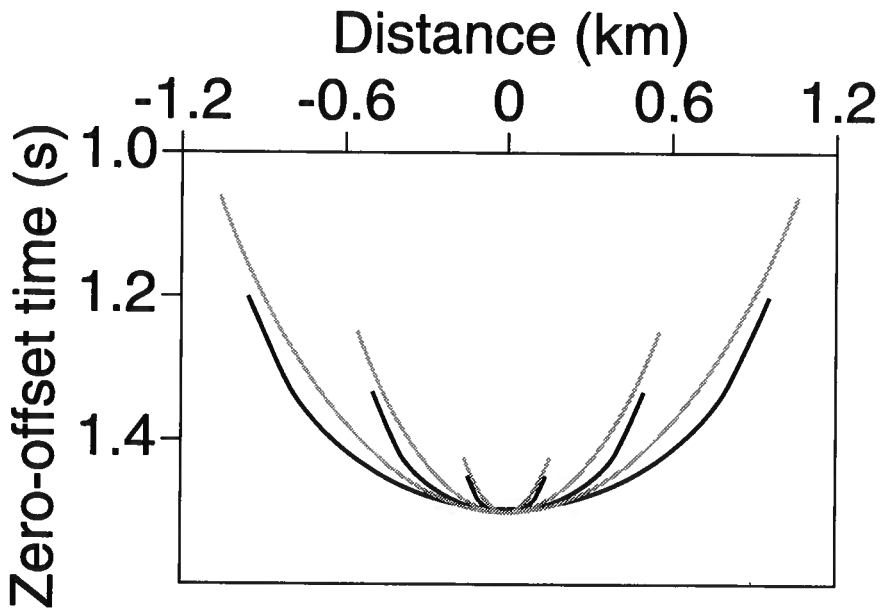

FIG. 4.6. DMO impulse responses in a VTI medium for three offsets given by X=1.0 km (the narrowest of the responses), X=2.0 km, and X=3.0 km (the widest of the responses). Here, t_n=1.5 s, $\eta = 0.1$, and $V_{\text{nmo}}(0)$=2.0 km/s. The responses of the VTI medium (black) are superimposed on the corresponding isotropic constant-velocity operators (gray).

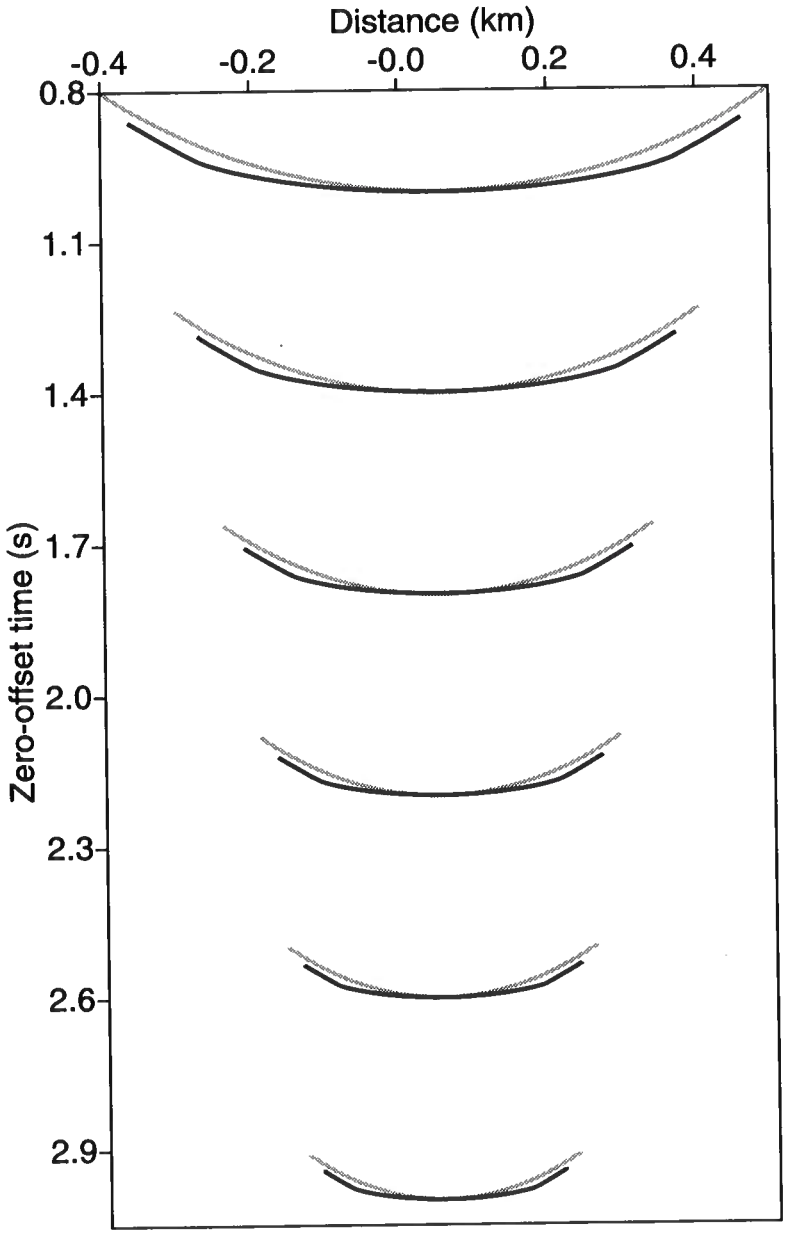

FIG. 4.7. DMO impulse responses in a VTI medium for scatterers at six different depths (i.e., six different values of t_n). Here, X=1.5 km/s, $\eta = 0.1$, and $V_{\text{nmo}}(0)$=2.0 km/s. Again, the responses for the VTI medium (black) are superimposed on the corresponding isotropic constant-velocity operators (gray).

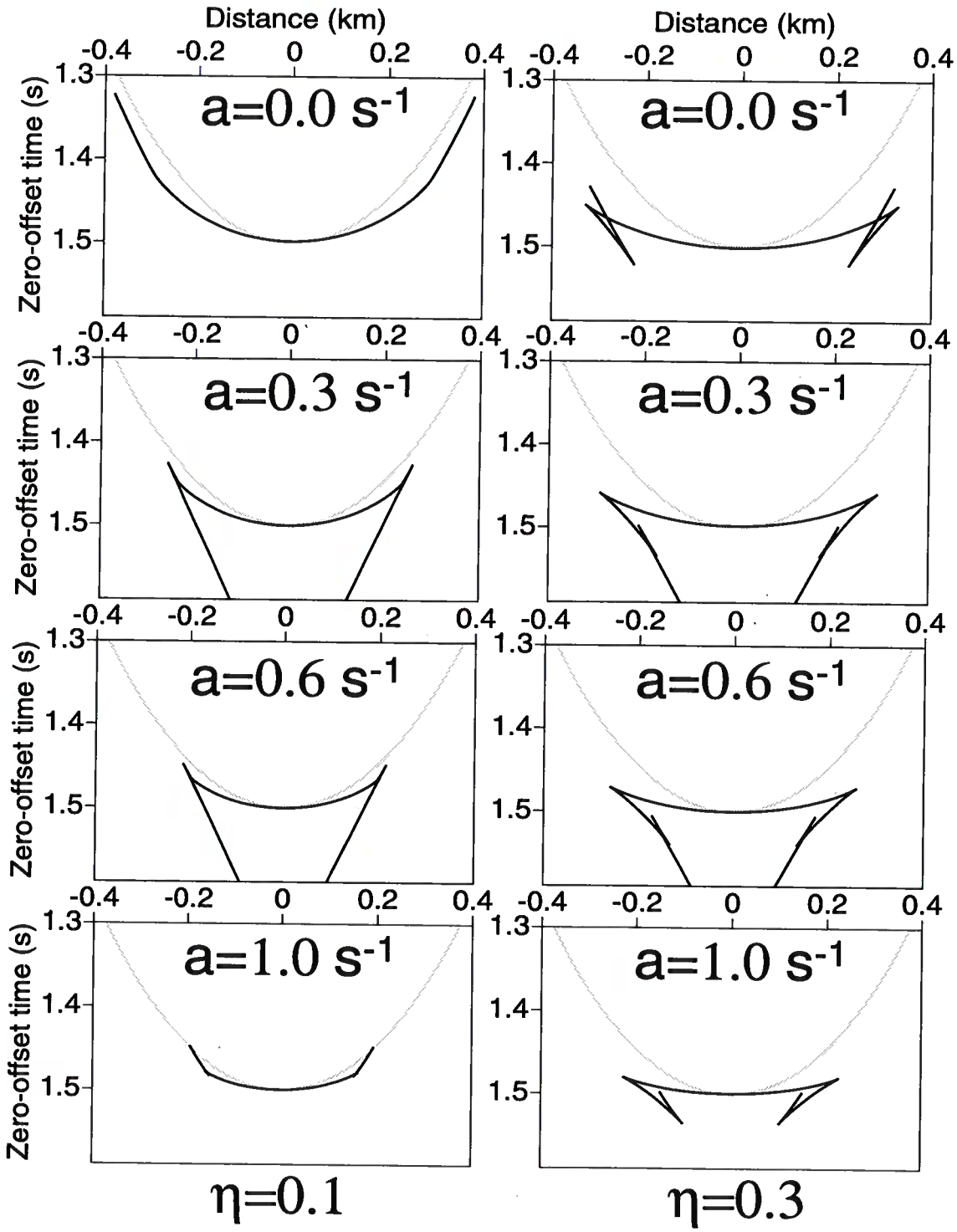

FIG. 4.8. DMO impulse responses in vertically inhomogeneous VTI media for various vertical velocity gradients. Here, offset=1.5 km, t_n=1.5 s, and $V_{\rm nmo}(0)$ at the surface is 1.5 km/s. η for the left column of plots equals 0.1 and for the right column equals 0.3 (black curves). The corresponding isotropic constant-velocity operators are shown in gray.

4.2.4 Dependence on vertical inhomogeneity

It has been observed that when the subsurface is both anisotropic and vertically inhomogeneous, DMO is often best done with an isotropic homogeneous operator (Gonzalez et al., 1992; Larner, 1993; Tsvankin, 1995). The validity of this choice depends on the nature and strength of both anisotropy and inhomogeneity. For example, this approach might be acceptable if anisotropy is weak enough; however, in media with typical values of η [i.e., the anisotropy levels usually associated with shales ($\eta \geq 0.1$), as we will see later in the field example], the anisotropy influence on the DMO operator exceeds that of the inhomogeneity.

All the examples so far pertain to homogeneous media. Now consider media in which velocities increase with depth. Figure 4.8 shows impulse responses in VTI media for $\eta = 0.1$ and $\eta = 0.3$, with the vertical velocity gradient a ranging between 0 and 1.0 s^{-1}. First note that the inhomogeneity introduces an additional branch corresponding to dips mostly beyond 90 degrees. This additional branch is similar to that observed by Artley and Hale (1994) in $v(z)$ isotropic media. For mild to moderate dips (dips up to 30 degrees), differences in responses for inhomogeneous media from those for the homogeneous case ($a = 0$), shown at the top of Figure 4.8, are generally small, if not negligible. Other than the additional branch, the shapes of the responses are generally similar to the homogeneous ones.

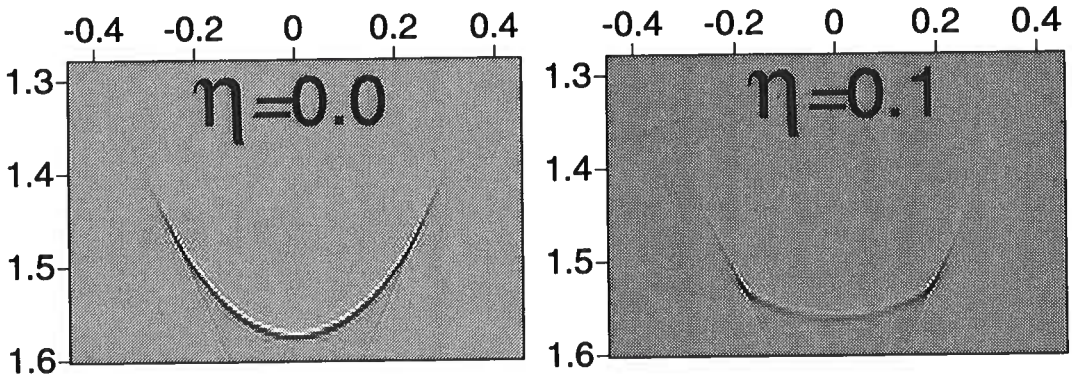

FIG. 4.9. DMO impulse responses in inhomogeneous isotropic ($\eta = 0.0$) and VTI media ($\eta = 0.1$). Here, offset=1.5 km, t_n=1.5 s, and $V_{\text{nmo}}(0)$=1.5 +0.6 z km/s.

Figure 4.9 shows actual impulse responses in $v(z)$ VTI media, with the energy distribution clearly displayed. As with the homogeneous case (Figure 4.4), such irregular energy distribution (e.g., the strong amplitudes where the curvature of the impulse response is largest) depends mainly on the shape of the impulse response.

The similarities between impulse responses in homogeneous and $v(z)$ VTI media, especially for mild and moderate dips, imply that typical anisotropy has a larger

influence on DMO than does inhomogeneity. Therefore, a homogeneous VTI DMO algorithm will likely give acceptable results in typical $v(z)$ media for mild and moderate dips. Where isotropic $v(z)$ DMO impulse responses can be well approximated by squeezed ellipses, similar approximations will not work effectively in VTI media, especially for dips exceeding 30 degrees.

4.3 Prestack migration impulse responses

Applying a zero-offset time migration to a DMO impulse response simulates a prestack time-migration impulse response for the same offset as that used in generating the DMO impulse response. This holds for VTI media, as well as for isotropic media.

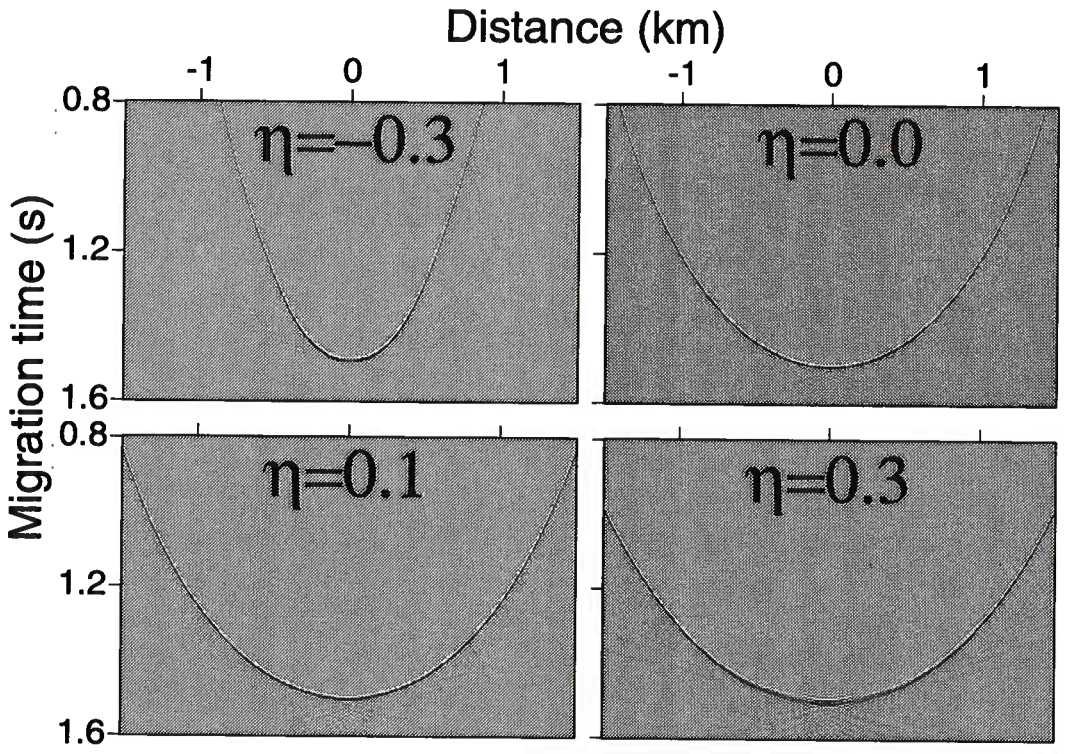

FIG. 4.10. Prestack migration impulse responses generated from the DMO impulse responses in Figure 4.3 for several η values. Here again, offset=1.5 km, t_n=1.5 s, and $V_{\rm nmo}(0)$=2.0 km/s.

Figure 4.10 shows such prestack migration impulse responses for an offset of 1.5 km (the same offset used in generating the responses in Figure 4.4). The time migration used here is the Gazdag (1978) phase-shift method modified for VTI media. Despite the complicated form of the DMO impulse responses in VTI media (e.g., the

triplication for larger η), the time-migration impulse responses are smooth. This can be expected because migration impulse responses represent wavefronts, and for P-waves in VTI media the wavefronts are known to be smooth (i.e., they cannot include triplications). Further, the width of the migration responses depends on η: from equation (2.1), negative η implies a smaller horizontal velocity than $V_{\text{nmo}}(0)$, resulting in a laterally squeezed migration response, whereas positive η implies a larger horizontal velocity, resulting in a stretched version. For η equal zero (isotropic or elliptically anisotropic media), the response shape is simply the familiar ellipse.

4.4 Application to a reflector model

Although the DMO algorithm, described above, handles $v(z)$ VTI media, the first example pertains to homogeneous media. The reason for this simplification is to show the significance of anisotropy and its influence on the data without any influence of inhomogeneity. Next, I will show results from a $v(z)$ medium to illustrate points regarding the $v(z)$ influence. The reflector model given by Figure 4.11a contains a wide range of reflector dips, so that we acheive a composite idea of the dependence of NMO velocity on dip.

4.4.1 Homogeneous medium

Figure 4.11b shows the zero-offset synthetic section for the homogeneous model in Figure 4.11a. The section has 401 traces, corresponding to 401 CMP locations, at a spacing of 0.025 km. The medium above the reflectors is VTI with V_{P0}=2.5 km/s, ϵ=0.3, and $\delta = 0.1$. For NMO and DMO purposes, such media can also be expressed by $\eta = 0.167$ and $V_{\text{nmo}}(0) = 2.78$ km/s. Figure 4.12a shows a 31-fold CMP gather prior to TZO for the CMP location marked by the dashed vertical line in Figure 4.11b. Reflections from dipping interfaces can be identified by their higher velocity (i.e., smaller moveout).

First, let us examine application of the conventional processing sequence designed for isotropic media. Figure 4.12b shows the same CMP gather of Figure 4.12a after an isotropic TZO (NMO and DMO) using $V_{\text{nmo}}(0)$, which approximates the stacking velocity obtained from velocity analysis for offset-to-depth ratio X/D <1. Although the reflections from horizontal interfaces are flattened at the near offsets, the nonhyperbolic moveout behavior caused by anisotropy leads to deviations at the far offsets. Such errors cannot be corrected using a hyperbolic moveout correction, and therefore a mute procedure would typically be applied to the far offsets to properly stack the data (Anderson et al., 1995). Reflections from dipping reflectors have even larger errors, which are caused primarily by ignoring anisotropy in DMO for the VTI medium. Such errors are described in detail by Larner (1993) and Tsvankin (1995).

Using anisotropic ray-tracing, DMO with the correct medium parameters flattens the moveout of all events properly at all offsets, as demonstrated in Figure 4.12c. Both the nonhyperbolic moveout and the dip moveout have been properly corrected for.

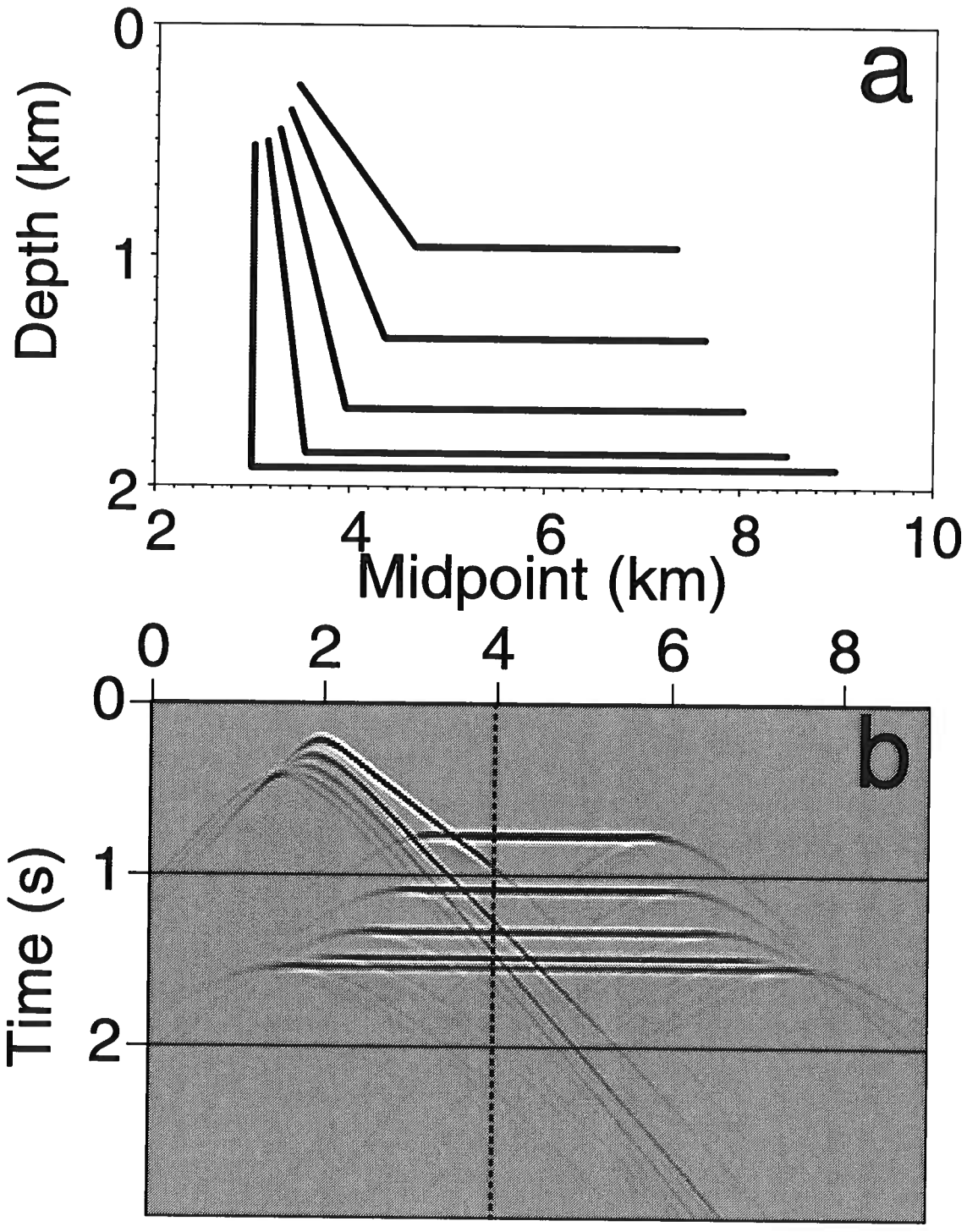

FIG. 4.11. (a) Reflector model containing reflectors dipping at 0, 30, 45, 60, 75, and 90 degrees. (b) Zero-offset seismogram generated from the model. The medium is homogeneous VTI with V_{P0}=2.5 km/s, $\epsilon = 0.3$, and $\delta = 0.1$ ($\eta = 0.167$). The dashed line shows the location of the CMP gather in Figure 4.12.

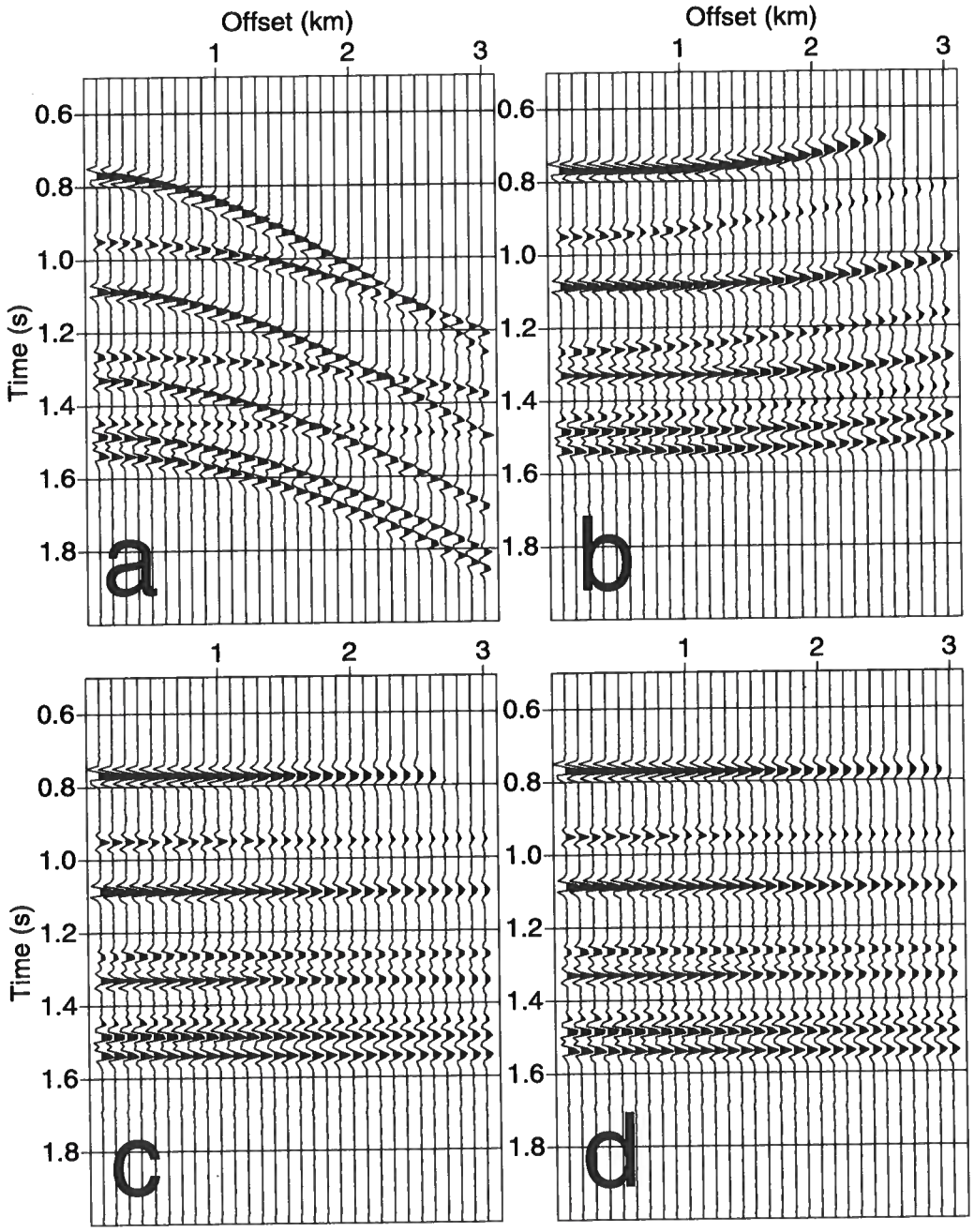

FIG. 4.12. (a) Uncorrected CMP gather for the model shown in Figure 4.11a. (b) Gather after isotropic TZO using $V_{\mathrm{nmo}}(0)$. (c) Gather after anisotropic TZO with the actual anisotropy parameters. (d) Gather after anisotropic TZO with the correct values of η and $V_{\mathrm{nmo}}(0)$, but with incorrect values of V_{p0} (V_{p0}=$V_{\mathrm{nmo}}(0) = 2.65$ km/s), δ (δ=0), and ϵ (ϵ=0.167). The three dipping reflectors shown here are at zero-offset times of 0.96 s (30-degree dip), at 1.26 s (45-degree dip), and at 1.44 s (60-degree dip).

Furthermore, Figure 4.12d shows the same perfect TZO correction using the correct values of $V_{\rm nmo}(0)$ and η, but with erroneous $V_{p0} = V_{\rm nmo}(0)$ [from equation (2.5)], corresponding to erroneous values $\delta = 0$ and $\epsilon = 0.167$. This confirms the result obtained by Alkhalifah and Tsvankin (1995) stated in Chapter 2, above, that NMO and DMO (or TZO), as well as time migration, depend only on η and $V_{\rm nmo}(0)$.

4.4.2 $v(z)$ medium

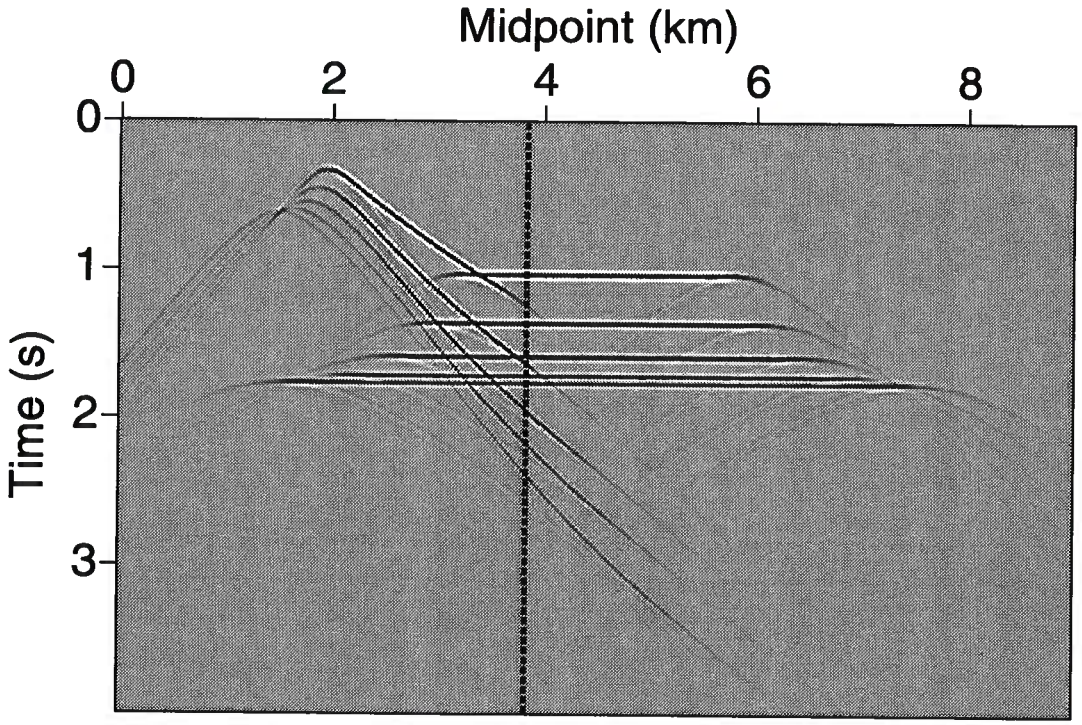

FIG. 4.13. Zero-offset seismogram generated from the model in Figure 4.11a, with the $v(z)$ VTI medium characterized by $V_{P0}(z)$=1.5+0.8z km/s, $\epsilon = 0.3$, and $\delta = 0.1$ ($\eta = 0.167$). The dashed line shows the location of the CMP gather in Figures 4.14 and 4.15.

Using the same model shown in Figure 4.11a, with velocity now varying with depth, $v(z) = 1.5+0.8z$ km/s, and with δ and ϵ the same as in the homogeneous model (equal 0.1 and 0.3, respectively), I get the zero-offset section shown in Figure 4.13. The medium considered here is referred to as a factorized TI medium (Shearer and Chapman, 1988), wherein although velocity is varying with depth, δ and ϵ remain constant. Such a limitation is dictated by the synthetic data generator that I use here (Alkhalifah, 1995a), which is based on this concept. The DMO algorithm, though, can accommodate vertical variations in all parameters. The vertical dashed line shown

in Figure 4.13 shows the location of the CMP gather given in Figures 4.14 and 4.15. Note that this CMP gather includes reflections from all reflector dips, which should give us a good idea of the performance of isotropic and VTI DMO algorithms.

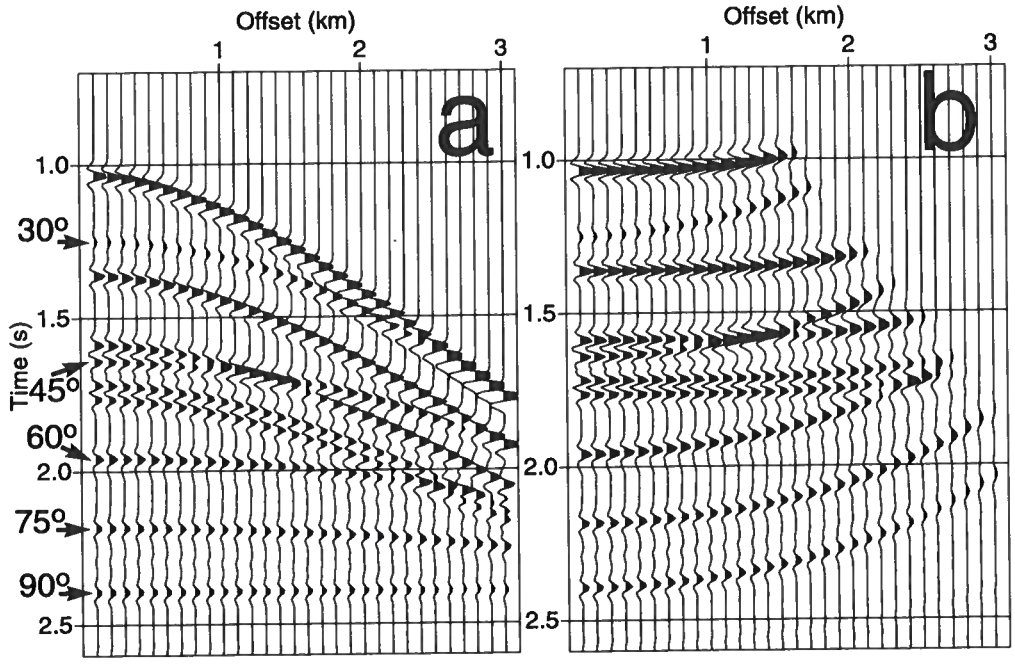

FIG. 4.14. (a) Uncorrected CMP gather for the $v(z)$ VTI model shown in Figure 4.11a. (b) Gather after NMO correction using the actual model NMO velocities. The arrows identify the reflector dips responsible for the reflections. The arrowless reflections are from horizontal reflectors.

Figure 4.14a shows a 31-fold CMP gather prior to TZO for the CMP location marked by the dashed vertical line in Figure 4.13. Figure 4.14b shows the same CMP gather after NMO correction. The disparity in the moveout should help discriminate between dipping and horizontal reflectors. Typically, moveout decreases with increase in moveout velocity and, therefore, with increase in reflector dip (Levin, 1971). Again, horizontal reflections suffer from the presence of nonhyperbolic moveout now due to both anisotropy and vertical inhomogeneity. As shown by Alkhalifah (1996b), the majority of the nonhyperbolic moveout is due to the anisotropy.

Figure 4.15 shows the result of applying various DMO corrections to the data shown in Figure 4.13. As expected, the VTI $v(z)$ DMO using the actual medium parameters, given by $v(z) = 1.5 + 0.8z$ km/s, $\delta = 0.1$, and $\epsilon = 0.3$, accurately corrects the moveout for all dips and offsets (Figure 4.15a). The homogeneous VTI DMO, using the rms velocity corresponding to time 1.4 s, also gives reasonable results (Fig-

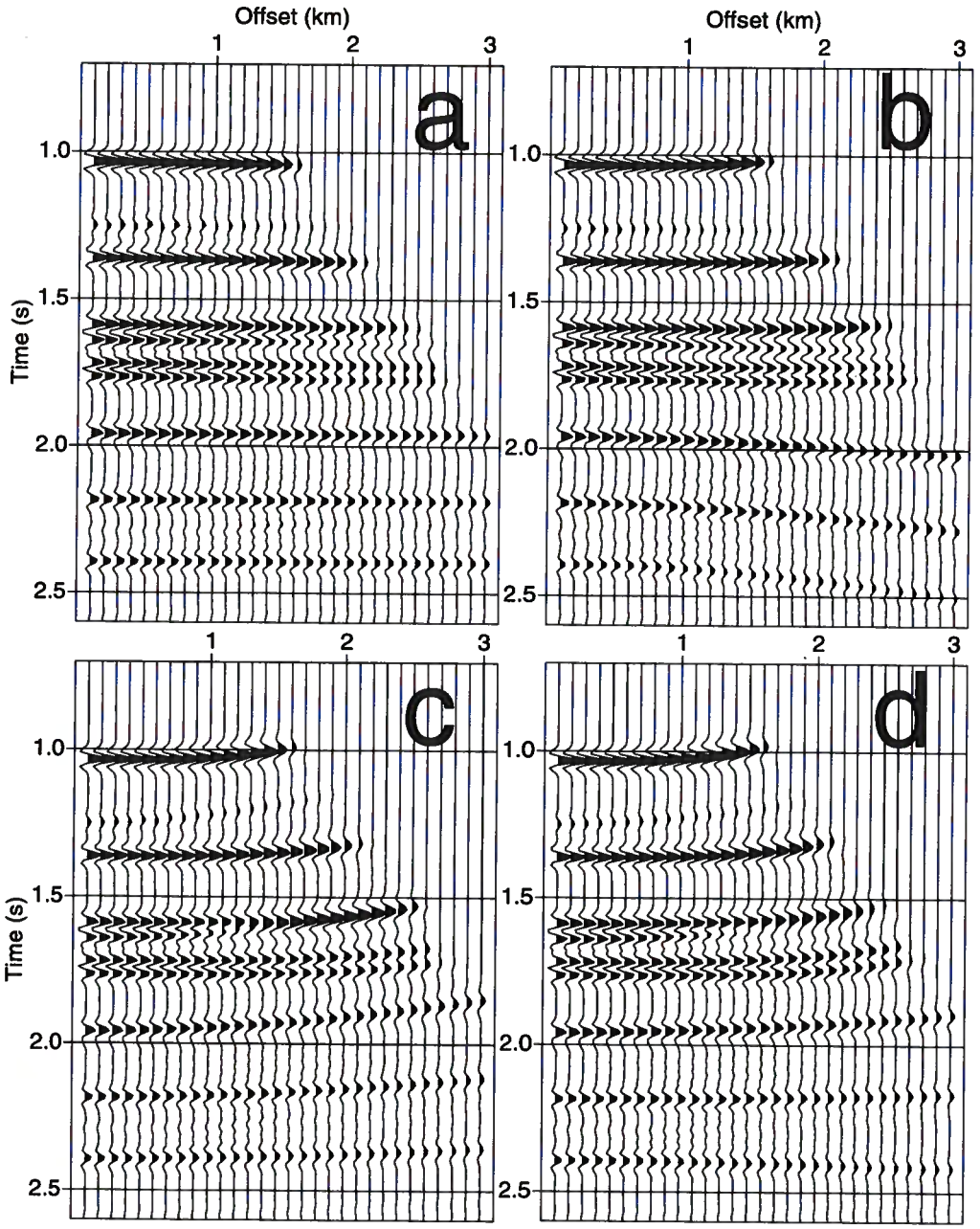

FIG. 4.15. (a) CMP gather for the model shown in Figure 4.11a after $v(z)$ anisotropic DMO correction using the proper parameters. (b) Gather after homogeneous anisotropic DMO using the V_{rms} at time 1.4 s. (c) Gather after isotropic $v(z)$ DMO with the actual $v(z)$ model. (d) Gather after isotropic homogeneous DMO. NMO correction for all gathers is the same and corresponds to the actual NMO velocities of the model.

ure 4.15b), especially near the 1.4 s. In fact, using the homogeneous VTI DMO, with some adjustment of velocity depending on time, for $v(z)$ media is an attractive option to reducing the cost of DMO. Note also that the nonhyperbolic moveout is reduced considerably using this DMO which suggests that the majority of the nonhyperbolic is due to the presence of anisotropy. The isotropic DMO operation clearly failed to correct the moveout. In fact, the isotropic $v(z)$ DMO, which purports to better honor $v(z)$ behavior than does the homogeneous DMO, gives the worst results. The isotropic homogeneous DMO, in this case, benefited from trade-off between the vertical inhomogeneity and anisotropy, mentioned earlier.

We can conclude from the above that typical anisotropy (e.g., that associated with shales) has a greater influence on DMO than does moderate vertical inhomogeneity. Therefore, when correcting the moveout for the influence of dip in anisotropic media, we must first and foremost treat anisotropy and then worry about the inhomogeneity.

Chapter 5

MIGRATION IN VTI MEDIA

Most migration algorithms used today are based on the assumption that the earth is isotropic, an approximation that is often not valid and thus can lead to position errors on migrated images. Larner and Cohen (1993) and Alkhalifah and Larner (1994) have studied the mispositioning of imaged reflectors that results when, as is typically done in practice, conventional P-wave data from transversely isotropic (TI) media are migrated with an algorithm that ignores anisotropy. Their conclusion points to the importance of using an anisotropic migration when the medium is anisotropic. Here, I outline the methodology used to implement Stolt and Gazdag migrations in TI media. I will also discuss depth migration, specifically Gaussian beam migration (GBM), and its place in processing data from TI media.

5.1 Time migration

Fourier-domain implementations of migration require that the medium be laterally homogeneous (excluding some approximations used to handle smooth lateral velocity variation). This inherent limitation of time-migration results, however, in implementations of migration that are efficient in the Fourier domain. In addition, the assumption of lateral homogeneity allows for the two-parameter representation of P-waves in VTI media. Likely, through the combined action of gravity and sedimentation, velocity variation with depth represents the most important first-order inhomogeneity in the earth. This is one reason why time migration works well in so many places.

5.1.1 Stolt migration

To migrate a zero-offset section in VTI media with the Stolt (1978) F-K migration algorithm, the conventional isotropic algorithm must be modified using a time-migration dispersion relation for TI media. The only substantial change required in the Stolt method is the replacement of the isotropic velocity by the dip-dependent phase-velocity function for transversely isotropic media (Kitchenside, 1991). A reference velocity equal to V_{P0} is needed to scale the vertical axis as follows (Anderson et al., 1995):

$$\frac{V_{P0}k}{2\omega_m} = \tan\phi\,, \tag{5.1}$$

and

$$\omega_0 = \omega_m \frac{V(\phi)}{V_{P0}} \sqrt{1 + \frac{V_{P0}^2 k^2}{4\omega_m^2}} = \frac{\omega_m}{\cos\phi} \frac{V(\phi)}{V_{P0}}. \tag{5.2}$$

Here, ω_0 is the zero-offset angular frequency for unmigrated data, ω_m is the angular frequency after migration, and ϕ is the dip associated with the reflector of interest. Note that equation (5.2) reduces to the isotropic cosine-of-dip Stolt relationship if $V(\phi)$ equals V_{P0}. For equation (5.2) to approximately handle $v(z)$ media, Stolt (1978) introduced a stretch technique, where the dispersion relation [equation (5.2)] is given by

$$\omega_0 = \omega_m (b + \frac{a}{\cos\phi} \frac{V(\phi)}{V_{P0}}), \tag{5.3}$$

$a = 1/s$ and $b = 1 - a$. As a result, equation (5.1) is now given by

$$\sqrt{s} \frac{V_{P0} k}{2\omega_m} = \tan\phi\,,$$

where s is the stretch factor, equal to unity for homogeneous media and, for smooth $v(z)$ media, s is typically set to equal 0.6. To prepare the data for this new dispersion relation [equation (5.4)], the time axis is stretched according to the following formula

$$\tau(t_0) = \sqrt{\frac{2}{v_0^2} \int_0^{t_0} t V_{\rm rms}^2(t) dt},$$

where v_0 is the velocity at the surface.

For factorized TI media, where the NMO velocity is given by the same rms relation used in isotropic media, the time coordinate transformation remains the same as in isotropic media. However, through empirical testing, I have found that an s value given by

$$s = \frac{s_{iso}}{1 + 8\eta}, \tag{5.4}$$

where s_{iso} is the stretch factor usually chosen for isotropic media, best migrates data in $v(z)$ anisotropic media. This $(1+8\eta)$ factor in the denominator of equation (5.4) is a factor usually encountered in layer-stripping formulas for the nonhyperbolic moveout term for horizontal reflectors in VTI media (Alkhalifah, 1996b). This is not surprising considering that reflection moveout from horizontal events has the same traveltime behavior as that of the zero-offset migration diffraction curve.

Figure 5.1 shows a VTI Stolt migration of zero-offset data generated from the model in Figure 4.11, with $V_{\rm nmo}$=2.0 km/s and η=0.1. Clearly, the migrated reflectors are imaged in their correct positions. The attenuation of the reflector with 90-degree dip and part of the one with 75-degree dip is due to the limited aperture used in the migration of this medium; energy from the 90-degree dip reflector in homogeneous media cannot be recorded at the surface. Figure 5.2 shows a VTI Stolt migration of zero-offset data generated from the same model used in Figure 5.1, with

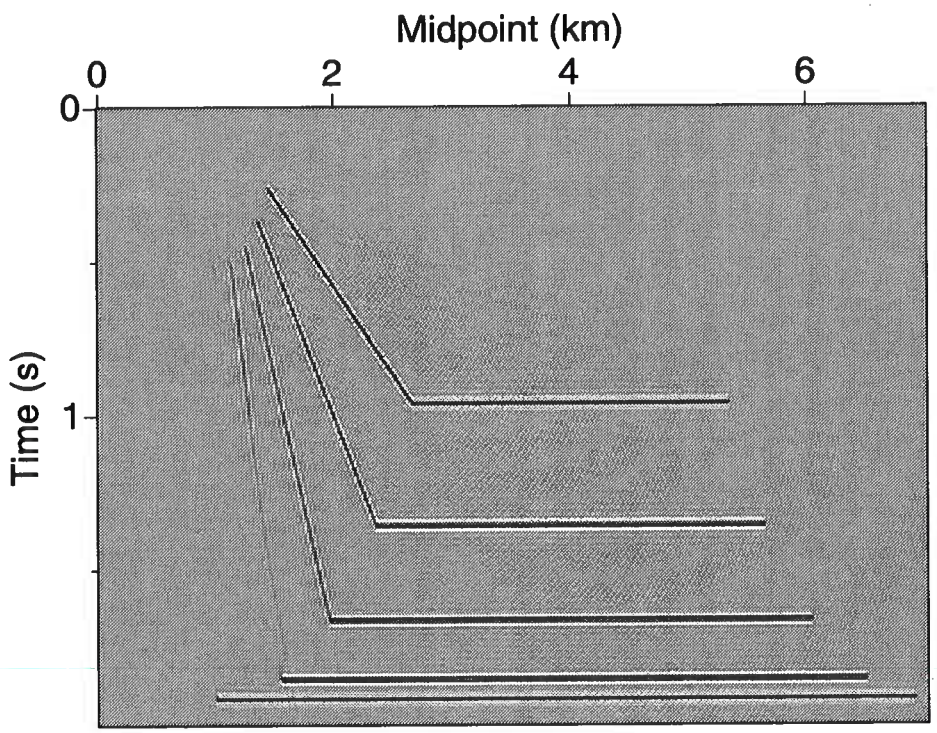

FIG. 5.1. Stolt VTI-migrated section of zero-offset data generated for the model in Figure 4.11. The medium is homogeneous VTI with V_{nmo}=2.0 km/s, $\epsilon = 0.1$, and $\delta = 0.0$ ($\eta = 0.1$).

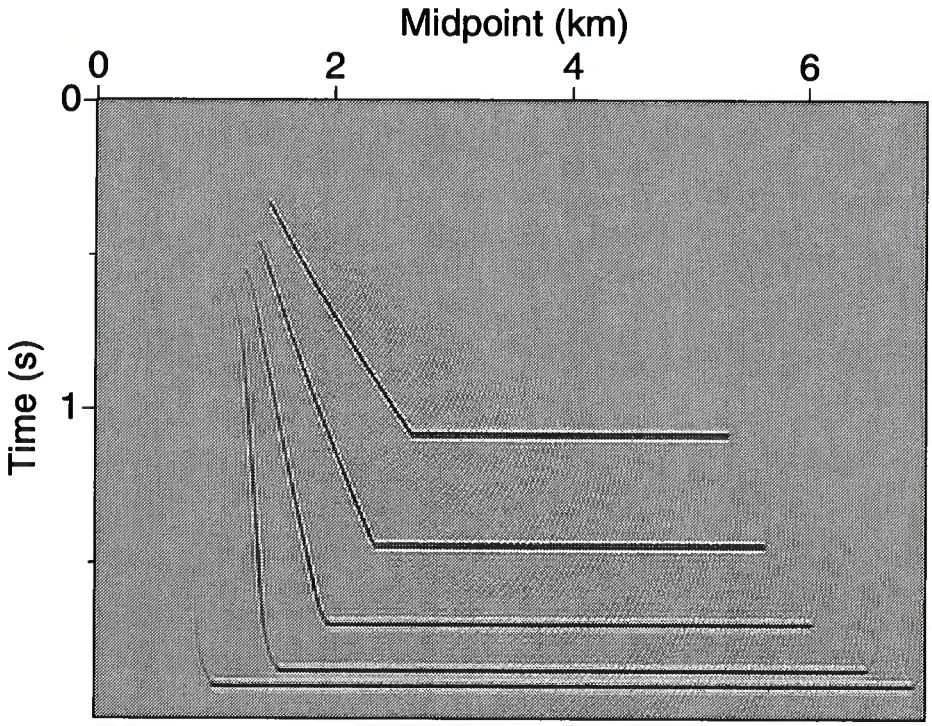

FIG. 5.2. Stolt VTI-migrated section of zero-offset data generated for the model in Figure 4.11. The medium is $v(z)$ VTI with $V_{P0}(z)$=1.5+0.6z km/s, $\epsilon = 0.1$, and $\delta = 0.0$ ($\eta = 0.1$). For the Stolt migration s_{iso} was chosen empirically to equal 0.6; a typical value used in isotropic media.

$V_{P0}(z)$=1.5+0.6z km/s and η=0.1. As expected, errors in imaging increase with increase in reflector dip. No aperture problems here; almost all the energy reflected from the 90-degree reflector, as well as from other reflectors, has been recorded at the surface because of the $v(z)$ nature of the medium. Nevertheless, reflections from steep events suffer from the shortcomings of the stretch approximation. The Stolt migration, however, has produced an overall reasonable image, especially for mild and moderate dips.

5.1.2 Phase-shift migration

Gazdag (1978) phase-shift method for depth extrapolation of a seismic wavefield in the frequency-wavenumber (ω, k_x) domain is given by

$$W(\omega, k_x, z) = W(\omega, k_x, z=0)\, A(k_x/\omega, z)\, e^{-i\omega \int_0^z d\zeta \frac{\cos\theta(k_x/\omega,\zeta)}{v(\zeta)}}, \tag{5.5}$$

where W is the wavefield, and $\theta(p_x, z)$ is the angle defined, for isotropic media, by

$$\sin\theta(p_x, z) = v(z)p_x,$$

and $A(p_x, z)$ is an amplitude factor that corrects for the $v(z)$ influence and is often omitted, in part because it goes to infinity as z approaches the turning point, that depth where $\theta(p_x, z) = \pm 90$ degrees. This erroneous infinite amplitude is similar to that encountered when performing Kirchhoff migration with WKBJ amplitudes determined by cartesian-coordinate ray tracing (non-dynamic).

Equation (5.5) is the WKBJ solution (e.g., Aki and Richards, 1980, 416) to the differential equation,

$$\frac{d^2W}{dz^2} + \left[\frac{\omega^2}{v^2(z)} - k_x^2\right] W = 0,$$

which is the wave equation, expressed in the frequency-wavenumber domain (Helmholtz equation).

The angle $\theta(p_x, z)$ defined above is the propagation angle at depth z of a plane wave that emerges at the earth's surface with angle θ_0 and velocity v_0 satisfying $\sin\theta_0 = v_0 p_x$.

For migration of zero-offset seismic data $f(t, x)$, we identify $W(\omega, k_x, z=0)$ as the Fourier transformed data $F(\omega, k_x)$ recorded at the earth's surface ($z = 0$). Inverse Fourier transformation of equation (5.5) from wavenumber k_x to distance x gives

$$W(\omega, x, z) = \frac{1}{2\pi} \int dk_x\, A(k_x/\omega, z)\, e^{-i\omega \int_0^z d\zeta \frac{\cos\theta(k_x/\omega,\zeta)}{v(\zeta)} + ik_x x}\, F(\omega, k_x), \tag{5.6}$$

and then evaluation of the inverse Fourier transformation from frequency ω to time t at $t = 0$ yields the subsurface image

$$g(x, z) = \frac{1}{2\pi} \int d\omega\, e^{-i\omega t}\, W(\omega, x, z)\,|_{t=0}$$

$$= \frac{1}{4\pi^2}\int d\omega \int dk_x\, A(k_x/\omega, z)\, e^{-i\omega \int_0^z d\zeta \frac{\cos\theta(k_x/\omega,\zeta)}{v(\zeta)} + ik_x x}\, F(\omega, k_x). \quad (5.7)$$

Equation (5.7) concisely summarizes the phase-shift migration method.

Output data after time migration, however, are usually presented as a function of two-way vertical time, τ, rather than depth. Substituting $\tau = 2\int_0^z \frac{d\zeta}{v}$ and $d\tau = 2\frac{dz}{v}$ into equations (5.6) and (5.7) yields

$$W(\omega, x, \tau) = \frac{1}{2\pi}\int dk_x\, \tilde{A}(k_x/\omega, \tau)\, e^{-i\frac{\omega}{2}\int_0^\tau d\zeta \cos\tilde{\theta}(k_x/\omega,\zeta) + ik_x x}\, F(\omega, k_x), \quad (5.8)$$

and

$$g(x, \tau) = \frac{1}{4\pi^2}\int d\omega \int dk_x\, \tilde{A}(k_x/\omega, \tau)\, e^{-i\frac{\omega}{2}\int_0^\tau d\zeta \cos\tilde{\theta}(k_x/\omega,\zeta) + ik_x x}\, F(\omega, k_x), \quad (5.9)$$

where $\tilde{\theta}(\tau) = \theta[0.5\int_0^\tau v(\zeta)d\zeta]$ and $\tilde{A}(\tau) = A[0.5\int_0^\tau v(\zeta)d\zeta]$.

In VTI media, velocity varies with phase angle, $\tilde{\theta}$, and therefore

$$\sin\tilde{\theta}(p_x, \tau) = V(\tilde{\theta}, \tau)p_x,$$

where V is the phase velocity, and

$$\tau = 2\int_0^z \frac{d\zeta}{V_{P0}(\zeta)},$$

where V_{P0} is the vertical P-wave velocity. As a result, equation (5.8) becomes

$$W(\omega, x, \tau) = \frac{1}{2\pi}\int dk_x\, \tilde{A}(k_x/\omega, \tau)\, e^{-i\frac{\omega}{2}\int_0^\tau d\zeta \frac{\cos\tilde{\theta}(k_x/\omega,\zeta)V_{P0}(\zeta)}{V(\tilde{\theta},\zeta)} + ik_x x}\, F(\omega, k_x), \quad (5.10)$$

and equation (5.7) becomes

$$g(x, \tau) = \frac{1}{4\pi^2}\int d\omega \int dk_x\, \tilde{A}(k_x/\omega, \tau)\, e^{-i\frac{\omega}{2}\int_0^\tau d\zeta \frac{\cos\tilde{\theta}(k_x/\omega,\zeta)V_{P0}(\zeta)}{V(\tilde{\theta},\zeta)} + ik_x x}\, F(\omega, k_x), \quad (5.11)$$

which concisely summarizes the phase-shift migration method in VTI media.

Gazdag (1978) migration is generally slower than the Stolt (1978) method, but Gazdag's method can exactly (within the limit of ray theory) handle the kinematics of $v(z)$ media. In fact, no factorized assumption is needed for Gazdag migration; vertical variations in all parameters are allowed.

Figure 5.3 shows a Gazdag migration of the model in Figure 4.11, with $V_{P0}(z)$=1.5+0.6z km/s and η=0.1 (same values used in Figure 5.2). Unlike the Stolt migration, reflectors from all dips have been imaged accurately. However, the cost of the Gazdag migration is about 5 to 6 times that of the Stolt migration. Both migration algorithms for VTI media are as efficient as there isotropic counterparts.

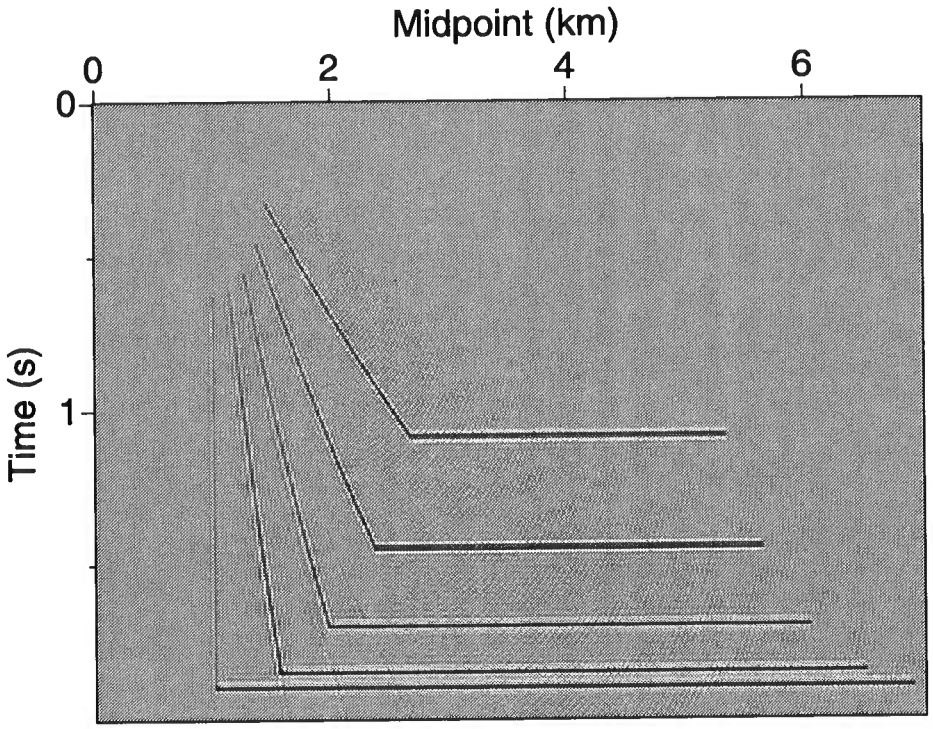

FIG. 5.3. Gazdag VTI-migrated section of a zero-offset section generated for the model in Figure 4.11. The medium is $v(z)$ VTI with $V_{P0}(z)$=1.5+0.6z km/s, $\epsilon = 0.1$, and $\delta = 0.0$ ($\eta = 0.1$).

5.2 Poststack time-migration velocity analysis

Faults are common in the earth's subsurface, and reflections from fault planes are usually recorded in surface seismic data. Typically the location of a fault on a seismic section is estimated from breaks in the continuity of reflections from horizontal (or subhorizontal) events. Therefore, fault locations can be considered as prior information that can be and is used typically to measure the performance of migration and migration velocities (Desegaulx et al., 1994). As shown in Chapter 2, time migration is sensitive to η; errors in η results in errors in positioning of dipping reflections, such as those from faults. Such errors, especially in the case of faults, are observable in migrated sections.

The NMO velocity is usually obtained from semblance velocity analysis applied to CMP gathers containing reflections from horizontal interfaces. This leaves η as giving the only degree of freedom in a $v(z)$ VTI medium that can be used to image the fault at its anticipated position. The accuracy of estimating η relies on the sensitivity of the fault positioning to changes in η. This sensitivity is expected to increase with increasing reflector dip, as we saw in Chapter 2.

A scan over migrated images obtained using different η values can be used to estimate the optimum η for migration. Stolt migration, because of its speed, is well suited for such an application. Figure 5.4a is a zero-offset section generated from a model that contains two dipping faults (30-degree and 50-degree dips) cutting through three horizontal reflectors. Figure 5.4b shows a Gazdag VTI migration of the zero-offset data using the actual model parameters given by $v(z) = 1.5 + 0.6z$ km/s and $\eta = 0.15$. Because Gazdag VTI migration gives accurate image positioning in VTI $v(z)$ media, we can use Figure 5.4b as a reference to judge the performance of Stolt migration. Figure 5.5 shows Stolt migrated sections for different values of η. As expected, the best overall image is obtained for the true value of $\eta = 0.15$. The bottom portion of the 50-degree dip fault, however, seems to be better imaged at $\eta = 0.1$. This inaccurate value is due to shortcomings of the stretch approximation used in this $v(z)$ medium. Such errors seem to increase with vertical time. Gazdag VTI migration, on the other hand, should not have such errors and therefore produces better results in $v(z)$ media. However, the cost of Gazdag migration might be unacceptable when it is necessary to scan over a large number of η values. Note that the included portion of the 30-degree dip fault in Figure 5.5 does not change with a variation of η, suggesting that for such a dip migration is very much insensitive to η. This observation is in total agreement with conclusions given by Alkhalifah and Larner (1994), stating that the influence of anisotropy on migration is not serious for dip less than about 50 degrees.

If η is also varying with depth, than the η values estimated using the above approach must be considered as effective ones (η_{eff}; a constant value that includes an average of the overburden influence). To derive interval η values from η_{eff}, we can use the inherent similarity between the reflection moveout from horizontal reflectors and the time-migration diffraction curve; therefore, layer-stripping relations derived

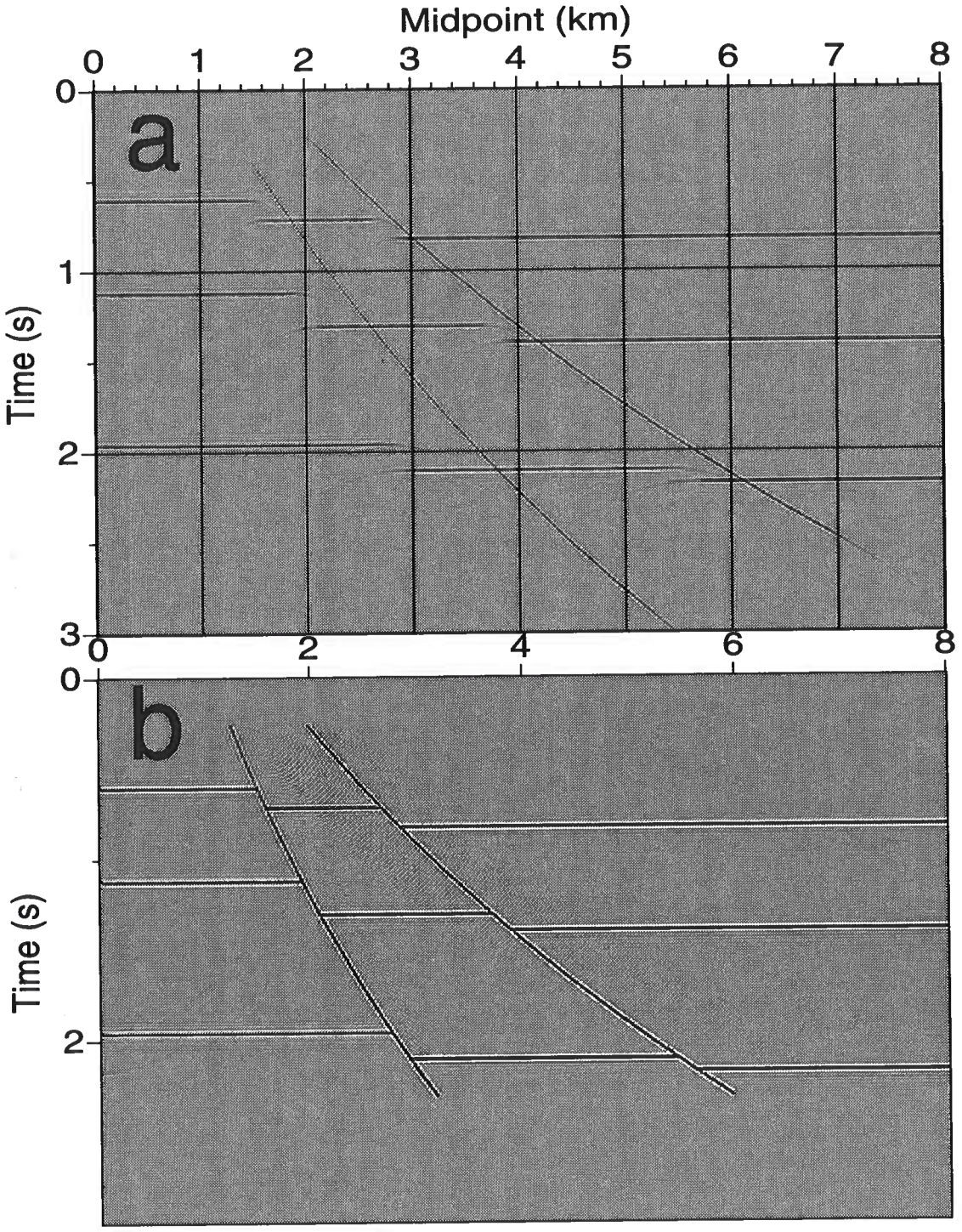

FIG. 5.4. (a) Zero-offset section generated for a model that contains two dipping faults penetrating through three horizontal reflectors. (b) VTI Gazdag migration of the zero-offset section using the actual medium parameters given by $V_{P0}(z)$=1.5+0.6z km/s, and $\eta = 0.15$.

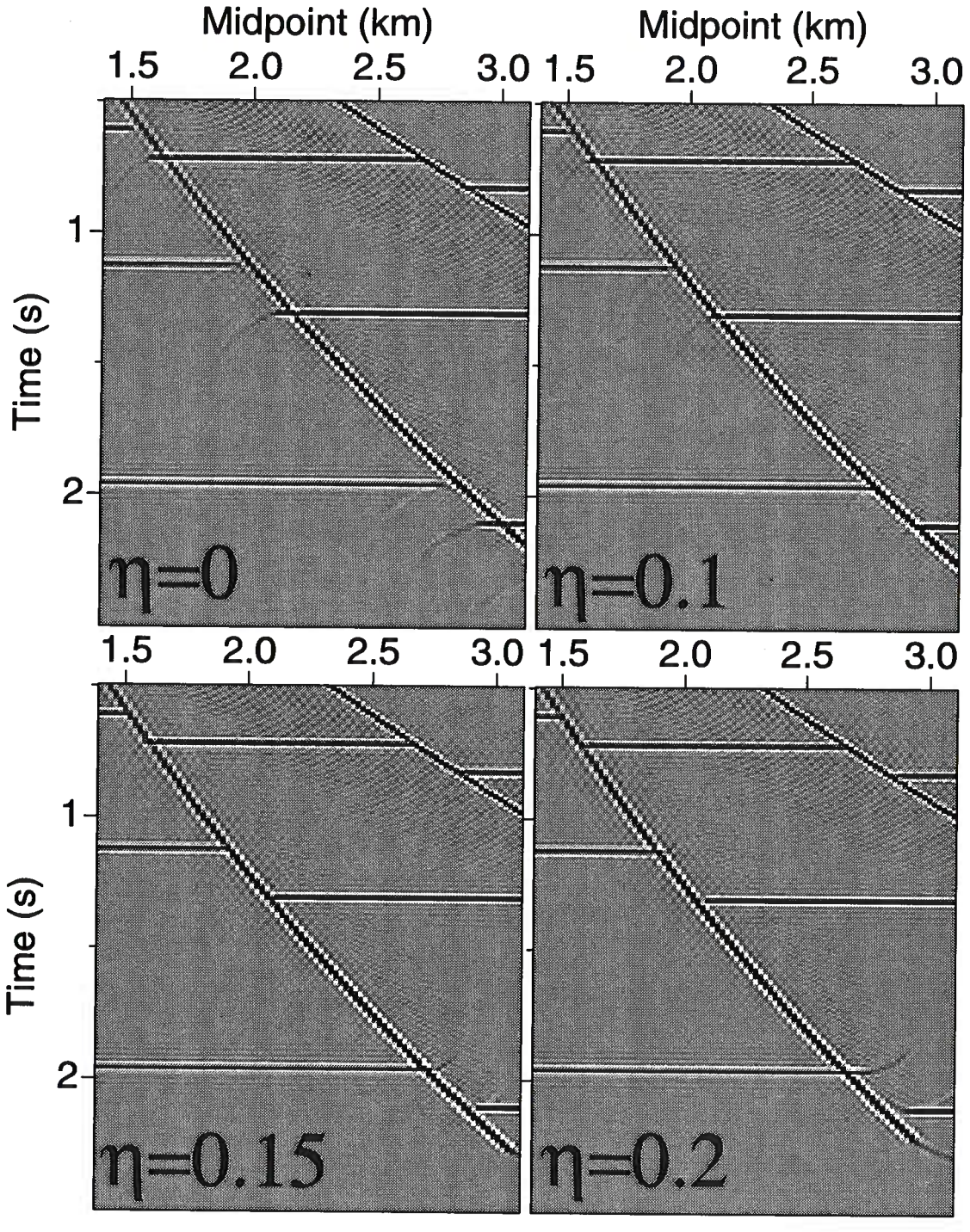

FIG. 5.5. Stolt TI migration of the zero-offset section in Figure 5.4a using different values of η. The medium is $v(z)$ VTI with $V_{P0}(z)$=1.5+0.6z km/s, and $\eta = 0.15$.

for the nonhyperbolic moveout term of the reflection moveout (Alkhalifah, 1996b) can be used here to derive interval values from η_{eff}. Because the layer-stripping equations are based on Taylor's series expansion around zero offset (zero ray-incident angle), the accuracy of these equations reduces with increasing offset (ray-incident angle). As a result, the accuracy of these equations for migration will reduce with increasing reflector dip.

5.3 Depth migration

Although depth migration does not lend itself to the two-parameter representation of P-waves in VTI media (the vertical P-wave velocity is needed for depth migration), it is still useful in areas of complex structure, where the lateral-homogeneity assumption breaks down. In this case, however, the vertical velocity, needed to implement the migration, must be estimated from observations other than surface seismic P-wave data, for example well-log data.

Gaussian beam migration (GBM) has emerged in the past few years as a desirable method for subsurface imaging (Hale and Witte, 1992). Among its features are acceptable computational efficiency, robustness with respect to ray caustics and shadows, the ability to image reflector dips greater than 90 degrees with turning waves, and straightforward extensions for migration of nonzero-offset sections and 3-D data (Hill, 1990; Hale, 1992).

For a couple of reasons, Gaussian beam migration is particularly suited for anisotropic media. Primarily, the relatively small amount of ray tracing needed to perform Gaussian beam migration minimizes the incremental cost in modifying the algorithm for anisotropic media. Second, the method can readily handle caustics that are associated specifically with anisotropic media, such as, for example, SV-wave caustics that arise even in homogeneous media. Also, the Gaussian beam method can readily treat data from general inhomogeneous and anisotropic media with any reflector orientation.

Here, I modify the isotropic Gaussian beam migration to handle general anisotropic media in two dimensions. The modification is based on anisotropic kinematic and dynamic ray-tracing. I show impulse responses for homogeneous and layered media, as well as successful migrations of synthetic data from inhomogeneous media.

5.3.1 Gaussian beam migration equations

First, let us review Gaussian beam migration, concentrating on the aspects that pertain most to the extension to anisotropic media. Detailed description of Gaussian beam ray tracing and migration can be found in Červený and Pšenčík (1984), Hanyga (1986), Hill (1991), and Hale (1992). Here, ray propagation and polarization will be constrained to the 2-D plane. Extension to three dimensions is straightforward since the general ray-tracing equations of Červený (1972) and Hanyga (1986) were actually developed for general anisotropy in three dimensions.

In Gaussian beam migration, one first subdivides a common-midpoint (CMP) stack section into overlapping subsets of stacked traces. The stacked traces within each subset are then multiplied by a centered Gaussian taper function over midpoint. These windowed data are then slant stacked to form beams in a range of directions characterized by different ray parameters (Hale, 1992).

The subsurface image $h_j(x,z)$ for a single beam denoted by the subscript j, at a position described by lateral position x and depth z, is calculated in GBM using the following equation (Hale, 1992):

$$h_j(x,z) = \int dp_x \left[A_R \tilde{b}(\tau_R,\tau_I) - A_I \tilde{b}_H(\tau_R,\tau_I)\right], \tag{5.12}$$

where $\tilde{b}$ is a local slant stack of the Gaussian-windowed surface seismic data, and $\tilde{b}_H$ is its Hilbert transform. A_R and A_I are the real and imaginary parts of the complex-valued amplitude (Appendix D), and $\tau_R(x,z,p_x)$ and $\tau_I(x,z,p_x)$ are the real and imaginary parts of the complex-valued time, both calculated by Gaussian beam ray tracing. p_x is the ray parameter, and $\tilde{b}$ is calculated using

$$\tilde{b}(\tau_R,\tau_I) = \frac{1}{2\pi}\int d\omega\, e^{-i\omega\tau_R} e^{|\omega|\tau_I} B_j(\omega,p_x), \tag{5.13}$$

where $B_j(\omega,p_x)$ is the local slant stack of the surface seismic data in the frequency (ω) domain, given by

$$B_j(\omega,p_x) = \frac{|\,\omega\,|}{2\pi} F_j(\omega,k_x=\omega p_x),$$

and $F_j(\omega,k_x)$ is obtained by applying a lateral shift and a frequency-dependent Gaussian taper to $F(\omega,k_x)$:

$$F_j(\omega,x) \equiv e^{-\frac{1}{2}\left|\frac{\omega}{\omega_l}\right|\frac{x^2}{l^2}} F(\omega,x+x_j), \tag{5.14}$$

where x_j is the center of the Gaussian window, and l is the width (standard deviation) of the Gaussian when frequency $\omega=\omega_l$. Finally, $F(\omega,k_x)$ is the 2-D Fourier transform of $f_j(x,t)$, the seismic data recorded at the surface $z=0$.

In the algorithm of Hale (1992), the critical loop needed to perform GBM is as follows:

Gaussian beam migration:

for all points (x, z) {
    $h(x, z) = 0$
}

for all $x_j = j\Delta$ *(all beam center locations)* {
    compute $f_j(t, x)$ *by shifting and tapering data* $f(t, x)$
    for all p_x *(all reflection slopes)* {
        compute filtered slant stack $b_j(\tau, p_x)$ *of* $f_j(t, x)$
        for all points (x, z) *within beam* {
            compute complex-valued $\tau_j(p_x, x, z)$ *and* $A_j(p_x, x, z)$
            accumulate contribution to $h(x, z)$ *from* $b_j(\tau, p_x)$
        }
    }
}

Here, $\tau_j(p_x, x, z)$ and $A_j(p_x, x, z)$ are the complex-valued time and amplitude, given by

$$\begin{aligned} \tau &= \tau_R + i\,\mathrm{sgn}(\omega)\tau_I \\ A &= A_R + i\,\mathrm{sgn}(\omega)A_I, \end{aligned}$$

and Δ is the spacing between the beam center locations x_j. Extension to anisotropic media requires calculating the complex-valued time and amplitude using anisotropic ray tracing, as discussed in Appendix D.

5.3.2 Initial beam width

In equation (E.3) (in Appendix D), we are representing the wavefront by a sequence of parabolic expansions. Let us examine the accuracy of these expansions, especially for strong anisotropy. Figure 5.6 depicts a point source in a homogeneous half-space, and a single ray emanating from this source. Again, s is the length along the ray, and n is the distance to the receiver in the direction of the normal to the phase-velocity direction. Although Gaussian beams are generally a combination of point and plane-wave solutions, for this homogeneous case the only error in the traveltime expansion at the receiver comes from the point-source contribution. For both isotropic and anisotropic media, plane-wave traveltime expansions are exact in a homogeneous medium. Clearly, as illustrated in Figure 5.6, in either type of medium, for plane waves the traveltime calculated at the receiver position is identical to that

along the ray at the point of the expansion [because Real $(\frac{\partial^2 T(s)}{\partial n^2})$=0 for plane waves]. However, this is not the case for point sources, where the wavefront is curved and approximated by equation (E.3), even in homogeneous media. In this test, I compare the traveltimes calculated using the parabolic expansion with the exact traveltimes.

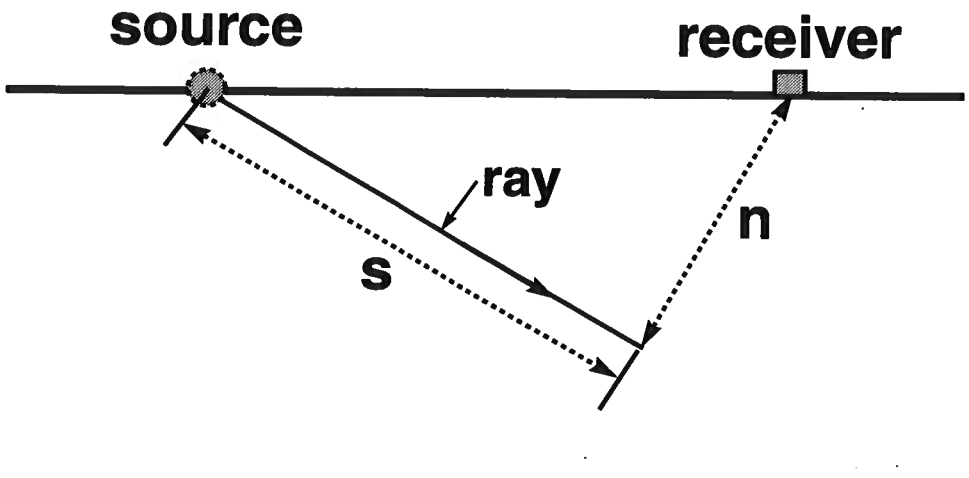

FIG. 5.6. Schematic vertical section illustrating the lengths s and n for a certain ray in a homogeneous medium.

Figure 5.7 shows the percent difference in those traveltimes, as a function of the ratio n/s. This ratio varies for the different rays that contribute to a given receiver position. Curves are shown for three different transversely isotropic media characterized by the δ and ϵ parameters of Thomsen (1986). Clearly, for low values of n/s, the errors are largest for strong anisotropy (i.e., large δ and ϵ). Overall, the errors ($\sim$ 0.5 percent) are small, but they indicate the limitations that the parabolic expansion has in approximating the wavefront in the presence of strong anisotropy.

Figure 5.8 shows the amplitude of the different beams contributing to the same receiver for a homogeneous isotropic medium and for a strongly anisotropic one. The location of our receiver is in a slightly more complicated (i.e., more highly curved) part of the wavefront for the strongly anisotropic medium. Interestingly, Figure 5.8 shows that the amplitude decay away from the central ray is greater for the anisotropic medium than it is for the isotropic medium. We can get a sense of what is happening by observing the example in Figure 5.9a. Figure 5.9a shows migration impulse responses for P-waves in a strongly anisotropic, homogeneous medium. The anisotropy accounts for the departure in shape of the impulse response from the familiar circular shape in isotropic media. For this case the beam width is smallest near vertical and near horizontal, where the wavefront has the highest curvature. In addition, the largest

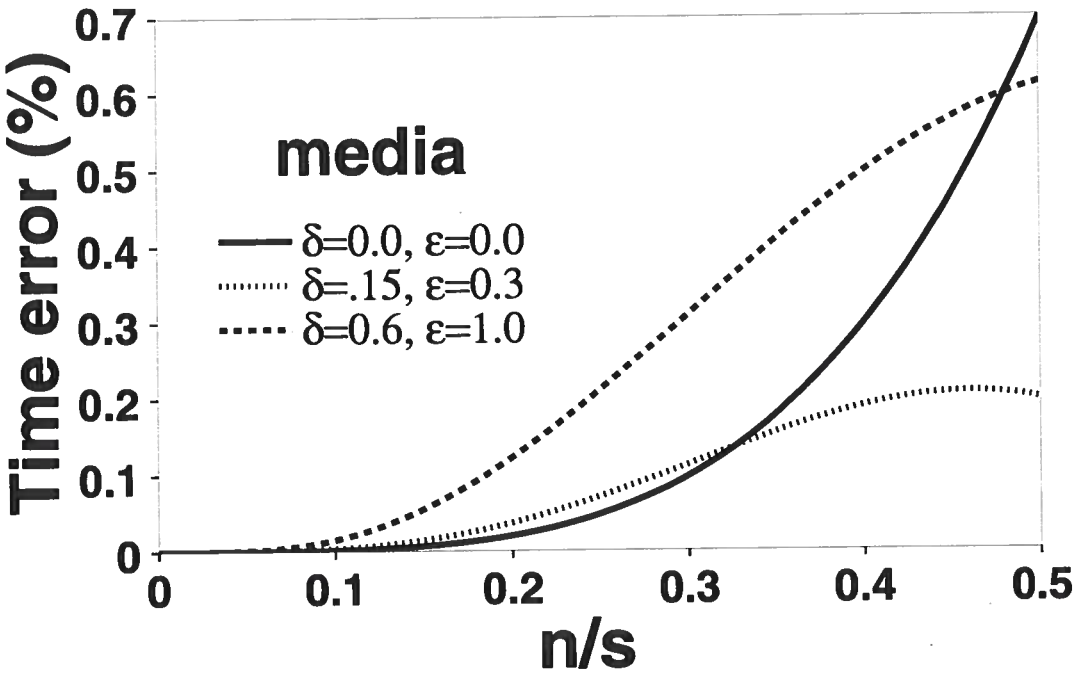

FIG. 5.7. Percentage time error as a function of n/s for the model shown in Figure 5.6.

concentration of rays occurs in the portions of the wavefront with highest curvature. In contrast, for the smoother parts, near 45-degree ray propagation, the beam width is much broader, and the wavefront is characterized by relatively few rays. It thus happens that, although in GBM the number of rays generated to calculate the wavefield may be the same for both isotropic and anisotropic media, the angular distribution of the rays differs.

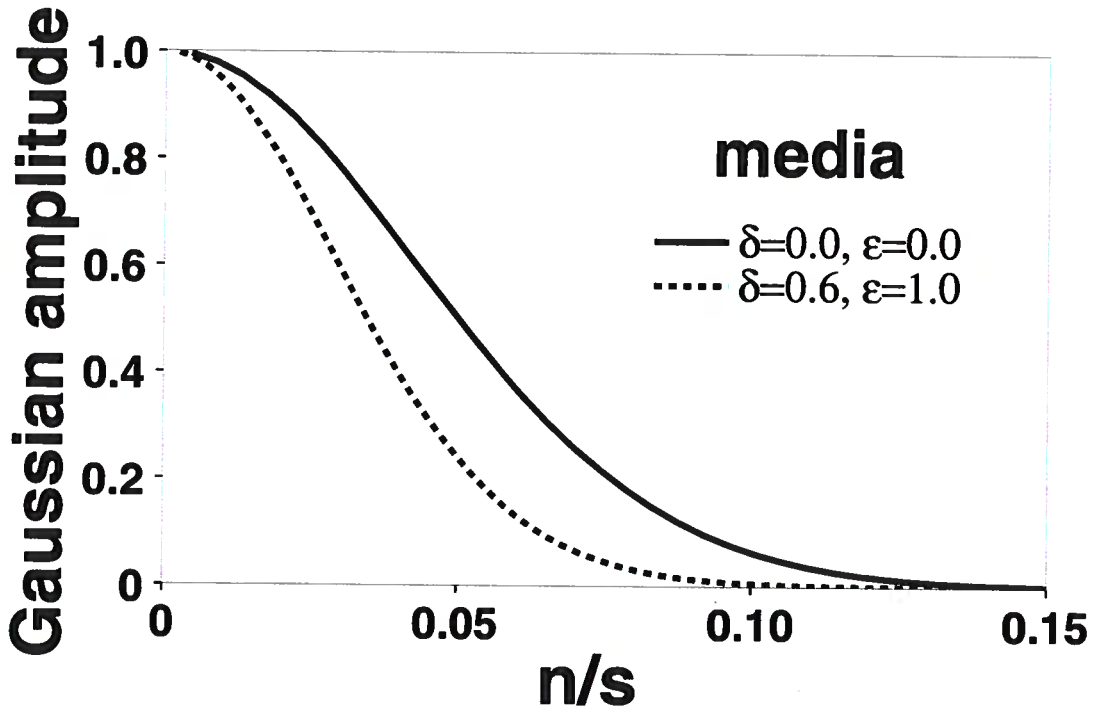

FIG. 5.8. Gaussian weighting away from the ray, as a function of n/s.

With a proper choice of initial beam width, the beam width, l, along the ray will not expand to large values of n/s. Here, I compute the initial beam width using the same equation used by Hill (1990)

$$l = \frac{v_{avg}}{f_{min}},$$

where f_{min} is the minimum frequency and v_{avg} is the average of the horizontal and vertical velocities over the entire grid.

5.4 Migration Cost

P-wave ray-tracing in a general anisotropic inhomogeneous medium is a much slower process than that in an isotropic medium. One reason is that ray tracing within symmetry planes in general anisotropic 2-D media requires six velocity fields, corresponding to the six position-variant elastic coefficients [$a_{1111}(x,z)$, $a_{3333}(x,z)$, $a_{1133}(x,z)$, $a_{1313}(x,z)$, $a_{1113}(x,z)$, and $a_{3313}(x,z)$], whereas ray tracing in isotropic media requires only one velocity field. A second and more important reason is that ray tracing in anisotropic media involves much more complicated and more computationally extensive equations than does that in isotropic media. However, isotropic ray tracing constitutes only about 2 percent of the cost of GBM for generally inhomogeneous models. Therefore, the substantially increased cost of ray tracing in anisotropic media raises the computation cost of the full GBM process by only a modest amount— generally by no more than 40 percent. This speed characteristic is not shared by Kirchhoff migration. For that method, ray tracing constitutes the major portion of the processing, so Kirchhoff migration must bear the full additional cost of ray tracing in general, anisotropic media.

In addition to its speed advantage for anisotropic migration, GBM can handle caustics and migrate accurately more than just the first *P*-wave arrivals. In contrast, Kirchhoff migration has serious problems in handling caustics, a common occurrence when migrating *S*-waves in anisotropic media.

The 40-percent difference in computation cost between isotropic and anisotropic GBM holds in symmetry planes of general anisotropic, inhomogeneous 2-D media. When considering only TI media or factorized TI media the cost difference reduces substantially, to about 10 percent.

The computer memory requirement is similar to that of isotropic GBM. The main difference is the additional number of input velocity files required to specify a particular form of anisotropic media.

5.5 Synthetic Examples

The changes from isotropic algorithms mentioned above do not limit GBM in any way. Specifically, it is still extendable to three dimensions, with its relative efficiency largely unchanged; relative to the cost of the migration, the cost of computing τ and A for anisotropic media is small.

5.5.1 Smooth media

Figure 5.9 shows the response of GBM to impulses at times 0.8, 1.6, and 2.3 s, with a constant vertical *P*-wave velocity of 2000 m/s and constant vertical *S*-wave velocity of 1000 m/s for (a) *P*-waves, and (b) *S*-waves, in the weathered-gypsum TI medium of Thomsen (1986). This medium has Thomsen anisotropy parameters $\delta = -0.14$ and the uncommonly large $\epsilon = 1.1$. As mentioned above, the wavefronts

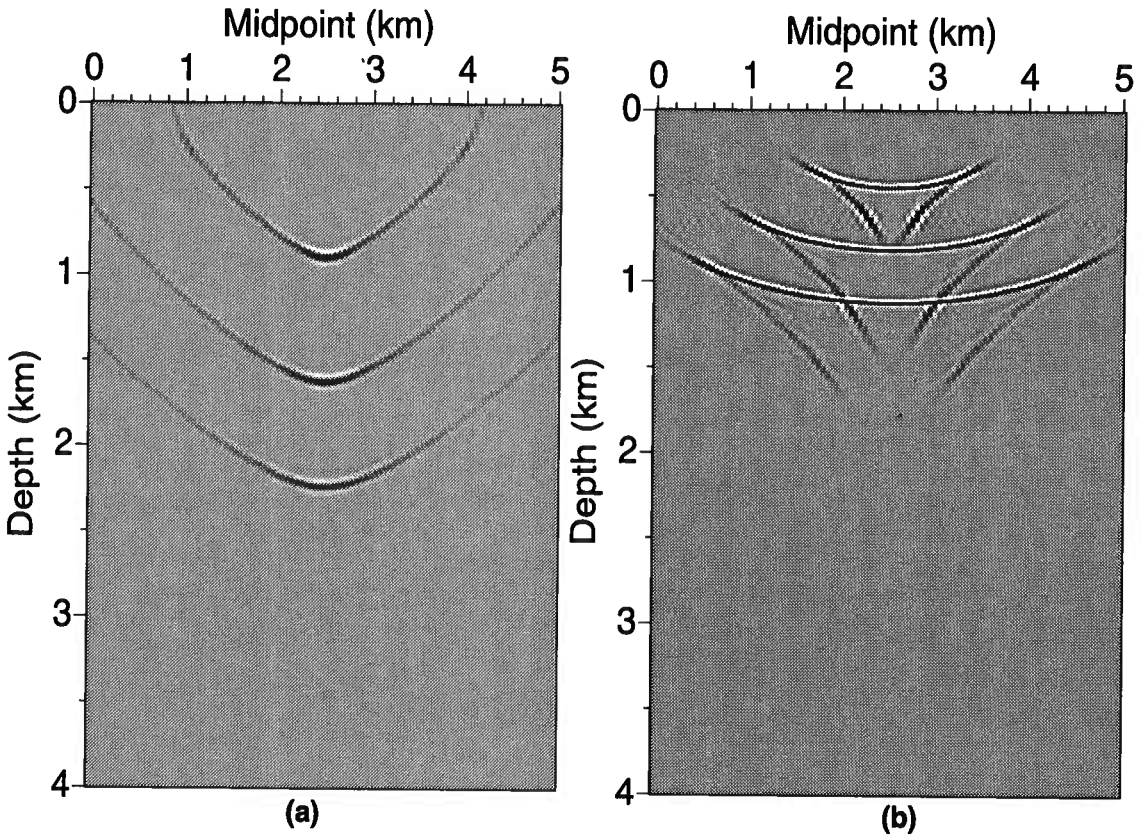

FIG. 5.9. GBM impulse responses for (a) P-wave, and (b) SV-wave in homogeneous weathered gypsum ($\delta = -0.14$, $\epsilon = 1.1$) with vertical axis of symmetry.

(and amplitudes along wavefronts) here are very different from the circular ones of an isotropic medium, especially for the SV-wave with its obvious triplication (caustics), which is handled without difficulty by the Gaussian beam migration.

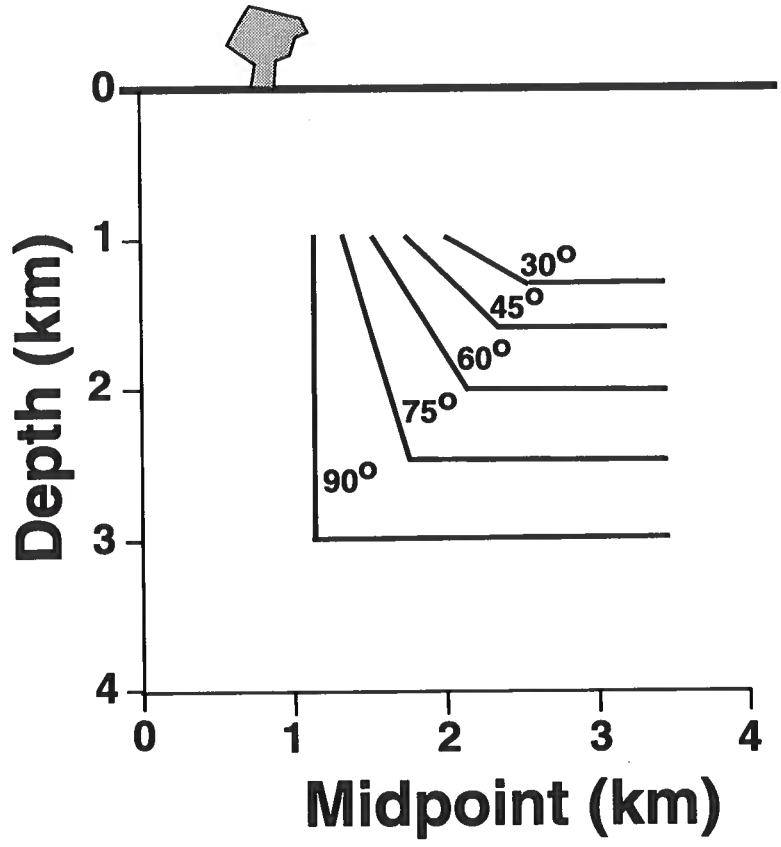

FIG. 5.10. Model of reflectors with dips of 0, 30, 45, 60, 75, 90 degrees. Note that the vertical reflector is at 1.2-km midpoint position.

Now, consider the depth model shown in Figure 5.10. It consists of five reflectors, each of which has a horizontal segment and a dipping one. Figure 5.11 shows synthetic zero-offset sections for this model in (a) an isotropic medium, and (b) a finely interbedded shale-limestone TI medium, with anisotropy parameters $\delta = 0.0$, $\epsilon = 0.134$, both with vertical velocity $v(z) = 3000 + 0.5\,z$ m/s. Figure 5.11a was generated using a Kirchhoff modeling program for an isotropic medium with a linear velocity increase with depth. Figure 5.11b was generated using a modified version of that modeling program that treats factorized transversely isotropic (FTI) media (Alkhalifah, 1995a), i.e., media for which δ and ϵ are independent of position. The dot shown in Figures 5.11a and 5.11b is for reference in comparing the positions of the reflections from the vertical reflector for the isotropic and TI media. Despite the

fact that the vertical velocity is the same for both the isotropic and TI cases, steep events are in different positions on the two sections. Therefore, we can expect that isotropic migration will leave features mispositioned on the TI data.

Figure 5.12 shows migrations of the anisotropic data in Figure 5.11b using (a) standard, isotropic GBM and (b) GBM modified for anisotropic media. The velocity used to derive medium velocities for the standard GBM is the best-fit stacking velocity for horizontal reflectors, whereas the correct medium parameters are used in the anisotropic GBM. Clearly the image in Figure 5.12b is superior to that in Figure 5.12a. The image from the isotropic migration, Figure 5.12a, not only is undermigrated, it is placed at too great a depth because stacking velocity exceeds the vertical root-mean-square (rms) velocity. This depth error is of the sort described by Banik (1984), Winterstein (1986), and VerWest (1989). In contrast, the reflector locations have been correctly imaged by the modified GBM, Figure 5.12b. Here, because I use a simple version of the anisotropic GBM that considers only FTI media, the computation cost difference between the isotropic and anisotropic GBM is less than 10 percent.

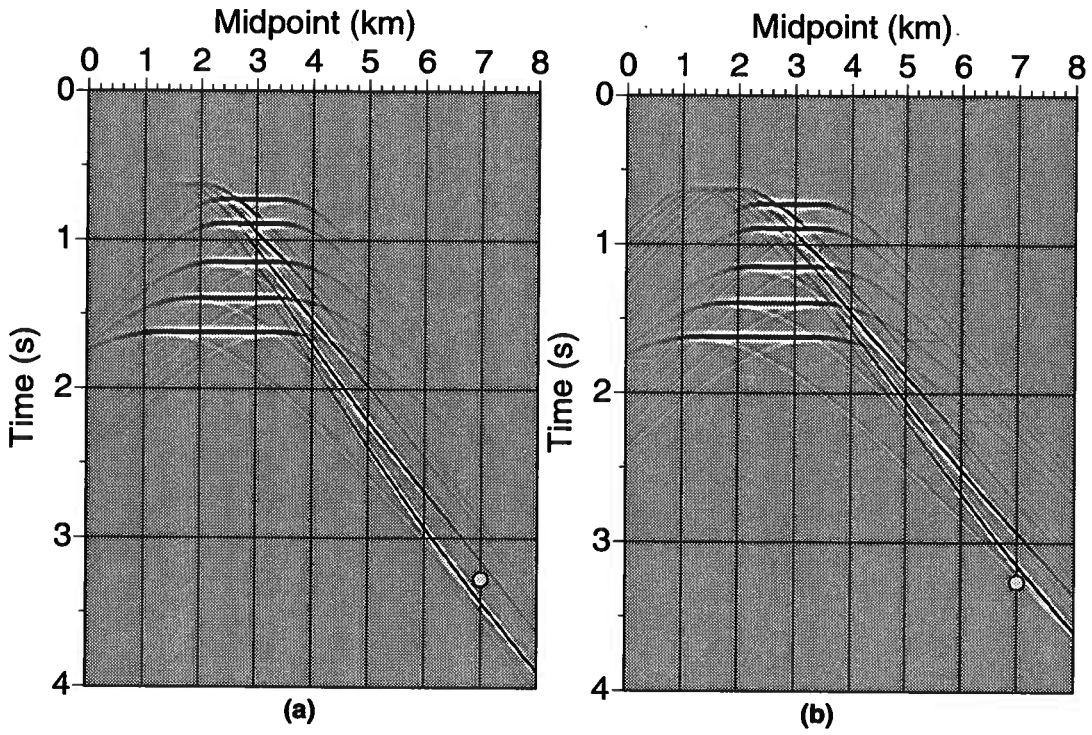

FIG. 5.11. Synthetic zero-offset seismograms for the structural model in Figure 5.10, for (a) an isotropic medium, and (b) a shale-limestone, transversely-isotropic medium. Both media have vertical velocity $v(z) = 3000 + 0.5\,z$ m/s, and reflector dips ranging from 0 to 90 degrees.

Figure 5.13 shows isotropic GBM and anisotropic GBM for the FTI Cotton Valley shale medium of Thomsen (1986), with anisotropy parameters $\delta = 0.205$, $\epsilon = 0.135$, and vertical velocity $v(z) = 3000 + 0.5\,z$ m/s, for the same structural model as in Figure 5.10 (unmigrated data not shown here). Although, it is unlikely that $\epsilon - \delta < 0$ (Thomsen, 1986), the Cotton Valley shale medium is a good model to demonstrate the flexibility of this migration. Following Larner and Cohen (1993), I used the best-fit stacking velocity (for horizontal reflectors) to minimize the lateral position errors in the isotropic migration. The isotropic GBM not only yields a considerably over-migrated image, it again results in large vertical shifts in the reflector position. As in Figure 5.12a, the depth error is caused by using the wrong migration velocity, namely the stacking velocity in the TI medium, and hence the wrong velocity for the vertical traveltime-to-depth conversion.

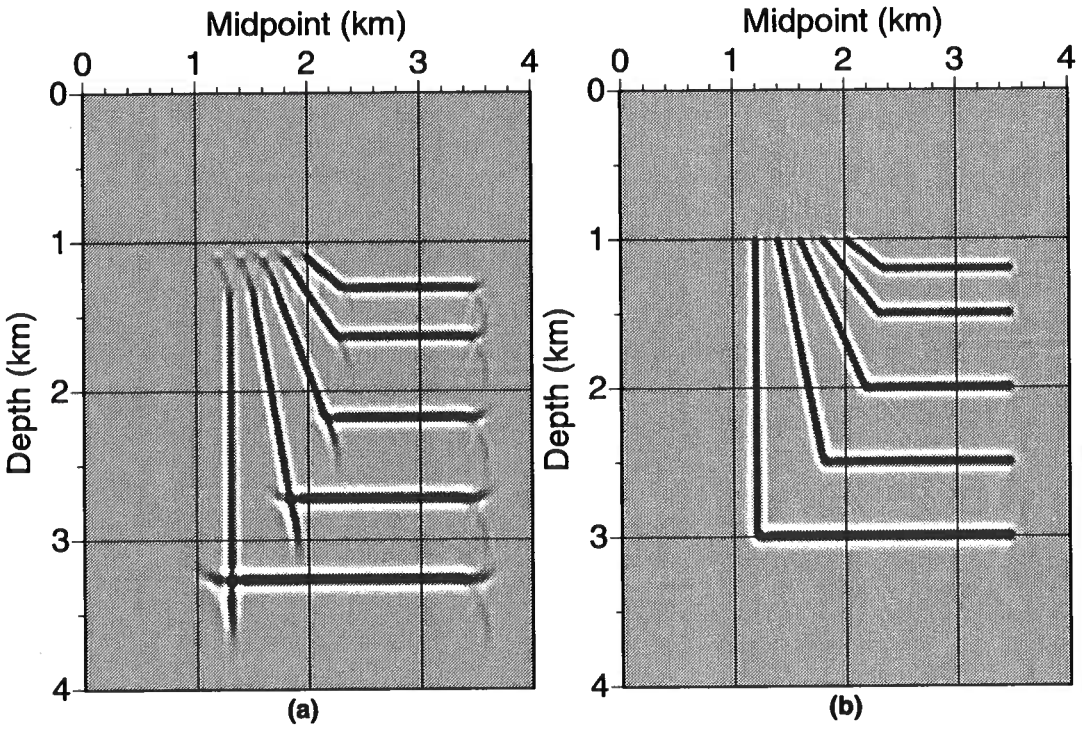

FIG. 5.12. Migration of the data in Figure 5.11b using (a) the isotropic GBM algorithm, and (b) anisotropic GBM, for the shale-limestone TI medium.

For both anisotropic media — shale-limestone and Cotton Valley shale — the anisotropic GBM (with the correct anisotropy parameters) gave a substantially better image of the reflector position than did the GBM that ignores anisotropy.

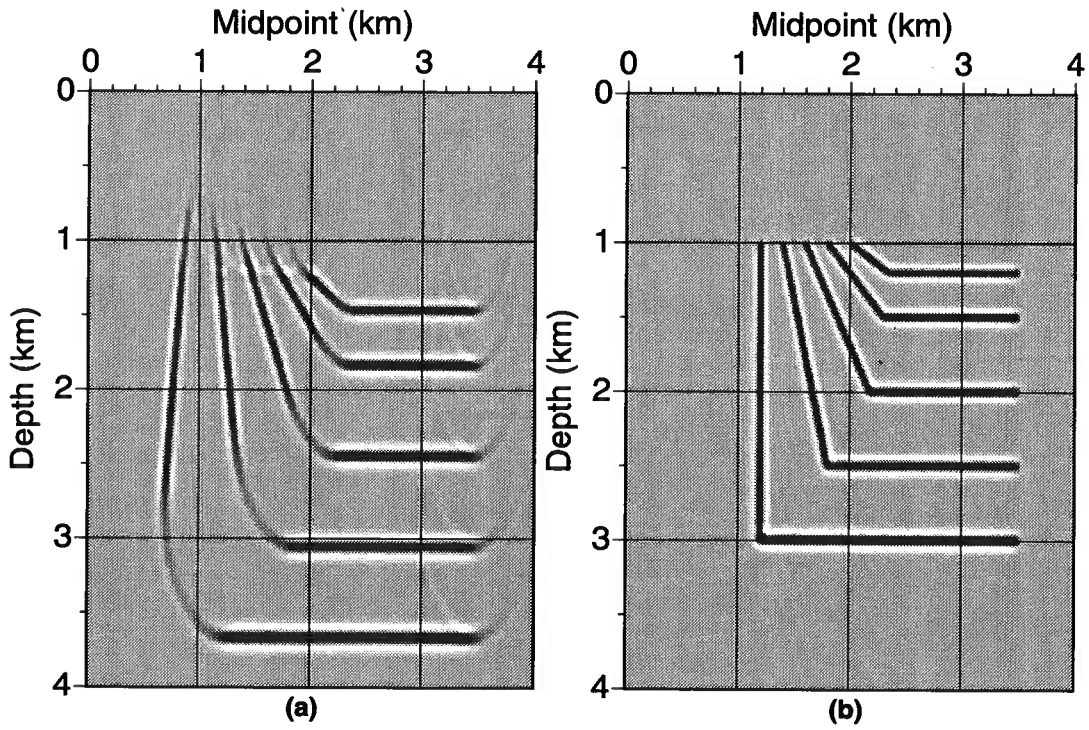

FIG. 5.13. Migration of data from the structural model shown in Figure 5.10 for Cotton Valley shale with $v(z) = 3000 + 0.5\,z$ m/s, using (a) isotropic GBM, and (b) anisotropic GBM.

5.5.2 Layered media

As in other high-frequency approximations, accuracy in the ray tracing for GBM requires some degree of smoothing of the input velocity field. For general anisotropic media, smoothing must be applied to all six needed velocity fields. If any of the velocity fields contains sharp velocity discontinuities, the quality of the migrated image will be degraded (because the ray-tracing computations require evaluation of derivatives of the velocity fields), with the degree of this degradation depending on the sizes and locations of the discontinuities.

Figure 5.14a shows a model of four homogeneous, transversely isotropic layers, with different anisotropy parameters in each layer. The vertical velocity is indicated by the shading level; the vertical velocity in the first layer is 1 km/s, and in the bottom layer, 3 km/s. For both these layers, the axis of symmetry is vertical. The arrow in the second layer shows the symmetry-axis direction, tilted by 30 degrees from the vertical. Figure 5.14b shows a smoothed version of the model. Although the smoothing is shown here for the vertical velocity, all needed velocity fields (corresponding to the elastic coefficients) are smoothed to the same degree. For the smoothing, the velocity field was convolved with a 2-D Gaussian-shaped, point-spread function. Here, the width of the Gaussian function (the half-amplitude point) was 0.1 km in all directions.

Figure 5.15a shows the impulse response for the model in Figure 5.14a for input pulses at three different times, all located at common-midpoint position 2.5 km. Figure 5.15b shows the corresponding impulse responses for the smoothed model in Figure 5.14b.

The importance of the velocity smoothing is evident from the comparison of these two sections. In particular, where the discontinuities are large, the impulse responses are obliterated for the unsmoothed model, a striking shortcoming of the high-frequency approximation. Clearly, the impulse responses associated with the smoothed model are much more coherent. Note that for impulses in and beneath the second layer, where the symmetry axis is tilted, the impulse responses in Figure 5.15b are also tilted. The extreme degradation shown in Figure 5.15a for impulse responses generated without smoothing exceeds the degradation usually associated with similar isotropic layered media. This poorer result probably arises because ray tracing in anisotropic media encounters discontinues in six velocity fields rather than the one in isotropic media.

This problem could be avoided be applying the necessary boundary adjustment using Snell's law or any perturbation technique (Jech and Pšenčík, 1989). Such boundary modifications, however, would reduce the efficiency of the migration process. Therefore, the alternative smoothing approach may be more attractive, particularly considering the uncertainty present in characterizations of velocity models for the earth's subsurface.

Using finite differences to generate a zero-offset synthetic section for the model in Figure 5.14a, but with a vertical symmetry axis in the second layer, results in the section shown in Figure 5.16a. Figure 5.16b shows an anisotropic GBM of the synthetic data using the same amount of smoothing of the velocity fields as in Figure 5.14b.

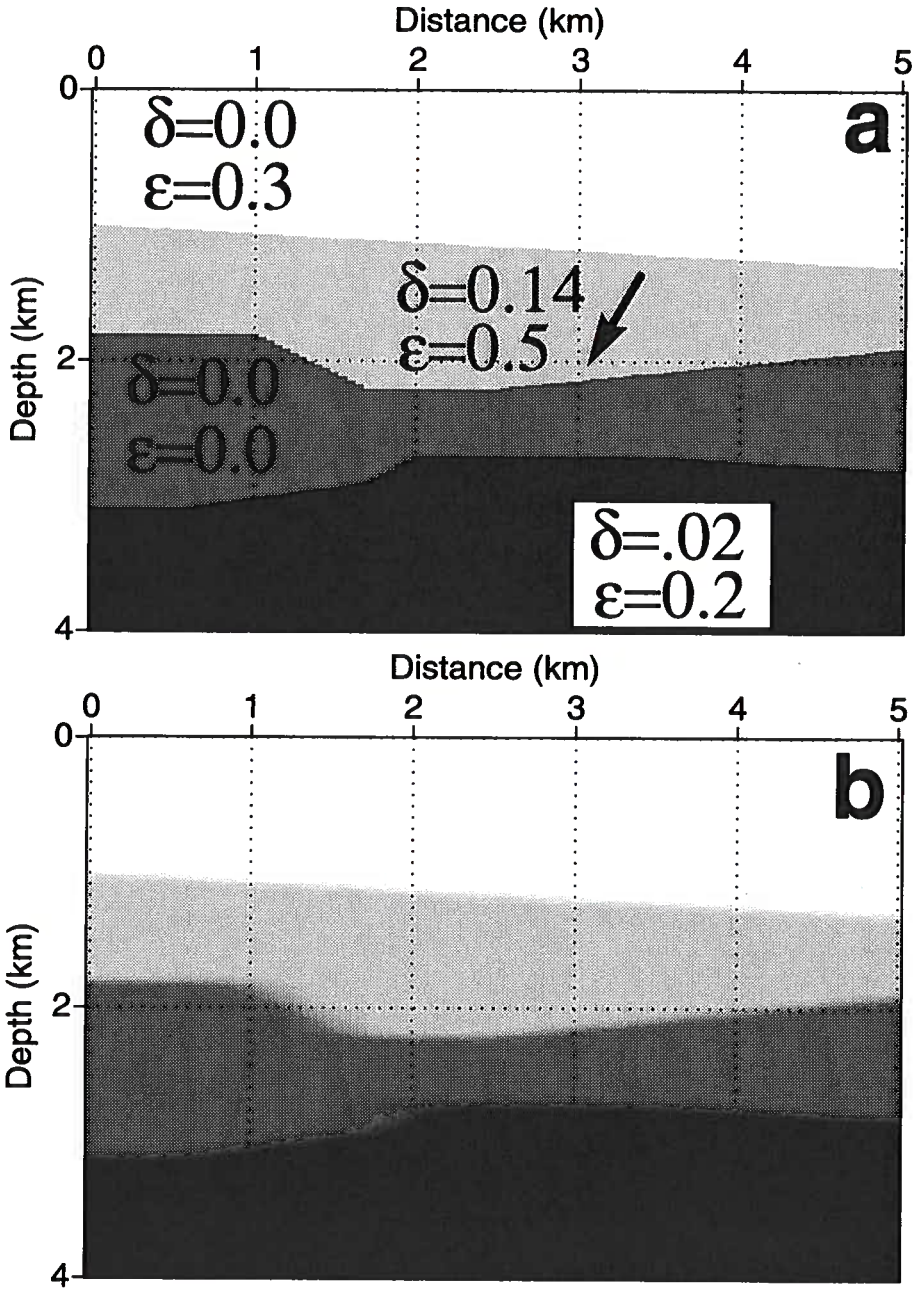

FIG. 5.14. (a) Model containing layers with different anisotropy parameters in each layer. All layers have vertical symmetry axis with the exception of the second layer where the symmetry axis is in the direction of the arrow. From top layer to bottom, the vertical velocity is 1.0 km/s, 1.5 km/s, 2.5 km/s, and 3.0 km/s. (b) Smoothed version of the above model.

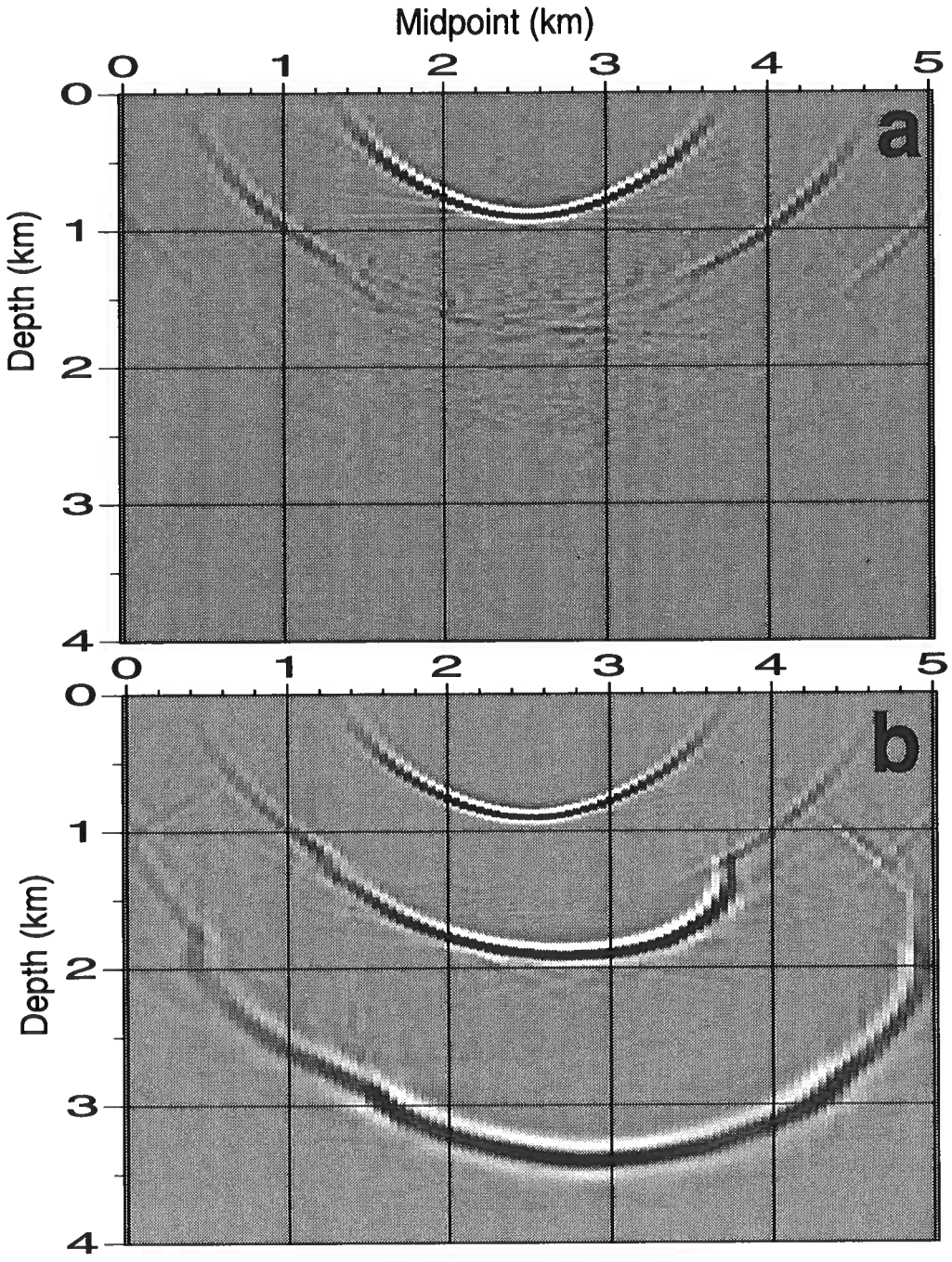

FIG. 5.15. (a) GBM impulse responses for the model in Figure 5.14a. (b) GBM impulse responses for the smoothed model in Figure 5.14b.

With this degree of smoothing the TI migration has produced an image that closely matches the correct depth model.

5.6 Use of depth migration in VTI media

Depth migration is commonly used in areas of complex structure where velocity varies in all directions. However, in such media, the two-parameter representation of P-waves in VTI media no longer holds; thus, at least three parameters, including the vertical velocity, are needed to implement the migration. The velocity analysis, derived in this thesis, strictly handles only laterally homogeneous media, with some tolerance to mild lateral velocity variation. It fails, however, in areas of complex structure. In this case, velocity should be estimated using information beyond the surface P-wave seismic data, for example well-log data.

Suppose that the shallow parts of the subsurface consists of sediments with mild laterally velocity variations. These sediments (predominantly shales) are typically the major source of anisotropy influence in our seismic data. In this shallow portion, the velocity-analysis methods described above for estimating anisotropy should work fine. On the other hand, the structure below the sediments is often complex (many salt formations and carbonates) with minor anisotropy influence. Therefore, anisotropy estimation in this portion is probably not needed. Based on this proposed model we can depth migrate the data using the anisotropy parameters derived for the top (smoothly varying) portion of the subsurface, along with the isotropic velocities derived for the bottom (complex) portions of the subsurface using isotropic methods. This model is similar to the first three layers of the model shown in Figure 5.14a, where the third layer is isotropic under a laterally inhomogeneous overburden, whereas the first two subsurface layers can be well approximated using the lateral homogeneity assumption.

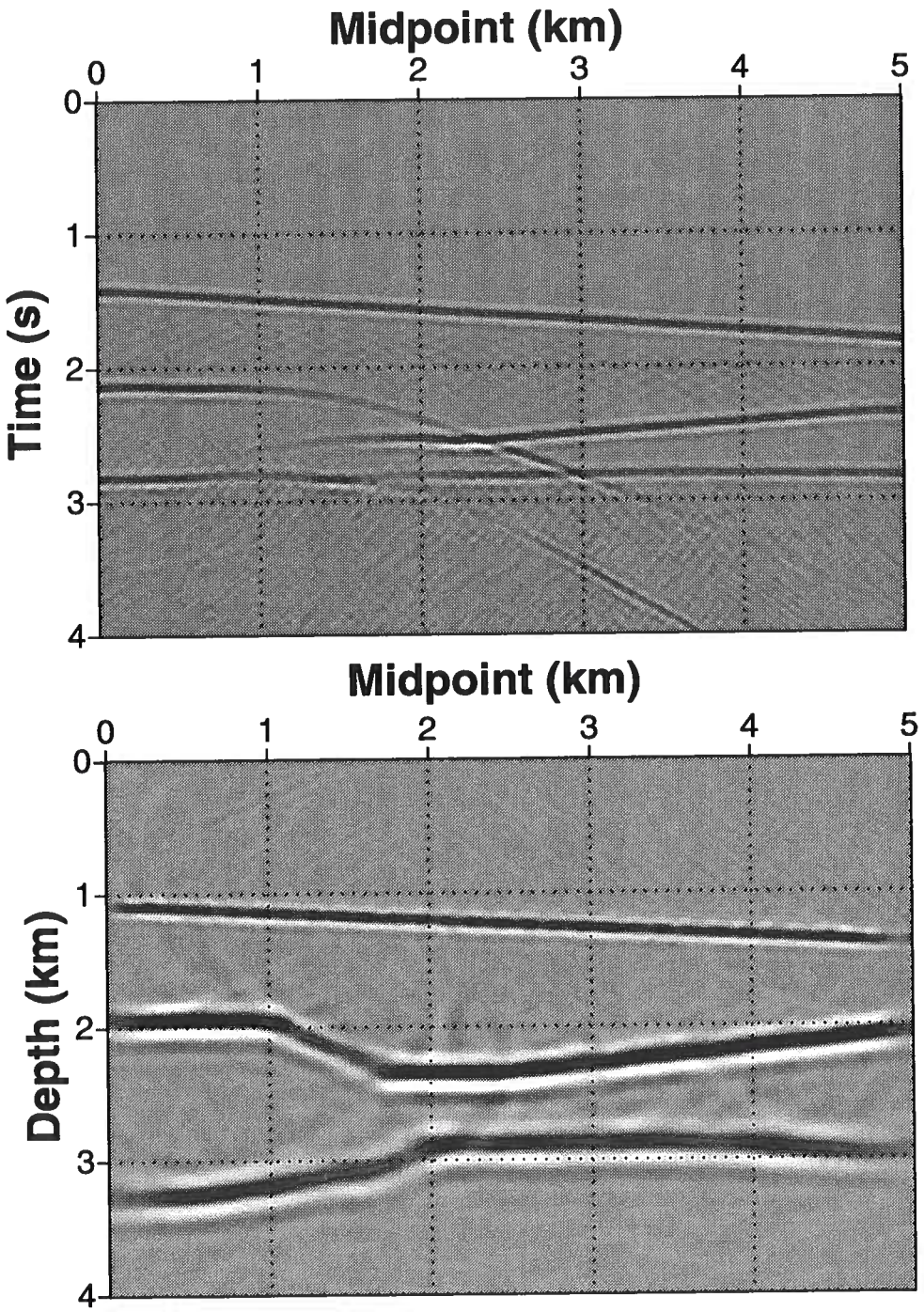

FIG. 5.16. (a) Synthetic seismogram generated using the model in Figure 5.14a, but with vertical symmetry axis in the second layer. (b) Anisotropic GBM migration of (a) using smoothed velocity fields similar to that of Figure 5.14b.

Chapter 6

FIELD DATA APPLICATION

Here, I apply the anisotropic processing sequence discussed above to data from offshore Angola as well as data from offshore Trinidad — two different regions which, although both are dominated by sediments, have substantially different subsurface content. For the Angola data, I first focus on a single fault in a structurally simple region. An example with many faults in a region of more complex structure is considered next. Then, I apply the anisotropic processing to the Trinidad data to demonstrate the method's versatility.

6.1 A single fault example

Figure 6.1 shows a seismic line from offshore Africa provided by Chevron Overseas Petroleum, Inc. The line was processed using a sequence of conventional NMO, DMO, and time-migration algorithms without taking anisotropy into account. While horizontal and mildly dipping reflectors are imaged well, steep fault-plane reflections (such as the one at a time of 1.5-2 s to the left of CMP 1000) show weak amplitude. Velocity analysis at CMP locations below the gray bar in Figure 6.1 shows a pronounced vertical velocity gradient of about 0.7 s^{-1}.

As we saw in Figure 1.1, these data are influenced by the presence of anisotropy in the region. The influence of anisotropy on the DMO operation is so large that it clearly shows (in Figure 1.1) even in the presence of vertical inhomogeneity, which usually has an opposite action on DMO (Gonzalez et al., 1992; Larner, 1993). Based on an inversion procedure for homogeneous VTI media, Alkhalifah and Tsvankin (1995) obtain an estimate of $\eta = 0.07$ for the area under the gray bar of Figure 6.1. Since an increase in vertical velocity with depth tends to reduce the estimated value of η, I expect that this estimate is lower than the value that could be attributed solely to the anisotropy of the medium. Therefore, let's call the value computed using the homogeneous model the "effective η." Application of anisotropic DMO based on the effective $\eta = 0.07$ allowed Alkhalifah and Tsvankin (1995) to improve the results of the conventional isotropic DMO. As they explained, however, their effective η, while useful for DMO, may be inappropriate for migration.

To take full advantage of the DMO approach developed here, I performed a $v(z)$ inversion, based on the method described in Appendix C, in order to obtain interval values $v_{\rm int}(\tau)$ and $\eta_{\rm int}(\tau)$, where τ is vertical time. Such interval values of the anisotropy parameter can then be used in both DMO and time migration.

Figure 6.2 shows $v_{\rm int}(\tau)$ and $\eta_{\rm int}(\tau)$, obtained from the $v(z)$ VTI inversion. This inversion is accomplished by estimating the NMO velocity as a function of ray para-

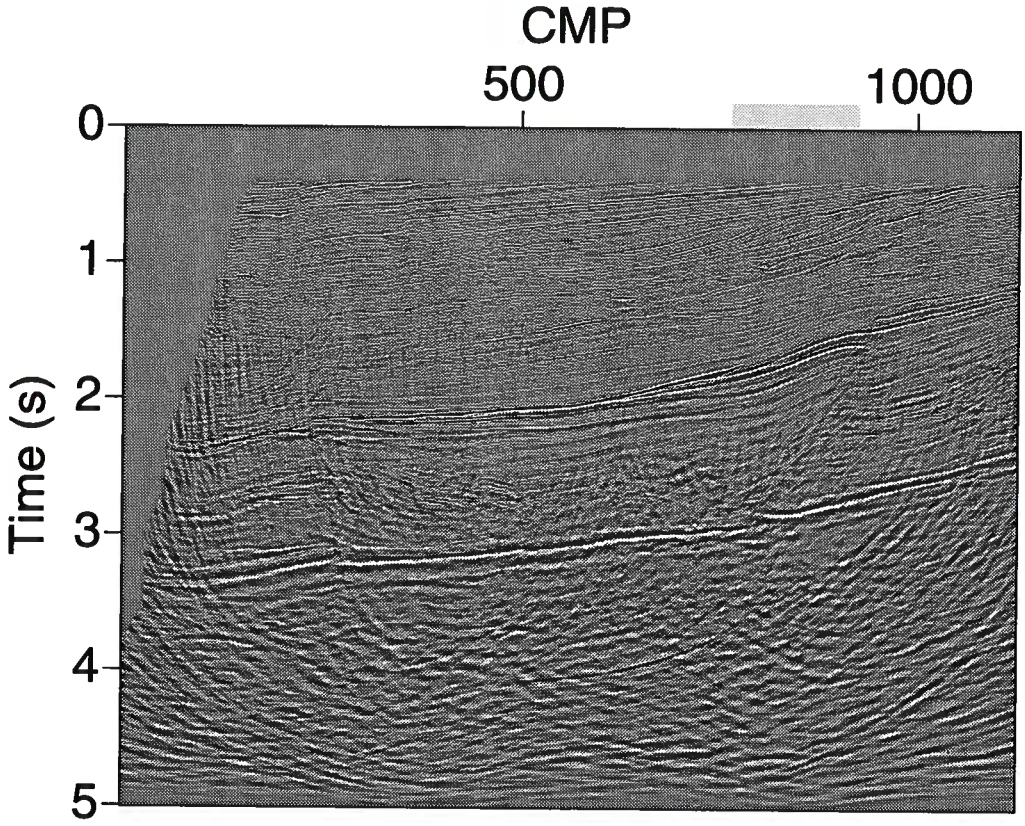

FIG. 6.1. Time-migrated seismic line (offshore Angola). The gray bar to the left of CMP 1000 shows the CMP locations that contain the unmigrated data from the fault of interest.

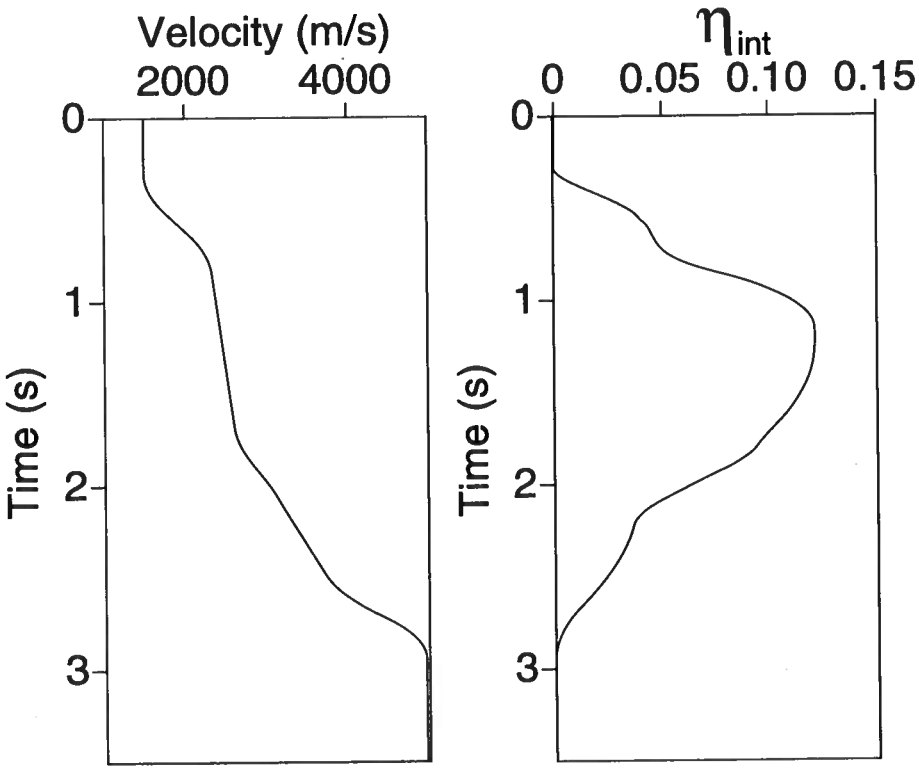

FIG. 6.2. Interval values v_{int} and η_{int} as a function of vertical time.

meter for the dipping fault at five different points along the fault, corresponding to five different vertical times. I assume no lateral velocity variation in the region of the fault; however, mild lateral velocity variation should not be a problem for the inversion: most DMO algorithms, while based on the assumption of lateral homogeneity, still produce acceptable results where lateral velocity variation is smooth. The continuous curves shown in Figure 6.2 are generated by linear temporal interpolation and smoothing of the velocities for both the mildly dipping reflectors (for simplicity I refer to them as horizontal reflectors) and the fault. In the water layer, v_{int} is equal to 1.5 km/s and η_{int} is equal to zero. The accuracy of these estimated curves of v_{int} and η_{int} depends on the accuracy of the stacking-velocity estimates for both dipping and horizontal reflectors. The idea underlying the inversion is that the $v_{\text{int}}(\tau)$ and $\eta_{\text{int}}(\tau)$ functions obtained are those that best focus the dipping fault and the horizontal reflectors at the same stacking (or NMO) velocity, for each vertical time at which velocity measurements are made.

In Figure 6.2, where $\eta_{\text{int}} = 0$, the medium is either isotropic or elliptically anisotropic. Because elliptical anisotropy for P-waves is not typical in the subsurface (Thomsen, 1986), one might infer that, where $\eta_{\text{int}} = 0$, the medium is more likely to be isotropic. The region above 2 s, which exhibits positive values of η_{int}, corresponds to a shale formation, which can be expected to be transversely isotropic and may thus be the major source of anisotropy in the data.

Figure 6.3 shows the result of VTI DMO applied to the data, based on the derived functions $v_{\text{int}}(\tau)$ and $\eta_{\text{int}}(\tau)$. We can clearly see the presence of a fault, which is dipping at an average angle of about 45 degrees. This angle exceeds the dips included in the first branch of the DMO impulse response. Recall that this first branch is the only branch that can be approximated by a stretched ellipse. Therefore, we cannot expect that for this medium isotropic constant-velocity or $v(z)$ DMO or a stretched version of the DMO ellipse would perform as well as has the $v(z)$ anisotropic DMO, here.

This expectation is supported by Figures 6.4a and 6.4b. Figure 6.4a shows the zero-offset section obtained by applying isotropic homogeneous DMO, and Figure 6.4b shows that obtained by applying isotropic $v(z)$ DMO. The isotropic homogeneous DMO used here is the frequency-wavenumber method of Hale (1984), and the $v(z)$ isotropic DMO is Artley and Hale's (1994) isotropic version of the DMO method described above. Clearly, the fault is poorly imaged by both isotropic algorithms, while VTI DMO yields a much better result (Figure 6.3). Figure 6.5 shows a representative VTI DMO operator used for these data. The shape is far from the isotropic ellipse or a squeezed version of it.

Not only did the $v(z)$ VTI DMO do a better job of imaging the dipping fault, it also improved the continuity of horizontal reflectors (e.g., the regions pointed to by the arrows in Figures 6.3 and 6.4) by correcting for nonhyperbolic moveout. Figure 6.6 shows CMP gathers at CMP location 700 after (a) $v(z)$ VTI DMO, (b) homogeneous isotropic DMO, and (c) $v(z)$ isotropic DMO. The same NMO correction was used for all three DMO examples. It is based on the stacking velocities obtained from a typical velocity analysis. All reflections shown in this figure are from horizontal reflectors.

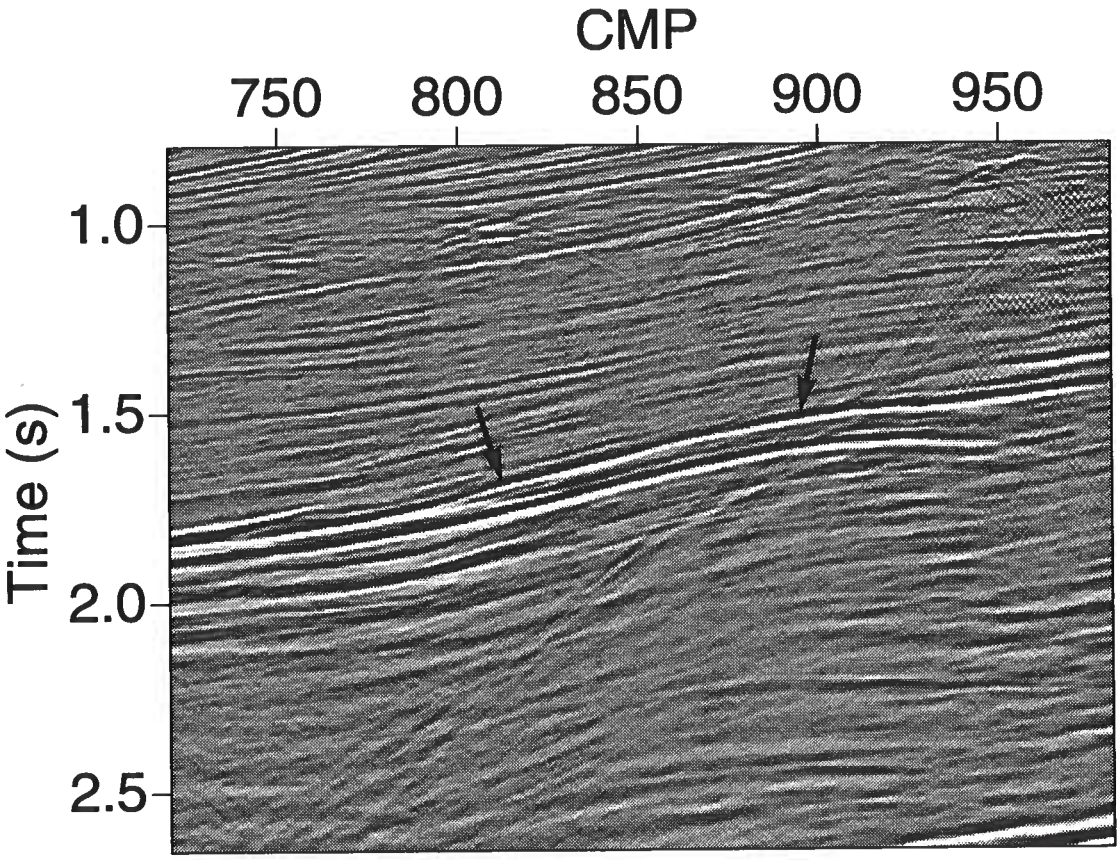

FIG. 6.3. Zero-offset section after a $v(z)$ anisotropic DMO using the parameters in Figure 6.2. The NMO correction is based on the velocities obtained from the conventional velocity analysis. The arrows point to regions of improved reflection continuity relative to that in Figure 6.4.

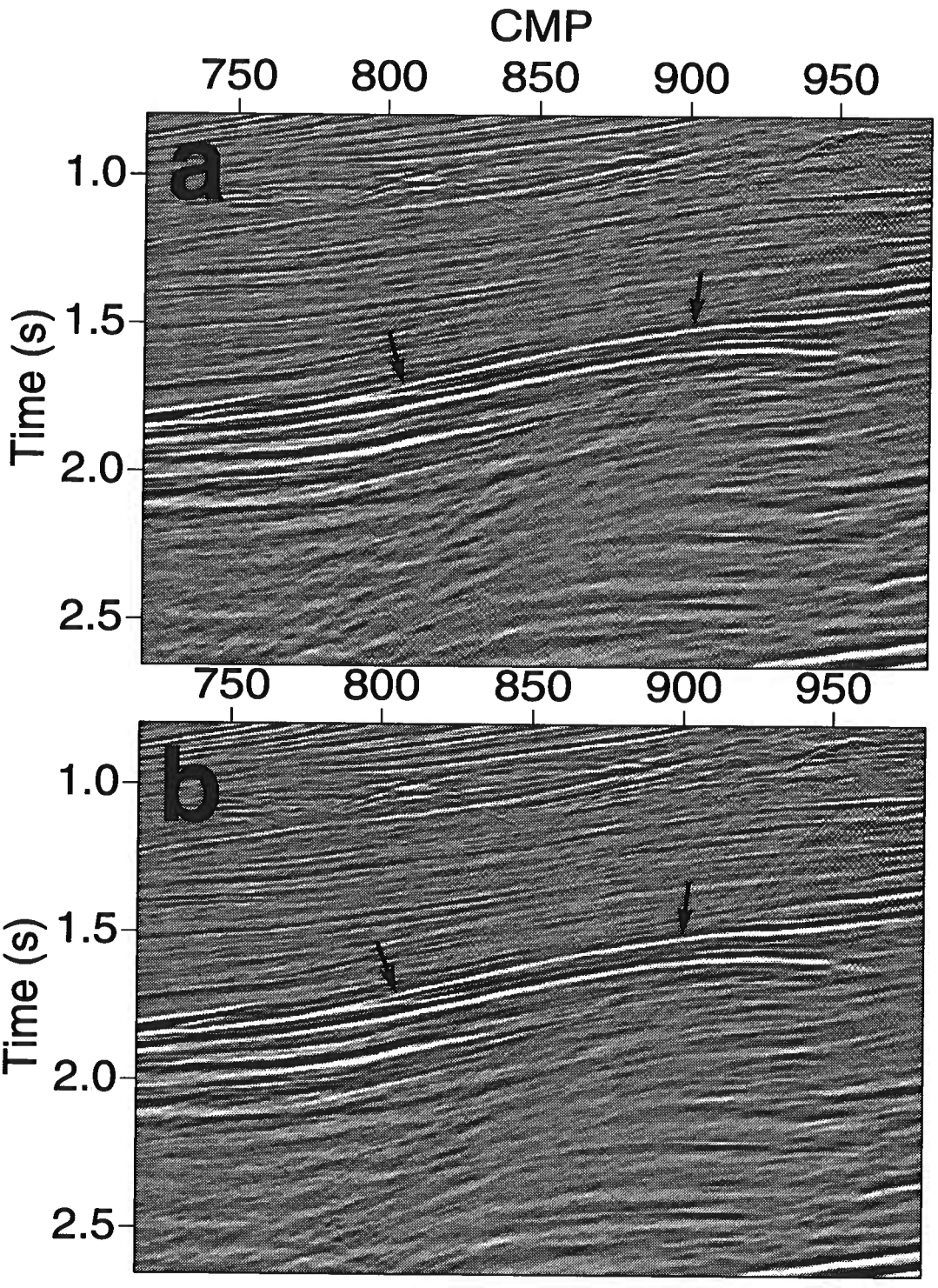

FIG. 6.4. Zero-offset section after (a) homogeneous isotropic DMO, and (b) $v(z)$ isotropic DMO. The NMO correction is the same as in Figure 6.3.

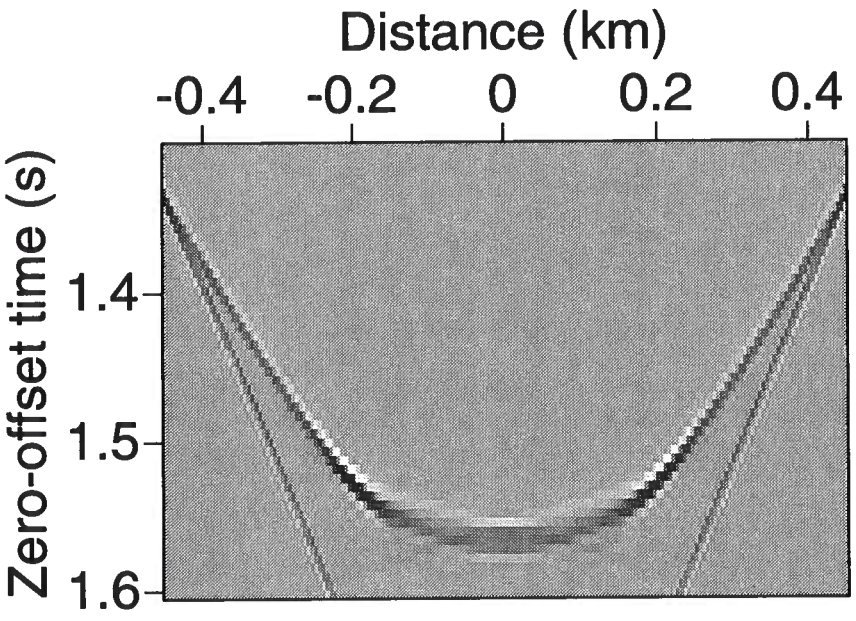

FIG. 6.5. VTI DMO impulse response for the parameters in Figure 6.2. The offset is 1.5 km.

Of the three approaches, only the $v(z)$ VTI DMO aligns the reflection just above 2 s for all offsets.

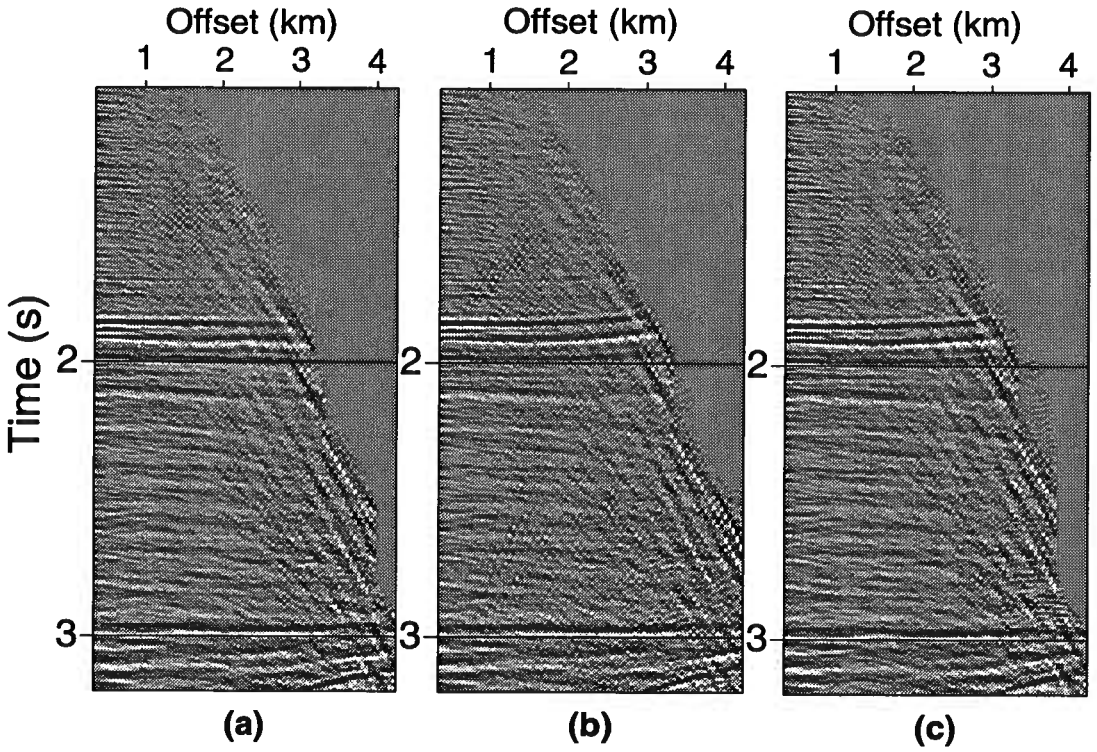

FIG. 6.6. CMP gathers for CMP location 700 after (a) $v(z)$ anisotropic DMO, (b) homogeneous isotropic DMO, and (c) $v(z)$ isotropic DMO. The NMO correction, based on the velocities obtained from velocity analysis, is the same for all three.

CMP location 700, in Figure 6.6, is to the left of the region of the imaged fault (see Figure 6.3). Figure 6.7 shows CMP location 845, which contains the imaged fault-plane reflection after (a) $v(z)$ VTI DMO, (b) homogeneous isotropic DMO, and (c) $v(z)$ isotropic DMO. The arrows point to the time of the fault reflection. Whereas the $v(z)$ VTI DMO aligns the weak fault clearly, the dipping event after isotropic DMO is misaligned.

Figure 6.8a shows a close-up of the fault imaged with phase-shift anisotropic time migration (using the inverted parameters of Figure 6.2) applied to the stack obtained from the $v(z)$ VTI DMO algorithm. For comparison, Figure 6.8b shows the result of conventional processing: phase-shift isotropic time migration applied to the zero-offset section obtained from the isotropic homogeneous DMO. Figure 6.8 gives a clear confirmation of the benefit of taking anisotropy into account in DMO prior to doing migration (the influence of anisotropy on the migration step is not large, here).

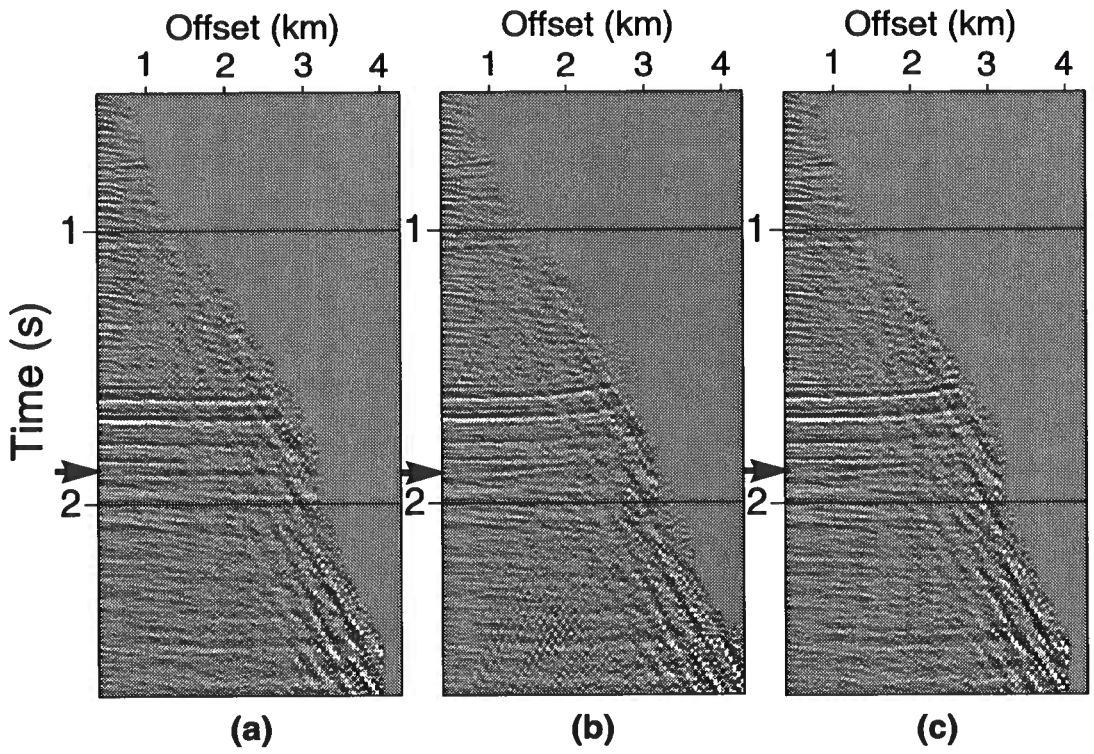

FIG. 6.7. CMP gathers for CMP location 845 after (a) $v(z)$ anisotropic DMO, (b) homogeneous isotropic DMO, and (c) $v(z)$ isotropic DMO. The NMO correction, based on the velocities obtained from velocity analysis, is the same for all three sections. The arrow points to the time of the dipping fault reflection.

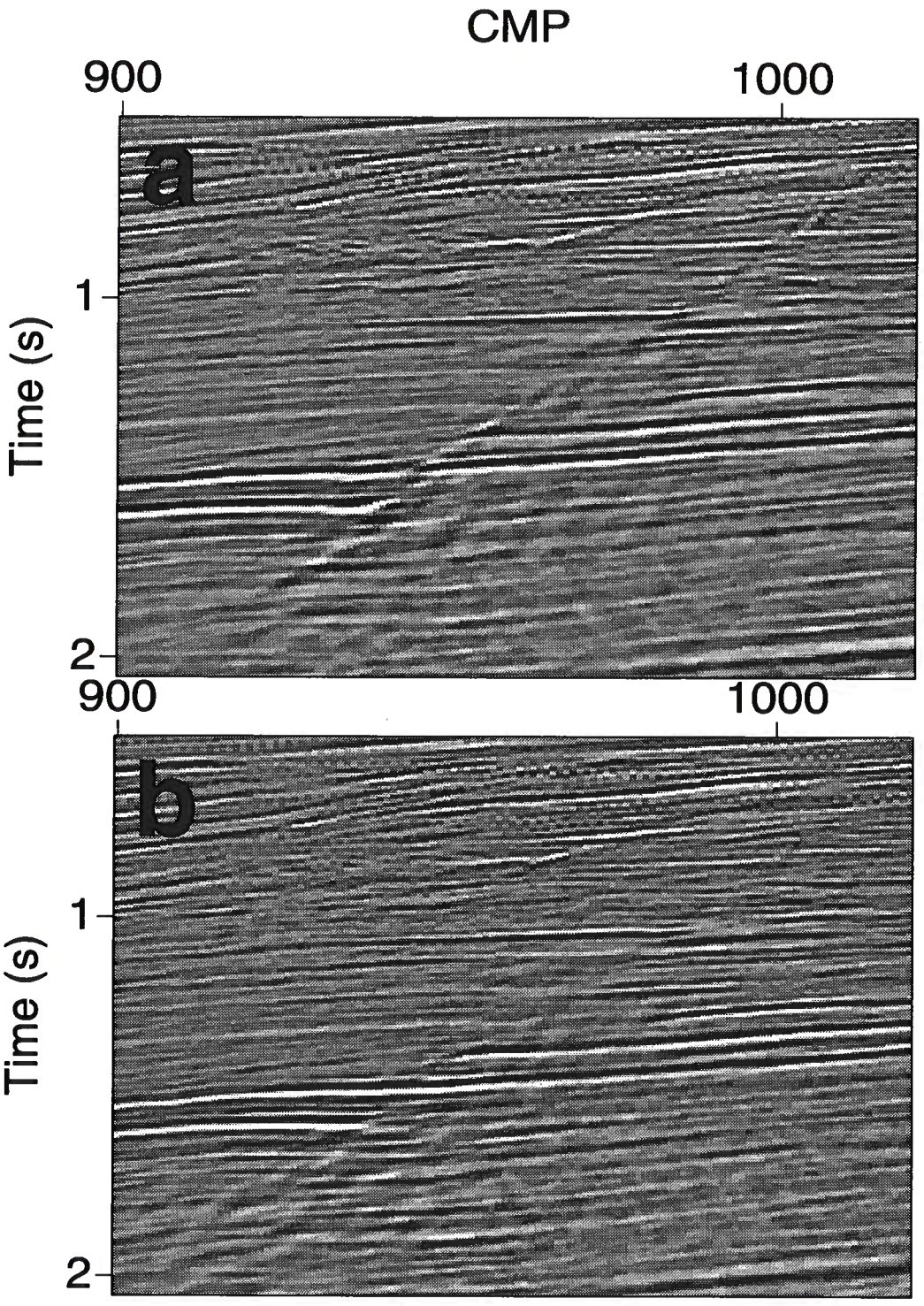

FIG. 6.8. Time migrated section using (a) anisotropic phase-shift migration of the data shown in Figure 6.3 using the parameters shown in Figure 6.2, and (b) isotropic phase-shift migration of the data shown in Figure 6.4a.

6.2 A more complex-structured region

Figure 6.9 shows a migrated section again from offshore Africa, provided by Chevron Overseas Petroleum, Inc., that contains reflections from a large number of dipping faults. This section is parallel to the one in Figure 6.1, but at deeper waters, and as a result the Tertiary shales (the source of the anisotropy) are thicker. The section was processed using a conventional 3-D processing sequence primarily without taking anisotropy into account. The one attempt to address the influence of anisotropy on the data was use of a stretched DMO (a DMO that is applied to data in which the offset is stretched with an empirically chosen stretching factor). A stretched DMO, however, gives only an approximation of the actual DMO signature in VTI media. Here, the upper layers are dominated by high-pressure shales that are believed to be the main source of anisotropy in the area. Chevron Overseas Petroleum, Inc., provided us with the data in hopes that we might improve on this section using an anisotropic processing sequence.

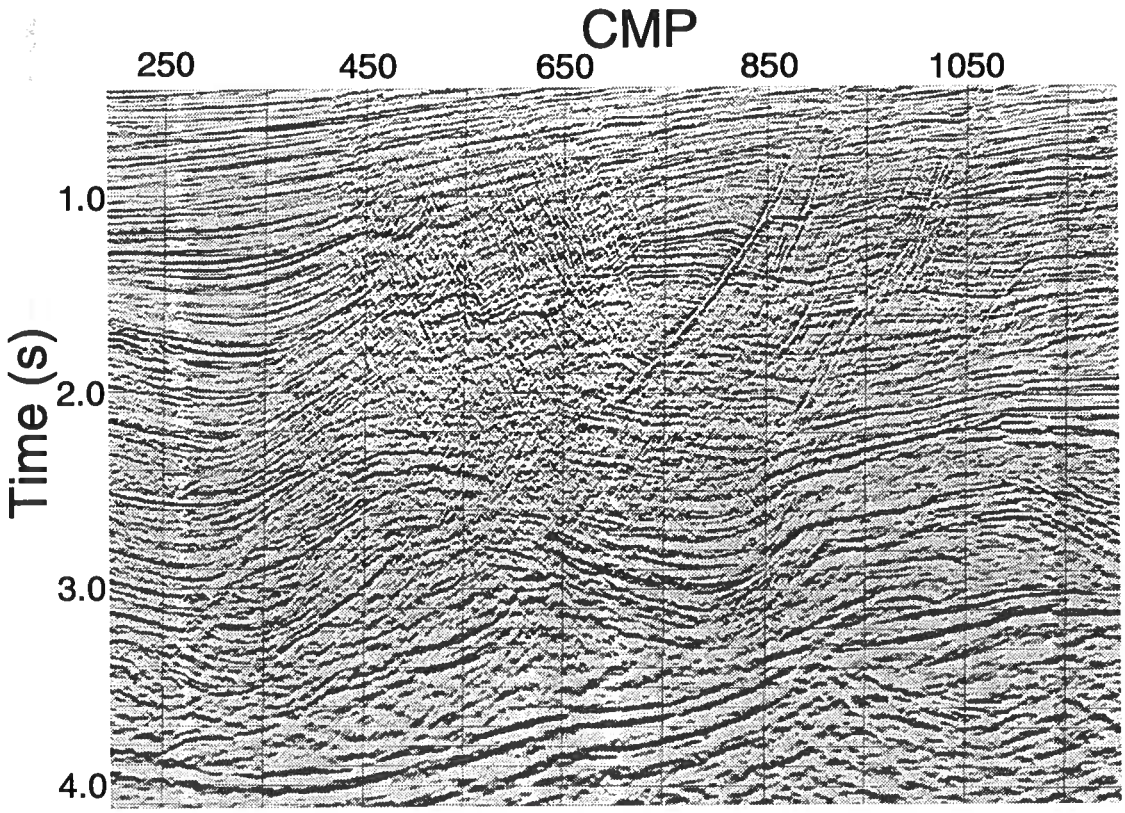

FIG. 6.9. Time-migrated section based on conventional 3-D processing.

Figure 6.10 shows a stacked seismic section of the same data. This section was processed using a sequence of conventional NMO and 2-D DMO without taking an-

isotropy into account, and no stretched DMO was used here. While some of the horizontal and mildly sloping reflections are imaged well, as we will see below, steep fault-plane reflections have been weakened because anisotropy was ignored. We should note that the predominant velocity variation in the section is vertical. In fact, in the area between CMP locations 400 and 800 and up to vertical time 3 s, the lateral variation in velocity is small ($< 5\%$).

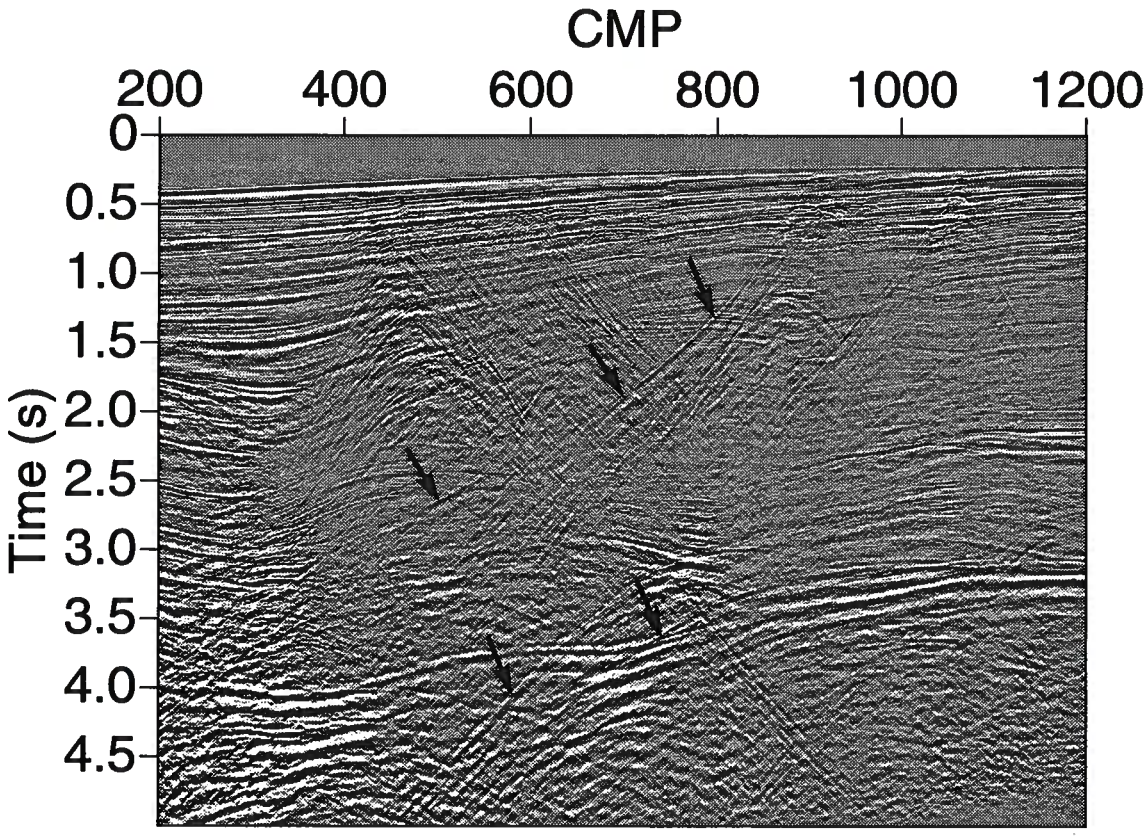

FIG. 6.10. Stacked section from offshore Africa, after applying NMO and isotropic homogeneous DMO. The arrows point to the sloping reflections used in the inversion for $\eta(\tau)$.

The arrows in Figure 6.10 point to the sloping reflections used to measure the stacking velocities for the inversion of $\eta(\tau)$. Likewise, $V_{\text{nmo}}(0)$ measurements are based on the moveout of sub-horizontal events. Although the sloping reflections used in the inversion seem to span the whole 5 s of data, the actual parameter information stops at about 3.5 s — the vertical (migrated) time corresponding to the deepest sloping reflection used in the measurement of stacking velocity. This difference follows from the relation between vertical time t_m and zero-offset time $t_0(p)$. A constant extrapolation of η was used for later migrated times. In addition to the picked reflections, η

at the surface is constrained to equal zero since these are marine data and the water layer is isotropic.

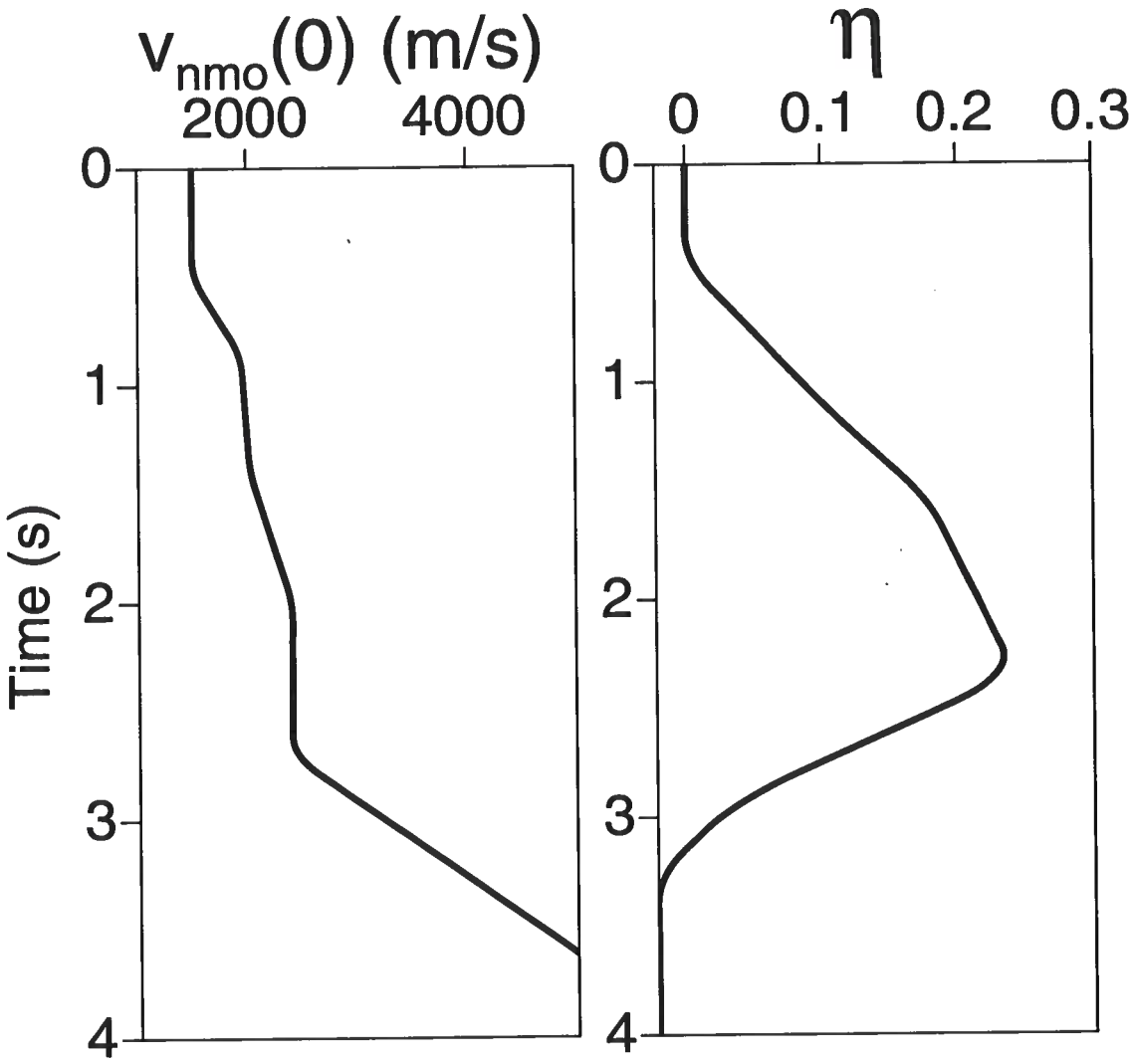

FIG. 6.11. Estimated interval values v_{nmo} and η as a function of vertical time.

Carrying out the inversion process described in Appendix C, using the measured values of stacking velocities and corresponding ray parameters, I obtain the functions $v_{\text{nmo}}(\tau)$ and $\eta(\tau)$ shown in Figure 6.11. As before, the inversion assumes no lateral velocity variation in the region of the picks. The smooth, continuous representation shown in Figure 6.11 is a direct result of fitting and smoothing a velocity model based on a piecewise linear η curve, as mentioned in Appendix C, for both the mildly dipping reflectors (for simplicity I refer to them as horizontal reflectors) and the faults. In the water layer, v_{nmo} is 1.5 km/s and η, as mentioned earlier, is zero. The accuracy of

the estimated curves of v_{nmo} and η depends on the accuracy of the stacking-velocity estimates for both dipping and horizontal reflectors. Based on the locations of the measured stacking velocities (Figure 6.10), as well as the extent of the lateral homogeneity, these inverted values can be considered representative of the area between CMP locations 450 and 950.

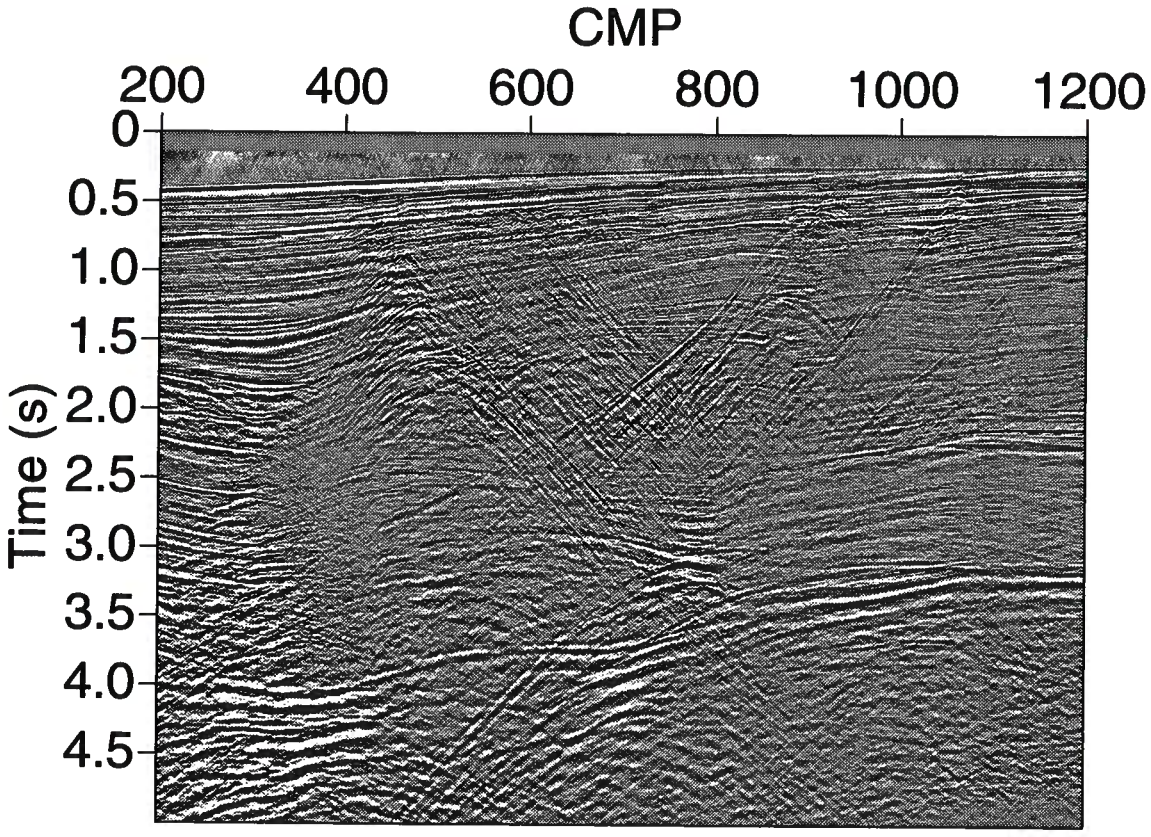

FIG. 6.12. Stacked section after $v(z)$ anisotropic DMO using the parameters in Figure 6.11. The NMO correction is based on the velocities obtained from the conventional velocity analysis. Compare with Figure 6.10.

The interval values of η in Figure 6.11 show an increase in the anisotropy with vertical time up to about 3 s. A smoothing operator was used to remove the sharp edges that arise at the measured stacking-velocity points. The η values after a time of 3.5 s were evaluated based on constant extrapolation because no η information was available at these times. The region above 3 s, which exhibits positive values of η, corresponds to a shale formation. Shale is often transversely isotropic (Banik, 1984) and appears to be the major source of anisotropy in the data.

Next, I apply a DMO algorithm that uses the derived functions $v_{\text{nmo}}(\tau)$ and $\eta(\tau)$ in Figure 6.11. Figure 6.12 shows the result of TI DMO applied to the data, based on the ray-tracing DMO algorithm described in Appendix C. One of the features of this

ray-tracing DMO is that it can correct for nonhyperbolic moveout associated with reflections from both horizontal or dipping events. Relative to the result of isotropic DMO given in Figure 6.10, this section is improved. Note, in particular, the reflections from the faults. The improvements extend throughout the whole section, including reflections not used in the inversion. This implies that the lateral variation in η, especially prior to 2 s, is relatively small.

Figure 6.13 shows representative VTI DMO operators used for these data. The shapes are far from the isotropic ellipse or even a stretched version of it. Therefore, we should expect the result of the anisotropic DMO to differ from that of the isotropic DMO or stretched DMO, and so it does.

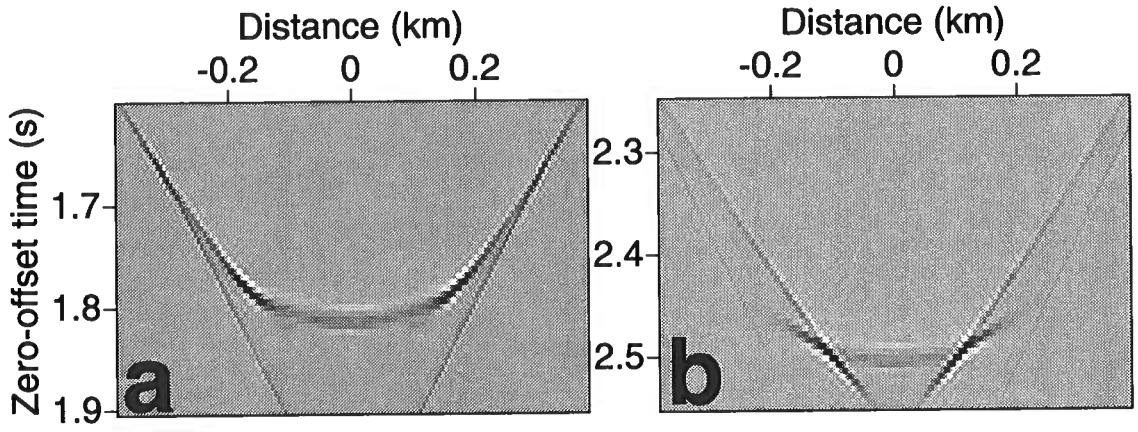

FIG. 6.13. VTI DMO impulse responses for the parameters in Figure 6.11. The offset is 1.5 km, and the apex is at (a) 1.8 s, and (b) 2.5 s.

Although most of the reflections here correspond to features within or near the vertical 2-D plane that contains the sources and receivers, some events may represent out-of-plane reflections that require 3-D processing. These out-of-plane reflections might be expected to stack better at a lower velocity (closer to the isotropic NMO velocity), and therefore focus better in the isotropic image. An example is the reflection at CMP location 825 between 3.5 and 4.0 s in Figure 6.10. Based on examination of parallel lines in the same area, this feature is found to be from out of the plane, but most reflections are confined to the dip plane of the section.

Figure 6.14 shows CMP gathers at CMP location 700 after (a) homogeneous isotropic DMO, and (b) $v(z)$ VTI DMO using the parameters in Figure 6.11. The same NMO correction, based on the stacking velocities obtained from conventional semblance velocity analysis, was used in both DMO examples. The arrows point to reflections from some of the dipping faults present in this highly faulted portion of the data. Note that the maximum offset is large (up to $X/D = 2$ for some of the times). Clearly, for the isotropic DMO result, the reflections from the dipping faults are not aligned. They have deviations caused by an NMO velocity that is smaller

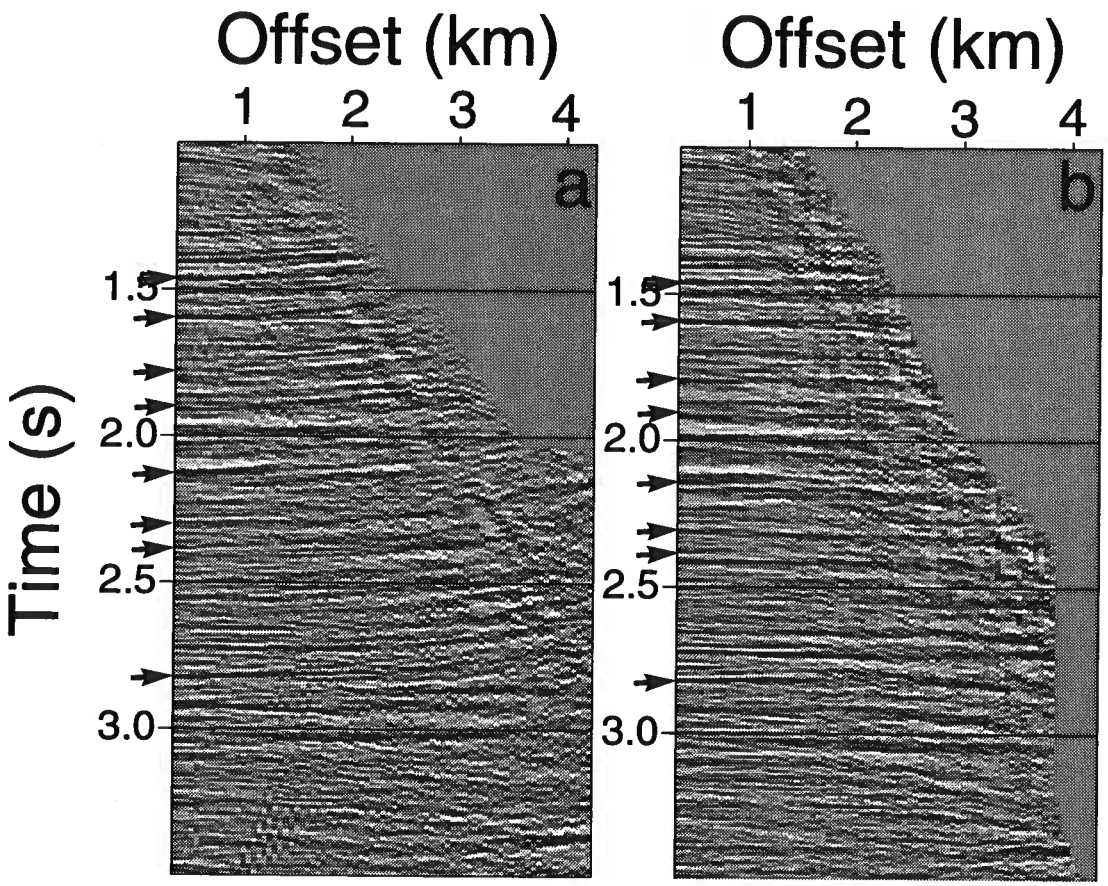

FIG. 6.14. CMP gathers for CMP location 700 after (a) homogeneous isotropic DMO, and (b) $v(z)$ anisotropic DMO. The NMO correction, based on the velocities obtained from velocity analysis, is the same for both examples. The arrows point to some of the reflections from the dipping interfaces present in this gather.

than what is needed for this anisotropic medium. Such deviations in the square of reflection traveltimes are proportional to X^2. Even the reflections from the horizontal events are not fully aligned. The misalignment for the horizontal reflections, however, is caused by the nonhyperbolic moveout associated with VTI media. The deviations for these horizontal events start at larger offsets, $X/D > 1$ (Tsvankin and Thomsen, 1994; Alkhalifah, 1996b), and are proportional to the quartic term X^4. This implies that the horizontal reflectors, as well as the dipping events, are less well focussed in Figure 6.10 than in Figure 6.12. Close comparison of these two figures reveals improvement in even the horizontal features as a result of anisotropic processing.

Figure 6.15a shows the result of conventional processing: phase-shift, isotropic time migration was applied to the zero-offset section obtained by the isotropic homogeneous DMO. For comparison, Figure 6.15b shows the data imaged with phase-shift anisotropic time migration (using the inverted parameters of Figure 6.11) applied to the stack obtained from the $v(z)$ VTI DMO algorithm. This comparison gives a clear picture of the benefit of taking anisotropy into account in DMO and migration. The improvements here are numerous and significant. One example is the fault located at CMP location 870, between 2.5 and 3 s. An interpreter using the isotropic processing result can easily extend the reflections across this fault ignoring it or suggest a minor subsidence to the left of the fault. However, the imaged result of the anisotropic processing (as well as the inverted values of η) suggests the extension of the shales down to 3 s under CMP location 800, and probably a larger subsidence has occurred. Another example is the region of the nearly horizontal events near CMP location 500, at 2.5 s. The improved continuity of the gently dipping events likely is a result of nonhyperbolic moveout correction in the anisotropic processing. Furthermore, anisotropic time migration placed the steep reflections close to their true time migrated position, while the isotropic migration generally mispositioned the sloping features relative to the horizontal ones.

Again, some events may represent out-of-plane reflections, requiring 3-D processing. Note their absence on the image obtained by anisotropic processing. An example is seen at CMP 600 and 2.5 s on Figure 6.15. Ignoring the three-dimensionality can cause mispositioning in some areas, especially where the fault reflections cross what seem to be continuous horizontal reflections. Most reflections here, however, are in or close to the dip plane of the section.

The 3-D section provided by Chevron Overseas Petroleum, Inc. (Figure 6.9, which was commercially processed) is only slightly better than the 2-D isotropic result shown in Figure 6.15b, even though a stretched DMO and 3-D processing were used. The time migration used to produce Figure 6.9 includes a small correction for lateral inhomogeneity but little consideration of anisotropy. Nevertheless, despite the presence of anisotropy, the fault reflections above 2 s in Figure 6.9 are accurately positioned. Perhaps, higher velocities than those derived from stacking velocity estimates were used in the time migration so as to help correct for anisotropy (Lynn et al., 1991). Larner and Cohen (1993) and Alkhalifah and Larner (1994) have shown that unless anisotropy is honored in the migration step, errors will arise in the final

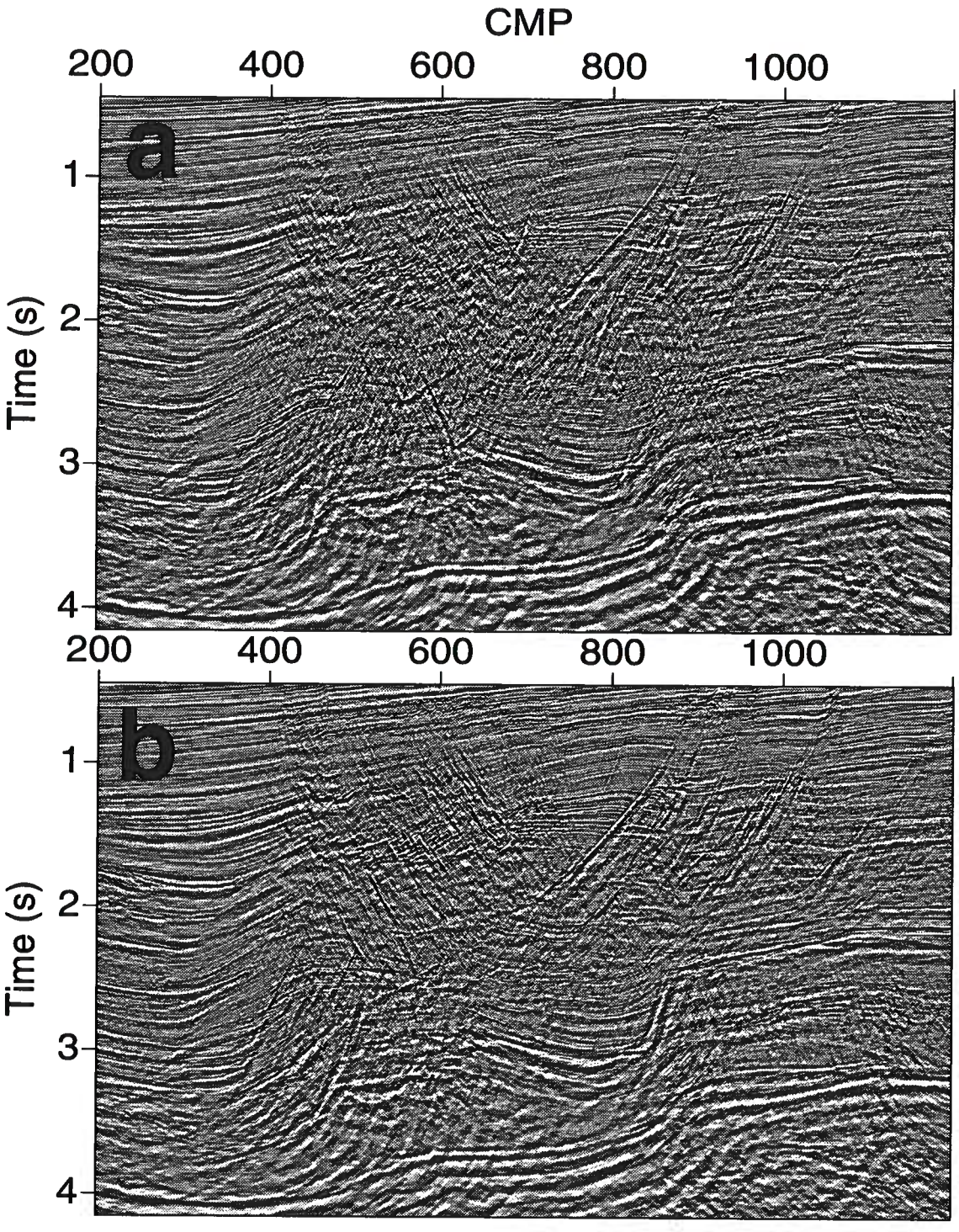

FIG. 6.15. Time migrated section using (a) isotropic phase-shift migration of the data shown in Figure 6.10, and (b) anisotropic phase-shift migration of the data shown in Figure 6.12 using the parameters shown in Figure 6.11.

image. Using higher velocities might work acceptably in a situation where we know the positions of the dipping reflectors in advance (i.e, most faults, as delineated by breaks in sedimentary bedding); however, in many cases positions of the reflectors are unknown. The possible use of higher velocities here, however, may explain what seems to be the overmigration of the bottom interface. Specifically, beneath CMP location 900, the imaged picture of this bottom reflection in Figure 6.9 seems overmigrated.

In contrast, the anisotropic processing result (Figure 6.15b) shows a significant overall improvement in the image compared with the section in Figure 6.9. Such improvements are similar to those observed earlier between the isotropic and anisotropic results shown in Figure 6.15, despite the use of stretched DMO in Figure 6.9. Again, the difference in the shape of the bottom interface between Figure 6.15b and Figure 6.9 can be attributed to the possible use of the too high velocity in Figure 6.9 in an attempt to compensate for the presence of anisotropy.

6.3 Field data from Trinidad

The subsurface at offshore Trinidad includes more sand and less shale than that of offshore Angola; therefore, the anisotropy influence is expected to be less dramatic than that observed in the Angola data. However, as we will see, the benefits of anisotropy processing, even in this less anisotropic region, remain significant.

Figure 6.16 shows a zero-offset section from offshore Trinidad that contains reflections from a large number of dipping faults. The data as well as stacking velocity information, were provided by Amoco (the Trinidad unit). I processed this section using a conventional 2-D isotropic processing sequence. The processing sequence included a conventional NMO, using the stacking velocities that Amoco provided, followed by a log-stretch (Notfors and Godfrey, 1987) version of Hale's (1984) DMO. Here, we have a mixture of sand-dominated and shale-dominated layers, so anisotropy is expected to vary with depth. As before, the shales are believed to be the main source of anisotropy in this region.

Carrying out the inversion process described in Appendix C, using the measured values of stacking velocities and corresponding ray parameters, I obtain the functions $v_{\text{nmo}}(\tau)$ and $\eta(\tau)$ shown in Figure 6.17. The inversion assumes no lateral velocity variation in the region of the picks; the lateral velocity variation in this region, especially the first 2 s, is exceptionally small. In the water layer, v_{nmo} is 1.5 km/s and η is zero. Again, the accuracy of these estimated curves of v_{nmo} and η depends on the accuracy of the stacking-velocity estimates for both dipping and horizontal reflectors, as discussed in Chapter 3.

The smoothed interval values of η in Figure 6.17 show increases and decreases that might depend on the shale-sand alterations. The litholigical interpretation of the η curve is outside of the scope of this thesis. Nevertheless, this η curve best fits the measured stacking velocities, and thus is expected to improve the image. The η values after a time of 4.5 s were evaluated based on constant extrapolation because no η information was available at these times.

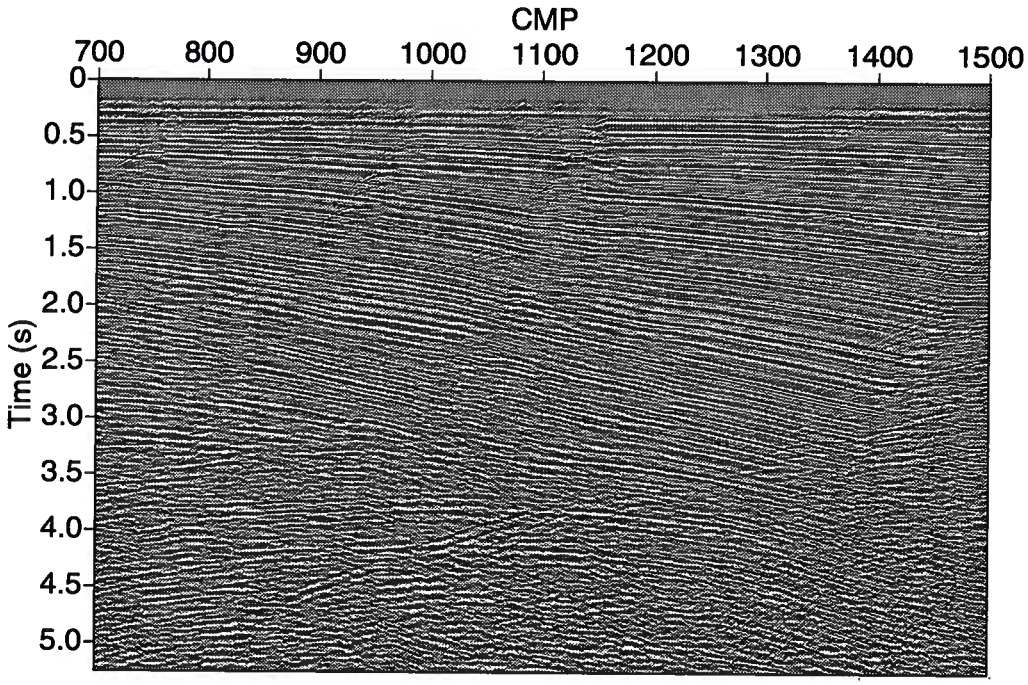

FIG. 6.16. Stacked section from offshore Trinidad, after applying NMO and isotropic homogeneous DMO. The NMO correction is based on the velocities provided by Amoco.

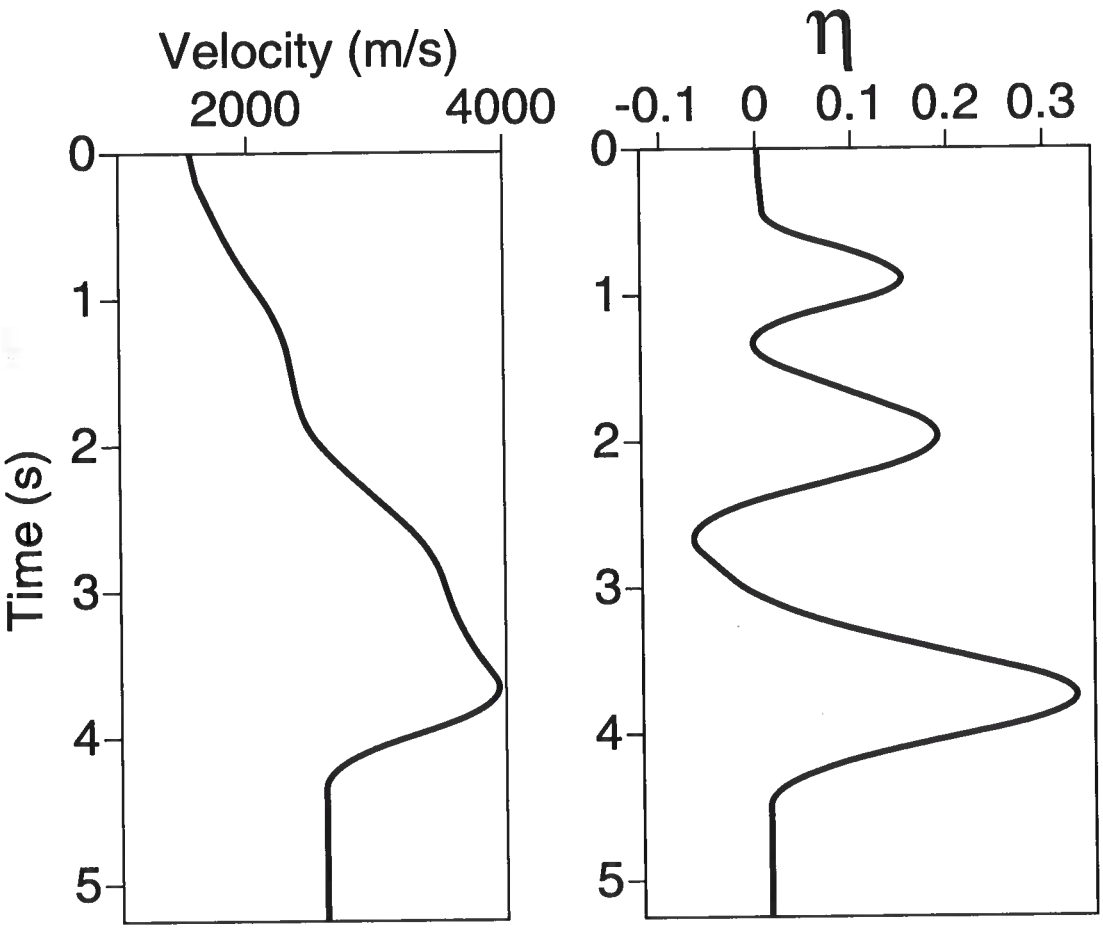

FIG. 6.17. Estimated interval values v_{nmo} and η as a function of vertical time.

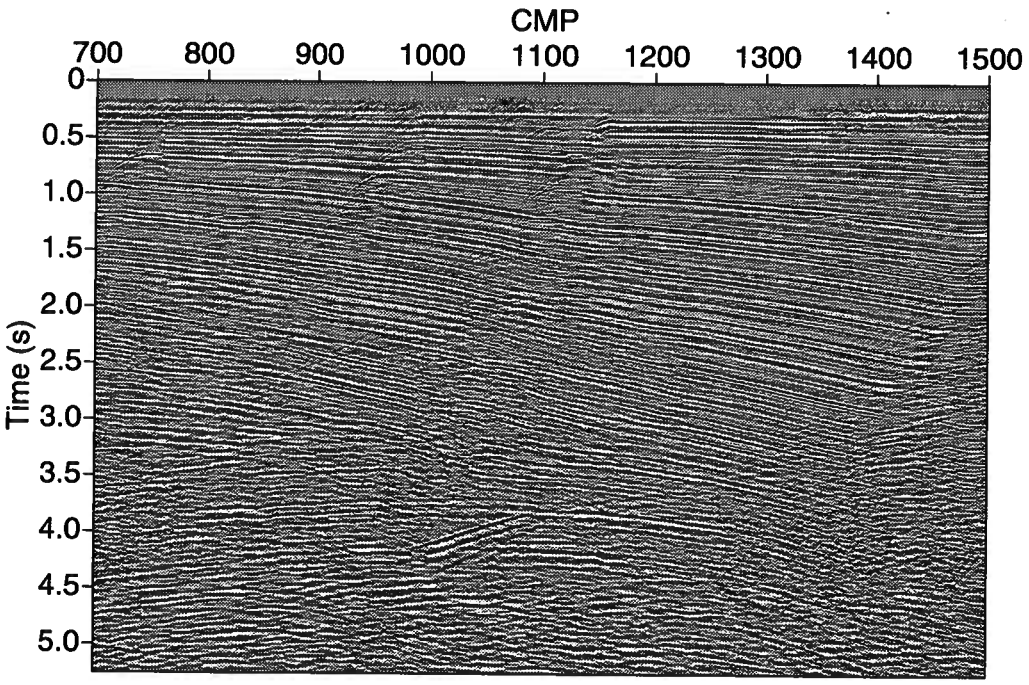

FIG. 6.18. Stacked section after $v(z)$ anisotropic DMO using the parameters in Figure 6.17. The NMO correction is based on the velocities obtained from the conventional velocity analysis using exceptionally short spreads.

Next, I apply a DMO algorithm that uses the derived functions $v_{\text{nmo}}(\tau)$ and $\eta(\tau)$ in Figure 6.17. Figure 6.18 shows the result of TI DMO applied to the data, based on the ray-tracing DMO algorithm described in Chapter 4. Relative to the result of isotropic DMO given in Figure 6.16, this section should be improved. A close-up look at Figures 6.16 and 6.18 (shown in Figures 6.19 and 6.20) shows such improvements. In Figure 6.19 note the vast improvement in focussing both the dipping fault and the subhorizontal reflections in the anisotropic DMO result (Figure 6.19a), as opposed to the isotropic one (Figure 6.19b). Such improvements in focussing are also observed at deeper times (i.e., Figure 6.20).

Figure 6.21 shows CMP gathers from CMP location 936, which contains the imaged fault-plane reflection shown in Figure 6.19a after (a) homogeneous isotropic DMO, and (b) $v(z)$ VTI DMO. The arrows point to the time of the fault reflection at this CMP location. Whereas the $v(z)$ VTI DMO aligns the fault reflection well, the dipping event after isotropic DMO is misaligned. Improvements are also achieved for subhorizontal events where DMO managed to correct for the nonhyperbolic moveout that is often largest for small dips.

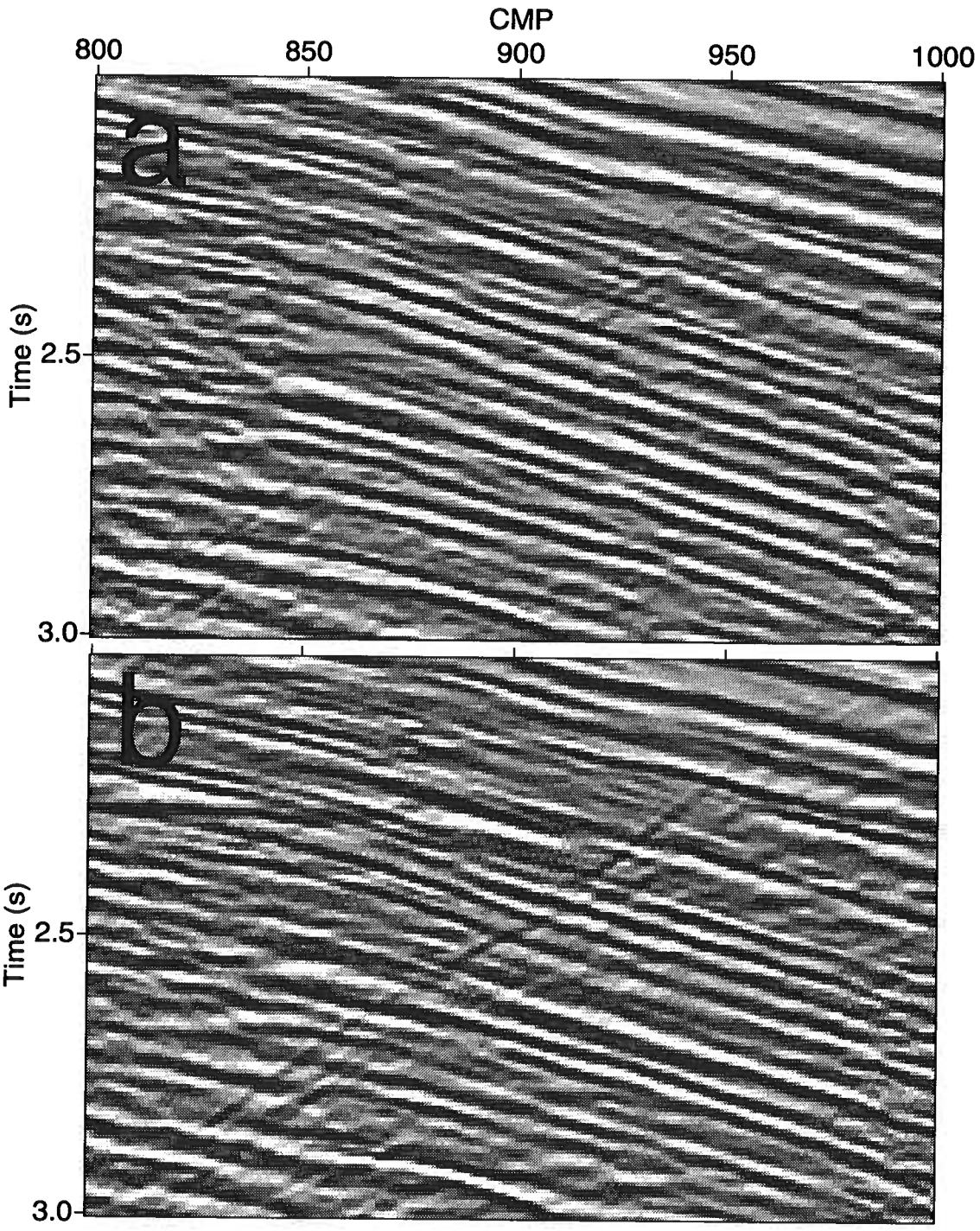

FIG. 6.19. (a) Detail of Figure 6.16, and (b) detail of Figure 6.18 in the same region.

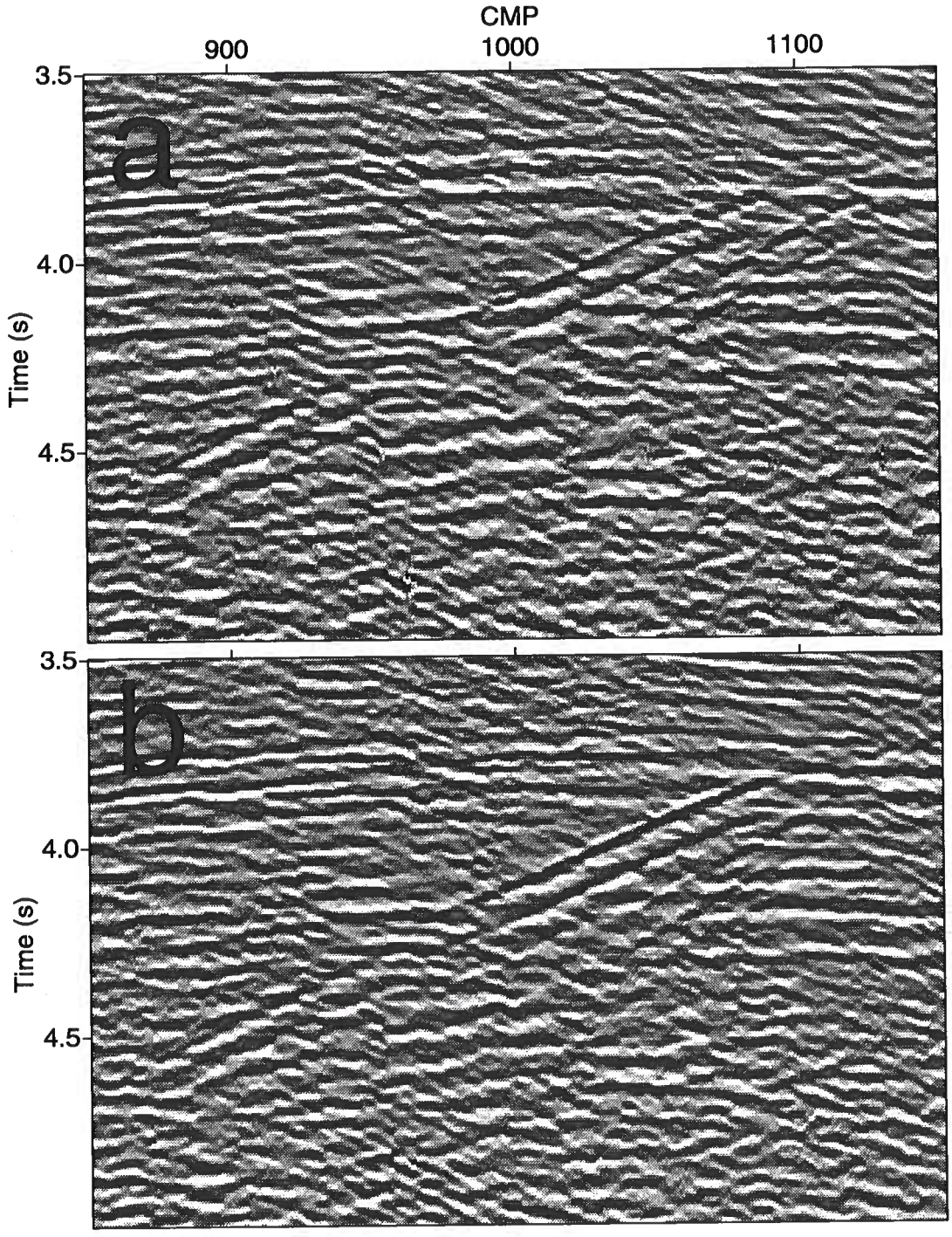

FIG. 6.20. (a) Detail of Figure 6.16, and (b) detail of Figure 6.18 in the same region.

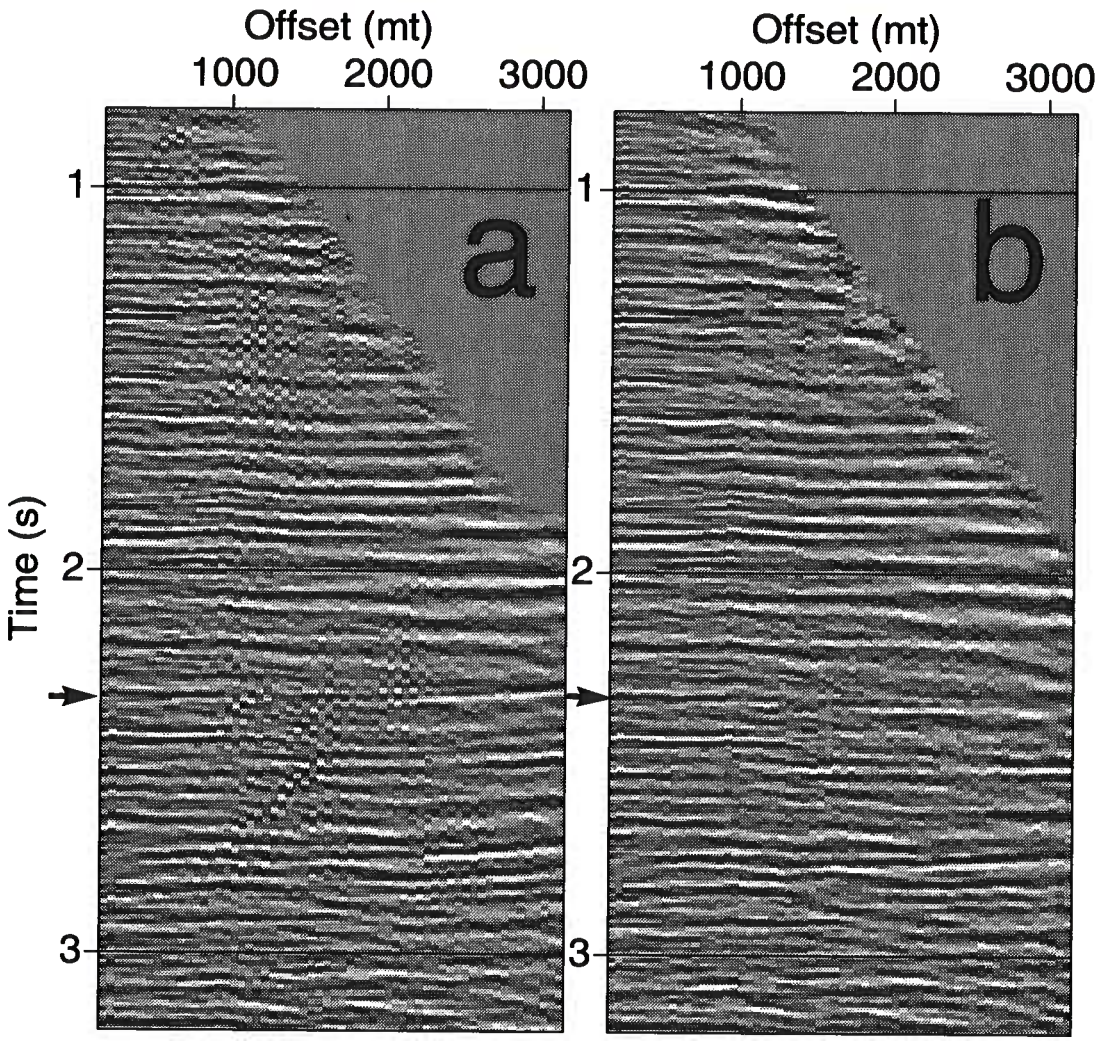

FIG. 6.21. CMP gathers for CMP location 936 after (a) homogeneous isotropic DMO, and (b) $v(z)$ anisotropic DMO using the parameters estimated in Figure 6.17. The NMO correction for the isotropic DMO result is based on velocities provided to us by Amoco, while the NMO correction for the anisotropic DMO is based on the velocities obtained from velocity analysis using short spreads. The arrow points to the time of the dipping fault reflection.

Chapter 7

CONCLUSION

I have suggested and tested on synthetic and field data a method of velocity analysis for transversely isotropic media based on the inversion of the dip-dependence of P-wave normal moveout velocities. The algorithm, operating with surface P-wave data only, requires that NMO velocities and ray parameters be measured for two different dips; more than two dips provide redundancy that can be used to increase the accuracy of the inversion.

Although this inversion cannot resolve the vertical velocity and anisotropic coefficients individually, it makes it possible to obtain a family of models that have the same moveout velocity for a horizontal reflector $V_{\rm nmo}(0)$ and the same effective anisotropic parameter $\eta = (\epsilon - \delta)/(1 + 2\delta)$. I have shown that these two parameters are sufficient to obtain NMO velocity as a function of ray parameter, describe long-spread (non-hyperbolic) reflection moveout for a horizontal reflector, and calculate poststack and prestack time-migration impulse responses. This means that the inversion of P-wave NMO velocities provides enough information to perform all major time-processing steps including dip moveout, prestack and poststack time migration.

To extend the inversion method to vertically inhomogeneous media, the inversion must be applied using an NMO equation for layered anisotropic media above a dipping reflector. The influence of a stratified isotropic or anisotropic overburden on moveout velocity can be stripped through a Dix-type differentiation procedure.

Using sloping reflections to extract velocity information in $v(z)$ media requires, among other things, positioning the reflections at their true (migrated) locations. This is accomplished by relating the zero-offset time to the vertical (migrated) time, and therefore positioning the extracted interval velocities at their true times (relative depths). Although this concept is beneficial for isotropic media, it is particularly important in anisotropic media, where such velocities are compared with those extracted from horizontal events and then used to invert for anisotropy information, specifically η. This inversion process is based on the rms (i.e., small-offset) assumption of stacking velocities for a given ray parameter. Such a relation, for horizontal reflectors, reduces to the familiar Dix (1955) expression. The idea underlying the inversion is that the $v_{\rm nmo}(\tau)$ and $\eta(\tau)$ functions obtained from the inversion are those that best focus reflections from the dipping interface and sub-horizontal reflectors at the same stacking (or NMO) velocity, for each vertical time at which a velocity measurement is made.

Analysis of dip moveout and time-migration impulse responses shows that, in vertically inhomogeneous VTI media, these processes depend solely on two parameters $v_{\rm nmo}(0)$ and η. Therefore, the results of the inversion [values of $v_{\rm nmo}(0)$ and η] can

be used to apply NMO, DMO, and time migration. To an extent, time migration can be used to evaluate the performance of the inversion in data that include reflectors with known positions (i.e., fault traces as delineated by terminations of sedimentary bedding). Specifically, the plausibility of results of the inversion for η can be checked by inspecting the quality of images generated by poststack migration using the same inverted parameters. If the image indicates undermigration, for example, the true η overall is higher than the estimated function.

Time-to-depth conversion, as well as depth migration, however, requires an accurate value of the vertical velocity, which cannot be found from P-wave NMO velocities alone. Clearly, the vertical velocity can be estimated directly if check shots or well logs are available.

Accurate transformation of prestack data to zero-offset, where the subsurface is transversely isotropic, must fully honor the anisotropy. Specifically, TZO based on anisotropic ray tracing can accurately treat data from TI media, with no dip or offset limitations. While the usual NMO and DMO sequence based on hyperbolic moveout correction ignores the sizable nonhyperbolic moveout associated with horizontal events in VTI media, the scheme presented here provides a method for computing traveltimes and using that information to apply accurate TZO for arbitrary depth-variable anisotropy parameters.

Similar to isotropic DMO operators, the impulse response in VTI media is practically velocity-independent; the shape of the response depends mainly on η. For $\eta = 0$ (isotropic or elliptically anisotropic media), the impulse response is an ellipse, but as η varies, the response takes on shapes that can differ substantially from that for elliptical media. For example, impulse responses in *homogeneous* VTI media with typical values of anisotropy ($\eta > 0$) can include triplications that arise for reflector dip of 30 degrees. The presence of the triplications exemplifies the large differences between DMO impulse responses for VTI media and those for isotropic media. Moreover, the complex shape of the impulse response in VTI media leads to an amplitude distribution along the DMO operator that differs significantly from that in isotropic media. With such large differences, we can expect isotropic DMO to be inadequate for typical VTI media. For example, stretching of the isotropic DMO impulse response clearly will fail to emulate the VTI DMO response for dips beyond about 30 degrees, where the triplications begin.

The impulse responses in VTI media typically deviate more from the isotropic operator than do those attributable solely to vertical inhomogeneity. For example, $v(z)$ isotropic DMO impulse responses can be well approximated by squeezed ellipses up to and beyond 90 degrees reflector dips (Hale and Artley, 1994). Thus, the influence of typical anisotropy (i.e., $\eta \simeq 0.1$) on DMO exceeds that of typical vertical inhomogeneity (i.e., average velocity gradient a=0.6).

In the field examples, isotropic DMO did not properly focus dipping reflectors. On the other hand, $v(z)$ VTI DMO based on the inverted values of $v_{\text{nmo}}(\tau)$ and $\eta(\tau)$ (which indicated that the medium is anisotropic) did focus such reflectors, and, because the method also takes nonhyperbolic moveout into account, it improved the focussing

of horizontal reflections as well. In addition, the 2-D anisotropic time migration based on the same two inverted parameters placed the steep in-plane reflections at their true time migrated position. In contrast, the isotropic migration, which used only the values of $v_{\text{nmo}}(\tau)$, mispositioned the sloping features relative to the horizontal ones.

The cost of anisotropic processing is close to that of its isotropic counterpart. In fact, the processing algorithms needed for both types of media run in about the same time. For example, although slower than the typical log-stretched DMO techniques, the DMO algorithm used here is as efficient as the isotropic $v(z)$ DMO of Artley and Hale's (1994). Moreover, the difference in computation effort for the isotropic and anisotropic algorithms in phase-shift time migration is negligible. The true additional cost of the anisotropic processing arises from the time needed to measure stacking velocities, as well as ray parameters, for the sloping reflections. Once the measurements are obtained, inverting for the parameters is not computationally intensive.

Applying an anisotropic parameter-estimation procedure, therefore, is appropriate for all data, whether the subsurface is anisotropic or not. If the medium is isotropic, then the lack of anisotropy will be reflected in small estimated values for the inverted parameter η. However, if η departs from zero by a relatively substantial amount (i.e., $\eta > 0.05$), then it is best to take anisotropy into account. Typical performance of isotropic DMO in practice suggests the presence of anisotropy in data. In particular, the fact that isotropic homogeneous DMO often works better than does isotropic $v(z)$ DMO in a vertically inhomogeneous medium suggests the presence of anisotropy because anisotropy typically reduces or overrides the influence of an increase in velocity with depth. Nevertheless, the fact that isotropic constant-velocity DMO often works better than does $v(z)$ DMO does not imply that the result is optimum. The DMO process can further benefit from the added degree of freedom embodied in the parameter η, which can be calculated from surface P-wave measurements and has a physical rather than *ad hoc* basis, specifically anisotropy. Because it has this physical basis, this same parameter provides the added degree of freedom needed for migration and correction for nonhyperbolic moveout as well, as well for DMO.

Extensions of algorithms described in this thesis to 3-dimensional data is an ongoing project in the Center for Wave Phenomena. Theoretically, 3-D processing applications require a simple addition of another axis to the formulation of most of the equations described here. Practically, it requires tackling problems dealing with irregular acquisition geometries, lower-order anisotropic symmetries, as well as computational issues. Some of these issues have been studied extensively for isotropic media and results of these studies should be applicable to anisotropic media. Future research should also include anisotropic prestack migration implementation and inversion so we can better handle complex structures in anisotropic media. Prestack depth migration, however, will require the full complement of Thomsen parameters, which will result in a more challenging inversion procedure. My intuition is that a lot of a-priori information will be required before such a problem can be solved.

REFERENCES

Aki, K., and Richards, P.G., 1980, Quantitative seismology: theory and methods, Volume I, W.H. Freeman and Company, San Francisco.

Alkhalifah, T., 1995a, Efficient synthetic-seismogram generation in transversely isotropic, inhomogeneous media: Geophysics, **60**, 1139-1150.

Alkhalifah, T., 1995b, Gaussian beam depth migration for anisotropic media: Geophysics, **60**, 1474-1484.

Alkhalifah, T., 1996a, Transformation to zero offset in transversely isotropic media: Geophysics, **61**, 947-963.

Alkhalifah, T., 1996b, Velocity analysis using nonhyperbolic moveout in transversely isotropic media: Center for Wave Phenomena, Colorado School of Mines (CWP-167).

Alkhalifah, T., and Larner, K., 1994, Migration errors in transversely isotropic media: Geophysics, **59**, 1405-1418.

Alkhalifah, T., and Tsvankin, I., 1995, Velocity analysis for transversely isotropic media: Geophysics, **60**, 1550-1566.

Anderson, J., and Tsvankin, I., 1995, Dip-moveout processing by Fourier transform in anisotropic media: Center for Wave Phenomena, Colorado School of Mines (CWP-146).

Anderson, J., Alkhalifah, T., and Tsvankin, I., 1995, Fowler DMO and Time Migration for Transversely Isotropic Media: Geophysics, in press.

Artley, C. T., 1992, Dip moveout processing for depth-variable velocity: M.S. thesis, Colorado School of Mines; also published as Center for Wave Phenomena report **CWP-115**.

Artley, C. T., and Hale, D., 1994, Dip moveout processing for depth-variable velocity: Geophysics, **59**, 610–622.

Ball, G., 1995, Estimation of anisotropy and anisotropic 3-D prestack migration, offshore Zaire: Geophysics, **60**, 1495-1513.

Banik, N. C., 1984, Velocity anisotropy of shales and depth estimation in the North Sea basin: Geophysics, **49**, 1411–1419.

Berryman, J.G., 1979, Long-wave elastic anisotropy in transversly isotropic media: Geophysics, **44**, 846-917.

Byun, B. S., and Corrigan, D., 1990, Seismic traveltime inversion for transverse isotropy: Geophysics, **55**, 192-200.

Červený, V., 1972, Seismic rays and ray intensities in inhomogeneous anisotropic media: Geophys. J. R. Astr. Soc., **29**, 1–13.

Červený, V., 1981, Computation of geometrical spreading by dynamic ray tracing: Stanford Exploration Project, **28**, 49–59.

Červený, V., and Pšenčík, I., 1984, Gaussian beams in elastic 2-D laterally varying layered structures: Geophys. J. R. Astr. Soc., **78**, 65–91.

Crampin, S., 1985, Evidence for aligned cracks in the earth's crust: First Break, **60**, no. 3, 12-15.

Crampin, S., 1986, Anisotropy and transverse isotropy, Geophysical Prospecting, **34**, 94-99.

Dale, C.T., Lopes, J.R., and Abilio, S., 1992, Takula Oil Field and the Greater Takula Area, Cabinda, Angola, in Halbouty, M.T., Ed., Giant oil and gas fields of the decade: 1978-1988: Am. Assoc. Petr. Geol., 197-215.

Deregowski, S.M., 1986, What is DMO?: First Break, **4**, 6-24.

Desegaulx, P., Piazz, J., Esteve, J., and Jeannot, J., 1994, Uncertanties in depth imaging: A multitechnique approach on real data, 64th Ann. Internat. Mtg., Soc. Expl. Geophys., Expanded Abstracts, 695-698.

Dix, C. H., 1955, Seismic velocities from surface measurements: Geophysics, **20**, 68-86.

Dong, Z., and McMechan, G.A., 1993, 3-D prestack migration in anisotropic media: Geophysics, **58**, 79-90.

Fei, T., and Larner, K., 1995, Elimination of numerical dispersion in finite-difference modeling and migration by flux corrected transport: Geophysics, **60**, 1830-1842.

Forel, D., and Gardner, G.H.F., 1988, A three-dimensional perspective on two-dimensional dip moveout: Geophysics, **53**, 604-610.

Fowler, P., 1984, Velocity-independent imaging of seismic reflectors: 54th SEG Annual Meeting, Expanded Abstracts.

Gazdag, J., 1978, Wave equation migration with the phase-shift method: Geophysics, **43**, 1342–1351.

Gonzalez, A., Lynn, W., and Robinson, W., 1991, Prestack frequency-wavenumber (f-k) migration in a transversely isotropic medium: Presented at the 61st Ann. Internat. Mtg. Soc. Expl. Geophys., Expanded Abstracts, 1155–1157.

Gonzalez, A., Levin., F. K., Chambers, R. E., and Mobley, E., 1992, Method of correcting 3-D DMO for the effects of wave propagation in an inhomogeneous earth, 62nd Ann. Internat. Mtg., Soc. Expl. Geophys., Expanded Abstracts, 966–969.

Hake, H., Helbig, K., and Mesdag, C. S., 1984, Three-term Taylor series for $t^2 - x^2$ curves over layered transversely isotropic ground: Geophys. Prosp., **32**, 828-850.

Hale, D., 1984, Dip-moveout by Fourier transform: Geophysics, **49**, 741-757.

Hale, D., 1992, Migration by the Kirchhoff, slant stack, and Gaussian beam methods: Center of Wave Phenomena (CWP), Report **121**, Colorado School of Mines.

Hale, D., and Witte, D., 1992, Migration: Progress and predictions: Presented at the 62nd Ann. Internat. Mtg. Soc. Expl. Geophys., Expanded Abstracts, 610–612.

Hale, D., and Artley, C., 1993, Squeezing dip moveout for depth-variable velocity: Geophysics, **58**, 257-264.

Hale, D., Hill, N.R., and Stefani, J., 1992, Imaging salt with turning seismic waves: Geophysics, **57**, 1453-1462.

Hanyga, A., 1986, Gaussian beams in anisotropic elastic media: Geophys. J. R. Astr. Soc., **85**, 473–563.

Helbig, K., 1983, Elliptical anisotropy–its significance and meaning: Geophysics, **48**, 825-832.

Hill, N. R., 1990, Gaussian beam migration: Geophysics, **55**, 1416–1428.

Hudson, J.A., 1981, Wave speeds and attenuation of elastic waves in material containing cracks: Geophys. J. R. Astr. Soc.,**64**, 133-150.

Jakubowicz, H., 1990, A simple efficient method of dip-moveout correction: Geophys. Prosp., **38**, 221–245.

Jech, J., and Pšenčík, I., 1989, First-order perturbation method for anisotropic media: Geophys. J. R. Astr. Soc., **99**, 367–376.

Kerbs, J. R., and Fora, D. R., 1995, Accurate migration using offset-checkshot surveys, 65th Ann. Internat. Mtg., Soc. Expl. Geophys., Expanded Abstracts, 1186-1188.

Kitchenside, P. W., 1991, Phase shift-based migration for transverse isotropy, 61st Ann. Internat. Mtg., Soc. Expl. Geophys., Expanded Abstracts, 993-996.

Krey, T., and Helbig, K., 1956, A theorem concerning anisotropy of stratified media and its significance for reflection seismic: Geophysical Prospecting, **4**, 294-302.

Larner, K., 1993, Dip-moveout error in transversely isotropic media with linear velocity variation in depth: Geophysics, **58**, 1442-1453.

Larner, K. and Cohen, J., 1993, Migration error in factorized transversely isotropic media with linear velocity variation with depth: Geophysics, **58**, 1454–1467.

Levin, F.K., 1971, Apparent velocity from dipping interface reflections: Geophysics, **36**, 510-516.

Lynn, W., Gonzalez, A., and MacKay, S., 1991, Where are the fault-plane reflections?, 61st Ann. Internat. Mtg., Soc. Expl. Geophys., Expanded Abstracts, 1151–1154.

McHargue, T. R., 1990, Stratigraphic Development of Proto-South Atlantic Rifting in Cabinda, Angola - A Petroliferous Lake Basin: AAPG Memoir, **50**, 307-326.

Meadows, M., and Abriel, W., 1994, 3-D poststack phase-shift migration in transversely isotropic media, 64th Ann. Internat. Mtg., Soc. Expl. Geophys., Expanded Abstracts, 1205-1208.

Notfors, C.D., and Godfrey, R.J., 1987, Dip moveout in the frequency-wavenumber domain: Geophysics, **52**, 1718-1721.

Phadke, S., Kapotas, S., Dai, N., and Kanasewich, E.R., 1994, Migration of P-wave reflection data in transversely isotropic media: Geophysics, **59**, 658-667.

Postma, G.W., 1955, Wave propagation in a stratified medium, Geophysics, **20**, No. 4, 780-806.

Press, W.H., Teukolsky, S.A. Vetterling, W.T., and Flannery, B.P., 1992, Numerical recipes in C, the art of scientific computing, 2nd Edition, Cambridge University Press, New York.

Roldan, K.K., Gonzales, A., Ebrom, D.A., 1994, Effect of transverse isotropy on dip-moveout processing: 64th SEG Annual Meeting, Expanded Abstracts, 1221-1223.

Sayers, C.M., 1994, The elastic anisotropy of shales: J. Geophys. Res., **99**, No. B1, 767-774.

Sena, A. G., 1991, Seismic traveltime equations for azimuthally anisotropic and isotropic media: Estimation of internal elastic properties: Geophysics, **56**, 2090–2101.

Sena, A. G., and Toksoz, M.N., 1993, Kirchhoff migration and velocity analysis for converted and nonconverted waves in anisotropic media: Geophysics, **58**, 265–276.

Shah, P.M., 1973, Use of wavefront curvature to relate seismic data with subsurface parameters: Geophysics, **38**, 812–825.

Shearer, P. M. and Chapman, C. H., 1988, Ray tracing in anisotropic media with linear velocity gradient: Geophys. J. Int., **94**, 575–580.

Stolt, R.H., 1978, Migration by Fourier tranform: Geophysics, **43**, 23-48.

Thomsen, L., 1986, Weak elastic anisotropy: Geophysics, **51**, 1954–1966.

Tsvankin, I., 1995, Normal moveout from dipping reflectors in anisotropic media: Geophysics, **60**, 268-284.

Tsvankin, I., and Thomsen, L., 1994, Nonhyperbolic reflection moveout in anisotropic media: Geophysics, **59**, 1290-1304.

Tsvankin, I., and Thomsen, L., 1995, Inversion of reflection traveltimes for transverse isotropy: Geophysics, **60**, 1095-1107.

Uren, N.F., Gardner, G.H.F., and McDonald, J.A., 1990a, Dip moveout in anisotropic media: Geophysics, **55**, 863-867.

Uren, N.F., Gardner, G.H.F., and McDonald, J.A., 1990b, The migrator's equation for anisotropic media: Geophysics, **55**, 1429-1434.

Uren, N.F., Gardner, G.H.F., and McDonald, J.A., 1990c, Normal moveout in anisotropic media: Geophysics, **55**, 1634-1636.

Uzcategui, O., 1995, 2-D depth migration in transversely isotropic media using explicit operators: Geophysics, **60**, 1819-1829.

Uzcategui, O. J., and Mujica, D. L., 1995, Anisotropic poststack depth migration, eastern Venezuela, 65th Ann. Internat. Mtg., Soc. Expl. Geophys., Expanded Abstracts, 1171-1174.

VerWest, B.J., 1989, Seismic migration in elliptically anisotropic media: Geophys. Prosp., **37**, 149-166.

Whitmore, N. D., Felinski, W. F., Gray, S. H., and Murphy, G. E., 1995, Common offset and common angle prestack depth migration applied to north sea data, 65th Ann. Internat. Mtg., Soc. Expl. Geophys., Expanded Abstracts, 884-887.

Winterstein, D. F., 1986, Anisotropy effects in *P*-wave and *S*-wave stacking velocity contain information on lithology: Geophysics, **51**, 661-672.

Winterstein, D.F., 1990, Velocity anisotropy terminology for geophysicists: Geophysics, **20**, 780-806.

Xu, S., and White, R.E., 1995, A new velocity model for clay-sand mixtures: Geophysics, **43**, 91-118.

Appendix A

DEPENDENCE OF NMO VELOCITY ON THE RAY PARAMETER

For the purposes of the inversion procedure, we need to recast the NMO velocity as a function of the ray parameter $p(\phi)$ (horizontal slowness) corresponding to the zero-offset reflection. The vertical (m) and horizontal (p) slownesses for P-waves in transversely isotropic media with a vertical symmetry axis (VTI) satisfy the following equation (e.g., Larner, 1993)

$$1 = 0.5\{(a_{11}+a_{44})p^2+(a_{33}+a_{44})m^2+\{[(a_{11}-a_{44})p^2-(a_{33}-a_{44})m^2]^2+4(a_{13}+a_{44})^2p^2m^2\}^{\frac{1}{2}}\},$$

where the a_{ij} are density-normalized elastic constants.

This equation can be solved for m, given a known value of the ray parameter p. If both slowness components are obtained, the phase velocity is simply

$$V(p) = \frac{1}{\sqrt{p^2 + m^2(p)}},$$

and the phase (dip) angle ϕ is given by

$$\phi = \sin^{-1}[V(p)p].$$

After the angle ϕ has been found, we can compute the derivatives of phase velocity needed in equation (2.1) and then obtain the P-wave NMO velocity as a function of ray parameter. The dependence $V_{\rm nmo}(p)$ can also be built parametrically by calculating $V_{\rm nmo}$ and p as functions of the dip ϕ.

Since phase velocity is a complicated function of the phase angle (or ray parameter) and anisotropic coefficients, it is hardly feasible to find a simple form for $V_{\rm nmo}(p)$ in general VTI media. Therefore, we consider the special cases of elliptical and weak anisotropy.

The normal-moveout velocity in elliptically anisotropic media ($\epsilon = \delta$) can be represented as (Tsvankin, 1995a)

$$V_{\rm nmo}(\phi) = \frac{V_{\rm nmo}(0)}{\cos\phi}\,\frac{V_P(\phi)}{V_{P0}} = \frac{V_{\rm nmo}(0)}{pV_{P0}}\,\tan\phi\,. \qquad \text{(A.1)}$$

Now we have to obtain the angle ϕ as a function of the ray parameter. The P-wave phase velocity for elliptical anisotropy, expressed through $\epsilon = \delta$, is given by (Tsvankin, 1995b)

$$V_P(\theta) = V_{P0}\sqrt{1 + 2\delta \sin^2\theta}\,, \tag{A.2}$$

where θ is the phase angle measured from the symmetry axis. Then

$$p(\phi) = \frac{\sin\phi}{V_{P0}\sqrt{1 + 2\delta \sin^2\phi}}\,. \tag{A.3}$$

Solving equation (A.3) for the dip ϕ yields

$$\sin\phi = \frac{pV_{P0}}{\sqrt{1 - 2\delta\, p^2 V_{P0}^2}}\,. \tag{A.4}$$

Calculating $\tan\phi$ from equation (A.4) and taking into account that $V_{\rm nmo}(0) = V_{P0}\sqrt{1 + 2\delta}$, we get from equation (A.1)

$$V_{\rm nmo}(p) = \frac{V_{\rm nmo}(0)}{\sqrt{1 - p^2 V_{\rm nmo}^2(0)}}\,. \tag{A.5}$$

Therefore, for elliptical anisotropy (which includes isotropy as a special case), P-wave NMO velocity is a function of the ray parameter and zero-dip moveout velocity, with no separate dependence on the coefficient δ.

Now we carry out a similar derivation for general transverse isotropy ($\epsilon \neq \delta$) using the weak-anisotropy approximation ($\epsilon \ll 1$, $\delta \ll 1$). The weak-anisotropy expression for NMO velocity as a function of the dip ϕ was derived by Tsvankin (1995a).

$$V_{\rm nmo}(\phi) = \frac{V_P(\phi)}{\cos\phi}\left[1 + \delta + 2(\epsilon - \delta)\sin^2\phi(1 + 2\cos^2\phi)\right]. \tag{A.6}$$

To find the dependence of normal moveout velocity on p, we have to obtain the angle ϕ as a function of the ray parameter. The P-wave phase velocity, linearized in the parameters ϵ and δ, is given by Thomsen (1986).

$$V_P(\theta) = V_{P0}\left(1 + \delta \sin^2\theta\cos^2\theta + \epsilon \sin^4\theta\right). \tag{A.7}$$

The ray parameter [equation (2.2)] then becomes

$$p = \frac{\sin\phi}{V_{P0}\left(1 + \delta \sin^2\phi\cos^2\phi + \epsilon \sin^4\phi\right)}\,. \tag{A.8}$$

After some algebra, formula (A.8) can be transformed into a quadratic equation for $\sin^2\phi$ with the solution (in the weak-anisotropy approximation)

$$\sin^2\phi = \frac{p^2 V_{P0}^2}{1 - 2\delta\, p^2 V_{P0}^2}[1 + 2(\epsilon - \delta)\, p^4 V_{P0}^4]\,. \tag{A.9}$$

Substitution of the angle ϕ from equation (A.9) into (A.6) and further linearization in ϵ and δ leads to the following expression for the NMO velocity:

$$V^2_{\rm nmo}(p) = \frac{V^2_{\rm nmo}(0)}{1 - p^2 V^2_{\rm nmo}(0)} \left[1 + 2\left(\epsilon - \delta\right) f(pV_{\rm nmo}(0))\right], \tag{A.10}$$

$$f \equiv \frac{y\left(4y^2 - 9y + 6\right)}{1 - y}; \;\; y \equiv p^2\, V^2_{\rm nmo}(0)\,.$$

In the derivation of equation (A.10), we have replaced the vertical velocity V_{P0} in the anisotropic terms with $V_{\rm nmo}(0)$ since the difference between V_{P0} and $V_{\rm nmo}(0)$ will change only the terms quadratic in the anisotropy parameters.

Appendix B

NMO EQUATION FOR A LAYERED MEDIUM WITH A DIPPING REFLECTOR

Here we generalize the NMO equation given by Tsvankin (1995a) for layered anisotropic media with a dipping reflector. We consider a layered anisotropic model consisting of a stack of horizontal homogeneous layers above a dipping reflector (Figure B.1). It is assumed that the CMP line is perpendicular to the strike of the reflector, and the incidence (sagittal) plane coincides with a plane of symmetry in all layers.

Under these assumptions, the kinematics of wave propagation is two-dimensional, i.e., phase and group velocity vectors do not deviate from the incidence plane. The same assumption was made by Tsvankin (1995a) in the derivation of the one-layer NMO equation.

Since the medium above the reflector is laterally homogeneous, the ray parameter p (horizontal slowness) of any given ray remains constant between the reflector and the surface. In this case, it is convenient to express the short-spread moveout velocity $V_{\rm nmo}$ in CMP geometry as follows (Hale et al., 1992; Tsvankin, 1995a):

$$V_{\rm nmo}^2(p_0) = \lim_{x\to 0} \frac{d(x^2)}{d(t^2)} = \frac{2}{t_0} \lim_{h\to 0} \frac{dh}{dp}, \tag{B.1}$$

where $h = x/2$ is half the source-receiver offset ($h > 0$ in the down-dip direction), p_0 is the ray parameter of the zero-offset ray ($x = 0$), and t_0 is the two-way zero-offset traveltime. Note that the zero-offset ray is not necessarily perpendicular to the reflector in the presence of anisotropy; it is the phase-velocity vector corresponding to the zero-offset ray that should be normal to the reflector.

Neglecting the displacement of the reflection point on short spreads, in equation (B.1) (Tsvankin, 1995a) we can represent h as

$$h = \left(\sum_{i=1}^{n} x^{(i)} - x_0 \right),$$

where $x^{(i)}$ is the lateral displacement of the ray in layer i, and x_0 is the total lateral displacement of the zero-offset ray, between the CMP (CRP) location and the reflection point (Figure B.1). Equation (B.1) now becomes

$$V_{\rm nmo}^2(p_0) = \frac{1}{t_0} \lim_{p\to p_0} \sum_{i=1}^{n} \frac{d(2x^{(i)})}{dp}. \tag{B.2}$$

Each component of the sum in equation (B.2) represents the squared NMO ve-

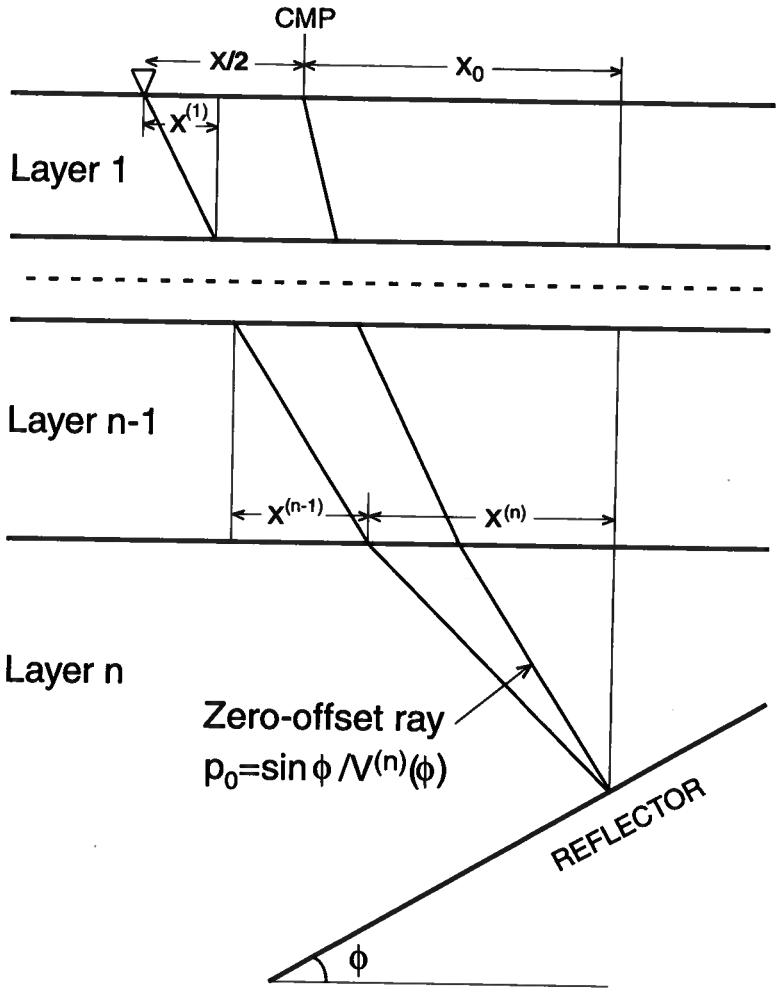
CMP
X/2
X_0
$X^{(1)}$
Layer 1
Layer n-1
$X^{(n-1)}$
$X^{(n)}$
Layer n
Zero-offset ray
$p_0=\sin\phi\,/V^{(n)}(\phi)$
REFLECTOR
ϕ

FIG. B.1.

locity in an individual layer multiplied by the corresponding zero-offset time (see equation (B.1); $x^{(i)} = h^{(i)}$). That is,

$$\lim_{p \to p_0} \frac{d(2x^{(i)})}{dp} = t_0^{(i)} \left[V_{\text{nmo}}^{(i)}(p_0)\right]^2 , \tag{B.3}$$

where $t_0^{(i)}$ is the two-way traveltime along the zero-offset ray in layer i.

Tsvankin (1995a) expressed $V_{\text{nmo}}^{(i)}$ analytically through the phase angle $\phi^{(i)} = \sin^{-1}[p_0\, V^{(i)}(p_0)]$ corresponding to the zero-offset ray, where $V^{(i)}$ is the phase velocity in layer i. In Appendix A and the main text we show how this NMO equation can be rewritten as a function of the ray parameter p_0.

Substituting formula (B.3) into the equation for the NMO velocity (B.2) yields

$$V_{\text{nmo}}^2(p_0) = \frac{1}{t_0} \sum_{i=1}^{n} t_0^{(i)} \left[V_{\text{nmo}}^{(i)}(p_0)\right]^2 . \tag{B.4}$$

Equation (B.4) includes the traveltime t_0 along the ray with the ray-parameter value p_0. Below, we derive an equation for $t_0(p)$ valid for isotropy or elliptical anisotropy. For both models, the moveout is purely hyperbolic, and

$$t_0^2(p) = t_0^2(0) + \frac{x^2}{V_{\text{nmo}}^2(0)} . \tag{B.5}$$

The offset x in equation (B.5) can be represented as $x = t_0 V_0 \tan\psi$ (V_0 is the vertical velocity, ψ is the group angle corresponding to the ray-parameter value p). Next, we express ψ through the phase angle θ using general relations for transverse isotropy (Thomsen, 1986) and equations (A.2) and (2.5):

$$\tan\psi = \tan\theta \frac{V_{\text{nmo}}^2(0)}{V_0^2} .$$

Equation (B.5) then becomes

$$t_0^2(p) = t_0^2(0) \left(1 + \tan^2\theta \frac{V_{\text{nmo}}^2(0)}{V_0^2}\right) . \tag{B.6}$$

Using the relation between the phase angle and ray parameter for elliptical anisotropy [equation (A.4)] and equation (A.5), we find

$$t_0(p) = t_0(0) \sqrt{1 + p^2\, V_{\text{nmo}}^2(p)} . \tag{B.7}$$

Appendix C

VELOCITY ANALYSIS IN LAYERED MEDIA

The first step of the inversion process involves estimating stacking velocities as a function of zero-offset traveltime from P-wave reflection data. These velocities are commonly considered a good approximation to the NMO velocity. Measuring stacking velocities is common practice in isotropic processing, but here we must estimate such stacking velocities for sloping, as well as horizontal, reflections. In addition, we must measure the ray parameters (reflection slopes in the zero-offset domain) corresponding to these reflections.

The inversion method can be applied using any number of dips through a least-squares approach. For simplicity, I constrain the description here to the model given in Figure C.1, where we have features with only two distinct dips (horizontal reflectors and a dipping fault). The medium is considered to be laterally homogeneous above the fault. Note that, because it is dipping, this single fault provides velocity information at several zero-offset times that can be used to extract vertical parameter variations with depth.

After obtaining stacking-velocity information as a function of ray parameter and zero-offset time, we need to construct an interval-velocity model that satisfies the measured stacking velocities based on equation (3.2). For horizontal reflectors ($p = 0$), construction of such a velocity model is straightforward, following the familiar method of Dix (1955). However, for the dipping fault, such an interval-velocity model depends on η, as well as the ray parameter, and what complicates things is that the ray parameter along the fault reflection varies with recording time due to the variation of velocity with depth. Therefore, the measured stacking velocities for the dipping fault at different vertical times correspond to different ray parameters.

Suppose we want to fit an interval-velocity model $v_{\text{nmo}}(p_{i+1}, \tau)$ between the measured stacking velocities $V_{\text{nmo}}[p_i, t_i(p_i)]$ and $V_{\text{nmo}}[p_{i+1}, t_{i+1}(p_{i+1})]$, where p_i and t_i are the ray parameter and zero-offset time, respectively, of the fault reflection used in measuring the stacking velocities. This interval-velocity model, as mentioned in the text, is based on a linear variation in η between the times associated with the measured stacking velocities. Such an η is also taken to be continuous at the measured stacking velocities times. The linearity and continuity conditions will assure us a unique *eta* curve satisfying the measured stacking velocities. Here, $t_i(0)$ is the two-way vertical traveltime for the reflection recorded at time $t_i(p_i)$, as shown in Figure C.1. Therefore, the initial η for the linear model between $V_{\text{nmo}}[p_i, t_i(p_i)]$ and $V_{\text{nmo}}[p_{i+1}, t_{i+1}(p_{i+1})]$ is $\eta[t_i(0)]$ calculated at vertical time $t_i(0)$. The interval η values in between the two

measured stacking velocities are then given by

$$\eta(\tau) = \eta[t_i(0)] + a_{i+1}[\tau - t_i(0)]\,, \tag{C.1}$$

where a_{i+1} is the constant gradient in η between vertical time $t_i(0)$ and $t_{i+1}(0)$, and τ is the vertical time that ranges between varies between $t_i(0)$ and $t_{i+1}(0)$. What we really know, however, is $t(p_{i+1})$, the zero-offset time corresponding to the measured stacking velocity $V_{\rm nmo}[p_{i+1}, t_{i+1}(p_{i+1})]$. Therefore, using the relation

$$t(p_{i+1}, \tau) = \int_0^{\tau} f[\eta(\tau_1), v_{\rm nmo}(\tau_1), p_{i+1}]d\tau_1, \tag{C.2}$$

where f, as mentioned in the text, is the operator that relates zero-offset time to vertical time, we increase τ until $t(p_{i+1}, \tau)$ reaches $t(p_{i+1})$, which takes place when $\tau = t_{i+1}(0)$.

For $i = 0$ (corresponding to the earth's surface), $t_0(p) = 0$, and the interval η values are estimated either by considering the medium to be homogeneous up to time $t_1(0)$ ($a_1 = 0$), or by using a value for η at the surface that satisfies a certain condition (i.e., for marine data, η at the surface is usually set to 0). Therefore, the only unknowns in equation (C.1) as we progress from the top to the bottom of the seismic section are the η gradients a_i.

Using the expressions for stacking velocities and traveltimes given above, equation (3.2) can be written as follows

$$V^2_{\rm nmo}[p_{i+1}, t_{i+1}(p_{i+1})]t_{i+1}(p_{i+1}) = \int_0^{t_i(p_{i+1})} v^2_{\rm nmo}(p_{i+1}, \tau)d\tau + \int_{t_i(p_{i+1})}^{t_{i+1}(p_{i+1})} v^2_{\rm nmo}(p_{i+1}, \tau)d\tau. \tag{C.3}$$

The first term on the right hand side can be calculated from the estimated values of η and $v_{\rm nmo}(0)$ prior to $t_i(0)$ [corresponding to $t_i(p_{i+1})$]. Let us assume that it equals f_1. If we are trying to determine a_1 corresponding to the region between the surface and the first measurement, then f_1 equals zero because $t_0(p_{i+1})$=0. Therefore, the only unknown in this first layer is a_1, and as we progress from top to bottom of the section the only unknowns we need to obtain are the a_i. In equation (C.3), $v_{\rm nmo}(p_{i+1}, \tau)$ is a function of the intantenous $V_{\rm nmo}(0)$ and η values at vertical time τ. This expression for a single τ is the same as the one for homogeneous media, given by Alkhalifah and Tsvankin (1995).

Substituting equation (C.1) into the second term of equation (C.3) results in a nonlinear equation in a_{i+1}. To solve equation (C.3) for a_{i+1}, I use the secant method with an initial $a_{i+1} = 0$. Fortunately, for such an initial value the problem is stable and the convergence is fast.

Each time a new η gradient is obtained, for example a_{i+1}, it is directly used to compute the interval η using equation (C.1) in the region between $t_i(0)$ and $t_{i+1}(0)$. Then, these interval η, along with the horizontal interval NMO velocities, are used to obtain interval NMO velocities in the same region corresponding to the ray parameter

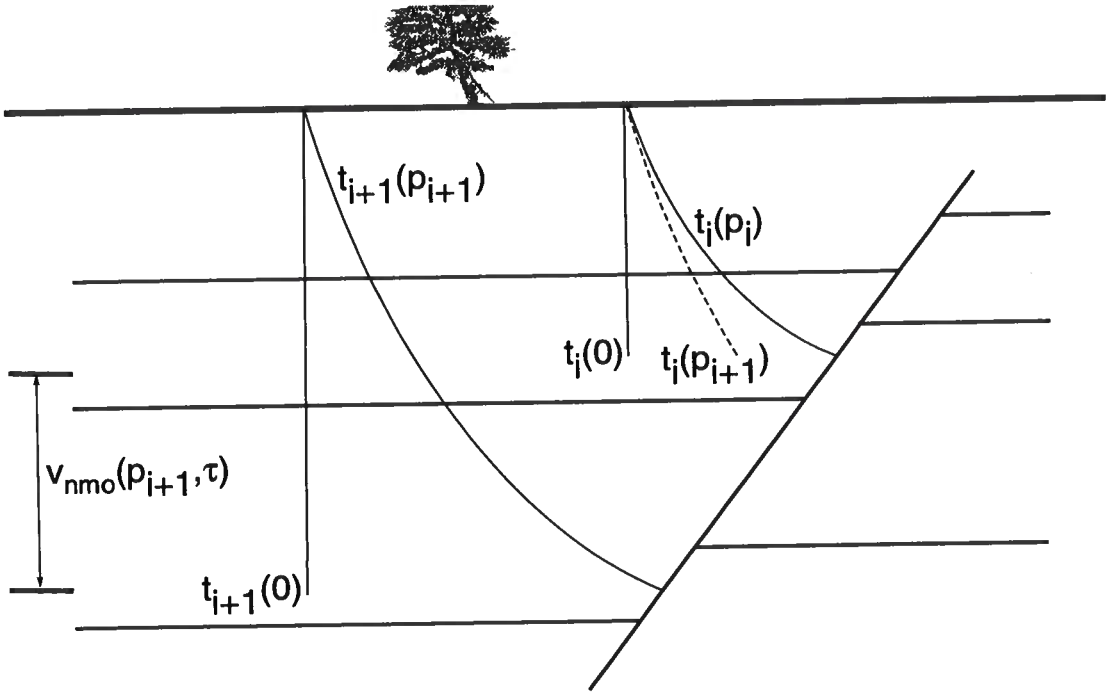

FIG. C.1. Depth model consisting of a fault and a number of horizontal layers. The rays drawn correspond to the measured stacking velocities ($V_{\text{nmo}}[p_i, t_i(p_i)]$ and $V_{\text{nmo}}[p_{i+1}, t_{i+1}(p_{i+1})]$) described in this Appendix. Such rays illustrate the relationship between the zero-offset time and the vertical time for reflections from the dipping fault.

of the next stacking velocity. These interval values are used in equation (C.3) to compute the first term, and again a_{i+2} becomes the only unknown in equation (C.3), which requires the same nonlinear inversion.

Appendix D

ANISOTROPIC RAY TRACING FOR TZO

Červený (1972) has derived an efficient ray-tracing system for general inhomogeneous, anisotropic media. This system is based on solving for the partial derivatives of the eigenvalues of the Christoffel 3×3 matrix, $\mathbf{\Gamma}$, rather than solving for the eigenvalues themselves. The components of this matrix are given by

$$\Gamma_{ik}(x_s, p_i) = a_{ijkl}(x_s) p_j p_l,$$

with

$$p_i = \frac{\partial \tau}{\partial x_i},$$

$$a_{ijkl} = c_{ijkl}/\rho,$$

where p_i are the three components of the slowness vector, τ is the traveltime along the ray, ρ is bulk density, x_s are the cartesian coordinates for position along the ray, s=1,2,3, and c_{ijkl} are elastic coefficients, in general, functions of x_s. In the above expression for Γ_{ik}, the summation convention for repeated indices is used.

From Červený (1972), the ray-tracing system for general inhomogeneous anisotropic media is given by

$$\frac{dx_i}{dt} = a_{ijkl} p_l g_j g_k,$$

$$\frac{dp_i}{dt} = -\frac{1}{2} \frac{\partial a_{njkl}}{\partial x_i} p_n p_l g_j g_k,$$

where g_i are the components of the eigenvector $\mathbf{g}$ (the direction of particle motion).

In 2-D, all out-the-plane components vanish, namely all components with subscript 2. The eigenvectors are then calculated as follows.

$$g_1 g_1 = \frac{\Gamma_{33} - G}{\Gamma_{11} + \Gamma_{33} - 2G},$$

$$g_3 g_3 = \frac{\Gamma_{11} - G}{\Gamma_{11} + \Gamma_{33} - 2G},$$

and

$$g_1 g_3 = \frac{-\Gamma_{13}}{\Gamma_{11} + \Gamma_{33} - 2G},$$

where G is the eikonal (described below) and $G = 1$ along the ray.

For TZO purposes the vertical axis, x_3, is conveniently replaced with vertical

time, τ. This can be accomplished by substituting the following equation

$$\frac{d\tau}{dx_3} = \frac{1}{V_{p0}} = \frac{1}{\sqrt{a_{3333}}}$$

into the ray-tracing system. Further, since we are considering a $v(z)$ medium, the ray parameter, $p_1 = p$, is constant and the ray tracing system in 2-D reduces to

$$\frac{dx_1}{dt} = a_{1jkl} p_l g_j g_k,$$

$$\frac{d\tau}{dt} = \frac{a_{3jkl}}{V_{p0}} p_l g_j g_k,$$

and p_3 is obtained using (Larner, 1993)

$$1 = 0.5\{(a_{1111} + a_{1313})p^2 + (a_{3333} + a_{1313})p_3^2 + \{[(a_{1111} - a_{1313})p^2$$

$$-(a_{3333} - a_{1313})p_3^2]^2 + 4(a_{1133} + a_{1313})^2 p^2 p_3^2\}^{\frac{1}{2}}\},$$

which involves solving a quadratic.

Also, both the phase velocity and phase angle need to calculated. They are given by

$$V(p) = \frac{1}{\sqrt{p^2 + p_3^2}},$$

and

$$\theta = \sin^{-1}(pV),$$

respectively. Both values are tabulated and used in solving the system of five equations for the ray trio mentioned prior to equation (4.1).

Appendix E

CALCULATION OF COMPLEX-VALUED TIME AND AMPLITUDE

E.0.1 Anisotropic kinematic ray-tracing

Červený (1972) has derived an efficient ray-tracing system in general inhomogeneous, anisotropic media. This system is based on solving for the partial derivatives of the eigenvalues for the Christoffel 3×3 matrix, $\mathbf{\Gamma}$, rather than solving for the eigenvalues themselves. The components of this matrix are given by

$$\Gamma_{ik}(x_s, p_i) = a_{ijkl}(x_s) p_j p_l,$$

with

$$p_i = \frac{\partial \tau}{\partial x_i},$$

$$a_{ijkl} = c_{ijkl}/\rho,$$

where p_i are the components of the phase vector ($p_1 = p_x$, etc.), τ is the traveltime along the ray, ρ is the bulk density, x_s are the cartesian coordinates for position along the ray, s=1,2,3, and c_{ijkl} are elastic coefficients, in general, functions of x_s.

From Červený (1972), the ray-tracing system for general inhomogeneous anisotropic media is given by

$$\frac{dx_i}{d\tau} = a_{ijkl} p_l g_j g_k,$$

$$\frac{dp_i}{d\tau} = -\frac{1}{2} \frac{\partial a_{njkl}}{\partial x_i} p_n p_l g_j g_k,$$

where g_i are the components of the eigenvector $\mathbf{g}$ (the direction of particle motion).

In two dimensions along a symmetry plane, all out-the-plane components are eliminated, namely all components with subscript 2. The eigenvectors are then calculated as follows:

$$g_1 g_1 = \frac{\Gamma_{33} - G}{\Gamma_{11} + \Gamma_{33} - 2G},$$

$$g_3 g_3 = \frac{\Gamma_{11} - G}{\Gamma_{11} + \Gamma_{33} - 2G},$$

and

$$g_1 g_3 = \frac{-\Gamma_{13}}{\Gamma_{11} + \Gamma_{33} - 2G},$$

where G is the eikonal, described below, and $G = 1$ along the ray.

Because the square-roots associated with calculation of the phase and group ve-

locities directly from the eikonal, G, have been eliminated, this is a relatively efficient method of ray tracing, especially in general anisotropic media.

E.0.2 Anisotropic dynamic ray-tracing

The parameters p and q, which relate a calculated central ray to a nearby projected paraxial ray, are given by Červený (1981) for isotropic media

$$\frac{dq}{d\tau} = v^2 p \qquad \frac{dp}{d\tau} = -\frac{v_{,nn}}{v} q,$$

where n is the normal to the ray direction (which is the same as phase direction for isotropic media), and v and $v_{,nn}$ are, respectively, the velocity and its second derivative with respect to n.

A paraxial ray is a ray (not actually traced) in the vicinity of the central ray. Its normal distance from the central ray is described by the value of q, and the difference in the two propagation angles is characterized by p.

For anisotropic media, the dynamic ray tracing is more complicated. The ray-centered coordinates are no longer orthogonal as they are for isotropic media, so we must compute an extra quantity, V, along the ray to compensate for the non-orthogonality. The dynamic ray-tracing equations given by Hanyga (1986) for anisotropic media are

$$\frac{dq}{d\tau} = Mp + Vq, \tag{E.1}$$

and

$$\frac{dp}{d\tau} = -Vp - Hq, \tag{E.2}$$

where M,V,H are derivatives of the eikonal with respect to n and p_n, the ray parameter in the direction of n, normal to the phase direction. These derivatives are given by

$$H = 0.5\frac{\partial^2 G_m}{\partial n^2} - 0.25(\frac{\partial G_m}{\partial n})^2$$

$$M = 0.5\frac{\partial^2 G_m}{\partial p_n^2} - 0.25(\frac{\partial G_m}{\partial p_n})^2$$

$$V = 0.5\frac{\partial^2 G_m}{\partial p_n \partial n} - 0.25\frac{\partial G_m}{\partial p_n}\frac{\partial G_m}{\partial n}.$$

Here, G_m, m=1,2,3 are the eigenvalues of the Christoffel equation

$$Det(\Gamma_{jk} - G_m \delta_{jk}) = 0.$$

G_m are the three eigenvalues representing the eikonal equation for the three wave types: quasi P-wave when m=1; quasi SV-wave when m=2; and quasi SH-wave when

m=3. G_m for anisotropic media is given by

$$G_m = a_{ijkl} p_i p_l g_j g_k.$$

E.0.3 Paraxial expansion and amplitude

Consider ray-centered coordinates (s, n), where s is the distance along the ray and n is the distance normal to the phase-velocity direction. The expansion of traveltime along n using Taylor's series gives the parabolic equation (Červený, 1981)

$$T(s,n) \cong T(s) + 0.5 \frac{\partial^2 T(s)}{\partial n^2} n^2. \tag{E.3}$$

$T(s)$ is the traveltime along the central ray obtained from kinematic ray tracing, described above, and $\frac{\partial^2 T(s)}{\partial n^2}$ is a complex variable for Gaussian beam ray-tracing given by (Červený and Pšenčík, 1984)

$$\frac{\partial^2 T(s)}{\partial n^2} = \frac{P}{Q} = \frac{p_1 + i p_2}{q_1 + i q_2},$$

where q_1, p_1 and q_2, p_2 are solutions of the dynamic ray-tracing for a plane source and a point source, respectively. The real part of this complex-valued term describes ray curvature, and the imaginary part is a factor associated with the Gaussian-shaped decay away from the ray.

This is the same equation used for the isotropic case; however, here n is in the direction normal to the phase direction, not to the ray direction. Furthermore, q_1, p_1, q_2 and p_2 are computed using anisotropic dynamic ray-tracing [equations (E.1) and (E.2)], where their initial values are taken to be $q_1 = 1$, $p_1 = 0$, $q_2 = 0$ and $p_2 = 1$.

The complex valued amplitude, whose components A_R and A_I appeared in equation (5.12), is calculated using dynamic ray-tracing. It is the same equation used in isotropic media, given by (Hill, 1990; Hanyga, 1986)

$$A(t) = A_0 \sqrt{\frac{v(t)}{Q(t)}},$$

where $Q = q_1 + i q_2$ and v is the group velocity at time t. The initial amplitude A_0 can be taken as constant or angular dependent depending on the type of source or receiver considered. For a scalar point source or receiver, a constant A_0 is sufficient. However, if the source or receiver has directivity, a more complicated radiation pattern is needed. For a vertical source or receiver, A_0 is given by the vertical component of the normalized polarization vector, g_3, multiplied by an initial amplitude.

As in isotropic media, two conditions must hold to keep the numerical calculation stable, even for rays traveling through caustics. The two conditions are $\mathrm{Im}(\frac{P}{Q}) > 0$

and $\mid Q \mid \neq 0$.

E.0.4 Ray-parameter spacing

For isotropic media, Hale (1992) uses as the ray-parameter increment

$$(\Delta p_x)_{iso} = \frac{2\pi}{3l\sqrt{\mid \omega_l \omega_h \mid}},$$

where ω_l is the lowest frequency of interest, ω_h is the highest; and l is the related initial beam width. This choice ensures adequate ray coverage to avoid aliasing and, therefore, to properly construct the wavefield. For anisotropic media, the values of p_{min} and p_{max} are different from those for isotropic media, given the same minimum and maximum angles of interest and the same vertical velocity. As a result, the following modified expression yields the the same amount of ray coverage as that used in the isotropic case.

$$\Delta p_x = (\Delta p_x)_{iso} \frac{2v_{min}}{V_{min}(p_{max}) + V_{min}(p_{min})}, \tag{E.4}$$

where v_{min} is the minimum vertical velocity found along the surface ($z = 0$), and $V_{min}(p_{max})$ and $V_{min}(p_{min})$ are the phase velocities corresponding to the maximum and minimum ray parameters, respectively, at the point on the surface where vertical velocity is v_{min}. Recall that ray angles differ from phase angles in anisotropic media, a fact that must be taken into consideration when determining the minimum and maximum ray parameter of interest. If the maximum and minimum ray angles are 90 and -90 degrees, respectively, in a transversely isotropic media with vertical symmetry axis, then equation (E.4) reduces to

$$\Delta p_x = (\Delta p_x)_{iso} \frac{V(0)}{V(90)},$$

where V is the phase velocity as a function of angle.

In anisotropic media, for each initial ray parameter p_x, I solve for the vertical ray parameter p_z using

$$p_z = \sqrt{\frac{1}{V^2(p_z)} - p_x^2},$$

where V is the phase velocity. For a 2-D symmetry plane, this turns out to be a quartic equation, which I solve by the secant method. For transversely isotropic media, however, the equation reduces to a quadratic.